Title
Magnetospheric Particle Injections and their Relation to Impulsive, Localized Electric Fields

Author
Lin, Christine Elizabeth Gabrielse

Publication Date
2014

Peer reviewed|Thesis/dissertation

UNIVERSITY OF CALIFORNIA

Los Angeles

Magnetospheric Particle Injections and their Relation to Impulsive, Localized Electric Fields

A dissertation submitted in partial satisfaction of the

requirements for the degree Doctor of Philosophy

in Geophysics and Space Physics

by

Christine Elizabeth Gabrielse Lin

2014

ABSTRACT OF THE DISSERTATION

Magnetospheric Particle Injections and their Relation to Impulsive, Localized Electric Fields

by

Christine Elizabeth Gabrielse Lin

Doctor of Philosophy in Geophysics and Space Physics

University of California, Los Angeles, 2014

Professor Vassilis Angelopoulos, Chair

Energetic particle injections in the near-Earth plasma sheet are critical for supplying particles and energy to the radiation belts and ring current. Their origin, however, has been elusive due to the lack of equatorial, multi-point observations. After the launch of NASA's Time History of Events and Macroscale Interactions during Substorms (THEMIS) mission in 2007, intense electric fields and elevated energetic particle fluxes have been observed to accompany localized (1-4 R_E wide) bursty bulk flows and to propagate from the mid-tail regions (at geocentric radial distances $R > 25R_E$) towards Earth, up to and at times inside of geosynchronous orbit (GEO, $R=6.6R_E$). Motivated by these observations, I model simultaneous multi-point observations of electron injections using guiding center approximation in prescribed but realistic electric and magnetic fields to better understand the nature of their acceleration. Additionally, I perform a statistical analysis of the electron and ion injections to better

understand their properties observationally. I find a good correlation between injections and azimuthally localized fast flows, dipolarization fronts and impulsive, dawn-dusk electric field increases. This correlation is present regardless of distance, from inside GEO out to 30 R_E. The findings are inconsistent with the classical concept of injections forming from an azimuthally wide injection boundary moving earthward from ~9-12 R_E to GEO under an enhanced, large-scale, duskward electric field. Modeling of electron injections assuming a localized, impulsive, potential electric field transported from mid-tail to near-Earth at bursty flow speeds of ~400 km/s successfully reproduces the observations at multiple spacecraft. Addition of a small, inductive electric field component, related to the dipolarizing magnetic field consistent with observations, further improves the agreement between modeled and observed electron spectra. The impulsive, localized, and vortical nature of the earthward-propagating electromagnetic pulse is what makes this model particularly effective in reproducing both the injection and the dispersed decrease in energy flux often observed simultaneously with the injection but at lower energies (~10-30 keV). The results suggest that particle acceleration and transport towards the inner magnetosphere can be thought of as a superposition of individual bursts of varying intensity and cadence depending on global geomagnetic activity levels.

The dissertation of Christine Elizabeth Gabrielse Lin is approved.

Margaret G. Kivelson

Lawrence R. Lyons

Vassilis Angelopoulos, Committee Chair

University of California, Los Angeles

2014

This dissertation is dedicated to my parents, sisters, and grandparents, all of whom played integral parts in encouraging my love for exploration,

to my husband, Lin Junwen, who has been my support and best friend as we traversed this adventuresome road together,

and to my Heavenly Father, whose grace has carried me all the way.

TABLE OF CONTENTS

LIST OF FIGURES

LIST OF TABLES

ACKNOWLEDGEMENTS

To quote one of UCLA's finest, "The main ingredient of stardom is the rest of the team" (Coach John Wooden). In that light, this thesis would not exist if not for the numerous individuals who have been my guidance, my support, and my inspiration. Firstly, I will be forever grateful to my adviser, Prof. Vassilis Angelopoulos, who has guided me through the field of space physics and who has shown me how to be a scientist. In taking me on during the THEMIS mission's first year in orbit, Vassilis provided me the opportunity to follow and participate in a mission from its main through its extended phases. With so many new data at our fingertips, Vassilis guided me through several different projects—such as timing substorm phenomena, correlating flapping waves in the neutral sheet to bursty bulk flows, and mapping ionospheric signatures into the magnetotail—before I started studying injections. This offered me a wider breadth of understanding than a single focus could provide, and provided the opportunity to meet and interact with a larger population of this great community. I am also thankful that Vassilis' door was always open—even though he has a multitude of responsibilities, he would always encourage his students to come by whenever we had questions. I have appreciated that Vassilis encourages a well-rounded individual, allowing me to begin presenting my work at conferences just months after starting graduate school, as well as to take part in enlightening external courses such as the Heliophysics summer school held in Boulder, CO, and the Substorms course held in Longyearbyen, Svalbard. All of his support and teaching has allowed me to spread my wings, carrying new tools to explore the physical world we live in.

This work would also not have been possible without the support and guidance of the THEMIS team here at UCLA. I am forever thankful to Andrei Runov, who has been another mentor throughout my entire graduate program. Andrei has taught me much about multi-

spacecraft missions, dipolarization fronts, and a multitude of other topics, not the least of which include the many facets of our role as researchers. Being quite active in the community chairing sessions and leading research teams, Andrei has been a shining example of how to be a team player. His guidance in my research projects has been immeasurably helpful, and I am thankful for his help in chapters 2-4 of this dissertation. I am also indebted to Xuzhi Zhou and Drew Turner whose suggestions and comments have greatly improved this work. Xuzhi has always been open and happy to help explain some physics concepts I had difficulty wrapping my brain around, and Drew's contagious excitement for space physics was always a great motivator. Drew contributed to Chapters 2 and 3. Those who spent time as graduate students with me, Jiang Liu, Xiaojia Zhang, Shanshan Li, Justin Lee, and Michael Hartinger were also a great source of support, and I am thankful to the now Dr. Jiang Liu for his explanations of dipolarizing flux bundles and for the portion they play in this dissertation.

The "team" behind this dissertation extends beyond our research group. I am so thankful to Prof. Margaret Kivelson for providing a much deeper understanding to the relationships between flows, magnetic fields and electric fields. With her help, physics that I only understood mathematically became clear conceptually, such as the causal relationship between a magnetic field and its inductive electric field. I am also indebted to Prof. Larry Lyons, who I had the opportunity to take several classes from (such as magnetohydrodynamics) and cannot speak more highly of his teaching methods. I also highly benefited from the fact that our two research groups met weekly, meaning I could learn his point-of-view on magnetospheric occurrences like fast flows and their relationship to ionospheric observations such as auroral streamers. Perhaps my general knowledge of space physics and the magnetosphere could best be attributed to Prof. Robert McPherron, who taught my first class on the subject here at UCLA. Bob not only helped

paint the backdrop of my understanding, he also relayed the importance of statistics to answering a scientific question, and thus to him I can attribute the development of my statistical study presented in Chapter 2. These three individuals have also honored me by agreeing to sit on my committee, and I am thankful for their help in the development of this dissertation. I am furthermore indebted to Prof. Ray Walker, who took the time to prepare me for my preliminary exam and truly trained me in how to think about space physics. Prof. Christopher Russell also has my thanks for sitting on my committee for the preliminary exam prior to the award of my Master's degree. I also want to thank Victor Sergeev for meaningful discussions regarding our model and Chih-Ping Wang for his help in describing the two-kappa phase space densities observed in the magnetotail. I acknowledge and thank Judy Hohl for her assistance with copy-editing, Patrick Cruce, Aaron Flores, Cindy Russell, and Brian Kerr for their help with software, programming, and computing issues, and Bill Harris for his help with everything IT related. Emmanuel Masongsong has also been a great source of help and support for various and sundry items, not the least of which was helping to get this dissertation into my committee's hands when I was overseas at EGU and the email system went down.

Besides support and guidance on the dissertation material, anyone who has gone through the process knows that there are others behind the scenes whose support makes it all possible. I am particularly thankful for the friendships of Jennifer Kissinger, Feifei Jiang, and Katherine Ramer, who traveled the grad school path with me at UCLA and who have been a constant source of support along the journey. I am thankful for all of the friends I met through University Presbyterian Church who have been a source of love and encouragement ever since I moved to Los Angeles.

I would also like to thank and acknowledge those who played an integral part in my development before graduate school. Prof. Ramon E. Lopez, Betsey Mitchell, Sandra Brogl, and Robert Bruntz were key players during my undergraduate years by first introducing me to the field of space physics and, even more specifically, to substorms. Without Ray Lopez's instruction and guidance as a research mentor, I would not be writing this dissertation today. Even prior to that, I have my junior high science teacher, Mr. Steve VanDrunen, to thank for introducing me to science and for giving me the backbone and character necessary to face the harshness of failure with the motivation to keep learning until I succeed. I carry his lessons from the classroom and the sports arena with me to this day.

Finally, I would like to thank my family for their love and support throughout my entire education process; without them I would not be here today. To my parents, Jon and Julie Gabrielse, for teaching me the love of discovery, learning, and outer space. Thank you, for all you have given and sacrificed in order to provide your children stellar opportunities and wonderful lives. To my sisters, Amy Gabrielse Holte, Heidi Cotton, and Sarah Gabrielse (soon-to-be Lutgendorff), for being my companions and adventure seekers throughout childhood and for being my support and inspiration as adults. To my grandparents, Larry and Marian Gabrielse and Weber and Joyce Van Der Puy, who helped raise me and gave me the confidence to shoot for my dreams. To my family in Singapore, parents Lim Chee Yong and Lee Lay Hong and brother Lin Junxian, for their love and encouragement that knows no borders. Ultimately, to my loving husband, Lin Junwen, whose love, support, and meaningful conversations have kept me sane, whose belief in me has given me courage, and whose friendship has built me into a better person.

I acknowledge NASA contract NAS5-02099 and NSF grant 1044495 for use of data from the THEMIS Mission; NASA grant NNX13AF81G for funding part of this work; C.W. Carlson and J.P. McFadden for use of ESA data; D. E. Larson and R.P. Lin for use of SST data; K. H. Glassmeier, U. Auster and W. Baumjohann for the use of FGM data provided under the lead of the Technical University of Braunschweig and with financial support through the German Ministry for Economy and Technology and the German Center for Aviation and Space (DLR) under contract 50 OC 0302; J. W. Bonnell and F. S. Mozer for use of EFI data. The AL indices were provided by the World Data Center for Geomagnetism, Kyoto. We thank the many geomagnetic observatories, institutions, and international organizations which kindly supply the data to their data center.

Chapter 2 is a version of *Gabrielse et al.* [2014].

Chapter 3 is a version of *Gabrielse et al.* [2012].

Chapter 4 contains text and figures that will be published at a later date.

Appendices 1-9 contain the license agreements for the use of previously copyrighted material within this thesis.

VITA

Education

2007 B.S. in Space Sciences, magna cum laude, Florida Institute of Technology, Melbourne, FL

2009 M.S. in Geophysics & Space Physics, UCLA, Los Angeles, CA

2010 AGF-345 *Polar Magnetospheric Substorms*, 10-credit course, University of Tromsø, NORWAY

Research Experience

08/07—present *Graduate Student Researcher, UCLA, Los Angeles, CA*
Dr. Vassilis Angelopoulos
Research projects heavily involve THEMIS data and software as well as IDL.

01/06—05/07 *Undergraduate Research Work-study, Florida Institute of Technology, Melbourne, FL*
Dr. Ramon Lopez
Substorm Energy Deposition and Correlation with Substorm Characteristics

06/06—08/06 *Research Associate, NASA Academy, Goddard Space Flight Center, Greenbelt, MD*
Research, team, and leadership development program.

05/05—12/05 *Undergraduate Researcher, Kennedy Space Center/Nanophysics Lab, Florida Institute of Technology, Melbourne, FL*
Researched properties of JSC Mars-1 and JSC-1 Mars and Lunar soil simulants.

Publications

Gabrielse, C., V. Angelopoulos, A. Runov, and D. L. Turner (2014), Statistical characteristics of particle injections throughout the equatorial magnetotail, *J. Geophys. Res.*, DOI: 10.1002/2013JA019638

Gabrielse, C., V. Angelopoulos, A. Runov, and D. L. Turner (2012), The effects of transient, localized electric fields on equatorial electron acceleration and transport toward the inner magnetosphere, *J. Geophys. Res*., 117, A10213, doi:10.1029/2012JA017873

Gabrielse, C., et al., Timing and localization of near-Earth tail and ionospheric signatures during a substorm onset, *J. Geophys. Res*., 114, A00C13, doi:10.1029/2008JA013583, 2009

Gabrielse, C., V. Angelopoulos, A. Runov, L. Kepko, K.-H. Glassmeier, U. Auster, J. McFadden, C. Carlson, and D. Larson, Propagation characteristics of plasma sheet oscillations during a small storm, *Geophys. Res. Lett*., 35, L17S13, doi:10.1029/2008GL033664, 2008

Liu, J., **C. Gabrielse**, V. Angelopoulos, N. A. Frissell, L.R. Lyons, J. P. McFadden, J. Bonnell, and K.H. Glassmeier, Superposed epoch analysis of magnetotail flux transport during substorms observed by THEMIS, *J. Geophys. Res*., 116, A00I29, doi:10.1029/2010JA015886, 2011

Runov, A., V. Angelopoulos, **C. Gabrielse**, X.-Z. Zhou, D. Turner, F. Plaschke, Electron fluxes and pitch-angle distributions at dipolarization fronts: THEMIS multi-point observations, *J. Geophys. Res*., doi: 10.1002/jgra.50121, 2013

Selected Honors and Awards

09/13 Eugene B. Waggoner Scholarship in recognition of academic performance and outstanding original research by a Ph.D. candidate, ESS Dept, UCLA

06/13 1st place award: Geospace Environmental Modeling (GEM) conference Student Tutorial

04/13 1st place award: UCLA Earth and Space Sciences Student Symposium presentation

04/07 Best of Student Showcase award, senior project, Florida Institute of Technology

04/06 Outstanding Junior in Space Sciences 2005-2006, Florida Institute of Technology

04/05 Outstanding Sophomore in Space Sciences 2004-2005, Florida Institute of Technology

03/05 Herbert-Levy Endowment Fund Scholarship, Society of Physics Students

Selected Education and Public Outreach

10-13—present *Undergraduate Research Mentor,* UCLA, Los Angeles, CA

01/14 Interviewing a MAARBLE (Monitoring, Analyzing and Assessing Radiation Belt Loss and Energization) Scientist: http://www.maarble.eu/outreach/index.php/interviewing-a-maarble-scientist--january-2014

01/13 THEMIS Interviews: *Snap Goes the Particle*. High school audience. http://cse.ssl.berkeley.edu/artemis/epo-interviews.html

Selected Professional Presentations

04/14 European Geophysical Union; Vienna, Austria; *Invited Talk*
Gabrielse, C., V. Angelopoulos, A. Runov, D. L. Turner, The effects of transient, localized electric fields on equatorial electron acceleration and transport toward the inner magnetosphere

12/13 American Geophysical Union; San Francisco, CA; *Invited Talk*
Gabrielse, C., V. Angelopoulos, A. Runov, D. L. Turner, The effects of transient, localized electric fields on equatorial electron acceleration and transport toward the inner magnetosphere

12/13 American Geophysical Union; San Francisco, CA; *Poster*
Gabrielse, C., V. Angelopoulos, A. Runov, D. L. Turner, Statistical characteristics of particle injections throughout the equatorial magnetotail

03/10 10th International Conference on Substorms; Pismo Beach, CA; *Talk*
Gabrielse, C., V. Sergeev, J. Liu, N. Frissell, S. Kiehas, E. Spanswick, T. Takada, S. Apatenkov, A. Runov, V. Angelopoulos, G. Reeves, Substorm Parameters: A Progress Report

12/09 American Geophysical Union; San Francisco, CA; *Poster*
Gabrielse, C., V. Angelopoulos, M. Kubyshkina, A. Runov, H. U. Frey, J. McFadden, D. E. Larson, K.-H. Glassmeier, S. Mende, C. T. Russell, Building Tools: Mapping the Aurora Downtail and Particles to the Ionosphere

05/08 9th International Conference on Substorms; Seggau, Austria; *Poster*
Gabrielse, C., V. Angelopoulos, A. Runov, X.-Z. Zhou, J. McFadden, D. E. Larson, K.-H. Glassmeier, S. Mende, C. T. Russell, H. U. Frey, THEMIS observations at a substorm onset on February 16, 2008

12/07 American Geophysical Union; San Francisco, CA; *Poster*
Gabrielse, C., V. Angelopoulos, A. Runov, L. Kepko, K.-H. Glassmeier, U. Auster, J. McFadden, C. Carlson, and D. Larson, Propagation characteristics of plasma sheet oscillations during a small storm

CHAPTER 1

Introduction

1.1 Particle Injections

Energetic particle injections—sudden particle flux enhancements at energies of 10s to 100s keV—are significant in providing the seed population for radiation belt particles, populating the ring current, and creating particle velocity space anisotropies that drive ion cyclotron or whistler mode chorus waves that are responsible for losses or further acceleration in the inner magnetosphere. It is therefore important to understand injection properties, spatial characteristics, dependence on activity and driver mechanisms. When injections are observed simultaneously with other plasma and fields measurements, they help elucidate potential mechanisms for particle transport and energization, a topic of great importance for understanding and modeling the magnetosphere. In particular, determining the source of particles in the inner magnetosphere is quite relevant to storm dynamics and space weather. The inner magnetosphere is the region within the zero energy Alfvén layer, where hot magnetotail electrons cannot ordinarily reach because of their gradient/curvature drifts. Injections, therefore, can play an important role in supplying the inner magnetosphere with a source population by "injecting" electrons past the Alfvén layer such that the electrons can become trapped onto closed drift orbits. Wave acceleration in the radiation belts can then further energize these seed populations to relativistic energies, at which point they pose a risk to societal assets like telecommunication and navigation satellites [*Kappenman et al*., 1997; *Chen et al*., 2007; *Turner et al*., 2010].

Injections can be classified as "dispersionless", "dispersed", and "inversely dispersed" (or, having "inverse velocity dispersion" [*Sarris et al.*, 1976; *Sarafopoulos and Sarris*, 1988]),

based on the observed timing of the flux enhancements in different energy ranges. If a satellite directly observes the injection at its source location, the flux enhancement occurs simultaneously over all energies and is called "dispersionless". If a satellite is azimuthally distant from the acceleration site, there is an energy-dependent delay in flux enhancement with more energetic particles arriving first due to energy-dependent $\nabla\mathbf{B}$ and curvature drift velocities, resulting in a "dispersed" flux enhancement signature [*Zaharia et al.*, 2000]. Within the inner magnetosphere, where the particles are on trapped orbits, the spacecraft may observe "drift echoes" by observing injections multiple times with progressively increased dispersion when the particles complete full drift orbits [*Lanzerotti et al.*, 1967].

As their name suggests, inversely dispersed injections are dispersed in the opposite sense—i.e., the flux at lower energy particles increases prior to more energetic ones. These injections were first observed as field-aligned streaming protons by *Sarris et al.* [1976] using IMP-7 around 35 R_E, and were explained as a manifestation of the time-evolution of the accelerating field-aligned inductive electric field [*Galeev,* 1979; *Zelenyi*, 1984]. Another explanation proposed by *Sarris and Axford* [1979] relied upon the spatial velocity separation effect that applies to reconnection-accelerated particles, which can be observed as a spacecraft travels out of the plasma sheet near the reconnection X-line, crossing reconnected field lines in the order that they underwent reconnection. Particles on field lines that reconnected earlier have had more time to travel away from the separatrix (with the energetic particles traveling faster), than particles on recently connected field lines that are filled with more energetic particles closer to the separatrix. As the spacecraft crosses these field lines from the neutral sheet outward, it observes lower energy particles first (where the faster, higher energies have already evacuated) and higher energy particles later.

Because of the plethora of satellites located at geosynchronous orbit, injections have largely been studied there [e.g., *Lanzerotti et al.*, 1967; *McIlwain*, 1974; *Walker and Kivelson*, 1975; *Mauk and Meng*, 1983; *Birn et al.*, 1997a, 1997b, 1998; *Li et al.*, 1998; 2003; *Thomsen et al.*, 2001; *Sarris et al.*, 2002]. With the Time History of Events and Macroscale Interactions during Substorms (THEMIS) satellites having orbital configurations that sweep across the magnetotail, radially covering from 6 to 30 R_E downtail [*Sibeck and Angelopoulos*, 2008], we now have a dataset available to extend the picture of injection formation painted from GEO data, adding depth and clarity with the additional multi-point information THEMIS provides.

1.2 Modeling Injections

Up until this point, ideas on how particles are energized and how the radiation belts are populated were developed based on injection observations at GEO. These studies have led to the concept of an "injection front" or "injection boundary", such that injection signatures are produced mainly by the earthward motion of a boundary between hot and cold plasma [*Mauk and McIlwain*, 1974; *Konradi et al.*, 1975; *Mauk and Meng*, 1983], or by a compression-like wave that heats and transports the plasma as it propagates from the tail into the inner magnetosphere [*Moore et al.*, 1981].

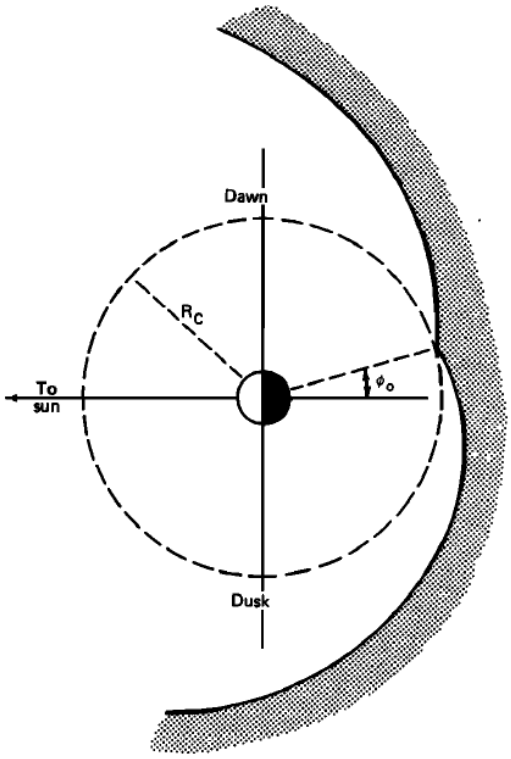

Figure 1.1 From *Mauk and Meng* [1983]. The geometry of the proposed injection boundary. This geometry would exist as shown only at the initiation of the injection (t = 0).

Birn et al. [1997a] demonstrated statistically that a spatially-dependent pattern exists for dispersionless injections which can be explained as two injection boundaries—one for electrons, one for ions—that are offset from each other (**Figure 1.2**). Typically, ion injections are observed towards dusk (~3 hours before midnight) and electron injections towards dawn (~2 hours after midnight). Both can be observed in between (electrons appear before ions towards the dawn, ions appear before electrons towards the dusk, and both occur simultaneously in the center). This pattern was corroborated by *Thomsen et al.* [2001], who used two geosynchronous satellites to show that the pattern occurs not only statistically, but also for individual injection events.

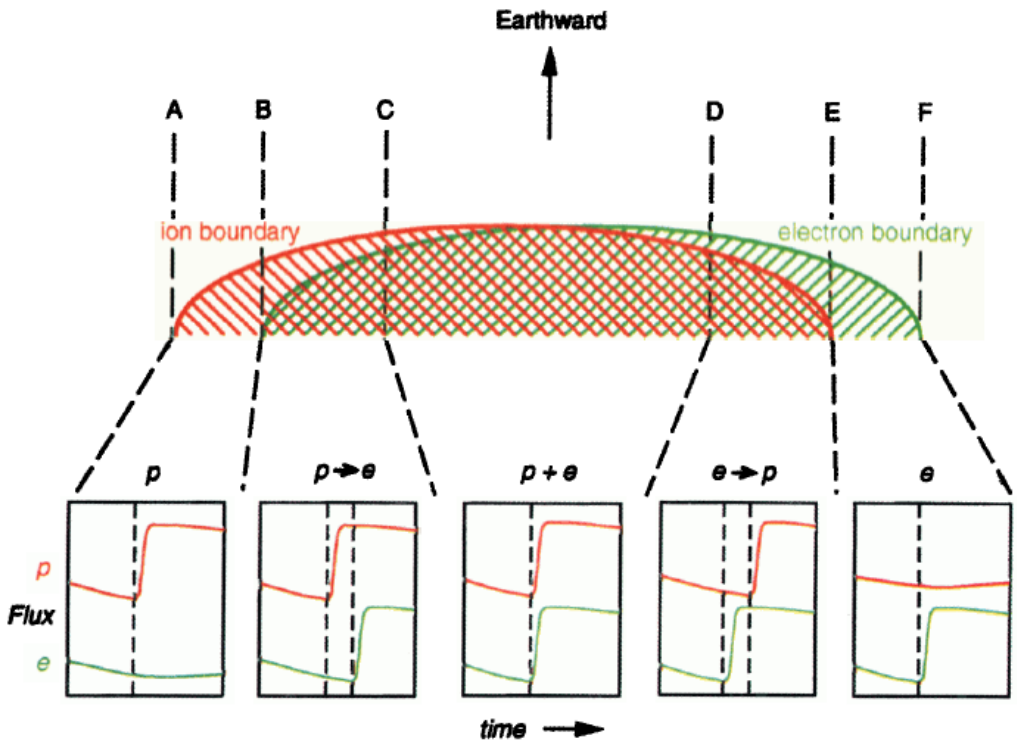

Figure 1.2 From *Birn et al.* [1997a]. Schematic of non-identical ion and electron injection boundaries in the equatorial plane, illustrating different categories of dispersionless injections (as defined in *Birn et al.* [1997a] after *Birn et al.* [1996]). If such boundaries move earthward toward positive x, dispersionless ion injections only would be observed between lines A and B, delayed p→e injections between lines B and C, simultaneous p+e injections (within a given time resolution) between lines C and D, delayed e→p injections between lines D and E, and electron injections only between lines E and F. Westward (left) of line A one would see dispersed ion events (and highly dispersed electron drift echoes) and eastward (right) of line E one would see dispersed electron events (and ion echoes). Similar effects would occur when the boundaries expand azimuthally.

The abundant observations at geosynchronous orbit also provided the data to test models of particle transport and acceleration. *Birn et al.* [1997b; 1998] traced particles in a three-dimensional MHD simulation of magnetic dipolarization in the magnetotail, finding that particles were largely accelerated via betatron acceleration as they were transported by a time-dependent dawn-dusk electric field from a weak magnetic field downtail to a stronger magnetic field at geosynchronous orbit. *Li et al.* [1998; 2003], *Sarris et al.* [2002], and *Ganushkina et al.* [2013] simulated geosynchronous injections numerically using an azimuthally wide, earthward traveling

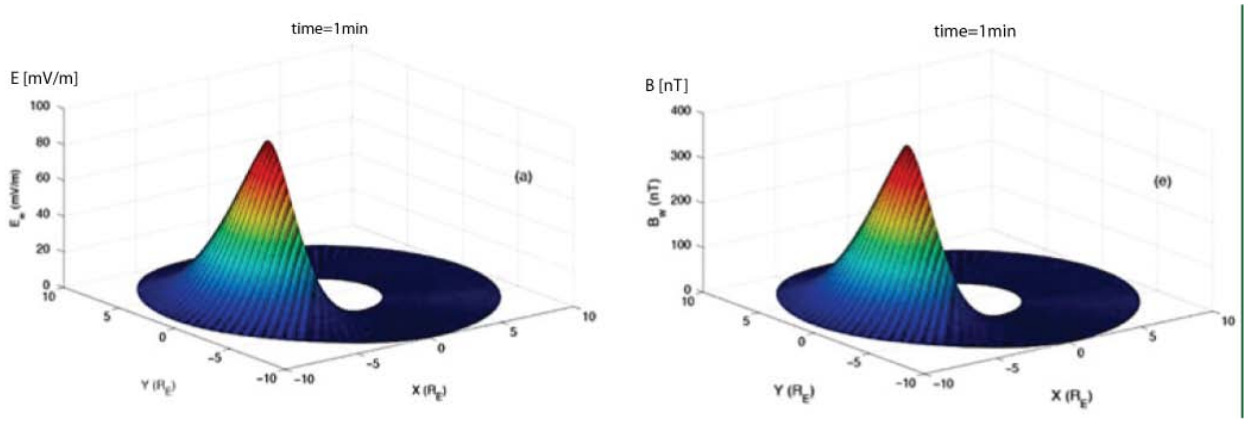

Figure 1.3 Adapted from *Ganushkina et al.* [2013]. Illustration of the electric and magnetic field from the electromagnetic field pulse defined by equations developed in *Li et al.* [1993; 1998; 2003] and *Sarris et al.* [2002]. Left panel is electric field, right panel is magnetic field. The two are related through Faraday's Law.

electromagnetic pulse originally developed by *Li et al.* [1993] (see Figure 1.3). A similar study was also done by *Zaharia et al.* [2000] but with a pulse of a different functional form. The conclusion from these studies is that injections can be caused by an earthward, compressional magnetic field perturbation and its associated electric field corresponding to a large-scale collapse of the magnetotail (i.e., global dipolarization). This effectively pushes particles in to geosynchronous orbit from ~9-11 R_E. Lack of consistent outer magnetospheric observations, however, made it impossible to constrain these models, leaving trans-geosynchronous injections (those at L-shells higher than 6.6 R_E) poorly characterized and disjoined from those at geosynchronous orbit.

Trans-geosynchronous injections have been observed as far out as ~60 R_E in the past [*Konradi*, 1966; *Armstrong and Krimigis*, 1968; *Sarris et al.*, 1976 and references therein], as well as in recent times by THEMIS (out to ~30 R_E). These observations suggest that the source of near-Earth injections may not be that of an azimuthally extended boundary moving earthward from ~12 R_E towards geosynchronous orbit, but rather that of a localized, transient acceleration

source, moving across large distances in the magnetotail. This acceleration mechanism appears to be related to bursty bulk flows (BBFs), continuous segments of magnetotail flow enhancement (~10-min), punctuated by ~1-min long intense flow and electric field bursts (V>400 km/s, $V_X B_Z$>2mV/m) [*Angelopoulos et al*., 1992; 1994a; *Schödel et al*., 2001]. Indeed, *Sergeev et al.* [2005] found that 75% of 28 dispersionless injections observed *in-situ* was seen within a 2-hour MLT-wide strip centered at the intrusion meridian of an auroral streamer. (Auroral streamers are considered ground observations of BBFs, as *Lyons et al.* [2012] showed using ground auroral data and THEMIS in-situ data to demonstrate the correlation between these two processes.) Similarly, *Runov et al.* [2009; 2011] used case studies to show that dipolarization fronts are associated with fast flows, transient electric fields, and energetic particle flux enhancements (See Figure 1.4).

The question of how particle acceleration and transport occurs in the magnetotail is therefore modified to: Are injections related to the narrow, transient fast flows and electric fields as recent case studies have suggested, or are they simply the result of an azimuthally wide injection boundary moving Earthward from ~11 R_E with a global dipolarization? This dissertation utilizes a statistical study of injections as well as an analytical model of the transient electromagnetic field pulse associated with narrow fast flows to claim that indeed injections are related to fast flows.

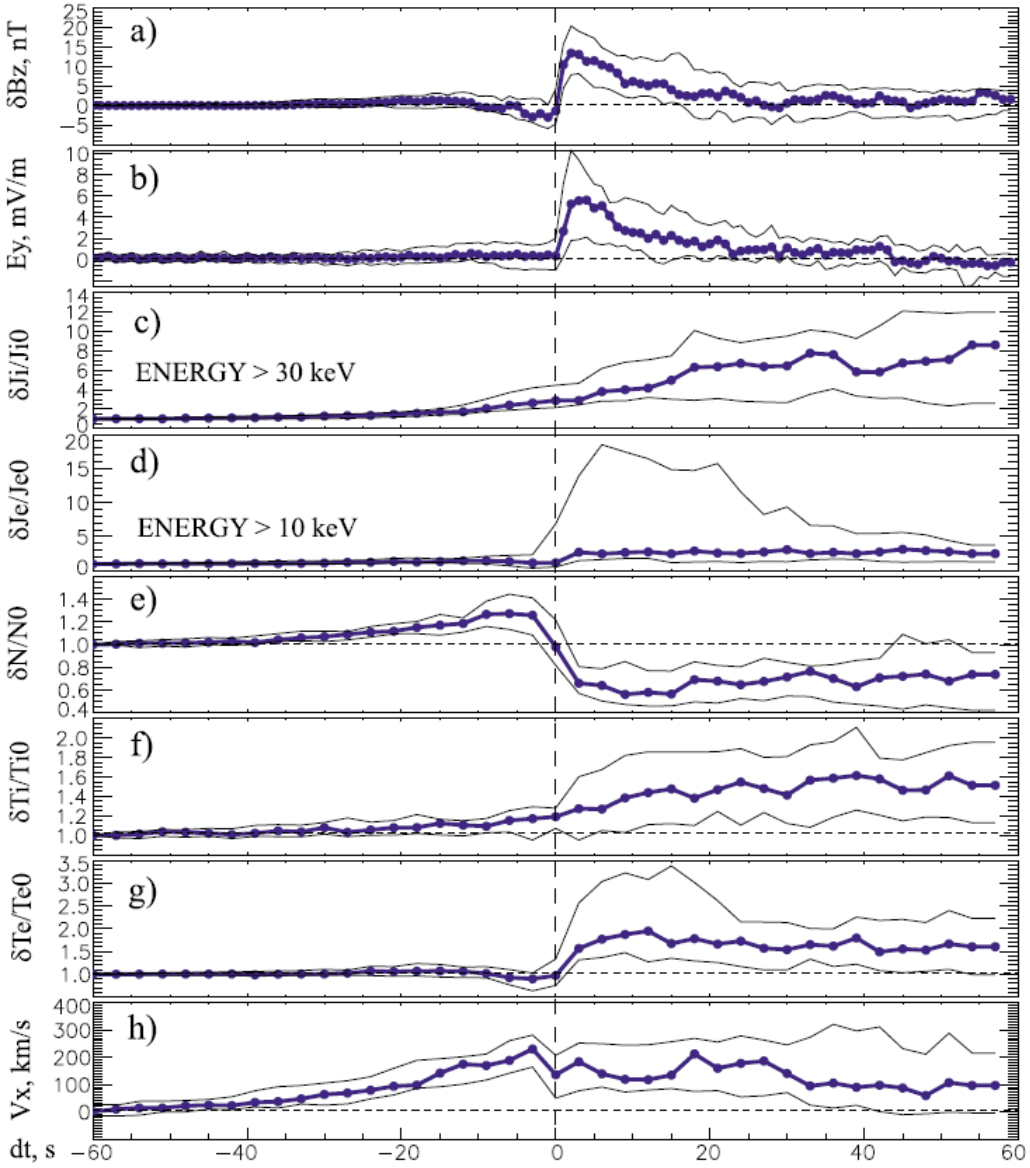

Figure 1.4 From *Runov et al.* [2011]. Superposed epoch analysis of magnetic field and particle observations. Median (thick blue lines) and lower and upper quartiles (thin black lines) of (a) Bz variations (ΔBz), (b) cross-tail electric field (Ey), (c) ion and (d) electron integrated energy fluxes, normalized by the initial value (δJi/Ji$_o$, δJe/Je$_o$), (e) normalized density (δN/N$_o$), (f) ion (δTi/T$_o$) and (g) electron (δTe/T$_o$) variations, and (h) X component of ion velocity. Here t_0 (vertical dashed line) indicates onset of the positive Bz variation. GSM coordinate system is used.

1.3 The THEMIS Data

Five identical THEMIS satellites (THA, THB, THC, THD, and THE) were launched in 2007 to study substorms with primary objectives to determine when and where substorms are

initiated as well as the timing between various key aspects of substorm phenomenology. Substorms, originally defined by *Akasofu* [1964], are now known to be the result of solar wind energy transferred to the Earth's magnetosphere when interplanetary magnetic field (IMF) lines become connected to Earth's magnetic field lines when the IMF is pointing southward. Energy is stored in the tail until a sudden release, resulting in particle heating and kinetic energy (and injections), global reconfigurations of the magnetosphere, and several space and ground observed phenomena. Because these phenomena are initially confined in space but quickly expand away from their initial location [*Ohtani and Kokubun*, 1991; *Sergeev et al*., 1996a; *Angelopoulos et al*., 1997], it was necessary to have several spacecraft aligned down the tail, parallel to the Sun-Earth line, to address the question of substorm onset. This particular configuration allows us now to study injections, along with their related plasma flows, dipolarization fronts, and electric fields, throughout the tail: from reconnection which initializes the events to GEO where we have thus far been constrained to study injections.

To study particle energization I utilize the electrostatic analyzer (ESA), which measures 5eV to 25 keV ion and electron distribution functions [*McFadden et al*., 2008], and the solid state telescope (SST), which detects high-energy (25 keV to 1 MeV) ion and electron fluxes [*Angelopoulos*, 2008]. I have applied background (penetrating) electron removal and accurate subtraction of spacecraft potential to the ESA data, and have removed sun-contamination from the SST data. The THEMIS software suite I used to collect SST data includes detector calibration and accurate partial moment computation from energetic particles. The first moments of the combined ESA and SST flux measurements were used to calculate the velocity data. I used the THEMIS fast survey data, which provided 90-second resolution data just after launch and 3-second resolution data in late 2009 THEMIS tail season onward.

The magnetic field was measured using the fluxgate magnetometer (FGM) at 3-second resolution, which measures the direct-current (DC) magnetic field [*Auster et al.*, 2008]. The electric fields were calculated using the velocity moments and the magnetic field measurements under the plasma approximation (**E**=**-V**×**B**).

1.4 Dissertation Outline

For this thesis, I rely on THEMIS data to perform a statistical study of injections and utilize an analytical model of impulsive electromagnetic fields to demonstrate that strong, localized and impulsive electric fields associated with earthward traveling dipolarizing flux bundles are capable of transporting and accelerating particles to flux levels consistent with observations.

Given that the four tail seasons of the THEMIS mission [*Angelopoulos et al.*, 2008] provide a wide swath of data across the tail (+/- ~20 R_E in Y_{GSM}), from the inner magnetosphere to ~30 R_E, I perform the first comprehensive statistical study of injections in the magnetotail that extends observations from the inner magnetosphere out to the typical location of the near-Earth neutral line (25-30R_E), in order to determine the relationship between injections and these transient features. In Chapter 2 I present our observations, demonstrating with superposed epoch analyses and spatial distributions that there is a good correlation between injections and fast flows, dipolarization fronts, electric field enhancements, and increases in geomagnetic activity (|AL| index). I also demonstrate that while little to no spectral hardening occurs from before to after an injection (seen also by *Christon et al.* [1988]), there is actually spectral hardening when we compare injections across different levels of geomagnetic activity. In other words, injections are incrementally heating the plasma sheet, and as activity increases, more injections occur and

along with them, there is increased spectral hardening. We follow with a discussion of our results in 2.4, explaining how a narrow flow channel associated with the dipolarizing flux bundle and resulting electric fields can best explain our observations.

In order to test this theory, I adapted a numerical model [*Angelopoulos et al*., 2002] of particle guiding-center (G.C.) motion in prescribed electric fields in the magnetosphere to provide a realistic means of studying impulsively accelerating particles, designing the prescribed electric fields to mimic the impulsive, localized fields typically measured during injections. Chapter 3 describes the model and the simulation process. It also provides two case studies in which I simulate injections observed by 3-4 THEMIS spacecraft around the same time, using data-model comparisons to constrain, by forward modeling, a small set of variable parameters. I show how the electric fields alone are capable of accelerating particles to their observed energies, without the aid of the dipolarized magnetic field. (In this chapter, the electric field is a potential electric field, with opposing dusk-dawn directed fields flanking the main dawn-dusk electric field such that $\nabla \times \mathbf{E} = 0$.) I backtrace particles in time, showing how their trajectories were altered by the impulsive electric field and where the particles originated from. I use Liouville mapping from prescribed phase space density sources (consistent with the data) to determine the final fluxes. Chapter 3 therefore demonstrates that impulsive, localized electric fields associated with bursty bulk flows are capable of accelerating particles to levels we observe.

Chapter 3 is my first step in answering how these localized, impulsive dipolarizing flux bundles might be capable of generating injection signatures. Having obtained positive results with a very simple description of the earthward traveling flow burst, I then improve the model in Chapter 4 by designing a more realistic description of the incoming dipolarizing flux bundle.

This new description excludes the infinite extension of the flow channel downtail from the simpler model, instead spatially confining the pulse in X_{GSM} on both earthward and tailward ends. This alteration appears to have large effects on the simulation results. Also, a $\partial B/\partial t$ term is included in the earthward-traveling field system by adding an inductive dawn-dusk electric field component to the potential electric fields modeled in Chapter 3. δB_Z is calculated from the inductive electric field using Faraday's Law. Using magnetic field observations as a guide, the inductive electric field consistent with the magnetic field increase that matched observations was necessarily small. I explain the design of the inductive electric field and its related magnetic field, which is modified from that used previously by *Li et al.* [1993; 1998; 2003], *Sarris et al.* [2002], and *Ganushkina et al*. [2005; 2012; 2013]. I also explain how I combine the inductive components to the pre-existing potential electric fields in the model. Following this, I simulate one of the case studies from Chapter 3—first with parameters very similar to those used in Chapter 3, and then with revised parameters obtained from revised forward modeling (with the new model) to obtain the best data-model comparison with the updated model. The objective of these new simulations is 1) to demonstrate that injections can still be simulated with a more realistic description of the earthward-traveling dipolarizing flux bundle and 2) to discover and to explain how the dipolarizing magnetic field plays a role in the acceleration process compared with the electric fields in the system. I demonstrate that the more realistic model presented in Chapter 4 improves the simulation results found in Chapter 3, and that it appears that the inclusion of the $\partial B/\partial t$ term and the inductive electric field only play a small role in the particles' fate. This is demonstrated by particle trajectories and direct comparisons of simulated spectra with and without the inductive component.

The final chapter is a summary of the thesis, revisiting our conclusions and discussing potential future work. I include the license agreements obtained for using copyrighted material in the appendices. A bibliography is attached at the very end.

CHAPTER 2

Statistical characteristics of particle injections throughout the equatorial magnetotail

2.1 Introduction

Energetic particle injections in the near-Earth plasma sheet are critical for supplying particles and energy to the inner magnetosphere. Recent case studies have demonstrated a good correlation between injections and transient, narrow, fast flow channels as well as earthward reconnection (dipolarization) fronts in the magnetotail, but statistical observations beyond geosynchronous orbit (GEO) to verify the findings were lacking. By surveying trans-geosynchronous injections using THEMIS, we show that their likely origin is the earthward-traveling, dipolarizing flux bundles following reconnection. The good correlation between injections and fast flows, reconnection fronts and impulsive, dawn-dusk electric field increases is not limited to within 12 R_E, but extends out to 30 R_E. Like near-Earth reconnection, both ion and electron injections are most probable in the pre-midnight sector. Similar to bursty bulk flows (BBFs), injection-time flow speeds are faster with increasing distance from Earth. With faster flows, injection intensity (amount of energy flux gain) generally increases and extends to higher energy channels. With increased geomagnetic activity, injection occurrence rate increases (akin to that of BBFs) and spectral hardening occurs (κ decreases). (Spectral hardening is quantified through the use of κ, the negative slope of the line when the particle distribution is plotted versus energy at high energies, typically >40 keV, in log-log space. This "high-energy κ tail" diverges off of the Maxwellian distribution which describes the particle population at lower energies. A smaller κ means the higher energies are being heated.) The occurrence rate increase within the

inner magnetosphere suggests that injections populate the radiation belts more effectively under enhanced geomagnetic activity. Our results are inconsistent with the classical concept of an azimuthally wide injection boundary moving earthward from ~9-12 R_E to GEO under an enhanced cross-tail electric field. Rather, particle injection and transport occur along a large range of radial distances due to effects from earthward-penetrating, azimuthally localized, transient, strong electric fields of recently reconnected, dipolarizing flux bundles.

2.2 Data and Selection Criteria

We rely upon THEMIS fast-survey data (3s cadence except for SST in 2007-early 2009, which had a 90s cadence) obtained while the spacecraft were in the plasma sheet (β>0.5, where β is the ratio of the plasma pressure to the magnetic pressure). We use energy flux and moments from the SST and ESA instruments and magnetic field from the FGM instrument [*Angelopoulos et al.*, 2008]. The AL data were collected from the Data Analysis Center for Geomagnetism and Space Magnetism, Kyoto University. After smoothing the energy flux (eflux) by 4 minutes using a boxcar average to improve counting statistics, our selection criteria for injections with onset at t_0 (including those with dispersion) are as follows:

For three consecutive energy channels:

- t_0 determined when energy flux (j) rate of increase reaches $(\Delta j/j)/\Delta t$ > 25%/min; derivative evaluated over 18s (6 data points)
- t_0 for the consecutive energy channels is within 5 min of each other
- The average energy flux 10 min after t_0 is at least two times greater than the 10 min average beforehand
- The energy flux remains elevated for at least 5 min
- β >0.5 for 15 consecutive minutes surrounding t_0, at least 4 min of which are prior to t_0 (because our smoothing is for 4 min)

To avoid selecting random fluctuations near instrument background, we disqualified the electron injection selection if the energy flux at t_0 was below 5e3 or 1e4 keV/str·cm^2·s·keV for the SST energy channels (26-201keV) or the ESA energy channels (8eV-20keV), respectively. For ions we used 1e3 and 1e4, respectively. These values were determined after looking through the data to find typical noise levels. The beta criterion proved adequate for removing plasma sheet recovery events for ion injections, though for electrons we removed selections that were made during sharp decreases in $|B_X|$. The 26 keV channel is fitted to fill in the data gap between the ESA and SST instruments, so when either the 30 keV SST channel or the 20 keV ESA channel were near background, the fit was discounted. This was evidenced when the energy flux of the 26 keV channel dipped below that of the 30 keV channel.

To differentiate between dispersionless and dispersed injections operationally, we checked the temporal separation of the lowest three consecutive energy channels that satisfied our injection selection criteria within the 20 minutes following the injection onset, t_0. If these channels were dispersed by more than a minute, the event was classified as dispersed. (We used the three lowest energy particles conservatively, because they are the ones drifting the slowest and are more prone to develop dispersion). We considered any fluctuations within the 10 min following injection to be related to that event, and thus did not select any new onsets during that time. We defined inverse injections as dispersed injections in the opposite sense (lower energies increased in flux before higher energies).

Our database contains 1624 dispersionless, 1201 dispersed, and 345 inversely dispersed electron injections and 1277 dispersionless, 690 dispersed, and 75 inversely dispersed ion injections. For an azimuthally localized acceleration, one would expect that a spacecraft would observe more dispersed injections than dispersionless, as it is more likely to be located outside of

the acceleration site and to observe the accelerated, drifting particles. However, dispersed injections are much weaker than dispersionless ones (their $(\Delta j/j)/\Delta t$ as well as their Δj are smaller), making them less likely to be selected by our criteria.

2.3. Observations

2.3.1 Case studies

Figures 2.1 and 2.2 demonstrate the selection of dispersionless (Figure 2.1 events 1 and 2), dispersed (Figure 2.1 events 3, 4, 5, 6, 7; Figure 2.2 events 1 and 2), and inversely dispersed injections (Figure 2.2 event 3), in both geosynchronous and trans-geosynchronous altitude ranges. In Figure 2.1, three consecutive "dipolarizing flux bundles" (DFBs) [*Liu et al.*, 2013] at ~03:48UT, ~04:10UT, and ~04:43UT, contribute to a growing dipolarization of the magnetic field and overall temperature increase. This is explained by flux pile-up between -10 to -11 R_E in X_{GSM}. Five of the seven injections occur just as the AL index begins to dip, while the other two occur in the recovery phase of the substorm. Four of the events exhibit near-simultaneous injections, dipolarization fronts (DFs), fast flows (and $-\mathbf{V}x\mathbf{B}$ electric field), and |AL| increases. This is not unexpected, since any observation made outside of the acceleration region would not necessarily observe the fast flow, dipolarization, or enhanced electric fields.

Looking closely at the timing of the flows, the DFBs, and the injections, it is likely that in event 4 the dawnward edge of an earthward flow passed over the spacecraft, resulting in the dispersionless nature of the injection at higher energies but a dispersed signature in the lower energies. This is evident from the +Vx peak accompanied by an even stronger $-V_Y$ peak and followed by a –Vx component, a signature of the flow vortex often observed as an incoming dipolarizing flux bundle (a.k.a. plasma bubble) pushes through the plasma sheet and diverts the

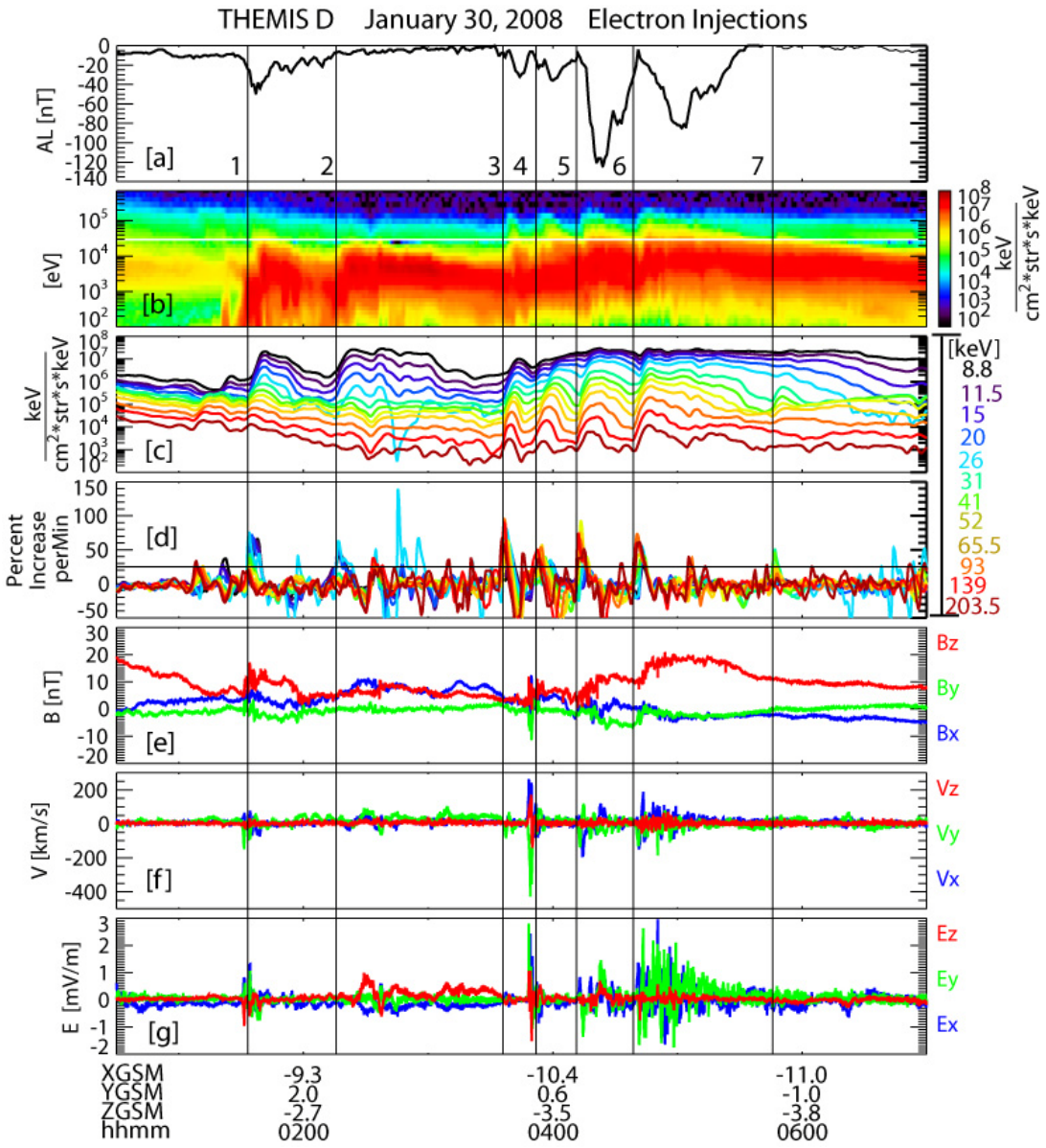

Figure 2.1. Seven electron injection events selected using our criteria. Events 1-2: Dispersionless. Events 3-7: Dispersed. (a) AL index. (b) Energy flux. (c) Energy flux (line spectra). Note that the ESA instrument goes near background levels around 02:00, 03:00, and 06:30 UT, explaining the behavior of the fitted channel between the ESA and SST instruments (26 keV). To avoid incorrectly selecting an injection from the fitted channel, we required that the energy flux at 26 keV be higher than that at 31 keV for selection. (d) Percent change in energy flux per minute [(Δj/j)/Δt *100] for each individual energy channel. Colors represent energy channels and correlate with the colors in the line spectra. Three consecutive energy channels must have a (Δj/j)/Δt that rises above the horizontal line at 25% for an injection to be selected. (e) Magnetic field in GSM coordinates. Increasing dipolarization is observed as each dipolarized flux bundle comes in, causing flux pileup around 04:00 UT. (f) Velocity in GSM coordinates. Flow reversals may represent vortices in the incoming flow and/or rebound in the flux pileup region. (g) Electric field in GSM coordinates calculated from **–V**x**B**.

surrounding flux tubes around it [e.g., *Keiling et al*., 2009].

In events 5 and 6, flow perturbations are evident. We interpret the signatures as due to a flow burst immediately to the dusk of the spacecraft (resulting in a dispersionless energy flux increase at high energies but a slightly dispersed signature at lower energies) that then moved over the spacecraft in agreement with the observed strong, persistent +Vx. Because of the flow vortex, the initial –Vx is an expected observation for a spacecraft located dawnward of the earthward flow. In the injection simulations we present in Chapter 3, several spacecraft were located within the tailward flow portion of a flow vortex dawnward of an earthward flow channel. These spacecraft still observed the injections as dispersed, since electrons that were accelerated within the earthward flow channel drifted dawnward.

At THEMIS D's location at 04:00 UT (-10.4, 0.6, -4.5 R_E in GSM), electrons are most likely on open drift paths and will exit through the magnetopause if not injected farther earthward. However, to show that events 3-6 are most likely new events and not drift echoes, we calculate the drift period at this L-shell. Where drift period in minutes equals 44/(LW(MeV)) [pg 54 from *Kivelson and Russell*, 1995] for 90° pitch angle particles, and $L=\sqrt{-10.4^2+0.6^2+-3.5^2}$=11 R_E, we find the drift period range for energies of 8.8 keV-203.5 keV is 19.7 min (for 203.5 keV) – 456 min (for 8.8 keV). While the higher energies could theoretically make it back under 20 min and be observed as a drift echo, it is clear that the degree of dispersion for each event cannot be described by drift echoes due to the lower energies' long drift period.

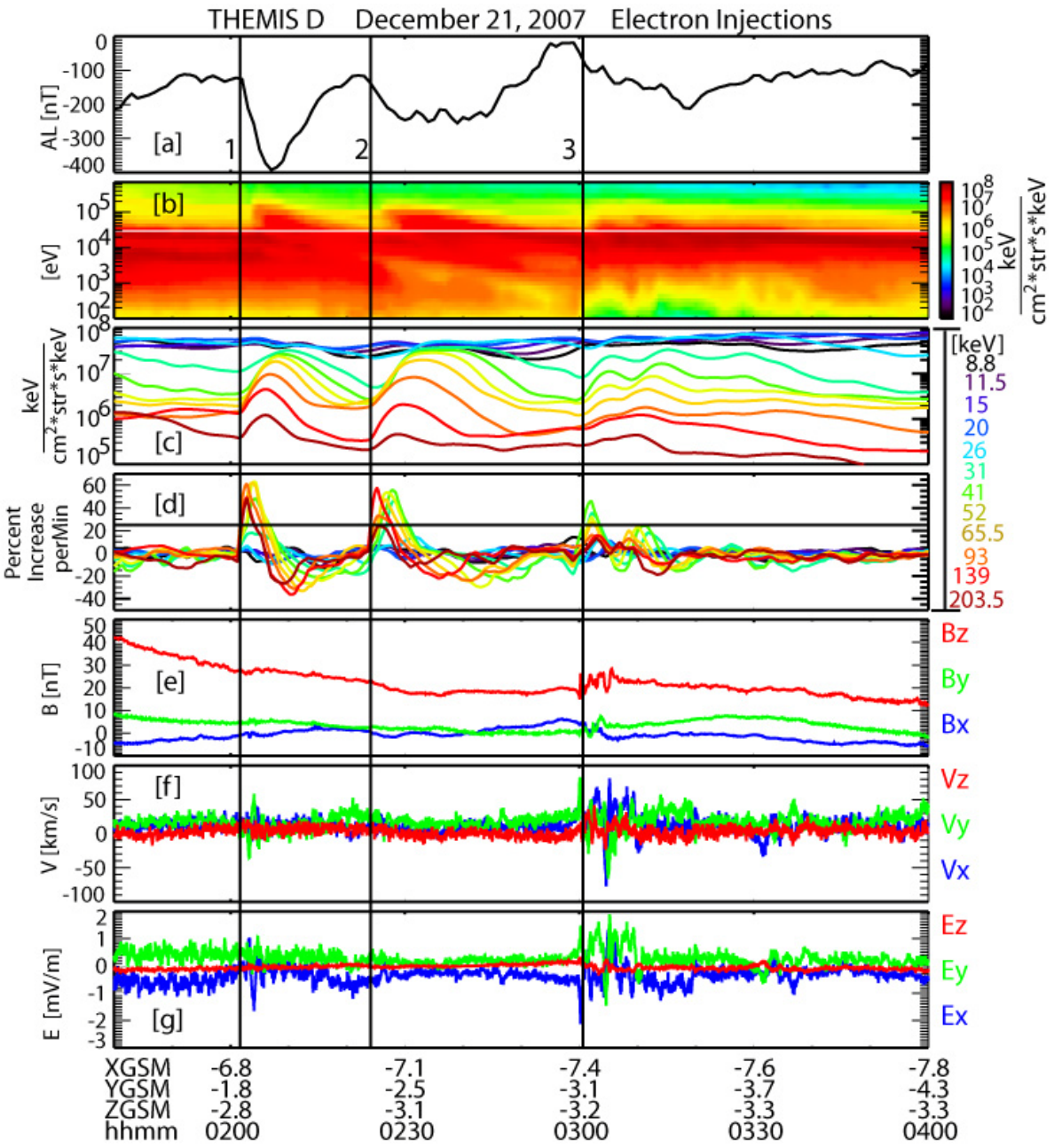

Figure 2.2. Three electron injection events selected using our criteria near geosynchronous orbit. Events 1-2: Dispersed. Event 3: Inversely dispersed. (a) AL index. (b) Energy flux. (c) Energy flux (line spectra). (d) Percent change in energy flux per minute [(Δj/j)/Δt *100] for each individual energy channel. Colors represent energy channels and correlate with the colors in the line spectra. Three consecutive energy channels must have a (Δj/j)/Δt that rises above the horizontal line at 25% for an injection to be selected. (e) Magnetic field in GSM coordinates. A dipolarization front is observed ~03:00 UT. (f) Velocity in GSM coordinates. Flow reversals may represent vortices in the incoming flow and/or rebound in the flux pileup region. (g) Electric field in GSM coordinates calculated from $-\mathbf{V}\times\mathbf{B}$. The dawn-dusk ($E_Y$) component increases with the flow and dipolarization front ~03:00 UT.

Figure 2.2 exhibits two dispersed injections near geosynchronous orbit, followed by an inversely dispersed injection. The injections' clear dispersion makes it evident that the spacecraft was far from the acceleration site. There is no accompanying DFB or flow burst. We understand the inversely dispersed injection to be associated with a braking DFB, evidenced by an oscillatory flow, consistent with flow burst rebound or flow vortex. [e.g., *Keiling et al*., 2009; *Keika et al*., 2009; *Ohtani et al*. 2009; *Panov et al.* 2010]. The prominent E_Y observed due to the strong magnetic field in this region can indeed allow particles to be accelerated while penetrating deeper into the inner magnetosphere. As in Figure 2.1, each of the injections is associated with a sharp increase in |AL|. The examples provided in Figures 2.1 and 2.2 are also consistent with previous detailed and extensive case studies that found similar correlations between particle energization, fast flows, dipolarization fronts, and dawn-dusk electric fields [*Runov et al.*, 2009; 2011; *Zhou et al.*, 2011].

2.3.2 Superposed epoch analyses

In order to examine whether these relationships between injections and fast flows, dipolarization fronts, dawn-dusk electric fields, and |AL| index are typical, we performed superposed epoch analyses for both electrons and ions. We explored how particle flux, electromagnetic field and flow variations during dispersionless injections are related to the magnitude of the earthward flow speed (Figure 2.3) and of the level of geomagnetic activity (Figure 2.4). For Figure 2.3, we binned the data based on the maximum Vx peak ("Vx_{max}") observed within +/-10 min of t_0, the injection start time; for Figure 2.4 we binned the data based on the average |AL| index measured from -10 to +30 min from t_0. Each figure provides three bins of approximately equal statistical significance. We averaged the (already quite similar)

values of the Vx_{max} tertiles between ions and electrons, as well as the |AL| tertiles between ions and electrons, so the binning in each figure would be same for the two datasets. The minimum, intermediate, and maximum bins are shown in Table 2.1. To be clear, the reason for the tertiles was simply to show how injection signatures differ when observed simultaneously with a fast flow compared to when they are observed with a slower flow. Instead of having just two bins (fast vs. slow), we include an intermediate bin. To ensure each bin is equally significant, we set the bin limits so that one third of all events is in each bin. After binning the data, we found the median values for each bin. These medians are what we plot in Figures 2.3 and 2.4. So for instance, each of the three colored lines in the Bz/B0 panel is the median change in Bz over time for a particular bin. Both Figures 2.3 and 2.4 plot the medians of the unsmoothed data, so the reason the sharp change in energy flux is at t_0+2min (dashed line) is because the sharp onset was smoothed out over $\pm$2 min (via boxcar averaging) as part of our selection process.

Table 2.1. Vx and |AL| Binning

Vx_{min} [km/s]	$Vx_{peak} < 90$
Vx_{inter} [km/s]	$90 < Vx_{peak} < 204$
Vx_{max} [km/s]	$204 < Vx_{peak}$
$\|AL\|_{min}$ [nT]	$\|AL\| < 39$
$\|AL\|_{inter}$ [nT]	$39 < \|AL\| < 134$
$\|AL\|_{max}$ [nT]	$134 < \|AL\|$

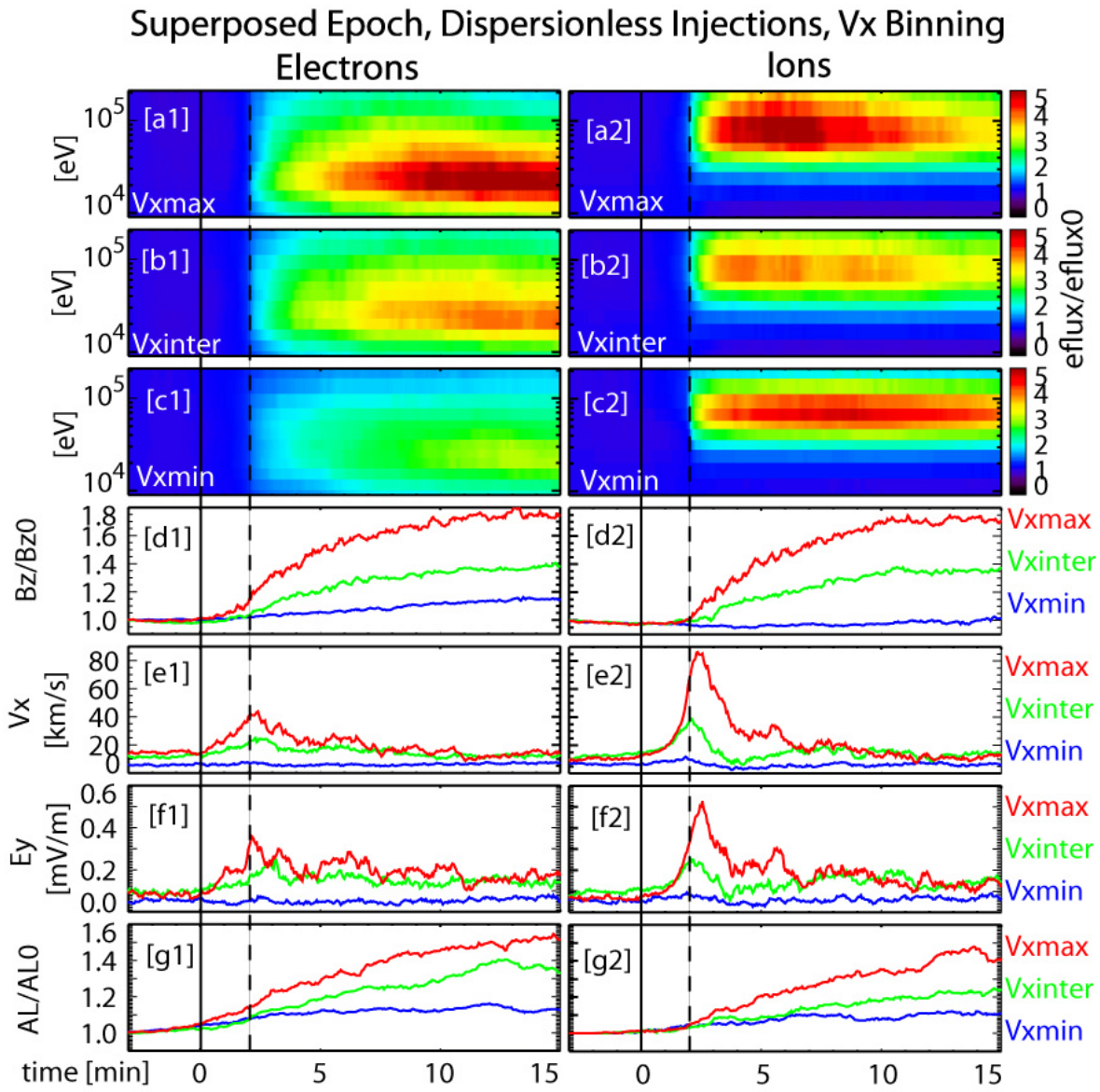

Figure 2.3. Superposed epoch analysis for dispersionless electron (left) and ion (right) injections divided into three bins (Vx_{max}, Vx_{inter}, and Vx_{min}) of approximately equal significance. The bins are defined by the average between ion and electron injection tertiles listed in Table 1. Peak Vx observed within +/-10 min of injection onset (t_0) was used for the binning. A solid vertical line is drawn at t_0 and a dashed vertical line is drawn 2 min later. The latter is to aid the eye: because we smoothed the data by 4 min via boxcar averaging prior to the selection process to avoid scatter, the sharp onset was smoothed out. This explains why the actual onset time is statistically about 2 min after t_0 as displayed in the *unsmoothed* data (panels (a-c)). Panels (a-c) are plotted with a three-point-average in energy and time. For panels (d-h), the three Vx bins—Vx_{max}, Vx_{inter}, and Vx_{min}— are plotted together as red, green, and blue, respectively. (a) Median change in energy flux for the fastest Vx bin; (b) Median change in energy flux for the intermediate Vx bin; (c) Median change in energy flux for the slowest Vx bin; (d) Median change in Bz; (e) Median Vx; (f) Median E_Y; (g) Median change in |AL|. The data are divided by the median value over -5 to -3 minutes prior to t_0 for each event to calculate the change over time.

In Figure 2.3, both electrons and ions show clear trends with increasing earthward flow: First, both the injection intensity (the relative energy flux increase) and the energies of the broad peak of the intensity increase with increasing peak flow velocity (Figures 2.3a-c). In other words, the particle flux increases and the energy gain are extended towards higher energy channels as the flow velocity intensifies.

Additionally, the degree of dipolarization increases (Figure 2.3d) with flow velocity. Note that the median change in B_Z remains high in the epoch plots for longer timescales than the few minutes that is typically observed for dipolarization fronts [*Liu et al*., 2013]. This can be understood by considering the time series of individual injections in Figure 2.1. When the spacecraft are located near ~10-12 R_E (where THEMIS has spent most of its time thus far), it is common for a DFB/injection to be followed by flux pileup of increasing amplitude with each incoming DFB. This pileup is in agreement with the picture that individual DFBs correspond to wedgelets comprising the large scale substorm current wedge [*Liu et al*., 2013]. In Figures 2.3d and 2.4d, all peaks are washed out and an overall increase in B_Z remains.

Figure 2.3f also shows that an increase in dawn-dusk electric field (E_Y) is associated with the increasing flow. Finally, we see an increase in |AL| enhancement, suggesting that these injections accompany increases in geomagnetic activity with a higher degree of correlation as the peak velocity increases. The flows rise prior to dipolarization and injection, a feature that both *Runov et al.* [2011] and *Zhou et al.* [2011] noted in their case studies. In fact, statistically, we find the peak flow occurs when the energy flux begins to increase sharply (~t_0+2 min). This flow signature prior to energy flux enhancement has been described by *Zhou et al.* [2011] as due to reflected and accelerated thermal plasma sheet ions that are not of a sufficiently high energy to be visible as an injection.

When we compare the ion injections with electron injections, we find the ion injections are better organized by fast flows than electrons, as evidenced by the higher Vx peaks associated with the ion injections. This does not mean that electron injections are not associated with fast flows, but rather that the timing of the flow arrival relative to electron injection is not statistically consistent, resulting in a median with a smaller peak. We also explored the possibility that injections may be better correlated with |**V**| than Vx, but obtained similar results for binning on |**V**| as in Figure 2.3. The fact that we observe enhanced B_Z, E_Y, and greater eflux gain along with faster flows is consistent with a picture in which the spacecraft is located at the center of the flow channel, where we expect the flow to be fastest, the dipolarization to be greatest, and the energization to be large.

We implement the same approach in Figure 2.4 as Figure 2.3, but bin by |AL|. Comparing between effectively no activity to some activity ($|AL|_{min}$ vs. $|AL|_{inter}$ and $|AL|_{max}$), there is better correlation with fast flows—again much more prominently among the ion injections—as well as with dipolarization. This could mean that flow velocity is quite small under low to negligible activity. There is little change in the velocity and magnetic field superposed epochs between the $|AL|_{inter}$ and $|AL|_{max}$ bins. This would be expected if our assumption is correct that the flow velocity and dipolarization magnitude is more related to the spacecraft location relative to the earthward flow channel. Binning by |AL| index means the spacecraft could be located anywhere within or without the flow channel, so statistically the observed velocity and dipolarization magnitude are the same regardless of activity (as long as there is *some* activity). Similarly, we do not see an overall increase in injection intensity (meaning eflux gain) with |AL| at energies <100 keV; however, it is clear that with greater geomagnetic activity, particles with higher energies (>100 keV) are more likely to be injected with increased intensity.

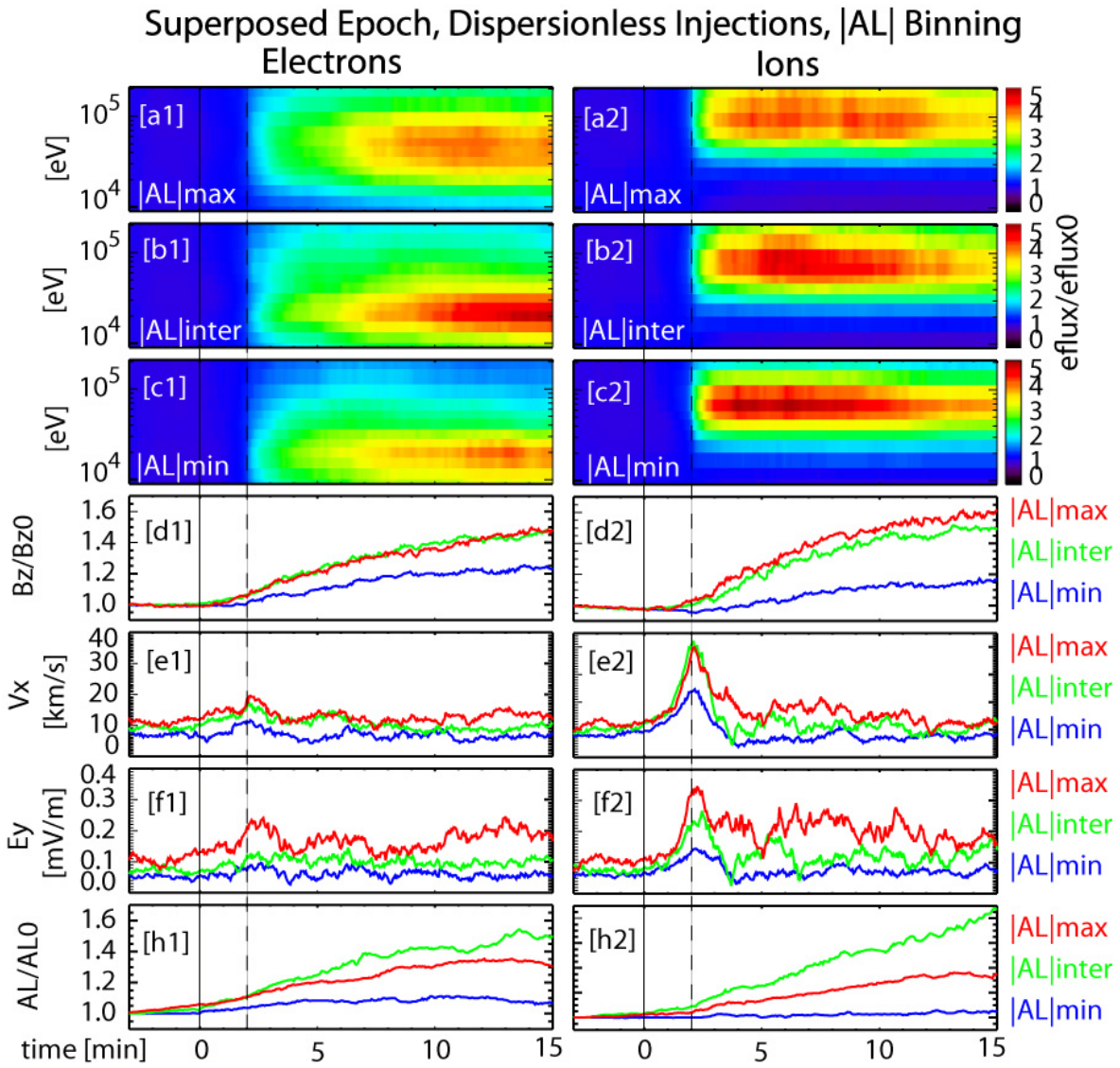

Figure 2.4. Epoch analysis for dispersionless electron (left) and ion (right) injections divided into three bins ($|AL|_{max}$, $|AL|_{inter}$, and $|AL|_{min}$) of approximately equal significance. The bins are defined by the average between ion and electron injection tertiles listed in Table 1. Average |AL| over -10 to +30 min of injection onset (t_0) was used for the binning. A solid vertical line is drawn at t_0 and a dashed vertical line is drawn 2 min later. The latter is to aid the eye: because we smoothed the data by 4 min (via boxcar averaging) prior to the selection process to avoid scatter, the sharp onset was smoothed out. This explains why the actual onset time is statistically about 2 min after t_0 as displayed in the *unsmoothed* data in panels (a-c). Panels (a-c) are plotted with a three-point-average in energy and time. For panels (d-h), the three |AL| bins—$|AL|_{max}$, $|AL|_{inter}$, and $|AL|_{min}$— are plotted together as red, green, and blue, respectively. (a) Median change in energy flux for the largest |AL| bin; (b) Median change in energy flux for the intermediate |AL| bin; (c) Median change in energy flux for the weakest |AL| bin; (d) Median change in Bz; (e) Median Vx; (f) Median E_Y; (g) Median change in AL. The data were divided by the median value over -5 to -3 minutes prior to t_0 for each event to calculate the change over time.

The positive correlation between the energy flux with |AL| is shown quantitatively in Table 2.2. At 2 minutes before t_0 and at 7 minutes after t_0, we fit the high energy kappa (κ) tail of the median distribution to a line in log-log space to find κ (the negative of the slope of the line) using least-squares fitting. We did this by first converting the median energy flux into phase space density (*f*). The full equation for energy flux is as follows:

$$eflux = \frac{E^2}{2\pi m^2} f(E,X,Y) \frac{keV}{cm^2 s\ keV\ str} \tag{2.1}$$

where

$$f = N\left(\frac{m}{2\pi\kappa W_0}\right)^{3/2} \left[\frac{\Gamma(\kappa+1)}{\Gamma(\kappa-0.5)}\right] \left(1+\frac{E}{\kappa W_0}\right)^{-(\kappa+1)} \tag{2.2}$$

and where $W_0 = E_0\left(1-\frac{3}{2\kappa}\right)$ is the most probable energy, $E_0 = Tk$ is the energy of peak particle flux (*k*=Boltzmann constant), *m*=mass, *N*=particle density, and *E*=particle energy. So at higher energies, the distribution is proportional to $E^{-\kappa}$, where E=energy (we used an energy range of 41-139 keV), and κ indicates the hardness of the spectrum or how much flux is in the higher energies [*Vasyliunas*, 1968; *Christon et al*., 1989; 1991; *Gloeckler and Hamilton*, 1987; *Kletzing et al*., 2003]. We then fit *f* to a line in log-log space: ln(*f*)=A-κln(E). We did a linear fit of the energy flux high energy tail (41-139 keV) in log-log space as well to extrapolate the energy flux at the fixed, nominal superthermal energy of 40 keV (Q_{40keV}) as a measure of the flux changes during injections. We used 40 keV because of its heritage in past studies. As *Anderson* [1965] wrote, "Most intensively studied to date has been the electron component above 40 keV in energy. Electrons above this energy are not only readily detectable but also of great scientific interest because (1) They occur in large fluxes over very large spatial regions surrounding the earth, (2) They are the component most sensitive to the existence of a magnetopause imposed by solar-wind pressure, (3) They represent in the clearest form the requirement that in the

Table 2.2. Comparing energy flux & κ over |AL|

		Before injection		After injection		κ change across injection	Q_{40keV} ratio across injection
		κ	$Q_{40keV}/10^4$	κ	$Q_{40keV}/10^4$		
i+	$\|AL\|_{min}$	7.1 ± 0.1	2.4 ± 1.6	7.1 ± 0.1	14.7 ± 1.5	0.0 ± 0.2	6.1 ± 4.7
	$\|AL\|_{inter}$	6.8 ± 0.1	6.0 ± 1.5	6.5 ± 0.1	29.7 ± 1.5	-0.3 ± 0.2	5.0 ± 1.5
	$\|AL\|_{max}$	6.5 ± 0.1	22.0 ± 1.5	5.7 ± 0.1	89.1 ± 1.1	-0.8 ± 0.2	4.1 ± 0.3
e-	$\|AL\|_{min}$	4.8 ± 0.1	6.0 ± 2.1	4.9 ± 0.1	18.0 ± 1.2	0.1 ± 0.2	3.0 ± 1.3
	$\|AL\|_{inter}$	4.6 ± 0.1	16.3 ± 1.1	4.8 ± 0.1	48.9 ± 1.2	0.2 ± 0.2	3.0 ± 0.3
	$\|AL\|_{max}$	4.4 ± 0.1	54.0 ± 1.3	4.6 ± 0.1	162.0 ± 1.7	0.2 ± 0.2	3.0 ± 0.1

		Before injection		After injection	
		κ change across |AL|	Q_{40keV} ratio across |AL|	κ change across |AL|	Q_{40keV} ratio across |AL|
i+	$\|AL\|_{inter}$-$\|AL\|_{min}$	-0.3 ± 0.2	2.5 ± 2.3	-0.6 ± 0.2	2.0 ± 0.3
	$\|AL\|_{max}$-$\|AL\|_{inter}$	-0.3 ± 0.2	3.7 ± 1.2	-0.8 ± 0.2	3.0 ± 0.2
e-	$\|AL\|_{inter}$-$\|AL\|_{min}$	-0.2 ± 0.2	2.7 ± 1.1	-0.1 ± 0.2	2.7 ± 0.2
	$\|AL\|_{max}$-$\|AL\|_{inter}$	-0.2 ± 0.2	3.3 ± 0.3	-0.2 ± 0.2	3.3 ± 0.1

immediate neighborhood of the earth, charged particles be accelerated from thermal or near thermal energies up to energies far above thermal." Table 2.2 lists these values and the κ value for each |AL| bin for both ions and electrons. To easily show how κ and Q_{40keV} change after injection as well as over geomagnetic activity, Table 2.2 also includes the change in κ from before to after the injection for each |AL| bin, the change in κ from one |AL| bin to the next for both t_0-2min and t_0+7min times, the ratio of Q_{40keV} between t_0-2min and t_0+7min times, and the ratio of Q_{40keV} between |AL| bins at both t_0-2min and t_0+7min times. Uncertainties were calculated as described for least-squares fitting in chapter 8 of *Taylor* [1997].

We see from Table 2.2 that the energy flux at 40 keV increases over the injection by a significant, consistent factor regardless of |AL| bin (~3 times for electrons, 4-6 times for ions). The energy flux at 40 keV also increases with increasing |AL| both before and after the

injections, demonstrating that the injection acts upon an already heated plasma sheet by elevating the fluxes even further. For both ions and electrons, κ of the injected particle distribution consistently decreases with increasing |AL|, indicating that with greater geomagnetic activity we observe a higher flux at higher energies (a harder spectrum) than in quiet times. (The uncertainties in the κ change would suggest these decreases are significant.) However, similar to what *Christon et al.* [1988] found, there is not much change in κ throughout what they called "plasma temperature transitions" (i.e., what we interpret as "from before to after the injection"). (The uncertainties, being sometimes larger than the κ change, also suggest the changes are not significant.) In other words, the small and erratic spectral index changes during an injection are negligible compared to the consistent spectral index decreases from lower |AL| to a higher |AL| bins.

The fact that the heating during injection preserves the spectral index but that spectral hardening does occur with increasing |AL|, along with the fact that the energy flux increases with increasing |AL| prior to injection, indicates that a process prior to the observed injection has already generated a sufficiently intense, high-energy, non-thermal component in the plasma sheet ion and electron populations, with increasing efficacy under increasing geomagnetic activity. We propose that this pre-heating of the plasma sheet is due to the cumulative effect of prior injections that may have been observed at a given spacecraft (as in Figure 2.1, events 3-6) or may have been missed due to the longitudinally narrow nature of the injection region. We suggest that drifting particles injected from different locations contribute to the plasma sheet population by various degrees in accordance with distance from the source, injection intensity, and time since injection, resulting in progressively harder spectra under increased injection rates at higher energy levels observed under greater geomagnetic activity. This picture is in agreement

with both the *Lyons et al.* [2012] observations of a one-to-one correlation between AL intensifications and dipolarization fronts arriving in the inner magnetosphere and the proposal by *Liu et al.* [2013] that the ground and space magnetic disturbance of a substorm (AL or substorm current wedge) is a compilation of dipolarizing flux bundle (DFB) current systems that represent elemental substorm current wedge activations ("wedgelets") coming into the inner magnetosphere. In fact, the suggestion of wedgelets as fundamental building blocks of the large-scale substorm perturbation comes not only from space observations [*Liu et al*., 2013], but also from ground-based magnetometers [*Rostoker*, 1991]. The picture of wedgelets incrementally adding to the substorm current wedge could otherwise be thought of in terms of the change in flux tube volume caused by the wedgelet, combined with the azimuthal flow away from the pileup region, as the source of the SCW. This is again in agreement with our results from the spectral index changes that plasma sheet heating is an aggregate response to individual injections of increasing frequency under increasing conditions of geomagnetic activity, each injection responsible for increasing the particle flux by a moderate amount.

Because the unitary heating event is the injection, and because |AL| increases are correlated with Vx increases, it is natural to hypothesize that the spectral changes with |AL| increases are due to the intensity and occurrence frequency of individual flow bursts. In fact, when we did a similar comparison as in Table 2.2 but used the Vx bins, we found that the amount of energization at 40 keV increased with increasing Vx. We suggest (and will discuss at more length in section 2.4.1) that the energizing mechanism behind injections related to increased activity can be understood and modeled as impulsive penetration of an enhanced electric field associated with the speed of the incoming flow, which, as shown in Figure 2.4, also increases with enhanced geomagnetic activity. The energy gained from the electric field as

particles are carried farther into the inner magnetosphere is consistent with the energy gained via betatron acceleration, a mechanism which would indeed preserve the particle distribution's spectral index.

2.3.3 Injection spatial distribution

In order to determine where in the magnetotail injections are occurring, we used the same Vx and |AL| bins to plot spatial distributions of injections per day in Figure 2.5. The Vx-binned distributions were normalized by dividing the number of injections observed in a 4x4 R_E bin by the total spacecraft orbit time spent in that bin. The |AL|-binned distributions were further normalized by dividing the total number of injections by the total spacecraft orbit time spent in that bin *while the AL index was within the stated range.* We required that the spacecraft spend at least 20 hours in a particular bin to include that bin in the analysis in order to improve statistics. If the spacecraft did not spend at least 20 hours in a bin, that bin was left empty in the plot, signifying poor coverage; if the spacecraft spent at least 20 hours in a bin but observed no injection, the bin was colored black. (For specific information on the total number of days spent in each bin and the total number of injections observed, see Appendix 2A.)

It is clear from Figure 2.5 that both electron and ion injections are associated with faster flows farther downtail, whereas injections observed near-Earth are associated with slower flows. This is evidenced by the low-to-negligible occurrence rates in the near-Earth bins for Vx_{max} in Figures 2.5c and 2.5f, and the higher occurrence rates in the near-Earth bins for Vx_{min} in Figures

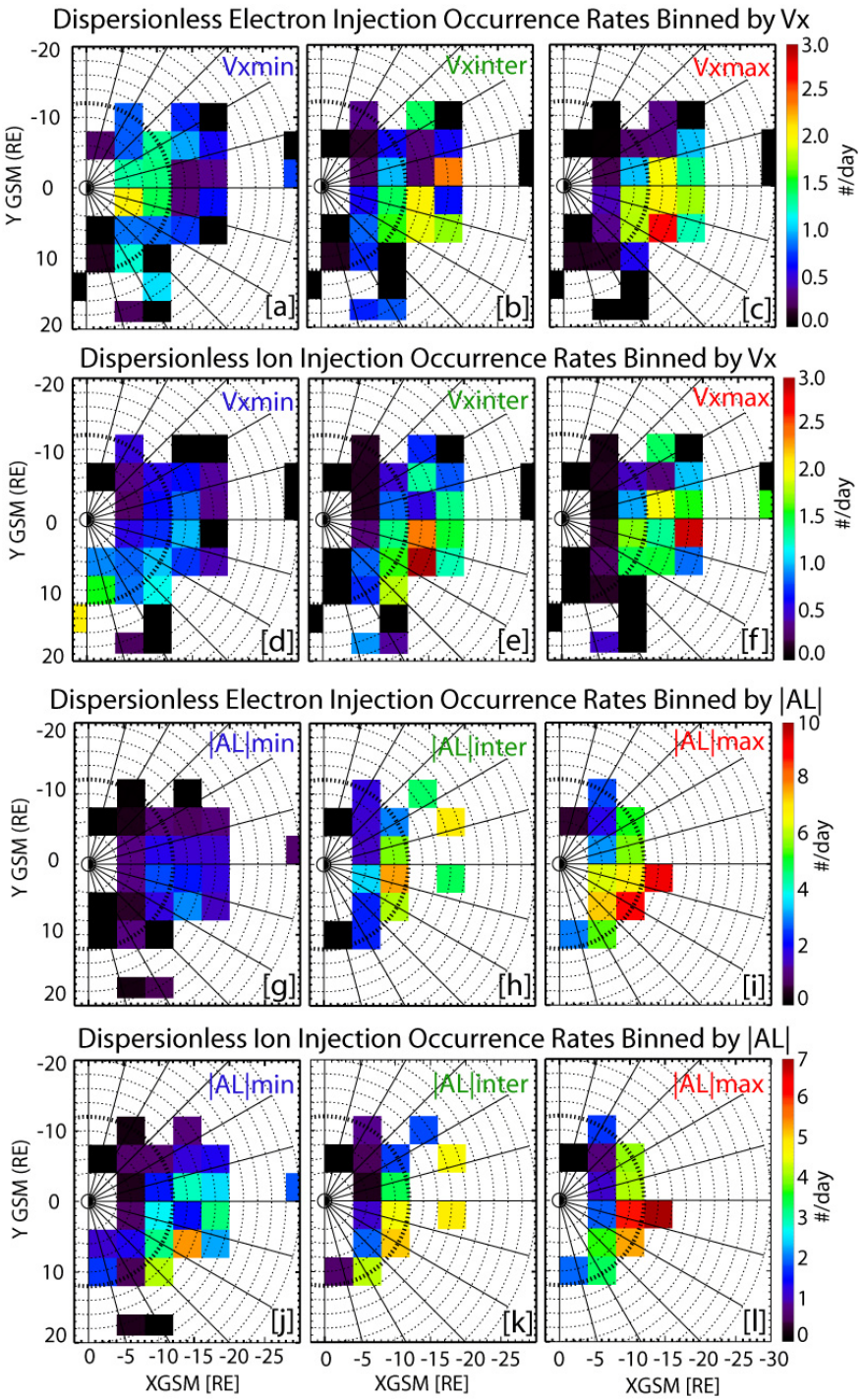

Figure 2.5. Spatial distributions of dispersionless injections binned by Vx and |AL|, plotted separately for electrons and ions as occurrence rates (#/day per 4x4 R_E bin). Panels (a-f) show that injections associated with the fastest flows are observed more frequently downtail, whereas those associated with slower flows are observed closer to Earth. Panels (g-l) show injections associated with higher geomagnetic activity can be observed near-Earth while those associated with lower |AL| levels are more frequently observed downtail. A bin was left blank (no color) if THEMIS did not spend at least 20 hours in that bin.

2.5a and 2.5d. This is expected, as previous work has already demonstrated the presence of flow braking in the higher magnetic field of the inner magnetosphere [e.g., *Keika et al.*, 2009; *Ohtani et al.*, 2009]. It is also clear from Figure 2.5 that both electron and ion injections have higher occurrence rates (1) with the faster flows (Figures 2.5b-c, 2.5e-f) than with the slower flows (Figures 2.5a and 2.5d) and (2) under higher |AL|. The fact that more injections are observed under greater geomagnetic activity agrees with a previous study by *Anderson* [1965] who found the same relationship between increased activity and "electron island fluxes", which they described as fluxes impulsively injected into the geomagnetic tail region. It is particularly apparent that higher |AL| indices result in higher occurrence rates within the inner magnetosphere. This suggests that with increased geomagnetic activity, injections can reach lower L-shells, which is necessary for populating the inner magnetosphere with energetic particles.

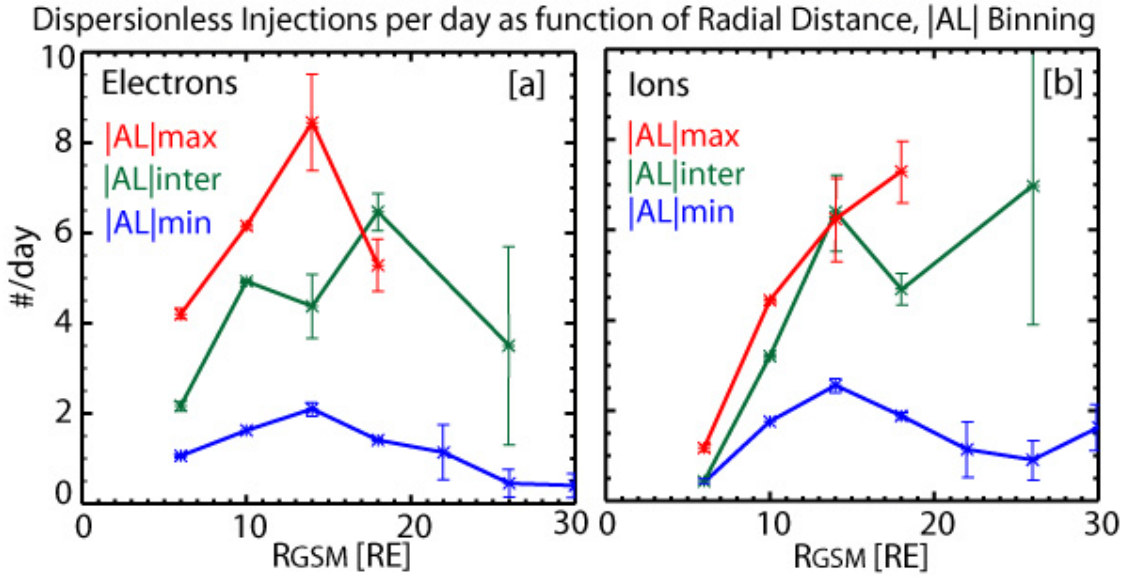

Figure 2.6. Injection occurrence rates as a function of radial distance separated by |AL| bins for (a) electrons and (b) ions. There is a general increase in occurrence rate with increasing |AL|, including the geosynchronous region. The uncertainty is calculated as $\pm\sqrt{N}/days$, where N is the number of events counted per bin and days is the total time spent in that bin.

The fact that injections more frequently reach lower L-shells under increased activity is further supported in Figure 2.6, which shows the injection occurrence rates as a function of radial distance for each |AL| bin (electrons in Figure 2.6a, ions in 2.6b). Since substorms typically occur about 4-6 times a day, we can make a statistical comparison with injection occurrence rates, seeing that at least 1-2 injections are observed per substorm. This is a lower limit, because although we do normalize the number of injections observed to the total number of days the spacecraft spent in a particular bin, the localized nature of these events mean we are much less likely to observe them than to observe the global effects of a substorm.

We also include a superposed epoch plot similar to Figures 2.3 and 2.4, but binned by radial distance from Earth, that supports these findings (Figure 2.7). Faster flows occur at larger distances from Earth along with more intense changes in energy flux. More energetic particles (especially electrons) are energized at larger distances perhaps because the flows are faster farther from Earth and because higher-μ particles are convecting at those distances (having not yet drifted away around the Earth). In contrast, the |AL| index increases more when injections are observed closer to the Earth. The larger |AL| near Earth supports our interpretation of Figures 2.5 and 2.6, that injections reach lower L-shells under greater activity.

After reconnection, fast flows released in the tail carry dawn-dusk electric fields that accelerate and transport particles, resulting in injection. When these flows, which represent the incoming speed of the dipolarizing flux bundle, reach the strong magnetic field of the inner magnetosphere, they start to brake. This braking is why we observe lower flow speeds closer to Earth. It is more likely for the flows to reach near-Earth under active time. Because these injections reach closer to Earth, just as *Liu et al.* [2013] and *Lyons et al.* [2013] demonstrated the structures behind them (dipolarizing flux bundles or “substorm current wedgelets”) contribute to

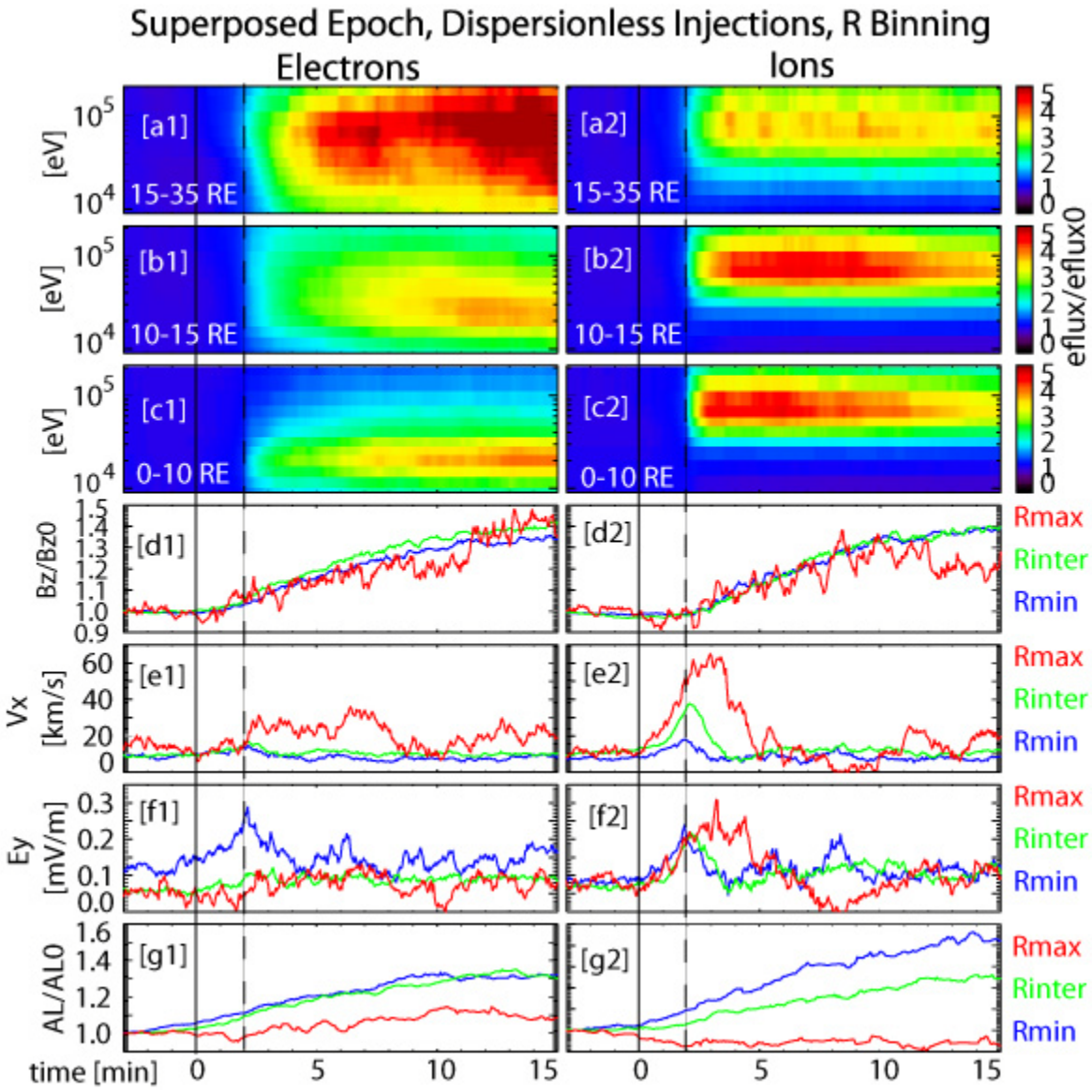

Figure 2.7. Dispersionless electron and ion injection-related signatures superposed and binned by radial distance from Earth (R_{min}=0-10 R_E, R_{inter}=10-15 R_E, R_{max}=15-35 R_E). Panels (a-c) are plotted with a three-point-average in energy and time. For panels (d-h), the three R bins—R_{max}, R_{inter}, and R_{min}— are plotted together as red, green, and blue, respectively. (a) Median change in energy flux for the largest R bin; (b) Median change in energy flux for the intermediate R bin; (c) Median change in energy flux for the smallest R bin; (d) Median change in Bz; (e) Median Vx; (f) Median E_Y; (g) Median change in AL. The data were divided by the median value -5 to -3 minutes prior to t_0 for each event to calculate the change over time.

the magnetic disturbance, causing a greater increase in |AL|. Figure 2.7 also supports case studies by *Runov et al.* [2009; 2011] which demonstrated that dipolarization fronts are self-consistent structures that do not undergo much change in Bz throughout their passage from 30 R_E downtail to the inner magnetosphere. The unchanging Bz amplitude over various distances is shown in A1. (d1-d2): the change in Bz at 15-35 R_E is the same as at 10-15 R_E and at 0-10 R_E. (The statistics are sparse for the largest R bin since the spacecraft spent less time there, so this bin is not as smooth as the others.)

We next explore and compare the spatial distributions of all dispersionless (Figure 2.8) and dispersed (Figure 2.9) electron and ion injections as functions of MLT in two broad radial bins (inside and outside 12 R_E). We define the "inner region" as $R<12$ R_E, not to be confused with the "inner magnetosphere" which is often understood to be approximately within geosynchronous orbit. We present the occurrence rates (Figures 2.8a, 2.8b, 2.9a, and 2.9b) and probabilities (Figures 2.8c, 2.8d, 2.9c, and 2.9d) versus MLT to provide an easier comparison with previous studies done at geosynchronous orbit. We also, however, include Figures 2.8e, 2.8f, 2.9e, and 2.9f to display occurrence rates (for electrons and ions, respectively) within 4x4 R_E bins in X_{GSM} and Y_{GSM} because of the localized nature of injections, flow bursts, and DFBs.

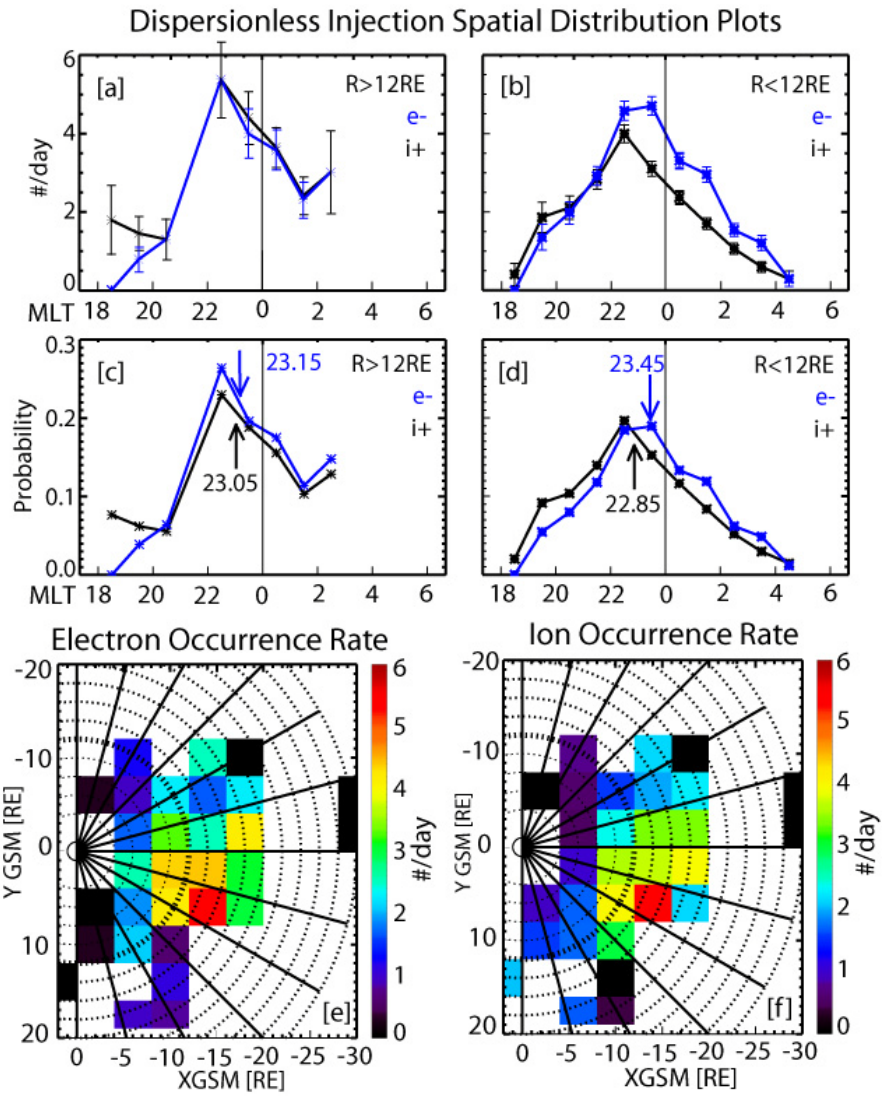

Figure 2.8. Spatial distributions of dispersionless injections plotted separately for electrons (blue) and ions (black). In a-d, each point on the graphs lies at the center of the 1-hour bin it represents (e.g., 21.5 represents 21-22 MLT, 22.5 represents 22-23 MLT, etc.). The uncertainty is calculated as $\pm\sqrt{N}/days$, where N is the number of events counted per bin and days is the total time spent in that bin. Bins in which the spacecraft spent fewer than 40 hours were not included. (a) Injection occurrence rates (#/day per 1 hour MLT bin) beyond 12 R_E. (b) Injection occurrence rates (#/day per 1 hour MLT bin) within 12 R_E. (c) Injection probability plotted per 1 hour MLT bin beyond 12 R_E. Arrow and accompanying MLT value represent the median of the occurrence rate distribution. Median absolute deviation (MAD) for e-: 1.08 h, for i+: 1.31 h. (d) Injection probability plotted per 1 hour MLT bin within 12 R_E. Probability defined as the occurrence rate for that MLT sector normalized by the total occurrence rate for that species. Arrow and accompanying MLT value represents the median of the occurrence rate distribution. MAD for e-: 1.36 h, for i+: 1.11 h. (e) Electron dispersionless injection occurrence rates plotted per 4x4 R_E bin. (f) Ion dispersionless injection occurrence rates plotted per 4x4 R_E bin. The heavy circle in (e) and (f) represents R=12 R_E, the separation between the outer and inner regions. The radial lines are drawn at each MLT hour. The 4x4 bins in which the spacecraft spent fewer than 20 hours were not included.

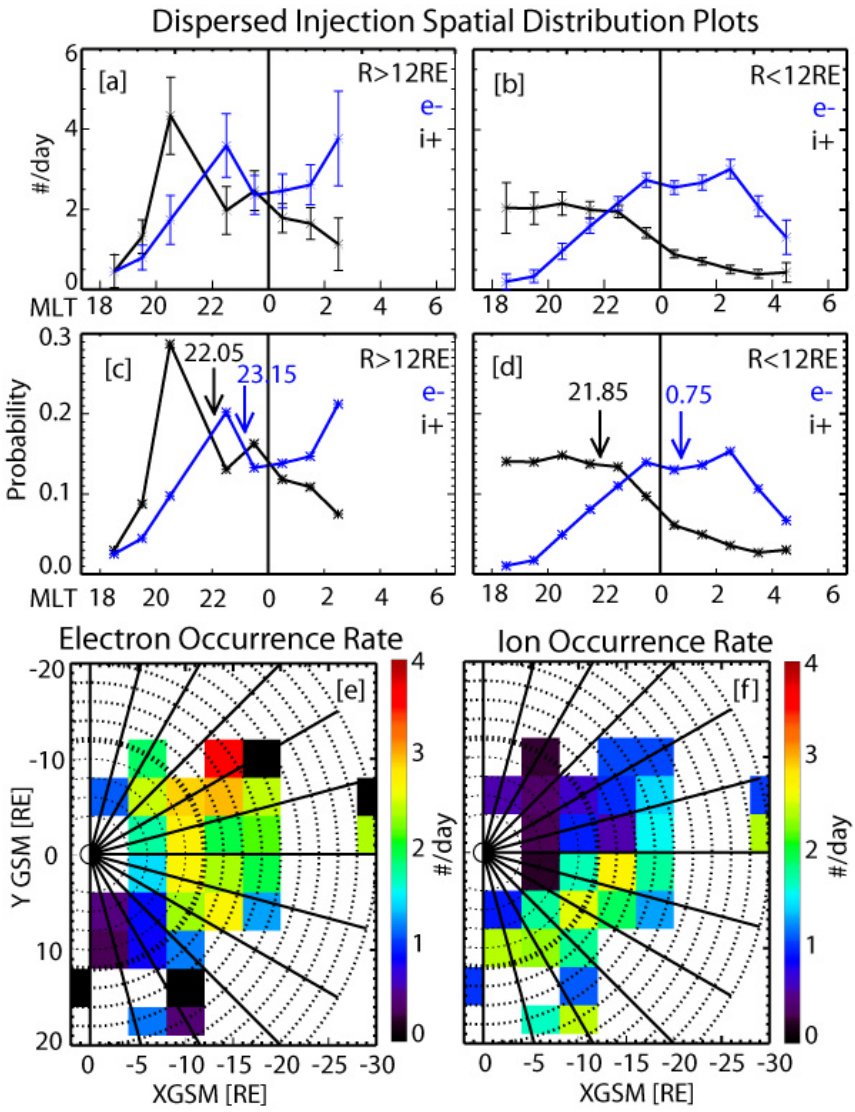

Figure 2.9. Spatial distributions of dispersed injections plotted separately for electrons and ions. Panels are the same as in Figure 5. (c) Medians noted with arrows. Median absolute deviation (MAD) for e-: 1.65 h, for i+: 1.98 h. (d) Medians noted with arrows. MAD for e-: 1.32 h, for i+: 1.43 h.

In all of the Figure 2.8 panels, both electron and ion injections occur predominantly in the pre-midnight sector. Figure 2.8c and 2.8d show that our findings agree with the geosynchronous injection "characters" as described in *Birn et al.* [1997a] and *Thomsen et al.* [2001]. The electron distribution is slightly offset to the dawn of the ion distribution, marked quantitatively by the difference in their median occurrence locations. This is true in both the outer and inner

regions, though in the outer region the electron and ion injection probabilities lie remarkably close to each other across the tail.

We next performed the same analysis for dispersed injections (Figure 2.9). As expected, the ions' duskward $\nabla \mathbf{B}$ and curvature drift results in a much greater presence of dispersed ion injections in the dusk sectors. Because the occurrence rate of the dispersionless electron injections peaks pre-midnight, it is not surprising to observe dispersed electrons with equal probability across most of the tail, but with a steady falloff duskward of the 20-21 MLT sector. The probability difference between dispersed electron and ion injections is much more pronounced in the inner region than the outer region.

Because our findings in Figure 2.4 demonstrated correlation between geomagnetic activity and injections, we suspected that some of the occurrence rate spikes could be due to statistically higher geomagnetic activity (|AL|) while the spacecraft spent time in those particular bins. Specifically, we wondered about the 2-3 MLT bin in the outer region (Figures 2.8a and 2.8c) which shows both electron and ion occurrence rates increasing, compared to the trend in which they were decreasing towards the dawn. To test the theory, we plotted the median |AL| in each 4x4 R_E bin for comparison (Figure 2.10). When we compare the |AL| median at the bin centered at X=-15, Y=-10 R_E with the occurrence rates displayed in Figures 2.8e and 2.8f for that bin (which corresponds to the occurrence rate peak in the outer region's 2-3 MLT bin), we see that indeed geomagnetic activity was generally higher in this bin. We discovered that for the months of December 2007 and January 2008, THEMIS C had its apogee there; coincidentally, this was a period of more active time.

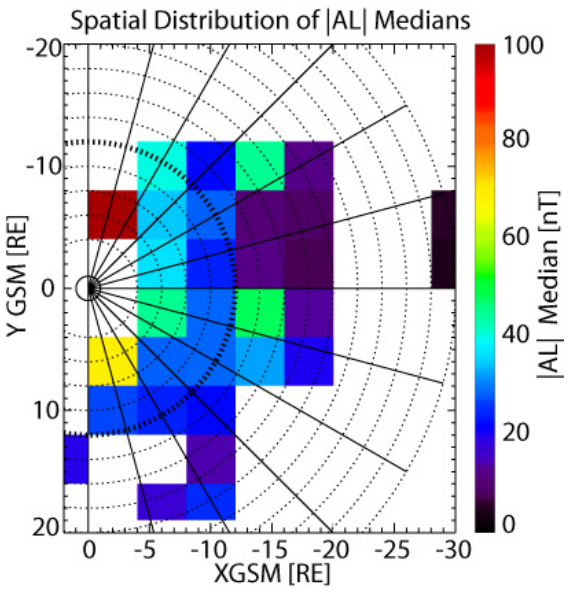

Figure 2.10. Median |AL| value per 4x4 R_E bin over entire spacecraft orbit. Bins in which the spacecraft spent fewer than 20 hours were not included.

So, excluding the abnormally active bin and the poorer statistics for R>12 R_E, a significant trend is apparent in the data even outside of R>12 R_E that is consistent with R<12 R_E. This suggests similar processes continue farther out. In particular, the midpoint of electron and ion injections is at pre-midnight, and the ion and electron occurrence rate medians are displaced relative to that midpoint by an increasing MLT distance as we proceed towards Earth. We interpret that as due to an increased drift rate of these particles closer to Earth, due to the increased magnetic field gradient there. The results are consistent with a longitudinally narrow acceleration site that energizes and launches particles into the plasma sheet with increasing drift rates as they propagate Earthward. The resultant observed dispersed injection rates are a combination of the spatial distribution of injection rates and drift rates in the ambient magnetic field.

Lastly, we explored the spatial dependence of our final classification, the inversely dispersed injections (Figure 2.11). We find that inversely dispersed injections are more likely to

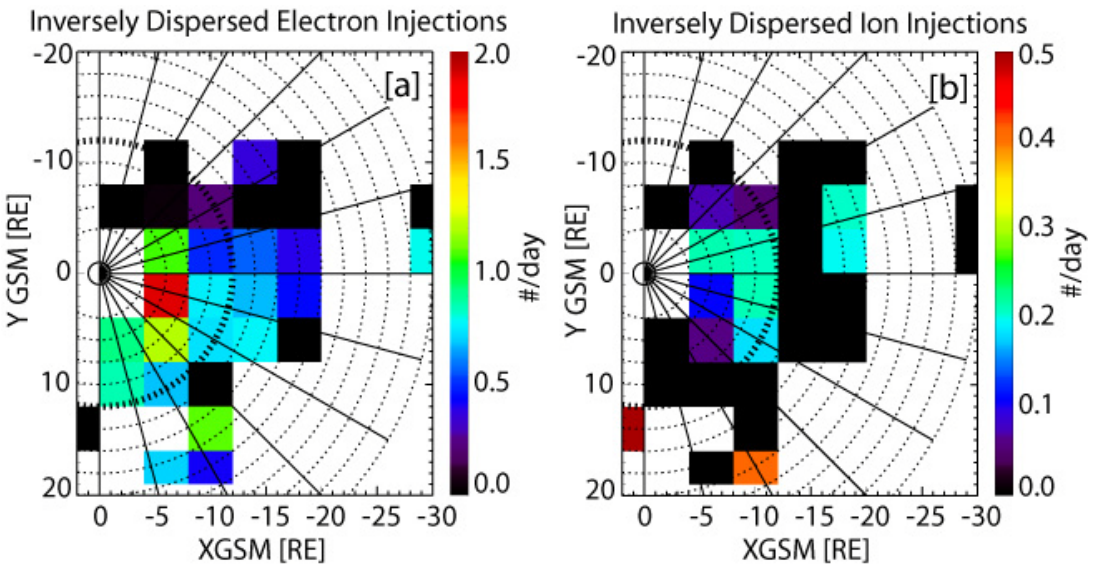

Figure 2.11. Spatial distribution of inversely dispersed (a) electron and (b) ion injections plotted as #/day within 4x4 R_E bins. There is a higher occurrence rate in the near-Earth region. Bins in which the spacecraft spent fewer than 20 hours were not included.

be observed close to Earth, lending support to our explanation laid out in Chapter 3 section 4.2.1 that these injections result from decelerating flows/weaker electric fields that also occur near Earth, where pressure increases, and are only strong enough to locally alter the Alfvén layer of low μ particles. Because the spacecraft is located inside the Alfvén layer, prior to injection the observed particles were on trapped drift orbits and did not move into stronger magnetic fields. In contrast, injected particles that come from downtail (where B is lower) must have a lower initial energy than their orbiting, constant μ counterparts (μ∝Energy/B) and thus undergo greater energization (via betatron acceleration) and carry more energy flux. The Alfvén layer for higher μ particles is at higher L-shells, meaning that higher μ particles must travel farther to reach the spacecraft after crossing their respective Alfvén layer than lower μ particles. Thus, the inverse dispersion occurs because of the delay in arrival time of the higher μ particles that originated downtail (see Figures 3.11 and 3.13 for a demonstration of this effect: we plot electron trajectories and show that pre-injection the electrons are on closed drift shells, post-injection they

come from downtail, and that lower energies arrive first). Conversely, if the spacecraft were located outside of the relevant Alfvén layers or if the electric field were much stronger (increasing the convection speed and reducing the delay in arrival), a dispersionless injection would be observed.

Therefore, a key factor in observing inverse dispersion is the spacecraft location relative to the relevant Alfvén layers. Even with dispersionless injections (defined here using the three lowest energy channels that met the injection criteria), an inverse dispersion can be seen at the highest energy channels due to the same effect (Figures 2.3a-c and 2.4a-c, energy channels ~>80keV). When injections are observed farther downtail, the spacecraft is located outside of the low μ Alfvén layers. Consequently, the Alfvén layer just tailward of the spacecraft will be for much higher μ particles, since gradient/curvature drift begins to dominate higher μ particle motion farther out. The result is a mostly dispersionless injection with a small inverse dispersion at the higher energy channels associated with the higher μ particles. This process may be linked to the previous suggestion for inverse velocity dispersion, which relied upon the time evolution of the accelerating field-aligned inductive electric field [*Sarris et al.* 1976; *Galeev et al.* 1979; *Zelenyi et al.*, 1984]. We place more emphasis on the relationship between the spacecraft and the relevant Alfvén layers to explain the inverse dispersion, a premise that predicts more inversely dispersed injections in the near-Earth region because the spacecraft is originally within most particles' Alfvén layer.

Although ions do not maintain adiabaticity as far out as electrons, both electron and ion inversely dispersed injections were observed more frequently near Earth (Figure 2.11), suggesting a similar acceleration process. The reconnection-related explanation for inverse velocity dispersion of streaming ions [*Sarris and Axford*, 1979] could, however, explain why we

see a second population beyond 16 R_E (and out to 30 R_E for electrons), closer to where near-Earth reconnection takes place. We leave further exploration for later studies.

2.4. Discussion

Thus far in Chapter 2 we have presented a statistical study of electron and ion injections observed throughout the magnetotail plasma sheet by THEMIS. The following is our working framework of the acceleration and transport mechanism for injected particles: (i) magnetotail reconnection presumably occurs [*McPherron et al*., 1973*; Baker et al*., 1996]; (ii) reconnected field lines spring back towards Earth, creating a "reconnection front" [*Angelopoulos et al.,* 2013] ahead of a localized dipolarizing magnetic flux bundle [*Liu et al.,* 2013]; (iii) earthward plasma acceleration at, and immediately after, the reconnection front occurs from increased curvature force density: the tailward pressure gradient decreases ahead of the front as the curvature force density increases behind it due to the increase in the magnetic field magnitude [*Li et al.,* 2011]; (iv) a transient electric field forms because of (a) the resulting flow (from $-\mathbf{V}\times\mathbf{B}$) and/or (b) the inductive changes in the magnetic field and/or (c) the Hall electric field resulting from ion-electron separation at a steep boundary [*Runov et al.,* 2011]; (v) as the front moves earthward, plasma is diverted around the plasma bubble, resulting in dusk/dawnward flows at the front as well as tailward flow and eastward electric fields on the flanks of the flow burst [*Sergeev et al.* 1996b; *Keiling et al.,* 2009]; (vi) as electrons/ions drift eastward/westward across the potential drop formed within the flow channel, they are energized; (vii) the strong electric field alters the Alfvén layers locally, enabling particle transport closer to Earth. (Instead of globally enhanced dawn-dusk electric field that squeezes the Alfvén layer closer to Earth, a narrow enhanced dawn-dusk electric field will locally move the Alfvén layer closer to Earth.) In the following discussion

we will provide evidence that injections are related to reconnection and the resulting narrow, transient fast flows and electric fields associated with earthward-traveling dipolarizing flux bundles.

2.4.1 Injection correlation with fast flows

As seen in Figure 2.3, there is a clear relationship between fast flows, their associated E_Y, and injections. The results from Figures 2.3 and 2.4 suggest that with stronger geomagnetic activity come better correlation with fast flows, stronger dipolarizations, stronger electric fields, and more energetic particles injected. Just as *Angelopoulos et al.* [1994b] found a positive correlation between BBF occurrence rates and geomagnetic activity, we see a positive correlation between injection occurrence rates and geomagnetic activity in Figure 2.5g-l. These findings are consistent with a picture relating the energizing mechanism behind injections to fast flows in the tail, thus providing statistical evidence in support of the findings in the *Sergeev et al.* [2005] and *Runov et al.* [2009; 2011] case studies. Faster flows are coupled with stronger localized E_Y, which in turn alters the Alfvén layers of the more energetic (higher μ) particles, permitting their injection to lower L-shells.

In a recent study by *Sergeev et al.* [2012], the authors demonstrated that only ~35-40% of flows observed at ~10 R_E by Geotail or THEMIS are seen as injections at geosynchronous orbit; the others stop at higher L-shells. They explain this low percentage with the bubble theory of magnetotail plasma flows, in which the lower-entropy flux tubes are able to penetrate more deeply into the inner magnetosphere. We interpret their results as the result of plasma-depleted flux tubes that form because of reconnection: curvature force density results from the magnetic field increase that builds up to compensate the density depletion within the dipolarized flow

burst, and it is this increased curvature force that allows density-depleted flux tubes to penetrate more deeply into the inner magnetosphere [*Li et al.* 2011]. Because the probability of deep plasma penetration greatly depends on how stretched the magnetospheric configuration is [*Sergeev et al.*, 2012] and increased stretching has been correlated with increased geomagnetic activity [*Lopez et al.*, 1993], we might also expect to see more injections close to Earth during more active times. This is indeed the case, as in Figure 2.5 we see a higher occurrence rate near Earth under $|AL|_{inter}$ than $|AL|_{min}$, and even higher occurrence rates under $|AL|_{max}$ than $|AL|_{inter}$. Increased |AL| index is thus indicative of the injections' ability to penetrate deeply into the inner magnetosphere as well as the injections' increased occurrence rate, as more injections and thus more substorm current wedgelets adding to the substorm current wedge will increase the magnetic perturbation.

Not only does a spatial relationship exist between |AL| and injection occurrence rates, but a spatial relationship also exists between flow peaks and injection occurrence rates. In Figure 2.5, we see that injections observed near Earth are associated with slow flows, whereas injections associated with faster flows generally occur farther from Earth. This fits the picture of an incoming fast flow that brakes in the stronger magnetic field of the inner magnetosphere, such that injections observed near Earth are associated with these slower, braking flows. Because the flows begin to brake within L~12 R_E, we examined the trans-geosynchronous injections observed past 12 R_E and found that 77% of dispersionless ion injections and 74% of dispersionless electron injections are associated with flows >100 km/s, i.e., a few times the quiet time plasma sheet average [*Angelopoulos et al.,* 1993] (the peak of the flow was observed within +/-10 min of t_0). In comparison, only 20% of ion injections and 19% of electron injections were associated with >400 km/s flows. We interpret this reduction in association with faster flow

bursts to the localized nature of the flow channels. For injections to be associated with a higher peak velocity (such as the 400 km/s used in the BBF definition) requires that the spacecraft fly through the center of the flow channel where the velocity peak is the highest. Particles may drift within the channel, however, and a dispersionless injection might be observed at the edge of the flow channel where the flow is weaker. The remaining ~23-26% of ion and electron dispersionless injections that were not associated with >100 km/s earthward flows may have been observed close to the channel but not within it, such that the spacecraft is observing particles that have drifted to its location but have not drifted far enough for appreciable dispersion to form.

These results explain why previous observations at geosynchronous orbit did not readily attribute the injection acceleration mechanism to fast flow-related phenomena, and corroborate the findings of *Sergeev et al.* [2012] that high-entropy flows do not reach the inner magnetosphere. First, particles may drift to the edge of the flow channel (or just outside it) and may be observed as dispersionless injections without the spacecraft observing the fast flow signatures. Second, since an incoming flux bundle preserves its magnetic flux, and because flow speeds die down in an increasing magnetic field, the electric field of incoming dipolarizing flux bundles (representing flux transport rate) is the primary observable feature associated with both particle acceleration and transport. The transient electric field, which is stronger than the background convection electric field, locally alters the Alfvén layers, allowing particles to penetrate deeper towards the inner magnetosphere.

2.4.2 Injection Asymmetries in the Magnetotail

Figures 2.8 and 2.9 paint a clear picture of asymmetry in MLT of electron and ion injections in both the inner and outer regions of the magnetotail with a preference for the pre-midnight sector. The enhanced asymmetry for dispersed ion injections and the more symmetric distribution of dispersed electron injections in MLT (Figure 2.9) are what we would expect to see when dispersionless injections mostly occur in the pre-midnight sector. As ions drift duskward, their dominance on the duskside increases; the reverse is true for electrons drifting dawnward. Note, however, that due to the preponderance of dispersionless injections well into the pre-midnight sector (Figure 2.8c-d), and because those represent the source of the dispersed injections, the dispersed electron injections are observed with high occurrence rates at pre-midnight, across midnight, and well into dawn (Figure 2.9d). The dispersed electron occurrence rates are therefore far more symmetric across midnight than dispersed ion injections.

Asymmetries in injection distributions—as well as other substorm-related phenomena—have been seen previously. Although *Sarris et al.* [1976] did not observe asymmetries in electron injection spatial distributions with IMP-7 at 35 R_E, they noted a preference towards pre-midnight in the high-energy ion injections. Because they did not differentiate between dispersionless and dispersed "particle bursts" in their analysis, their findings were likely a mixture of dispersed and dispersionless injections. From the occurrence rates of Figures 2.8a and 2.9a, it is evident that at R>12RE such a mixture would be rather symmetric about midnight. Thus, the *Sarris et al.* [1976] results of an electron injection distribution symmetric about midnight and an ion distribution leaning towards pre-midnight are fairly consistent with our findings.

Energetic particle injections are not the only substorm-related phenomenon to have an asymmetric occurrence distribution across the tail. A dawn-dusk asymmetry of fast flows with

higher occurrence rate in the pre-midnight sector has been independently reported by *Raj et al.* [*2002*] using WIND data, *Runov et al.* [2005] using Cluster data, and *McPherron et al.* [2011] using THEMIS data. *Liu et al.* [2013] also used THEMIS data to find a greater pre-midnight prevalence of dipolarizing flux bundles. In addition, reconnection has been reported to have an asymmetric occurrence distribution favoring pre-midnight: *Imber et al.* [2011] found statistically that flux ropes and traveling compression regions were predominantly pre-midnight (80%); their results indicate that earthward flows are similarly asymmetric in the midtail region. Meanwhile, *Eastwood et al.* [2010] (using Cluster data) and *Nagai et al.* [2013] (using Geotail data) considered flow reversals as reconnection indicators to demonstrate a pre-midnight preference in reconnection.

These studies are evidence of the growing understanding that during substorms, reconnection is more likely to initiate in the pre-midnight sector. As a result, the processes following reconnection are similarly asymmetrically distributed across the tail. Observing both electron and ion injections with the same dawn-dusk asymmetry not only in the inner magnetosphere but *throughout the tail* suggests that injections are due to localized transient flow bursts linked to transient tail reconnection rather than enhancements in the global dawn-dusk electric field. Injection association with reconnection and earthward-traveling DFBs/fast flows was previously difficult to delineate because of the lack of consistent data past geosynchronous orbit, but with our database of THEMIS-observed injections from the inner magnetosphere to ~30 R_E, a consistent picture is emerging.

2.4.3 Ion versus Electron Injection Spatial Distributions

Additional pieces to the puzzle of particle acceleration include the salient features of the spatial distributions of ion versus electron injections (Figures 2.8 and 2.9). When injections were studied statistically at geosynchronous orbit by *Birn et al.* [1997a] and in multi-spacecraft case studies by *Thomsen et al.* [2001], the distribution of five injection "characters" (from proton-only injections far pre-midnight to the electron-only injections post-midnight) led the authors to suggest that two separate injection fronts exist—one for electrons and another for ions—azimuthally offset from each other (with the electron front dawnward of the ion front), both protruding earthward from the near-Earth plasma sheet. In extending their observations to larger distances, we also find an azimuthal offset between ion and electron dispersionless injection occurrence rates (Figures 2.8b and 2.8d) within 12 R_E. At even larger distances, however, there is very little difference between ion and electron injection occurrence rates across the width of the tail (Figures 2.8a and 2.8c), implying that such an offset between electron and ion injection "fronts" may be quite small. (By converting the offsets in the outer and inner regions from MLT hours to R_E along Y_{GSM} at the median radial distances of the spacecraft orbits in each region—0.45 R_E calculated at 17 R_E and 1.57 R_E at 10 R_E—we see that the minute offset in the outer region is not merely an error in mapping a localized-in-Y_{GSM} acceleration site to polar coordinates, as the offset still increases by almost four times.) Because the probability distributions between dispersionless electron and ion injections are nearly identical, both species are likely accelerated by the same process. We take this to be a localized enhancement in the electric field from transient flow bursts linked to magnetotail reconnection. The "injection front" is therefore related to the "reconnection front" [*Runov et al.*, 2011; *Angelopoulos et al.*, 2013], rather than to an injection boundary protruding from the near-Earth plasma sheet into the inner

magnetosphere. (The term “reconnection front”, coined in *Angelopoulos et al.* [2013], refers to the dipolarization front earthward of magnetotail reconnection, and the anti-dipolarization front tailward of reconnection. For our purposes, it is synonymous with the earthward-traveling dipolarization front that follows reconnection.)

In this context, the small offset is explainable as follows: as particles are transported earthward via the fast flows, they are being energized as they $\nabla\mathbf{B}$ drift across the dawn-dusk electric field in the flow channel. As electrons drift dawnward and ions drift duskward, the two species separate so that on the dawnward edge of the flow (and immediately outside of it), dispersionless electron injections are more easily observed, whereas on the duskward edge of the flow (and immediately outside it), dispersionless ion injections are more easily seen. We will demonstrate in Chapter 3 how more energetic particles drift quickly enough such that they can exit the flow channel in shorter timescales than the flow’s lifetime, indicating that $\nabla\mathbf{B}$ drift is a significant factor. Therefore, the rapidly drifting, accelerated particles can be observed outside of the acceleration site (the flow channel) as dispersionless injections without the accompanying signatures of a velocity burst, dipolarization front, or enhanced electric field. Because our selection criteria allow for a 1 min delay in energy flux rise between consecutive energy channels, there is a region outside of the flow channel where particles have drifted but have not yet dispersed by 1 min, accounting for observations of somewhat displaced electron and ion injection probability distributions. The same argument can also explain the slightly smaller offset in the outer region (Figures 2.8c and 2.9c) than the inner region (Figures 2.8d and 2.9d) as well as the offset observed previously at geosynchronous orbit: The $\nabla\mathbf{B}$ drift effect is greater in the inner magnetosphere than in the outer magnetosphere due to the much stronger magnetic field

near Earth, resulting in a more exaggerated offset as ions and electrons drift more quickly away from each other and from the center of the acceleration site.

This drift effect can also explain the difference between our observed offsets (0.1 hour MLT for the outer region and 0.6 hour MLT for the inner region) and the larger, 1-2 hour MLT offset reported by *Thomsen et al.* [2001] and *Birn et al.* [1997a] at geosynchronous orbit. Because their studies classified any injection with dispersion greater than 2 min as a dispersed injection, whereas our study uses the stricter 1 min criterion, their selection criteria allowed even more time for particles to drift away from the localized acceleration site and yet still be classified dispersionless. To test whether or not the dispersion criterion affects the offset between ion and electron injections, we repeated our analysis (using THD and THE for all four seasons) with a 2 min delay criterion (instead of 1 min delay) and plotted the results for the inner region in Figure 2.12. We see that the offset between the median occurrence rates has now increased by 0.5 hours to 1.1 hours MLT, which is in better agreement with the previous studies.

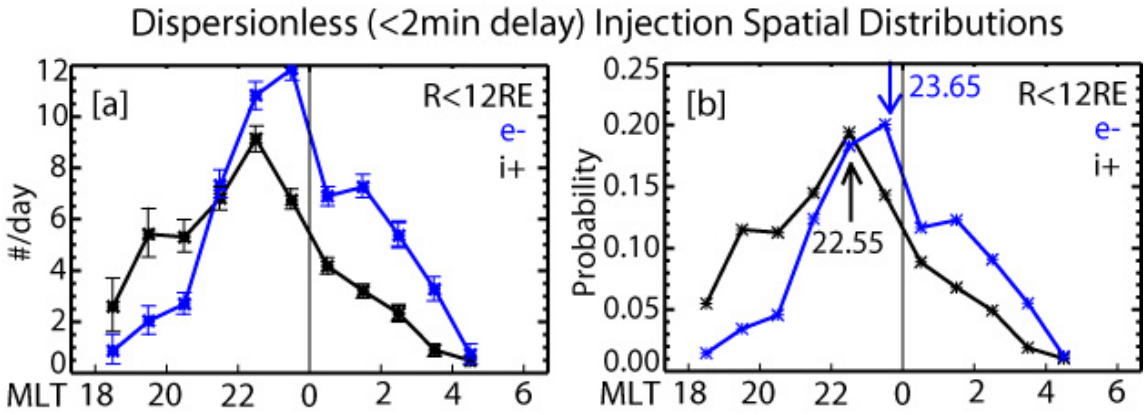

Figure 2.12. Similar to Figures 2.8b and 2.8d, except that the criterion that defines an injection as dispersionless was relaxed from a <1 min delay between energy flux increase at consecutive energy channels to a <2 min delay. The offset between the occurrence rate medians of electron and ion injections in the inner magnetosphere increases by 0.5 hours MLT relative to Figure 2.8, making the total offset of 1.1 hours MLT, similar to what previous studies that used a <2min delay found at geosynchronous orbit. Medians noted with arrows. Median absolute deviation (MAD) for e-: 1.25 h, for i+: 1.11 h.

To further investigate this effect, we plotted the spatial distributions of events that include *both* an electron and ion injection at the same spacecraft within 10 min of each other alongside the spatial distributions of events with *only* electron injections and *only* ion injections (Figure 2.13). It is clear from Figure 2.13d that in the inner region, the highest probability of observing both electron and ion injections during the same event (i.e., "coincident injections") is from ~22.5-23.5 MLT. This is the region spanning precisely where the electron- and ion-only probability distributions cross, with electron injections more probable than ion injections dawnward of the coincident injection probability peak and ion injections duskward of the peak. The probability distributions in the outer region (Figure 2.13c) follow a similar trend; however, poorer statistics may explain the higher probability of coincident injections in the dawn sector.

The graphs in Figure 2.13 for the outer region represent 135 ion-only injections, 119 electron-only injections, and 45 coincident injection events (where each coincident electron and ion injection is counted as one event, not two). In the inner region there are 792 ion-only injections, 1138 electron-only injections, and 322 coincident events. The fact that we observe many more singular injection events than coincident events implies that the regions dawnward and duskward of the acceleration site where electron-only and ion-only injections, respectively, are observed, are wider than the narrow acceleration site itself. We can estimate how much wider by comparing the total occurrence rates of each, which we calculate by integrating under the curves in Figures 2.13a and 2.13b.

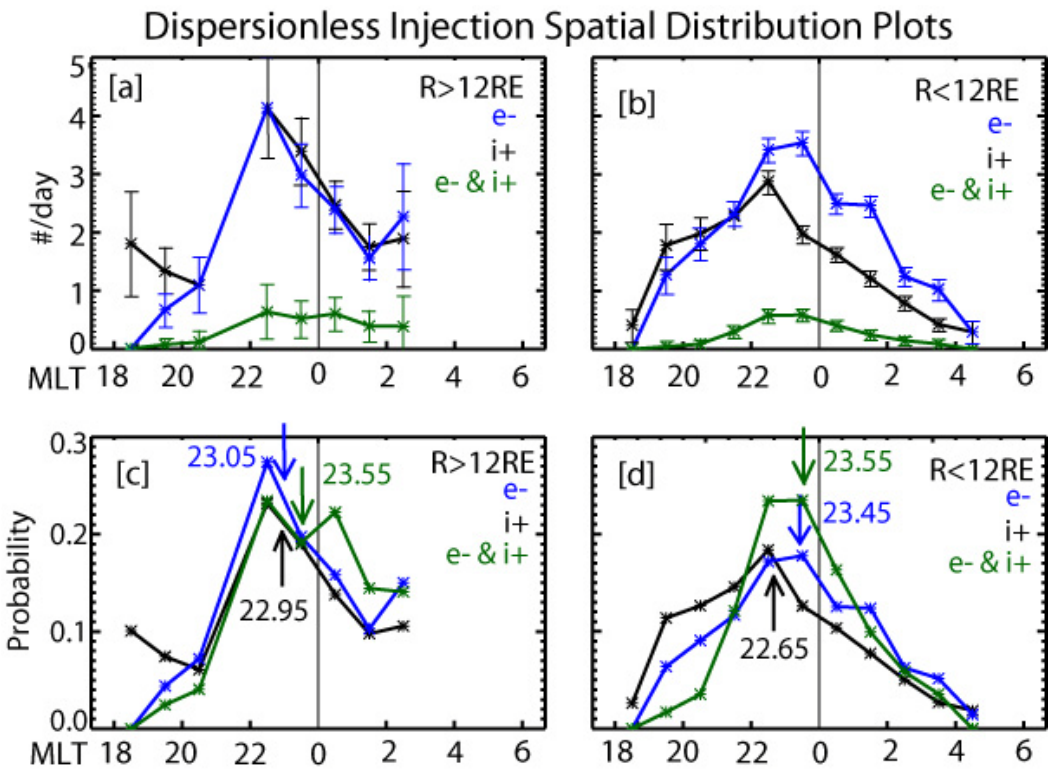

Figure 2.13. Spatial distributions of dispersionless injections, plotted separately for electron-only events (blue), ion-only events (black), and events in which both an electron and an ion injection were observed by the same spacecraft within 10 min of each other (green). (a) Injection occurrence rates (#/day per 1 hour MLT bin) beyond 12 R_E. There are 135 ion, 119 electron, and 45 with both ion and electron injection events beyond 12 R_E. (b) Injection occurrence rates (#/day per 1 hour MLT bin) within 12 R_E. There are 792 ion, 1138 electron, and 322 with both ion and electron injection events within 12 R_E. (c) Injection probability plotted per 1 hour MLT bin beyond 12 R_E. Medians noted with arrows. Median absolute deviation (MAD) for e-: 1.23 h, for i+: 1.58 h, for coincident: 0.81 h. (d) Injection probability plotted per 1 hour MLT bin within 12 R_E. Medians noted with arrows. MAD for e-: 1.19 h, for i+: 1.19 h, for coincident: 0.94 h. Bins in which the spacecraft spent fewer than 40 hours were not included. The uncertainty is calculated as $\pm\sqrt{N}/days$, where N is the number of events counted per bin and days is the total time spent in that bin.

Comparing outer region ion-only and electron-only injections with coincident events, we find factors of 6.5 and 5.8, respectively. Comparing inner region ion-only and electron-only injections with coincident events, we find factors of 6.2 and 8.0, respectively. Thus, for the case in which both electrons and ions are injected simultaneously within a 1 R_E-wide region centered on a narrow flow channel, dispersionless electron-only or ion-only injections might still be

observed within a region 6.2-8.0 R_E from the flow's center. It is likely that near the dawnward edge of the flow burst, only electron injections are observed, while near the duskward edge only ion injections are observed, making the width of coincident injections smaller than the width of the flow burst proper. This interpretation is in agreement with our observation that at least 74-77% of dispersionless injections observed in the outer region were associated with flows >100km/s, even though only ~33-38% of the outer region injections were coincident events. An additional reason that the singular injection regions external to the narrow flow channel are so much larger than the narrow acceleration site is that particles may travel via serpentine or Speiser motion, which is faster than gradient-curvature drift alone. In either case, our results suggest that the source of the injected particles is likely a few to several times smaller than the regions over which dispersionless injections are observed. Multi-spacecraft studies of injections are a reasonable way to reach closure on the exact extent and distribution of injected particles around the acceleration site.

2.4.4 Superposed Epoch Analysis of Coincident Electron and Ion Injections

As a final test to substantiate our theory describing injections as the result of narrow flow channels, we performed a superposed epoch analysis using only the 352 coincident events (Figure 2.14), regardless of Vx or |AL|, in which t_0 is the ion injection onset time. We seek confirmation of our hypothesis that coincident injections are observed at the flow's center and single injection events are typically observed at the flanks, after particle drift occurs. There are several key points to note. First, the results are similar to the signatures seen in the Vx_{max} bin (Figure 2.3a2, 2.3d2-g2 for ions and Figure 2.3a1 for electrons), implying that most coincident events fall into the Vx_{max} bin (a fact that we also verified by looking at the individual coincident

events). Thus, singular injection events are less likely to be associated with strong flows, consistent with our explanation that they represent particles that have drifted outside of the narrow channel of the fast flow (or near its edge) and are thus observed without a strong attending velocity burst, dipolarization front, or associated dawn-dusk electric field. The fact that coincident events are associated with the faster flows while singular events are not indicates that when the center of a narrow fast flow passes directly over the spacecraft, both ion and electron injections are observed.

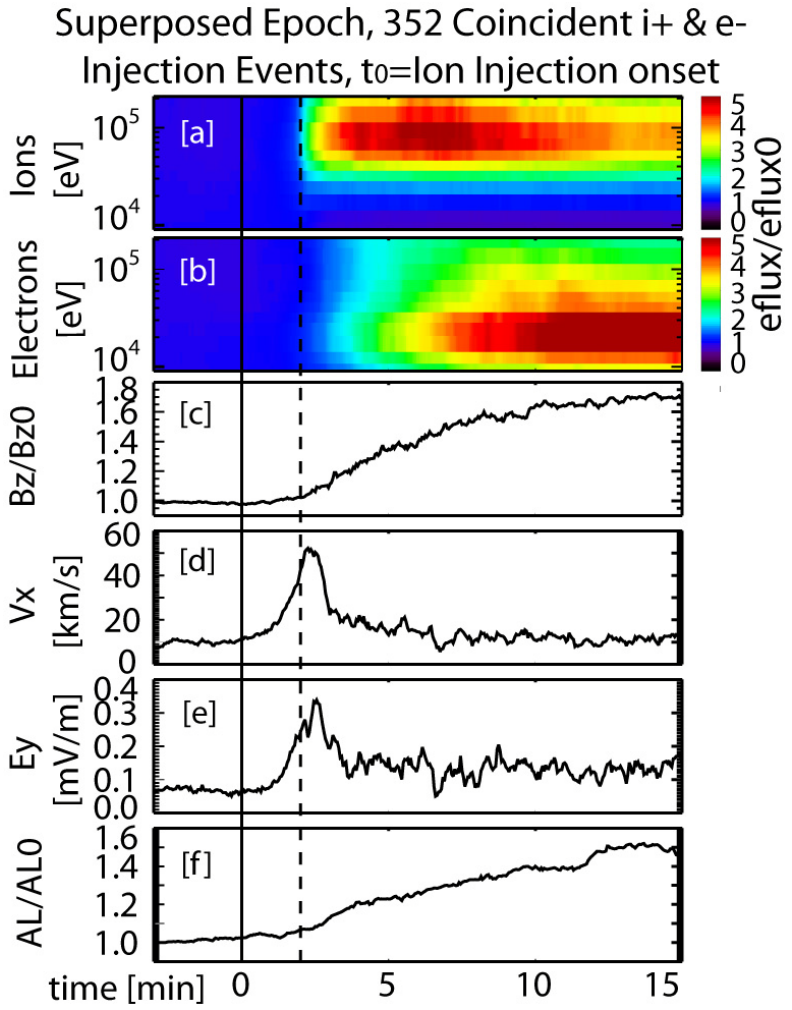

Figure 2.14. Similar to Figure 2.3, except instead of binning by Vx, the superposed epoch plot is of only the 352 coincident electron and ion events. Panels (b-e) look remarkably like those for Vx_{max}, except that the velocity burst in panel (d) is temporally narrower than the velocity burst in Figure 2.3. This demonstrates that the coincident events fall largely within the Vx_{max} bin.

Second, there is a slight delay between the rise in electron energy flux after both the rise in ion energy flux and the dipolarization. This delay suggests that the ion injections are better organized by the flow burst and dipolarizing flux bundle than the electrons. The delay in electron injection onset is consistent with the superposed epoch analysis based off of electron t_0 (Figure 2.3a1-h1 and Figure 2.4a1-h1) which demonstrated less prominent relationships than that based off of ion injection onset (Figure 2.3a2-h2 and Figure 2.4a2-h2).

Finally, although their general signatures are quite similar, the velocity burst in Figure 2.14d has a smaller half-width than the one in Figure 2.3e2, which represents the Vx_{max} bin (red). We suggest that this is because the coincident electron and ion injections are observed within the narrow flow burst, that the flows are much better organized about t_0 in Figure 2.14 than in Figure 2.3. Figure 2.14 better represents the short, approximately 1 min timescales of the fast velocity burst within the ~10 min long bursty bulk flows.

2.5 Summary

Through a statistical study of THEMIS-observed electron and ion injections in the Earth's magnetotail ranging from within geosynchronous orbit to ~30 R_E, we demonstrate a clear correlation between injections and transient, localized, earthward-traveling dipolarizing flux bundles (or plasma bubbles) through their accompanying features such as fast flows, dipolarization, and enhanced electric field. Specifically, 74% of electron injections and 77% of ion injections observed beyond 12 R_E were associated with flows >100km/s.

Enhanced geomagnetic activity is directly linked to each of these features: with increased |AL| we observed better flow correlation (via larger median values), stronger dipolarizations, and stronger dawn-dusk electric fields, as well as increased injection occurrence rate and an increase

in the energy of the broad peak of the flux enhancement. Higher |AL| indices are also correlated with higher injection occurrence rates within the inner magnetosphere. This suggests that during active times, injections can more easily reach lower L-shells and thus more effectively populate the inner magnetosphere with energetic particles.

Analyzing how the spectra vary under different levels of geomagnetic activity, we found a definite, positive correlation between increasing |AL| and spectral hardening. As in *Christon et al.* [1988], we found that the κ of the high-energy tail on particle distributions changed only a little after injection, indicating a heating process consistent with betatron acceleration. This can be shown mathematically:

Conserving the first adiabatic invariant, $\frac{W_{\perp i1}}{B_i} = \frac{W_{\perp f1}}{B_f}$ where $W_{\perp \mathrm{i1}}$ and $W_{\perp \mathrm{f1}}$ are the initial and final (perpendicular) energies of particle 1, respectively, and B_{i1} and B_{if} are the initial and final magnetic field values at particle 1's location. Betatron acceleration is the increase in energy particle 1 undergoes as it travels from B_{i1} to a higher magnetic field, B_{f1}. If we now include a second particle, $\frac{W_{\perp i2}}{B_i} = \frac{W_{\perp f2}}{B_f}$. We can rearrange these two equations to read: $\frac{B_f}{B_i} = \frac{W_{\perp f1}}{W_{i1}} = \frac{W_{\perp f2}}{W_{i2}}$. This demonstrates that under betatron acceleration, the particles' energy will increase by the same degree $\left(W_{\perp i} \times \frac{B_f}{B_i}\right)$ regardless of their initial energy ($W_{\perp i}$). Since κ is the negative slope of the distribution plotted in log-log space (refer to equation 2.2), if $W_\perp$ increases by the same degree for all energies, then κ will not change. Thus, a constant κ observed from before to after injection implies betatron acceleration.

Additionally, the flux at a fixed energy (40 keV) increases by a relatively consistent factor regardless of the geomagnetic activity index. The observed flux increase with little spectral hardening is consistent with local heating of the distributions by the injection. However,

the small increase in flux and the minor change in κ relative to the larger variations of both of these parameters in the ambient plasma sheet with increased geomagnetic activity suggest that the individual injection does an incremental part of the plasma sheet heating. We suggest that multiple injections associated with individual reconnection fronts and associated wedgelets act cumulatively from a number of locations to change the spectra throughout the plasma sheet. At any given location, each injection contributes particles not only in accordance with its strength but also in accordance with which energies have propagated to that location from the acceleration site and how much time has passed since the injection. Thus, as |AL| increases due to an intensifying substorm current wedge, heating and spectral changes in the plasma sheet occur gradually because of the cumulative effect of the injections associated with individual wedgelets. In this picture, the |AL| index is simply an indicator of the number and intensity of wedgelets that are occurring, building up the substorm current wedge while their associated injections are heating up the plasma sheet.

In addition to probing injection dependence on geomagnetic activity, we explored their spatial distribution. A dawn-dusk asymmetry with a tendency towards pre-midnight in injection occurrence (~23 MLT) was revealed for both electrons and ions throughout the magnetotail, extending similar asymmetrical observations from geosynchronous orbit to the trans-geosynchronous altitudes. This asymmetry is in agreement with previous studies of reconnection-related phenomena, such as signatures of near-Earth reconnection (flow reversals), flux ropes and traveling compression regions, fast earthward flows, and dipolarizing flux bundles. The slight dawnward offset of electron from ion injection occurrence rates (peak occurrence rate offset is 0.1 MLT at $R>12\ R_E$ and 0.6 MLT at $R<12\ R_E$) can be explained by the gradient/curvature drift of the particles energized by the flow bursts. As the particles approach

Earth, their drift speeds increase because of Earth's magnetic field increase. As particle drift speeds increase, ions and electrons drift more quickly away from each other but still lack dispersion times larger than our operational, 1 min delay between energy flux rise times, allowing them to be classified as "dispersionless" even outside the flow channel. At the edges of the flow where electrons may still be dispersionless on the dawnside (and ions on the duskside), the ions (or electrons) would not be energized sufficiently, further reducing the occurrence rate of "coincident" injection events compared to "electron-only" and "ion-only" injections. Coincident injection observations are likely to be constricted to the very center of the narrow flow channel, which is already small compared to the entire region accessible to injected and drifting ions and electrons.

By surveying the smaller population of coincident electron and ion injection events, we found that the median signatures for the change in energy flux, the change in B_Z, earthward velocity, enhanced dawn-dusk electric field, and change in |AL| closely match the median signatures plotted for the Vx_{max} bin. This is because most of the coincident electron injections fall into the Vx_{max} bin, demonstrating again that injections are caused by particles undergoing energization by drifting across the potential drop created by the strong, localized electric field associated with flow bursts and dipolarizing flux bundles. The slower velocity bins (Vx_{inter} and Vx_{min}) are therefore mostly comprised of "ion-only" and "electron-only" injection events because the particles have drifted away from the faster flow at the center of the flow channel. This explains both why these injections are not associated with faster flows and also why they are not seen coincidently with the other species. Figure 2.15 is a (not-to-scale) schematic of this concept.

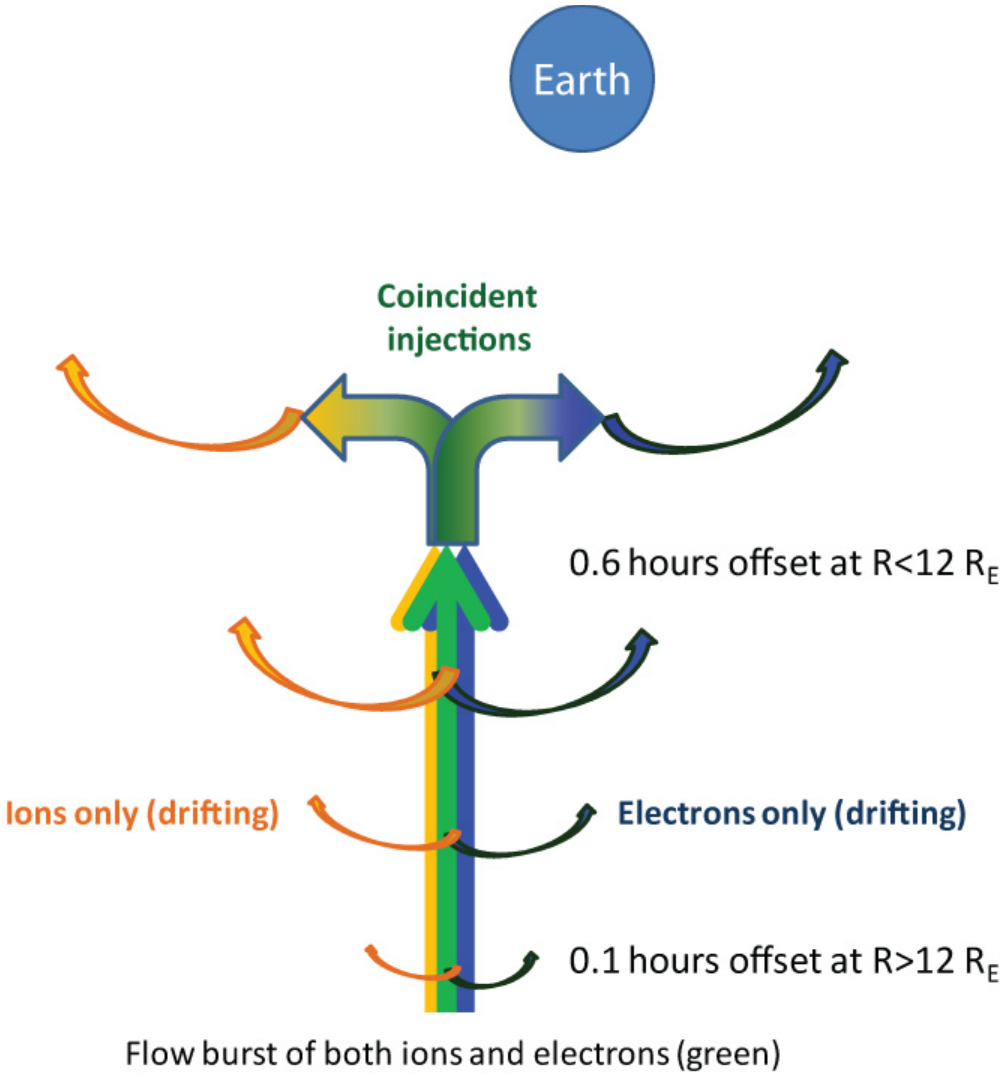

Figure 2.15. A schematic of the narrow, earthward-traveling flow that statistically occurs in the pre-midnight sector. At the center of the flow channel both electron and ion dispersionless injections can be observed (green) while only dispersionless electron injections are observed to the dawn (blue) and dispersionless ion injections to the dusk (yellow). The offset between the dispersionless electron and ion injections increases closer to Earth due to faster gradient drifts.

Our study complements the understanding of particle energization that began developing with geosynchronous observations, but opens up a new understanding of injections, plasma heating, and geomagnetic activity: From statistical analysis it supports the findings of previous case studies that injections are related to transient, localized fast flows and dipolarization fronts in the tail. Instead of an azimuthally wide "injection boundary" that moves earthward under an

enhanced global electric field, the source of particle acceleration is a transient, localized electric field following a reconnection front that launches energized particles as it travels earthward. Moreover, since injections are associated with dipolarizing flux bundles, which are accompanied by wedgelets (elemental increases to the substorm current wedge with direct effect on |AL|), it is evident why elemental plasma sheet heating through injection and propagation of energized particles acts collectively to enhance plasma sheet temperature and spectral hardening in conjunction with increased geomagnetic activity.

Appendix 2A

To provide the reader with specifics on the statistics, we also include Figure 2A.1 that demonstrates the total number of injections observed in each 4x4 bin that is used throughout Chapter 2, classified by type: dispersionless electron or ion injections (2A.1a and 2A.1b), dispersed electron or ion injections (2A.1c and 2A.1d), inverted electron or ion injections (2A.1e and 2A.1f). In Figure 2A.1g we plot the total number of days spent by THEMIS in each 4x4 bin. Dividing 2A.1a-2A.2f by 2A.1g results in the occurrence rates plotted in Figures 2.8e-f, 2.9e-f, and 2.11a-b.

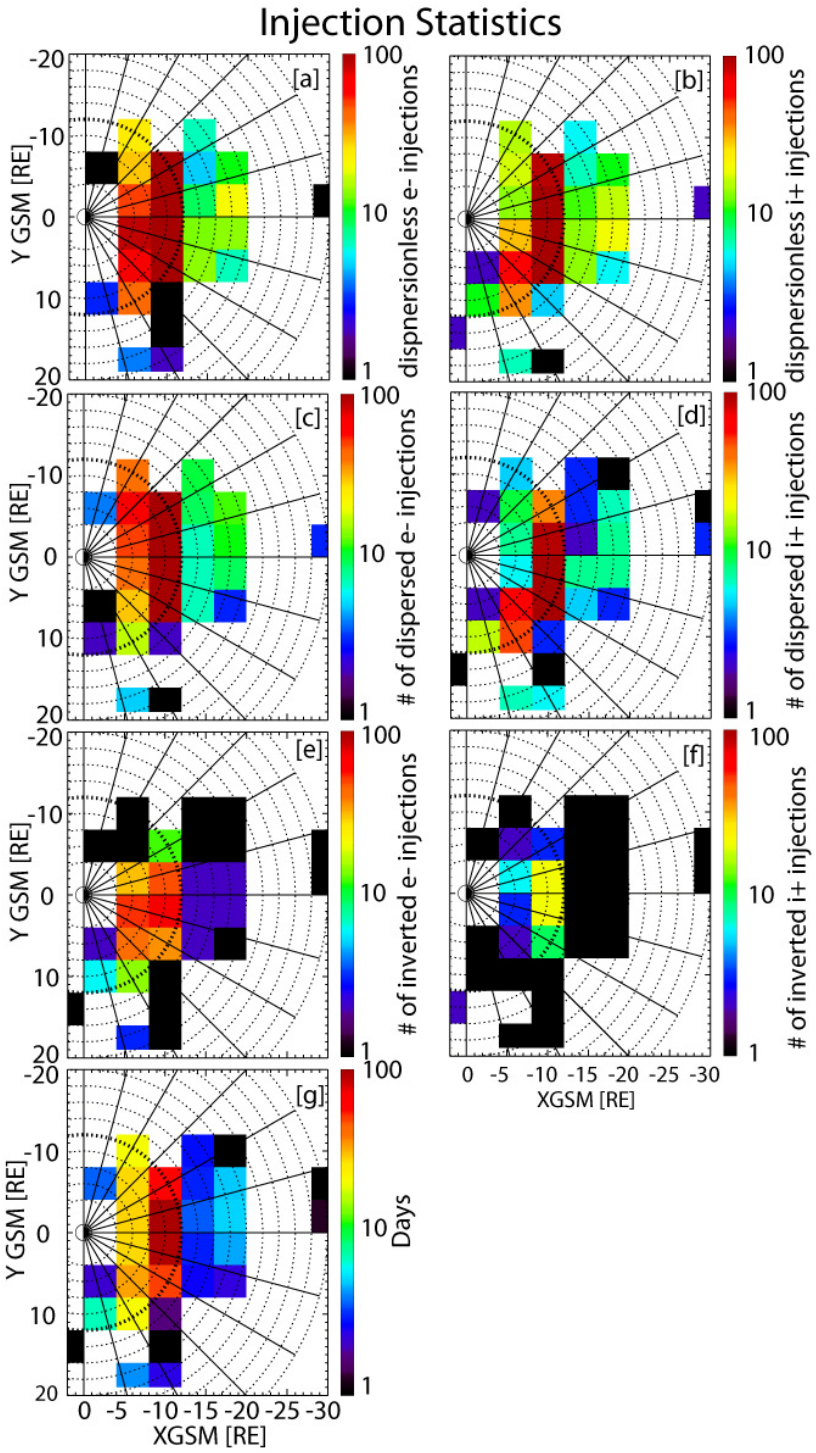

Figure 2A.1. Information plotted in 4x4 R_E bins akin to Figures 2.8e and 2.8f. (a) Number of dispersionless electron injections observed. (b) Number of dispersionless ion injections observed. (c) Number of dispersed electron injections observed. (d) Number of dispersed ion injections observed. (e) Number of inverted electron injections observed. (f) Number of inverted ion injections observed. (g) Number of days THEMIS spent in each bin. A bin was only included (assigned a color) if THEMIS spent at least 20 hours in that particular bin.

CHAPTER 3

The effects of transient, localized electric fields on equatorial electron acceleration and transport toward the inner magnetosphere

3.1. Introduction

A dominant contributor to plasma sheet transport (60-100%), bursty bulk flows (BBFs) are continuous segments of magnetotail flow enhancement (~10-min timescales), punctuated by 1-min long intense flow and electric field bursts (V > 400 km/s and VxBz >2mV/m), typically associated with geomagnetically active times [*Angelopoulos et al*., 1992; *Angelopoulos et al*., 1994; *Schödel et al*., 2001]. Their origin and dynamics likely result from localized, impulsive reconnection [*Semenov et al*., 2005]. Their inward propagation has been described energetically by the plasma bubble model: after reconnection, localized and under-populated flux tubes carrying an enhanced magnetic field can penetrate the near-Earth region [*Pontius and Wolf*, 1990; *Sergeev et al*., 1996; *Wolf et al*., 2009; *Dubyagin et al*., 2011; *Li et al*., 2011]. The dynamics of their motion is described by the driving curvature force of the reconnected flux tubes and the restoring effects of the increased plasma pressure ahead of them [*Li et al*., 2011]. Specifically, *Li et al*. [2011] showed using THEMIS data that flow bursts accompanied by a large-amplitude dipolarization front will penetrate deeper into the dipole-dominated, near-Earth plasma sheet due to the predominance of the curvature force density. This force results primarily from the magnetic field increase that builds up to compensate the density depletion within the dipolarized flow burst.

Observations [e.g., *Keiling et al*., 2009; *Keika et al*., 2009; *Ohtani et al*. 2009; *Panov et al.* 2010] and MHD models [*Birn et al*., 2011] have shown that when a BBF reaches the strong,

dipolar magnetic field, tailward flow and/or vortices result from overshoot and rebound (because of high pressure gradients, the plasma must be redirected, and vortices form with flows of opposite sense at the eastward and westward edges of the earthward flow). Vortices have been observed [*Sergeev et al*., 1996; *Shi et al*., 2011] and modeled in both MHD [e.g., *Birn et al*., 2004] and Rice Convection Model (RCM) [e.g., *Yang et al*., 2008; *Yang et al*., 2011] simulations in the context of plasma bubble transport. In this situation, a flow shear forms ahead of and around the bubble perimeter as the high-entropy flux tubes are displaced around it, and thus vortices and associated tailward flow may be significant at any location in the tail where the bubble travels. Furthermore, *Gallardo-Lacourt et. al* [2014] have used THEMIS all-sky imagers and Super Dual Auroral Radar Network (SuperDARN) radars to observationally demonstrate the tailward flows at the edge of the earthward flow by studying streamers in the ionosphere. Their observations are consistent with the spatial relationship between flow shear and upward field-aligned currents in plasma sheet flow bursts.

Another feature of plasma acceleration and transport observed in the magnetotail is the energetic particle injection. Injections have been largely studied at geosynchronous orbit partly because of the plethora of satellites there [i.e., *McIlwain*, 1974; *Mauk and Meng*, 1983; *Birn*, 1997a,b; 1998], however, energetic particle flux increases have also been observed as far as 60 R_E downtail [*Anderson*, 1965; *Konradi*, 1966; *Armstrong and Krimigis*, 1968; *Sarris and Krimgris*, 1976 and references therein] and now are often seen in the THEMIS dataset covering the near-Earth and midtail regions [*Runov et al*., 2009, 2011]. Their observational signature is a sudden flux enhancement at energies of tens to hundreds of keV (protons and/or electrons), typically correlated with increased geomagnetic activity such as substorms and storms. If the spacecraft directly observes the injection near its source, the injection is “dispersionless” (flux

increases occur simultaneously over a broad range in energy). If the injection is "dispersed", with the flux increasing first at higher energies, energy-dependent ∇B and curvature drifts are considered responsible for the delayed lower-energy particle arrival times [e.g., *Zaharia et al*., 2000]. After particles are injected—previously proposed as a result of time-dependent shifting of Alfvén layers earthward by a sudden increase in the large-scale electric fields [e.g., *Walker and Kivelson*, 1975]—and are entrapped on closed drift orbits (presumably after the global electric field has been reduced), injections can be observed multiple times with progressively increased dispersion and are termed "drift echoes" [*Lanzerotti et al*., 1967].

Launched in 2007, the five-spacecraft (THA, THB, THC, THD, THE) THEMIS mission provides the means to study injections with unprecedented temporal and spatial detail, having orbital configurations that result in different azimuthal and radial separations in the magnetotail [*Angelopoulos et al*., 2008]. Pre-THEMIS modeling of geosynchronous injections has relied on a near-Earth electric field increase (often called an injection boundary [*Mauk and Meng*, 1983]) because high-altitude observations were too scarce to be well correlated with the routinely available geosynchronous satellite data. Although previous attempts to study inward-propagating pulses using large-scale electric field models have been relatively successful, they could not be spatially constrained due to the lack of multi-spacecraft measurements in the source region, the outer magnetosphere (>6.6 R_E). Observations of energetic particle flux intensification at distances 6.6-60 R_E ("trans-geosynchronous" injections), as reported in Chapter 2, imply a spatially localized acceleration mechanism beyond the near-Earth region. However, the cause of these trans-geosynchronous injections (TGIs) and their relationship to traditionally studied geosynchronous injections has been unclear, primarily due to the lack of multi-spacecraft data in the equatorial plasma sheet. With the advent of THEMIS's equatorial, multi-point dataset, a

continuum of injections (from the geosynchronous region to the 20-30 R_E mid-tail region) has been revealed, the statistics of which were presented in Chapter 2. In fact, such injections have been observed nearly simultaneously at multiple nearby locations with varying intensities, suggesting a common source over extended regions of the equatorial plasma sheet. Often accompanied by flow bursts and magnetic field dipolarizations, such injections are frequently seen to propagate earthward from the region of magnetic reconnection (typically >20 R_E) to the inner magnetosphere (~6.6 R_E) when spacecraft are fortuitously aligned. The origin of the plasma acceleration and intense low frequency electric fields have recently been attributed to the curvature force of the newly reconnected field lines [*Li et al*. 2011].

Injections play an important role in the dynamics of the inner-magnetosphere by providing a source population (10-300 keV ions and electrons) for the ring current and outer radiation belt. Recent studies indicate that wave-particle interactions accelerate this seed population of electrons to relativistic energies, which can cause radiation damage to telecommunication and navigation satellites [*Turner et al*., 2010; *Chen et al*., 2007; *Kappenman et al*., 1997]. It is therefore no surprise that models have been developed to try to understand the physical processes behind such injections as modes or signatures of transport.

Such models [*Li et al.,* 1993; 1998; *Sarris et al*., 2002; *Delcourt et al*., 2002; *Zaharia et al*., 2000; 2004; *Ganushkina et al*., 2005] have utilized an earthward propagating electromagnetic pulse to sweep particles earthward from a location of lower magnetic field strength to that of higher magnetic field strength, thus energizing particles by betatron and Fermi acceleration under conservation of the magnetic moment and the 2nd (“bounce”) invariant. Particle trajectories are modeled via the guiding center equations of motion subject to external electric and magnetic fields [*Northrop*, 1963]. In such studies, the simulated electric field pulse is often

initiated near the inner edge of the plasma sheet (~10 R_E) and is associated with magnetic dipolarization: a sharp, large-amplitude increase in the magnetic field Z-component that often occurs during substorms. This signature has been modeled to have a wide azimuthal extent (~30-180°) to correspond to an inward collapse of a good fraction of the entire magnetotail (global dipolarization). For example, *Zaharia et al.* [2004] reproduced the properties of a geosynchronous, dispersionless injection at local midnight caused by an electric field pulse approximately the size of the substorm current wedge (azimuthal width of 60°). As shown in their Figure 4 (Figure 3.1), this results in a pulse width ~8 R_E across at X =-6 R_E, and ~12 R_E across at X=-11 R_E. Such wide pulses may work at geosynchronous altitudes, however, they are not observed in the THEMIS data traversing greater distances (>10 R_E) where recent observations of TGIs (e.g., *Runov et al*., 2009; 2011) have been made. In fact, these TGIs correlate with flow bursts and electric fields that are azimuthally localized ($\delta Y \sim 1\text{-}4 R_E$, see *Nakamura et. al* [2004]), providing strong evidence for localization of the observed impulses.

Advancing our current understanding of particle acceleration and transport in the magnetosphere thus requires a synthesis of the abundant THEMIS observations of reconnection flows, injections, electric fields and dipolarization fronts with a simple, interpretative model. A successful model should bridge our understanding from previous observations of impulsive tail reconnection and geosynchronous injections to recent observations of dipolarization fronts, flow bursts and energetic particle flux enhancements captured on multiple THEMIS spacecraft as they travel from the mid-tail to the inner magnetosphere [*Runov et al*., 2009*; Runov et al*., 2011, *Zhou et al*., 2011]. For this work, we therefore incorporate a more accurate picture of impulsive, localized electric fields as surmised from recent observations, initiating in the near-Earth tail (at distances of ~20 R_E).

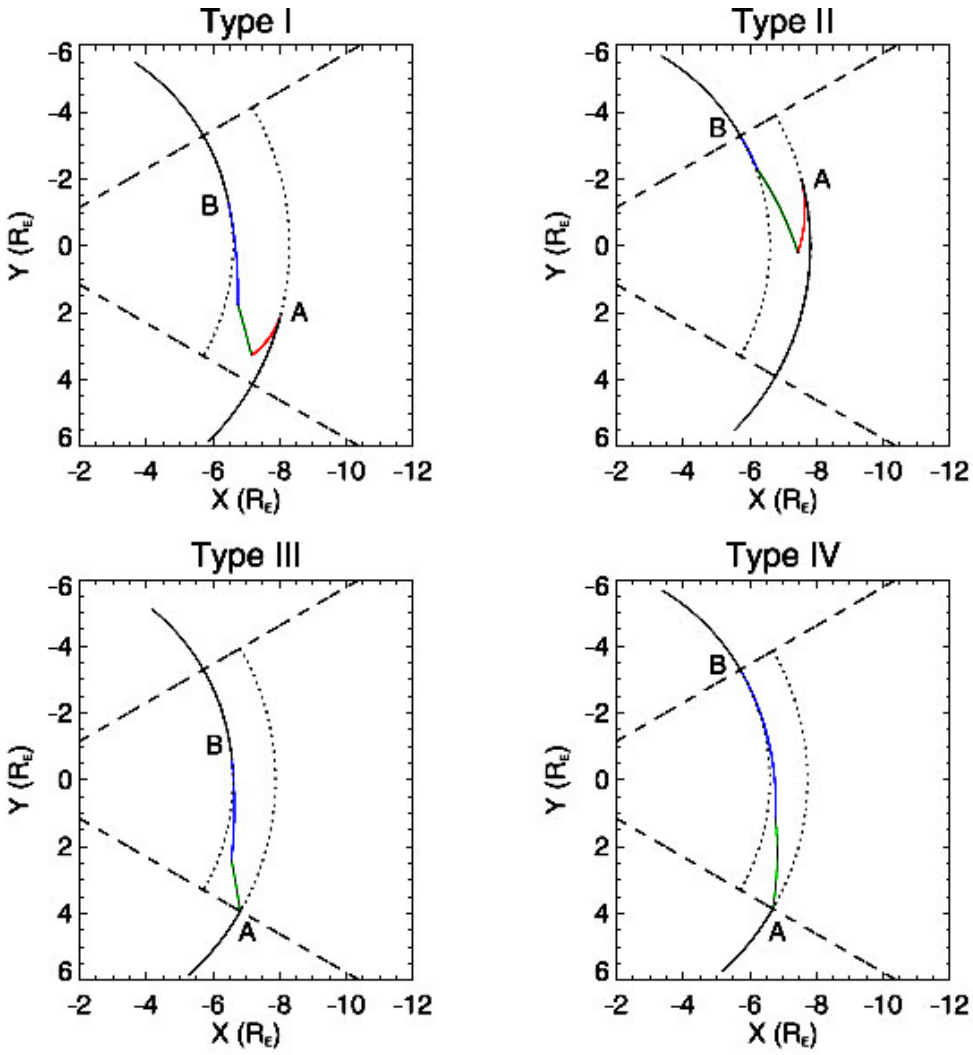

Figure 3.1. Figure 4 from *Zaharia et al.* [2004]. Demonstrating electron trajectories through the electromagnetic field pulse. The figure demonstrates the large azimuthal extent of the pulse in their model.

We seek to explain particle acceleration and injection signatures both at geosynchronous altitude and farther downtail with a single, simple model. Those signatures observed downtail may not be on closed drift orbits; however, since the energizing and transporting mechanism is the same downtail as at geosynchronous, we keep a consistent definition of injections as sudden energy flux enhancements. In the following section we describe the details of an electric field model used for this purpose as well as explain the steps behind our modeling of the energy flux

enhancements observed during injections. Electron injections during two events in which TGIs were observed by multiple THEMIS spacecraft are modeled and presented as case studies in section 3.3 for equatorially-mirroring electrons; these simulations serve to describe the model properties and capabilities. In section 3.4 we use particle trajectories to explain the physics behind the simulated flux depletions and enhancements, comparing our results with previous studies in section 3.5. It should be noted that in this initial presentation of the model, we do not attempt to replicate the precise electromagnetic environment of the pulse, but rather to demonstrate the validity of the model concept when even the simplest of assumptions (i.e., a dipole field and a potential flow) are used. (A magnetic field and its inductive electric field are added to the model in Chapter 4.) Thus, for this chapter, we assume minimal zero-order effects from the change in the ambient magnetic field by the dipolarization fronts. We also assume for now that the portion of the electric field induced by the (localized) change in magnetic field has a minimal effect on the flux at most locations. So, in Chapter 3, we use only potential electric fields to represent the environment surrounding a flow burst. More realistic stretched and dynamic magnetic fields and the associated inductive electric fields will be included in future endeavors to fully address their effects on particle transport and acceleration in direct comparison with this simplified picture. A discussion on the possible effects of our simplifications is included in section 3.5.

3.2. Particle Acceleration and Transport Modeling

3.2.1 Particle Motion

We have adapted a numerical model [*Angelopoulos et al*., 2002] of particle guiding-center (G.C.) motion in prescribed electric fields in the magnetosphere to provide a realistic

means of impulsively accelerating particles, breaking their quasi-steady convection orbits and thus opening up the Alfvén layers of different particle energies to earthward transport from the tail. Particle motion is determined by integrating the relativistic equations of motion of the guiding-center in a dipole field and an instantaneous arbitrary global convection pattern. For simplicity, we only investigate equatorially mirroring particles here (arbitrary pitch angles can be traced also by our model but such effects are left for a future study). For such particles, the guiding-center equation of motion is:

$$\mathbf{V}_{GC} = \frac{d\mathbf{r}}{dt} = \mathbf{V}_{ExB} + \mathbf{V}_{\nabla B}, \tag{3.1}$$

Where

$$\mathbf{V}_{ExB} = \frac{\mathbf{E}x\mathbf{B}}{B^2}; \tag{3.2}$$

$$\mathbf{E} = \mathbf{E_{DD}} + \mathbf{E_{COR}} + \mathbf{E_{transient}}; \tag{3.3}$$

$\mathbf{E_{DD}}$ is the global dawn-dusk electric field, $\mathbf{E_{COR}}$ is the electric field due to corotation, and $\mathbf{E_{transient}}$ is the prescribed electric field implemented to impulsively accelerate the particles.

In the dipole approximation, electrons will remain adiabatic within the boundary of our simulation (-22 R_E < X_{GSM} < 15 R_E and -20 R_E < Y_{GSM} < 20 R_E), so the first adiabatic invariant will always be conserved. With the T96 model [*Tsyganenko and Stern*, 1996] of a stretched magnetic field, 50 keV electrons may lose adiabaticity at approximately X_{GSM}<-17 R_E at Y_{GSM}=0, though this boundary decreases in X_{GSM} as Y_{GSM} moves away from 0. Thus, even for a moderately stretched tail, electrons would act adiabatically within the region of interest.

The generalized equipotentials in Figure 3.2 demonstrate trajectories for electrons of a finite first adiabatic invariant, μ=0.18 J/nT. (We define "generalized" equipotentials as the path a particle will take defined by equation 3.1, including both electric potential terms and the energy-dependent ∇B drift term in the calculation.) Electrons will travel earthward along the contours

under the influence of a duskward-directed convection electric field, or will orbit in a counter-clockwise sense around Earth if trapped within their Alfvén layer. One can therefore glean an understanding of how the particles will move, given any initial or final position, by plotting these generalized equipotentials as a function of time. Under a large-scale cross-tail potential drop generated by a global, dawn-dusk electric field, thermal and energetic particles drift across the tail due to ∇B and gain energy, but because of such a drift they cannot penetrate close to Earth. Figure 3.2a demonstrates this by plotting contours of motion defined by equation 3.1 for μ=0.18 J/nT particles when $\mathbf{E}_{\mathbf{transient}}$=0 (the quiescent state), as well as a μ=0.18 J/nT particle's forward trajectory (in blue) launched from X_{GSM}=19 R_E, Y_{GSM}=1.8 R_E (with tick marks every 5 minutes). The strength of $\mathbf{E}_{\mathbf{DD}}$ directly affects the Alfvén layer's location, as a stronger $\mathbf{E}_{\mathbf{DD}}$ will push a given finite μ Alfvén layer inward and only the highest energies will be trapped, whereas a weaker $\mathbf{E}_{\mathbf{DD}}$ will allow the Alfvén layer to expand such that more energies can be trapped.

Localized, intense electric fields ($\mathbf{E}_{\mathbf{transient}}$, see Appendix 3A) with a significant potential drop (e.g., ~2-10 kV) over a short cross-tail distance (as expected of flow bursts [*Angelopoulos et al*., 1994]), however, can distort the Alfvén layers of 0 to >100 keV particles, allowing the particles to gain kinetic energy by drifting across a strong yet localized potential drop without exiting the system laterally. Figure 3.2b demonstrates how the μ=0.18 J/nT particle's trajectory is altered (in red) when the transient electric field is included in equation 3.1, plotting the trajectory on top of the contours of motion. (The insert within Figure 3.2b shows the magnitude of $\mathbf{E}_{\mathbf{transient}}$ plotted against the Y_{GSM} axis; the details of the $\mathbf{E}_{\mathbf{transient}}$ model will be further discussed in section 3.2.2.) Zero μ particle contours of motion represent electric equipotentials, as zero μ particles do not ∇B drift.

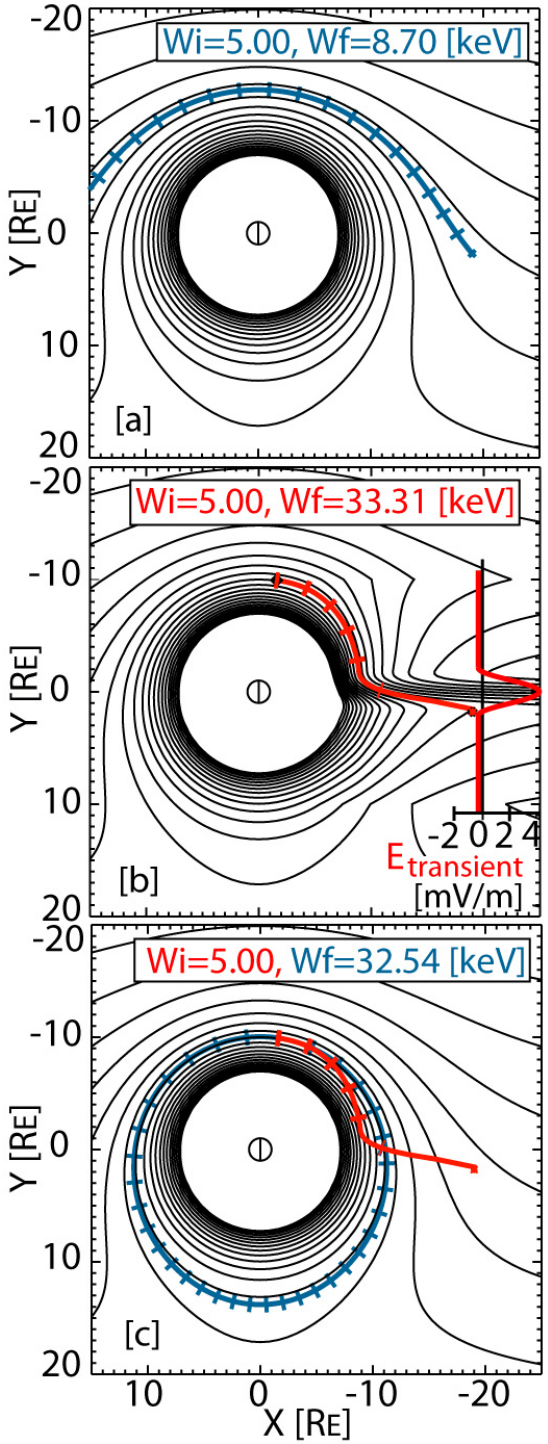

Figure 3.2. Gray lines: "generalized equipotentials," i.e., contours of motion for constant μincluding gradient drift (eqn 3.1). Blue trace: e- motion under E_{DD}, corotation, and ∇B drift. Red trace: e- motion when $E_{transient}$ is applied. Five minute tick marks. (a) Pre-$E_{transient}$. (b) $E_{channel}$ applied from Y_{GSM}= -2 to 2 R_E; E_{return} +/-10 R_E from channel center. Electron injected farther in as Alfvén layer is broken, energized by betatron acceleration or equivalently by drifting across the equipotentials. (c) Post- $E_{transient}$: After injection (red), energized e- is trapped in a closed orbit (blue).

As finite μ particles cross the electric equipotentials due to their additional ∇B drifting, they gain kinetic energy at the expense of potential energy while their generalized equipotential remains constant. Generally, thermal and energetic electrons drift dawnward and thus gain energy subject to a dawn-dusk electric field. Consistent with the energy gain from the potential drop is the betatron acceleration process as particles come from low-B in the tail (B~0 at the reconnection site) to higher B in the inner magnetosphere. This is also depicted by the higher final energy (W_f=33.31 keV) the particle achieves in Figure 3.2b after it has been transported earthward, compared to the lower final energy (W_f=8.7 keV) listed in Figure 3.2a in which the particle had to drift around its Alfvén layer.

When the transient electric field dies away (corresponding to the fast flow deceleration), the energized particles find themselves trapped inside an Alfvén layer closer to Earth; thus the inner magnetosphere is suddenly populated with energized particles. Consequently, closed drift paths host injected (now trapped), energized particles executing closed orbits that result in drift echoes (blue trajectory in Figure 3.2c). Therefore, this simple model simulates particle acceleration due to impulsive, localized electric fields and particle inward transport due to the temporal evolution of Alfvén layers. Our independent, analytic models based on adiabatic invariant conservation mapping confirm the guiding center motion of different energy particles in fixed electric and magnetic field, providing full insight into the physics of acceleration and transport from both macroscopic conservation laws and from an individual drifting/bouncing particle trajectory perspective.

3.2.2 Simulating the Spectra

The crux of our methodology is to simulate observed injection signatures in the particle spectra with our model, constraining adjustable parameters of $\mathbf{E}_{\mathbf{transient}}$ and thus gaining a better understanding of the nature of the driving fields (caused by the fast flows), the energetic particle acceleration (resulting from drifts across the potential drop), and the resultant particle transport towards the inner magnetosphere (permissible through the fields opening up the classical Alfvén layers). When a spacecraft observes an injection (enhanced energy flux or "eflux"), it is observing particles that were previously affected and energized by the transient electric field in the flow burst. Thus, the simulation entails tracing particles of various energies backward in time (backtracing) from the spacecraft's point of observation (via the equation of motion described in equations 3.1-3.3) to find how much they have been energized by $\mathbf{E}_{\mathbf{transient}}$. Knowing how much they have been energized allows us to calculate the eflux at the spacecraft location. We then tune the $\mathbf{E}_{\mathbf{transient}}$ field parameters assuming fixed sources to match the observed spectra (i.e., we perform "forward modeling"). The details of this process are described in the following subsections.

3.2.2.1 Phase Space Density

3.2.2.1.1 Phase Space Density Description

Backtracing a representative particle of observed final energy W_f determines its source location and initial energy (W_i) prior to betatron acceleration. Knowing the particle's W_i prior to its interaction with $\mathbf{E}_{\mathbf{transient}}$ is crucial, because it tells us what its phase space density is (assuming we have a reasonable constraint on the function at the source location), which is necessary to calculate the eflux we are simulating. According to Liouville's theorem, the volume

in phase space that the particle represents will retain its density over the entire trajectory. By using such a reasonable distribution function at the representative particle's source location, we can model its phase space density (PSD) at the initial energy and can thus calculate its energy flux and simulate the spectra at the spacecraft location (where we now take PSD = *f*):

$$eflux = \frac{W_f^2}{2\pi m^2} f(W_i, X_i, Y_i) \frac{keV}{cm^2 s\ keV\ str} \tag{3.4}$$

This is obtained from defining *eflux* = $\vec{Q} = W \int \vec{v} dN$ (3.5)

$$d\vec{Q} = W\vec{v}dN = W\vec{v}f d^3v \tag{3.6}$$

$$d\vec{Q} = v\overrightarrow{W}f\left(\vec{E}\right)v^2 dv d\Omega \tag{3.7}$$

$$= 2\frac{v^2}{2}\overrightarrow{W}f\left(\overrightarrow{W}\right)d\left(\frac{v^2}{2}\right)d\Omega \tag{3.8}$$

$$= \frac{2}{\mathrm{m}^2} W\overrightarrow{W}f(W)dWd\Omega \tag{3.9}$$

$$\therefore \frac{d|\vec{Q}|}{dWd\Omega} = \frac{2}{\mathrm{m}^2} W\left|\overrightarrow{W}\right| f(W) = \frac{2}{\mathrm{m}^2} W^2 f(W) \tag{3.10}$$

where we divide by 4π to calculate directional flux. Since the energy flux is a function of PSD times energy squared, nominally it is$W_f^2 \cdot PSD > W_i^2 \cdot PSD$, and eflux is enhanced during earthward transport (injection) into a stronger field.

Different forms of the PSD have been used in the past to model plasma sheet particles; a kappa distribution with $2<\kappa<6$ being a rather typical approach [*Vasyliunas*, 1968; *Christon et al*., 1989; *Christon et al*., 1991; *Gloeckler and Hamilton*, 1987; *Kletzing*, 2003]. Magnetotail observations have shown that two-component distributions are often needed to account for particle mixing from different source regions [*Peterson et al*., 1981; *Lennartsson and Shelley*, 1986]. To incorporate this, various studies have implemented a two-component Maxwellian distribution [*Wing and Newell*, 1998] or a two-component kappa distribution [*Wang et al*., 2007]:

$$PSD = PSD_{hot} + PSD_{cold}$$

$$= N_h \left(\frac{m}{2\pi\kappa_h W_{0_h}}\right)^{3/2} \left[\frac{\Gamma(\kappa_h + 1)}{\Gamma(\kappa_h - 0.5)}\right] \left(1 + \frac{E}{\kappa_h W_{0_h}}\right)^{-(\kappa_h+1)}$$

$$+ N_c \left(\frac{m}{2\pi\kappa_c W_{0_c}}\right)^{3/2} \left[\frac{\Gamma(\kappa_c+1)}{\Gamma(\kappa_c-0.5)}\right] \left(1 + \frac{E}{\kappa_c W_{0_c}}\right)^{-(\kappa_c+1)} \quad (3.11)$$

where $W_0 = E_0\left(1 - \frac{3}{2\kappa}\right)$ is the most probable energy, $E_0 = Tk$ is the energy of peak particle flux (*k*=Boltzmann constant), *m*=mass, *N*=particle density, and *E*=particle energy. Note that a kappa distribution becomes a Maxwellian in the limit $\kappa \rightarrow \infty$. In the opposite extreme, the high energy tail flattens as $\kappa \rightarrow 1.5$.

3.2.2.1.2 PSD Determination

Here we followed *Wang et al.* [2007] and utilized the two-component kappa distribution representing a hot and cold population. We found that our case studies were not well represented by statistical averages of PSDs at various distances, however, so we established the source properties by fitting modeled PSDs to measured PSDs prior to the injections assuming a nominal dawn-dusk electric field. By varying the density, temperature, and kappa of the source population (obtained through backtracing in the nominal field), we calculated the modeled PSD and energy flux through minimizing chi-squared relative to the observed spectra, then varying the parameters to focus the fit on the higher energies of interest. We thus determined the source population hot and cold densities, temperatures, and kappa values (N_h, N_c, T_h, T_c, κ_h, and κ_c respectively) that resulted in the best match with the observed pre-injection spectra at the spacecraft. These source values are then used for the entire interval being modeled. Figure 3.3 shows an example of this fitting for the four spacecraft in Case 2 at 05:30 UT, prior to the injection (see section 3.2).

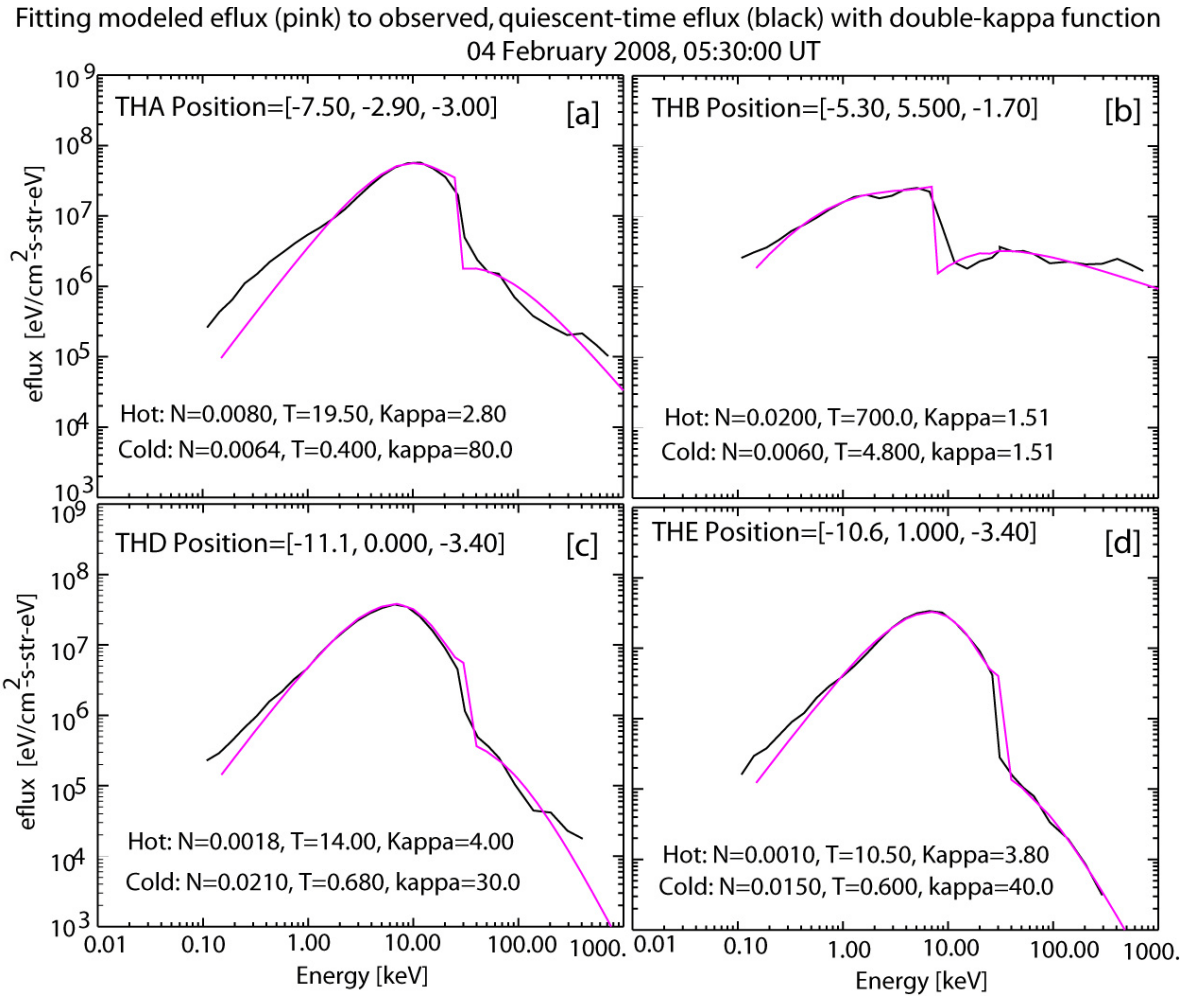

Figure 3.3. Fitting the modeled eflux with observations with a 2-component kappa distribution function at 05:30 UT on 2008-02-04 for four THEMIS spacecraft. The sharp fall-off in eflux marks the separation between the higher energies that are trapped orbiting and the lower energies that are drifting outside the Alfvén layer. The spacecraft positions as well as the parameter values used in the fit (hot and cold) are listed.

The process requires estimating the global dawn-dusk (convection) electric field ($\mathbf{E_{DD}}$) since it plays a role in particle tracing (reference equation 1). Although other methods exist to determine its value, for this study it is estimated by determining which energies are trapped within the Alfvén layer at the spacecraft position, since the strength of $\mathbf{E_{DD}}$ directly affects the Alfvén layer's location. When the THEMIS spacecraft are located in the near-Earth or midtail region (as in our case studies), there is a distinct difference in the energy spectrum of the distribution function between the hot (trapped) population and the cold population (particles

drifting earthward from downtail. This discontinuity in the spectrum is a robust feature of the observed and modeled distribution function regardless of the fit quality (since the discontinuity—separating the two particle populations—depends only on E_{DD}). Thus, utilizing E_{DD} as an input parameter to fit the modeled and the observed discontinuity, E_{DD} can be approximated. (Although the discontinuity in Figures 3.4a, 3.4c, and 3.4d may be exaggerated by the difference in the SST and ESA instruments, a difference in hot versus cold populations is still apparent. We also observe this discontinuity at other energies when THEMIS is located elsewhere, so we know this feature is not instrumental.) Applying this method to several THEMIS spacecraft at different locations and finding the best fit between them with a single $\mathbf{E_{DD}}$ provides additional confidence in the result. Once E_{DD} has been determined, we next fit the observed differential directional energy flux to determine the source parameters.

3.2.2.2 Backtracing Details

Losses are not included in the tracing procedure, as it is understood that for electrons the loss-cone is too small to affect the fluxes at large distances even in the limit of strong diffusion. Backtracing is stopped after 24 hours or after the particle reaches $L = 20\ R_E$; uniformity of the source PSD across local times is assumed. If, however, when the particle reaches 20 R_E it lies within the intense electric field channel, backtracing is allowed to extend further downtail to 22 R_E, i.e., to a somewhat smaller equatorial magnetic field. This is designed to replicate the lower equatorial magnetic field in the reconnection region. The low initial B_z-field of reconnected particles within the channel allows them to obtain larger energization from betatron acceleration than particles engulfed in the $\mathbf{E_{channel}}$ at smaller distances.

We ran the backtracing using 43 energy steps across the THEMIS ESA and SST instrument range of energies (0.015-1000 keV) for the duration of interest (1.5 hours for both cases presented). We performed a 3-point average over the spectra in energy and time to reduce noise related to fluctuations in the backtracing final positions.

3.2.3 The Transient Electric Field Model

The transient electric field in our model, "$\mathbf{E}_{\mathbf{transient}}$", is superimposed on the electric fields from global (slow, uniform) convection and corotation. It consists of several components described in Appendix 3.A and illustrated in Figure 3.4. The specific values for the electric field and THEMIS spacecraft locations are those chosen from our second case study, and will be further detailed in section 3.4.2. Contours are equipotentials arising from the sum of the global dawn-dusk electric field ($\mathbf{E}_{\mathbf{DD}}$) and the transient electric field ($\mathbf{E}_{\mathbf{transient}}$). The strongest potential gradient (i.e., electric field) points westward; it is within the localized flow channel and is shaded blue. There the field "$\mathbf{E}_{\mathbf{channel}}$" is modeled as a sinusoidal function of the Y_{GSM} position with a maximum (E_c) at the channel center and zero at the edges (Y_{min}, Y_{max}). The $\mathbf{E}_{\mathbf{channel}}$ component of $\mathbf{E}_{\mathbf{transient}}$ therefore is the electric field associated with the fast flow channel.

To model the return (tailward) portion of the flow vortex typical on the flow channel's eastward and westward flanks, we include another term in $\mathbf{E}_{\mathbf{transient}}$: dawnward-directed ($E_{Y,\,GSM}<0$), constant electric field, "$\mathbf{E}_{\mathbf{return}}$", across the entire vortex (shaded gray in Figure 3.4). The net Y_{GSM} -component of the transient electric field as a function of Y_{GSM} is shown by the second red line in the Figure 3.2b insert, representing $\mathbf{E}_{\mathbf{channel}}$ (the sinusoid from Y_{min} to Y_{max}) and $\mathbf{E}_{\mathbf{return}}$ (the negative and constant value across the vortex: $+/-L_{vortex}$). L_{vortex} is the vortex half width. We have observed a largely –Vx component in the vortical flow by spacecraft in the tail

and by radar measurements of ionospheric flows, though an additional reason we model a “180 degree reflection” is for simplicity of the model. Instead of adding more parameters by adding angles to the electric fields, we use a simple picture of enhanced dawn-dusk electric field for the earthward flow, and a much weaker dusk-dawn electric field for the tailward flows. Although simple, this is to be expected in a flow vortex, however, particularly those that create the observed field-aligned currents in the ionosphere. Although arbitrary return flows are possible to model, for the purposes of this paper we fix the magnitude of the opposing $\mathbf{E}_{\mathbf{return}}$ so that its total potential drop cancels the potential drop due to $\mathbf{E}_{\mathbf{channel}}$.

Thus, outside of the vortex (white area in Figure 3.4), the equipotentials are completely unaffected by the presence of the transient field and are conveniently identical to what is expected from a global dawn-dusk electric field in the absence of a flow vortex. We have found that the details of the net magnetic flux transport, which we here define as the net flux transport averaged over the whole width of +/- L_{vortex} region (zero in this case) have a minor effect on the qualitative evolution of the distributions. Further exploration of the net flux transport from details of the particle distributions is left for future work assuming a sufficiently dispersed spacecraft fleet to better constrain the return flow independent of the channel flow’s potential drop. Given that the net magnetic flux transport is zero, L_{vortex} and the strength and width of $\mathbf{E}_{\mathbf{channel}}$ fully determine the strength of $\mathbf{E}_{\mathbf{return}}$, thus rendering it a derived quantity. In Chapter 4, we improve the model to allow for flux transport.

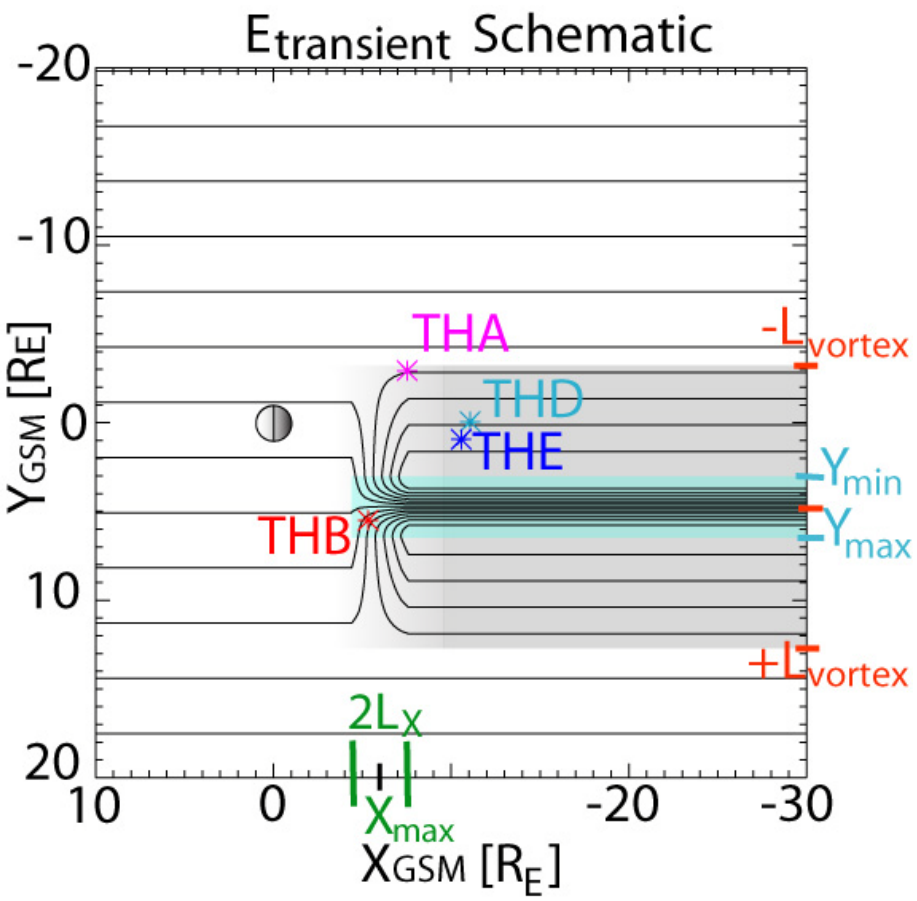

Figure 3.4. Equipotentials of $\mathbf{E_{DD}}$ and $\mathbf{E_{transient}}$ only, where $\mathbf{E_{transient}}$ is the entire system of imposed electric fields. E_{DD}=0.24 mV/m, $\mathbf{E_c}$=5.5 mV/m. L_{vortex}=8 R_E, Y_{min}=3, Y_{max}=6.4, X_{max}=-6.0, L_x=1.5 R_E. Light blue box is the region where the sinusoid $\mathbf{E_{channel}}$ is applied. The gray box represents the area in which $\mathbf{E_{return}}$ exists. The gradient within $2L_x$ is the transition region where $E_{transient}\ \hat{y}$ (i.e., $E_{channel}\ \hat{y}$ + $E_{return}\ \hat{y}$) is decreasing in magnitude while $E_{return}\ \hat{x}$ has appeared. THEMIS spacecraft and $\mathbf{E_{transient}}$ parameters are those used in Case 2, shown in the XY-GSM plane.

The electric field magnitudes at the front and rear of $\mathbf{E_{transient}}$ fall off, by construction, over a fixed distance (we used a value of 6 R_E, i.e., a half-width L_x=3 R_E for Case 1, and 3 R_E or L_x=1.5 for Case 2 based on Figure 4 from *Birn et al.* [2011]), as illustrated by the reduced westward gradient in equipotentials between the green vertical lines surrounding X_{max} (+/-L_x) in Figure 3.4. Further discussed in Appendix 3A, the falloff in electric field strength is associated with the bulk plasma flow accelerating at the front of the BBF as it travels earthward, and the braking of the fast flow once it reaches the inner magnetosphere. The relative importance of the

temporal versus spatial falloff ahead of $\mathbf{E}_{\mathbf{transient}}$ is an item for future consideration based on comparisons with data. An electric field in the x-direction, consistent with flow diversion around the incoming flow burst, is also needed within this transition region to close the equipotentials (in other words, $\partial E_x/\partial y = \partial E_y/\partial x$ such that it is a potential electric field and has no $\partial B/\partial t$ term). Individual particles associated with this electric field turn around in the vortex and transition from moving earthward to tailward or veer earthward around the Earth, as demonstrated by the equipotentials (also contours of zero energy particle motion) in Figure 3.4. Because these fields contain the only x-component of the entire vortex system, we label them "$E_{return}\ \hat{\boldsymbol{x}}$". The transient electric field is therefore described as:

$$\boldsymbol{E_{transient}} = E_{channel}\hat{\boldsymbol{y}} + E_{return}\hat{\boldsymbol{y}} + E_{return}\hat{\boldsymbol{x}} \tag{3.12}$$

Its components, all functions of (X_{GSM}, Y_{GSM}), can be found in Appendix 3A.

In this paper we implement the temporal appearance of $\mathbf{E}_{\mathbf{transient}}$ in two ways. In our first case we simply turn $\mathbf{E}_{\mathbf{transient}}$ on and off at its fixed location, allowing us to study the effects of the electric fields on particle acceleration and transport without the additional parameter of a moving structure. In the second case we demonstrate the effect of a velocity parameter that enables the entire flow vortex structure to travel earthward along the x-direction from 20 R_E at a constant velocity until it reaches a set stopping point.

The physical processes leading to the formation of electric fields described by the model, resulting in electron energization and transport are as follows: (i) reconnection occurs; (ii) reconnected field lines spring back towards Earth, creating a localized dipolarization front separating the energetic particle population in the flow burst dipolarized magnetic flux bundle and the ambient colder plasma ahead of the front; (iii) earthward plasma acceleration at and immediately after the dipolarization front occurs from increased curvature force density: because

of the pressure buildup ahead of the front, there is a decrease in the tailward pressure gradient force ahead of the front while curvature force density increases behind the front due to the increase in the magnetic field magnitude [*Li et al.*, 2011]; (iv) a transient electric field forms because of the resulting flow from –**V**x**B**; (v) as the front moves earthward, plasma is diverted around the plasma bubble, resulting in dusk/dawnward flows at the front and their associated E $\hat{\boldsymbol{x}}$, as well as tailward flow and eastward electric fields on the flanks of the flow burst; (vi) as electrons drift eastward across the potential drop formed within the flow channel, they are energized; (vii) the strong electric field alters the Alfvén layers, enabling particle transport closer in towards Earth. Note that for simplicity we have ignored the δBz, $\partial B/\partial t$, and induced electric field associated with the flow burst. They will be considered in Chapter 4 (see also discussion in section 3.6.2.2). While the effects of a dipolarizing magnetic field with inductive electric field signatures may be important in realistic magnetic field configurations, we expect them to be small compared to errors introduced from our other simplifying assumptions (e.g., dipole field, equatorially mirroring particles).

3.2.4 Model Parameters

We keep the model realistic but simple in order to clearly understand how each model parameter affects the final distribution. In early development stages, we experimented with a "step function" electric field that is simply turned on and off in the region of interest and found the resulting spectra to contain most of the features required to explain the observations. (This is used in Case 1.) Later we developed a more sophisticated model in which the structure carrying $\mathbf{E}_{\mathbf{transient}}$ has a finite earthward velocity, either constrained by timing observations or chosen by supplying typical flow burst peak velocity values. $\mathbf{E}_{\mathbf{transient}}$ can extend tailward indefinitely (to

reduce the reconnection B_z arbitrarily) or can be confined within a fixed X_{GSM} distance from the front so that the front and tail travel together (akin to a plasma bubble).

Table 3.1 describes our parameter list. Adjustable ones are those that are varied to acquire the best fit to the observed spectra. The final values chosen were found after trying different sets of parameters to obtain good agreement between the modeled and observed injected eflux. The sets were not chosen blindly, however, because each parameter affects different attributes of the injection signature. The relationships that guided our selection of parameter sets are discussed in Appendix 3B.

Because we rely on only a few adjustable (free) parameters, we can distinguish how each parameter affects particle injection properties through modeling case studies. A robust model should predict injection signatures at different locations in the tail as well as describe the particle distributions throughout the entire region from the source to the location of the observations that constrain the injection properties, resulting in a powerful method to determine particle properties across large regions of the inner magnetosphere.

Table 3.1. Model Parameters

Parameter	Type	Description
Y_{min}	Adjustable	Minimum extent in Y of $\mathbf{E}_{\mathbf{channel}}$
Y_{max}	Adjustable	Maximum extent in Y of $\mathbf{E}_{\mathbf{channel}}$
X_{min}	Measured/Fixed	Tailward radial extent of $\mathbf{E}_{\mathbf{transient}}$
X_{max}	Measured/Fixed	Inward radial extent of $\mathbf{E}_{\mathbf{transient}}$
L_{vortex} (half width)	Adjustable	Distance from $\mathbf{E}_{\mathbf{transient}}$ center to apply opposing **E**
Lx_{min}	Fixed	Distance it takes for vortex to turn on tailward side
Lx_{max}	Fixed	Distance it takes for vortex to turn on earthward side
E_c	Adjustable	Magnitude of electric field at channel center
t_0	Measured/Constrained	$\mathbf{E}_{\mathbf{transient}}$ start time
$\mathbf{V}_{\mathbf{transient}}$	Constrained	The velocity of $\mathbf{E}_{\mathbf{transient}}$ in the x-direction
lifetime at X_{max}	Measured/Constrained	Time $\mathbf{E}_{\mathbf{transient}}$ is turned ON after reaching X_{max}
$\mathbf{E}_{\mathbf{transient}}$ ramp-down	Measured/Constrained	Time for $\mathbf{E}_{\mathbf{transient}}$ to turn OFF: linear decrease in $\lvert\mathbf{E}\rvert$
E_{DD}	Measured/Modeled	Magnitude of the dawn-dusk electric field

3.3. Case Studies

We systematically examined cases in 2008 (a year when THEMIS spacecraft separations were relatively large--on the order of 2 R_E or greater, and typically ~5 R_E) by exploring test cases in which at least three of the five THEMIS spacecraft observed an injection. In particular, we wanted to be able to study the dispersed signatures, so we looked for cases in which dispersion was evident in at least two spacecraft data. We also attempted to find cases in which the spacecraft were in the plasma sheet, near the neutral sheet (determined by B_x ~ 0.) Many such examples exist in the data. We selected two events that demonstrate a wide range of modeling capabilities. The injection observed around 9:50 UT on 10 January 2008 (Case 1) was selected because of the clarity of the dispersion signatures observed by three spacecraft in the plasma sheet, all east of the flow channel. The second case at ~5:40 UT on 4 February 2008 was selected because one spacecraft was located within the flow channel, demonstrating this geometry's contributions to constraining the electric fields. They were both also selected because of the observed dip prior to and during injection, enabling us to explore this unstudied feature of dispersed injections.

3.3.1 Case 1: 10 January 2008

An overview of the injection on 10 January 2008, ~09:50 UT at THEMIS E (THE) is shown in Figure 3.5. Figure 3.5a shows the particle spectra over time, in which the dispersed injection signature clearly begins at energies over 100 keV at ~09:46. At the same time there is a slight depletion in electron density as one would expect from accelerated plasma within dipolarization fronts (*Runov et al*., 2011). However, although THE is in the plasma sheet ($|B_x|$<5 nT throughout the interval), it does not observe the dipolarization front. The electric field in

Figure 3.5c**,** calculated from –**V**x**B**, is variable throughout the interval with a slightly higher peak in E_Y at the time of the injection that indicates a very small earthward flow increase. Note that the plasma moments are computed from a combination of the ESA and SST ion instruments. Based on the above observations, although there is a depletion in plasma density, we can be confident that THE was not within the flow channel. We initially took this to be a single injection, although the prolonged increased eflux levels (over 20 minutes) in conjunction with a second, smaller peak in eflux observed more clearly at THD and THE at ~10:05 UT (see Figures 5c and 5e) suggest a secondary injection followed. As this is not resolvable, we treat the entire event as a single injection by a prolonged $\mathbf{E}_{\mathbf{transient}}$.

Using the methods described in section 3.2.2.1.2, we determined the background, global electric field to be 0.15 mV/m during the pre-injection interval. PSD fits with a double kappa distribution result in the parameters shown in Table 3.2. The cold population kappa values were effectively infinity (170 was our upper limit in the fit). There may be losses due to wave-particle scattering, but as we do not calculate them, the densities provided must be lowered in order to fit the observation. Low densities could also be the result of lobe plasma mixing with the plasma sheet. THD and THE were very close to each other, so it follows that their fitted PSDs would be the same. Although the particles observed at THC are also traced to L=20 R_E, the backtrace follows a different path and leads to a different source location than THD and THE, so their PSDs are slightly different. Choosing to average the PSD parameters does not drastically change the results, but we kept the best fit for each individual spacecraft to allow for slight variations between the particle histories at each spacecraft.

Figures 3.6 and 3.7 show the comparison between observed and modeled spectra, the color spectrograms being useful to compare the general fit and the line spectra being easier to see

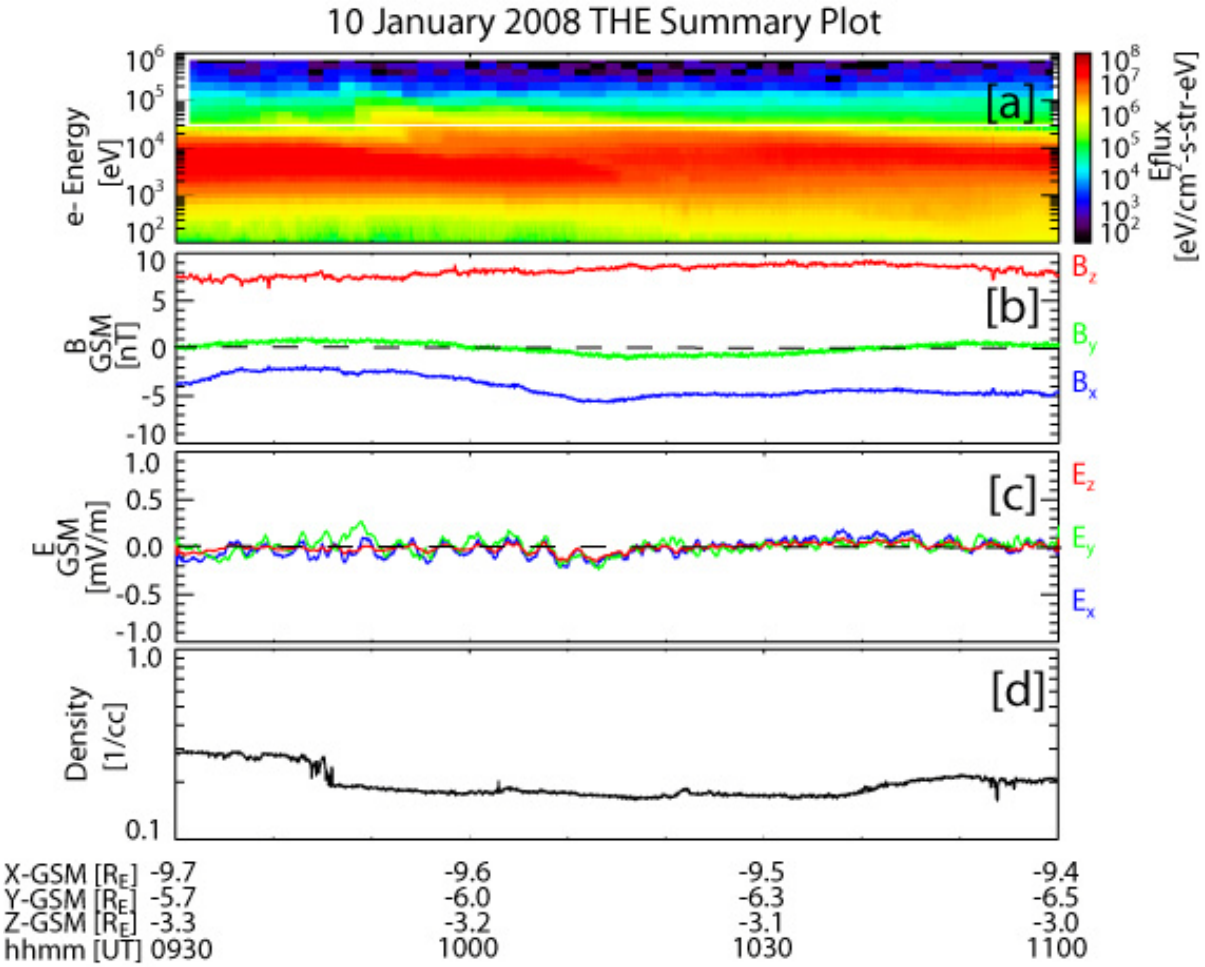

Figure 3.5. THEMIS E data observed on 10 January 2008. (a) Electron eflux measured by the SST and ESA instruments. (b) Magnetic field measured by the FGM in GSM coordinates. (c) Electric field calculated from **-V**x**B**, where velocity is calculated from the SST and ESA data weighted by the densities measured. (d) Density calculated from the ion measurements by the SST and ESA instruments.

Table 3.2. Case 1 PSD Fit Parameters			
Parameter	**THC**	**THD**	**THE**
$\mathbf{N_h}$ **[1/cc]**	0.0018	0.0003	0.0003
$\mathbf{T_h}$ **[keV]**	10	18	18
$\boldsymbol{\kappa_h}$	3.3	3.8	3.8
$\mathbf{N_c}$ **[1/cc]**	0.012	0.02	0.02
$\mathbf{T_c}$ **[keV]**	0.47	0.55	0.55
$\boldsymbol{\kappa_c}$	170	170	170

exactly when dips and injections occur at each energy. Note that the modeled spectra are calculated for a stationary spacecraft, where the location was chosen at the time the actual spacecraft first observed effects from the flow burst. Spacecraft motion is only a secondary effect in this study that deals with satellites near apogee and injection durations of 1hour or less. It is evident from Figure 3.6 that the prominent features observed are also apparent in the model; for instance, the greater dispersion of injected electrons at energies from ~140 keV to ~15 keV observed at THC (GSM position=[-5.5, -8.2, -1.4] at 09:50:45 UT) is also observed in the model, and is due to THC being the farthest from $\mathbf{E_{channel}}$. In this case all three spacecraft saw dispersed injections, so we know the channel must be east of them all. As further discussed in Appendix 3B, the spacecraft distance from the channel boundary (Y_{min} = -1 R_E) is determined by fitting the dispersion. A typical flow burst channel width of 4 R_E was assumed, making Y_{max}=3 R_E (other widths were tested and did not fit as well). The strength of E_c=2 mV/m was determined by fitting the maximum energy accelerated at each spacecraft. A slight dip in eflux is most apparent on THC in the 15-30 keV energy range starting before the injection signature (~09:30 in Figures 3.6a and 3.7a, ~09:37 in Figures 3.6b and 3.7b). Similar dips are also seen in the following panels in Figures 3.6 and 3.7 at THD and THE. The red tick marks on the spectral lines in Figure 3.7 indicate the time when the eflux starts to dip at the observed energy. The shape of the dip is most affected by the L_{vortex} parameter because, as we will discuss at length in section 3.5, we found the dip is caused by particles that are swept out by the return flow, losing energy as they travel to weaker magnetic fields while drifting across the eastward pointing $\mathbf{E_{return}}$. Due to the weak but noticeable presence of return flow (i.e., the small dip in eflux), we found L_{vortex} = 15 R_E, allowing for a weaker $\mathbf{E_{return}}$ of -0.143 mV/m.

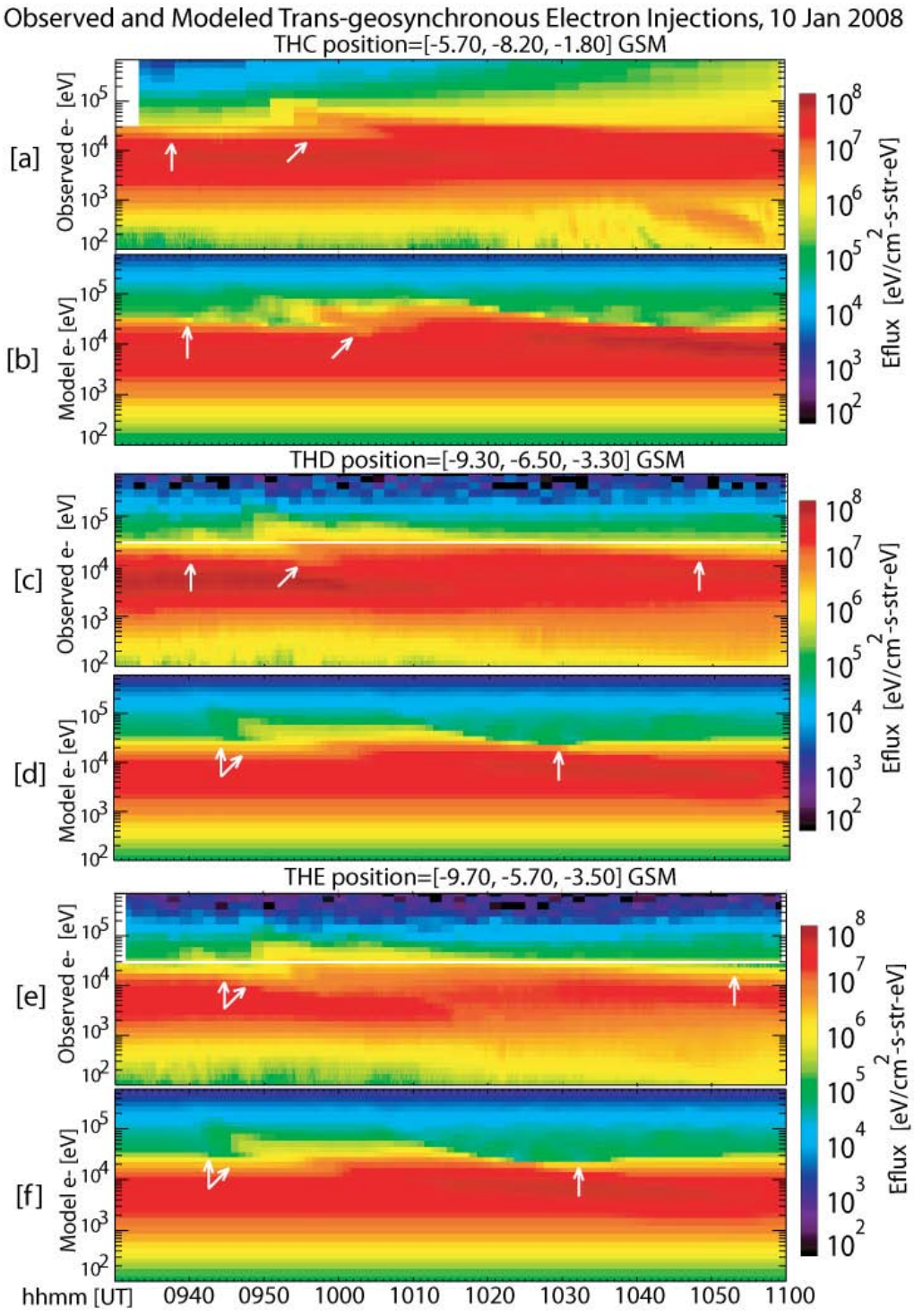

Figure 3.6. Comparison between observed and modeled trans-geosynchronous injections seen in the spectra at three THEMIS spacecraft on 10 January 2008. White arrows point out dips in eflux. Positions listed are those at which the spacecraft observed the injection. E_{DD} = 0.15 mV/m, E_C =2 mV/m, Y_{min} = -1 R_E, Y_{max} = 3 R_E, L_{vortex} = 15 R_E, X_{min} = -6.6 R_E, L_X = 3 R_E, t_0 = 09:37, lifetime at X_{max} = 25 min.

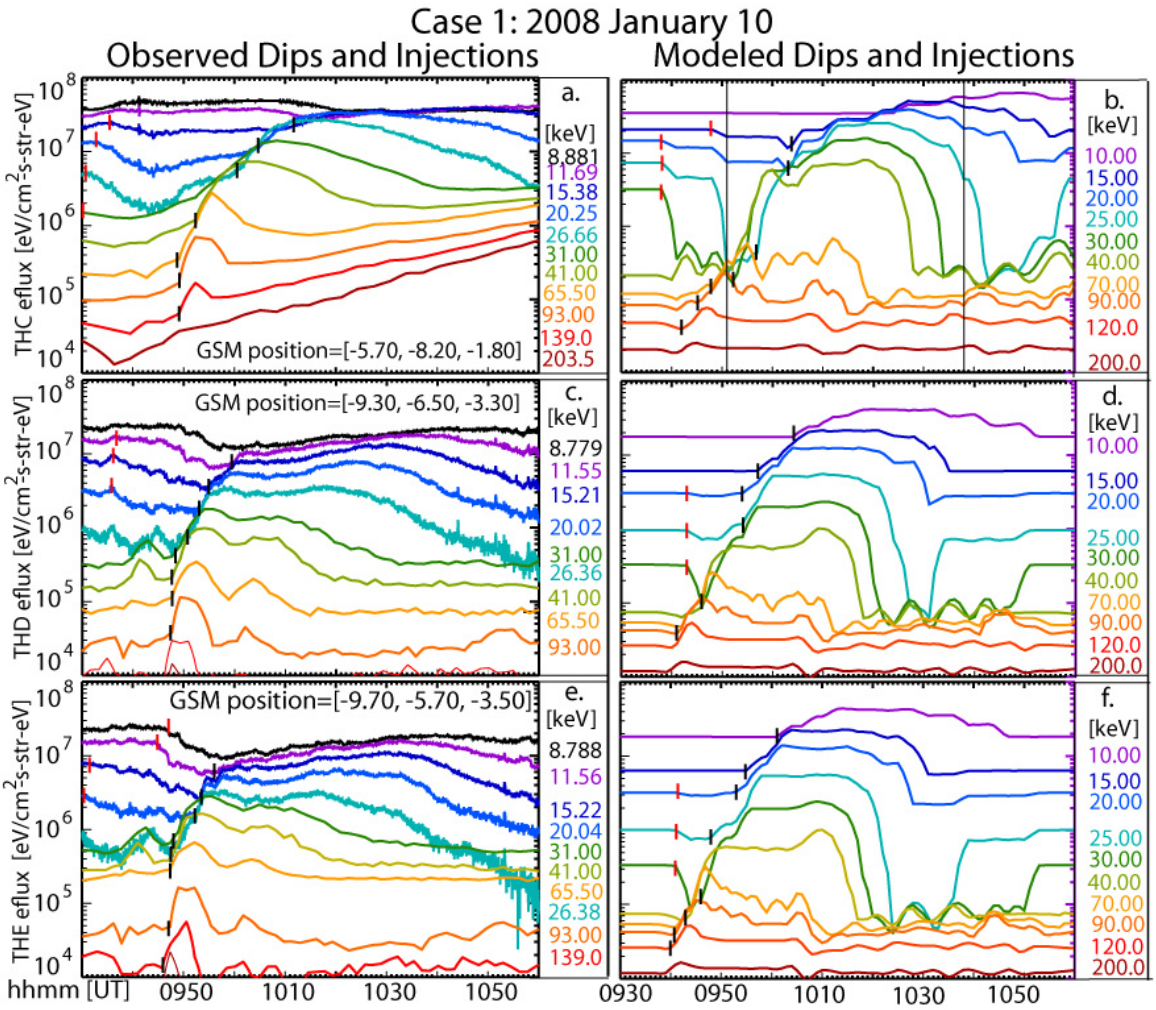

Figure 3.7. Comparison between observed and modeled TGIs using line spectral plots. Red tick marks on individual lines mark where that energy began to dip in eflux. Black tick marks indicate where that energy began to increase in eflux. Almost simultaneous dips in the model are due to a wide E_{return} that turns on instantaneously at all spacecraft. Azimuthal separation from $E_{channel}$ results in the dispersed injection signature. Vertical lines and bolded spectral lines in Figure 3.7b mark the times and energies, respectively, that are used for the Figure 3.12 backtraces.

As discussed previously, in Case 1 we demonstrate the efficacy of the simple model that relies on $\mathbf{E}_{\mathbf{transient}}$ turning on and off instantaneously everywhere within the transient region (start time t_0=09:37). We kept $\mathbf{E}_{\mathbf{transient}}$ on for 25 minutes to match the duration of the elevated fluxes. Note that t_0 is not the time that the injection is observed at a satellite, but rather it is the time $\mathbf{E}_{\mathbf{transient}}$ is turned on. Spacecraft east of $\mathbf{E}_{\mathbf{channel}}$ (as in this case) observe the injection signatures once the electrons have drifted to their location.

As we can see, even with the most simple of assumptions—a dipole magnetic field and a step function $\mathbf{E}_{\mathbf{transient}}$—the model of a localized, impulsive electric field with a corresponding return flow is capable of reproducing the observed trans-geosynchronous injections at three THEMIS spacecraft located at different azimuthal locations (GSM positions of THC=[-5.7, -8.2, -1.8]; THD=[-9.3, 6.5, -3.3]; THE=[-9.7, -5.7, -3.5]) . Just how the electric fields accelerate and transport the particles will be further discussed in section 3.5.

3.3.2 Case 2: 04 February 2008

For our second case, we deliberately chose an event where at least one spacecraft (THB) was within the flow channel, as inferred from the overview of THB observations on 04 February 2008 in Figure 3.8. THB observed a dispersionless injection (or, in fact, an inverse velocity dispersion) starting at ~05:44:30 UT, implying that its location (GSM position=[-5.2, 5.5, -1.7]) was within the channel (Figure 3.8a). The proximity to the flow channel is further demonstrated by the dipolarization front (Figure 3.8b) and the increase in E_Y (Figure 3.8c) at the time of the injection. Because the spacecraft was moving to higher L-shells at the time, the density decreases over time (Figure 3.8d). It is difficult to correlate all the density changes to the injection, however, note that a density increase ahead of a dipolarization front accompanying a flow burst, followed by a rapid density decrease, as observed here, are rather typical flow burst signatures.

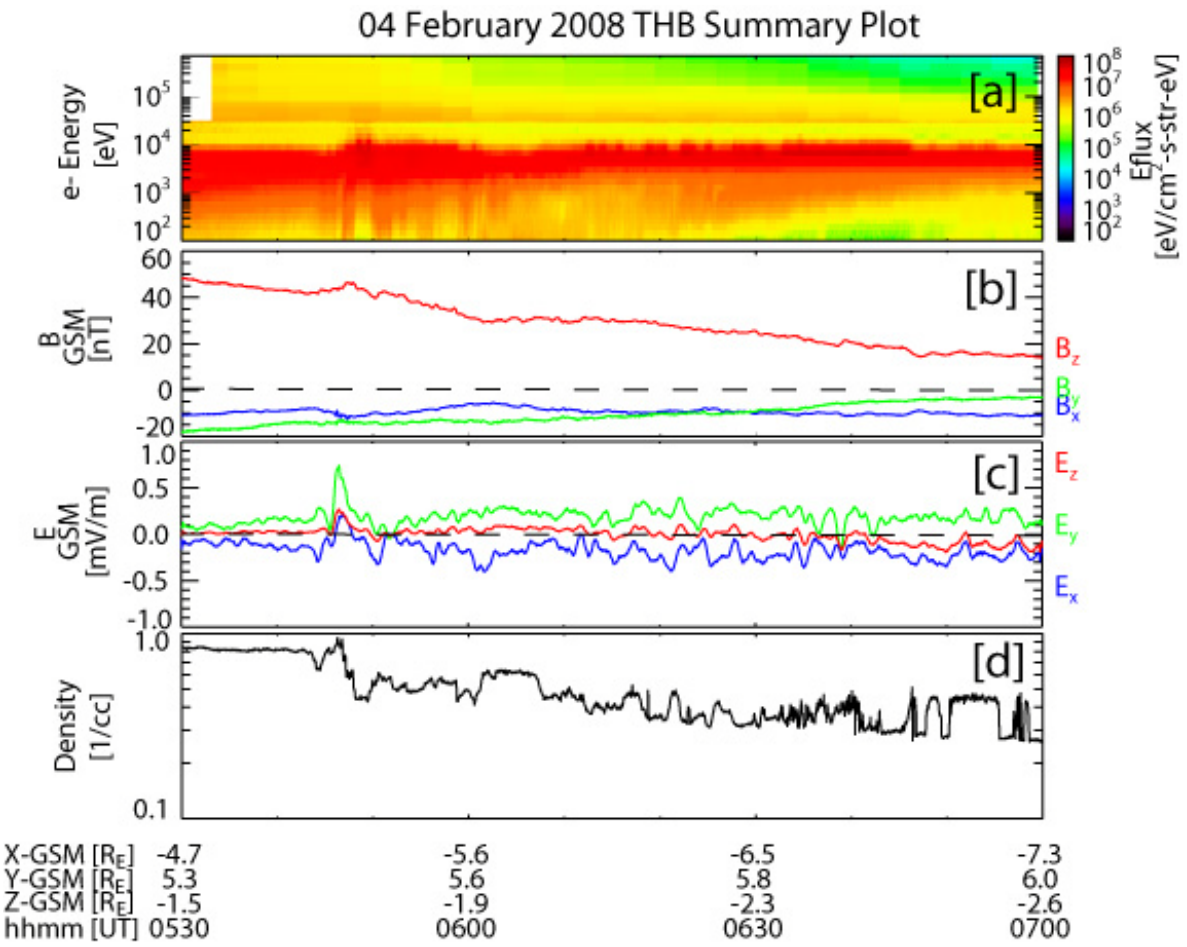

Figure 3.8. THEMIS B data observed on 4 February 2008, similar to Figure 3.5. THB observes (a) a dispersionless/inverse velocity injection, (b) a dipolarization signature in B_z, (c) and an increase in E_y signifying earthward flow at ~05:46:15. (d) Density calculated from the ion measurements by the SST and ESA instruments.

Additionally, being near geosynchronous altitude, THB provides insight into the $\mathbf{E}_{\mathbf{transient}}$ front's most inward propagation distance, demonstrating it must at least make it this close to Earth so as to be observed by THB. The dipolarization is observed at THD (Figure 3.9b, GSM position=[-11.1, -0.1, -3.6]) at 05:53 UT and at THE (not shown, GSM position=[-10.7, 0.8, -3.4]) at 05:51:50 UT after a time delay from the injection signature. Expected from an azimuthally expanding dipolarized region [*Angelopoulos, et al.*, 2008], this fits the picture of a localized fast flow and dipolarization front passing west of THD and THE, followed by the dipolarization's azimuthal expansion.

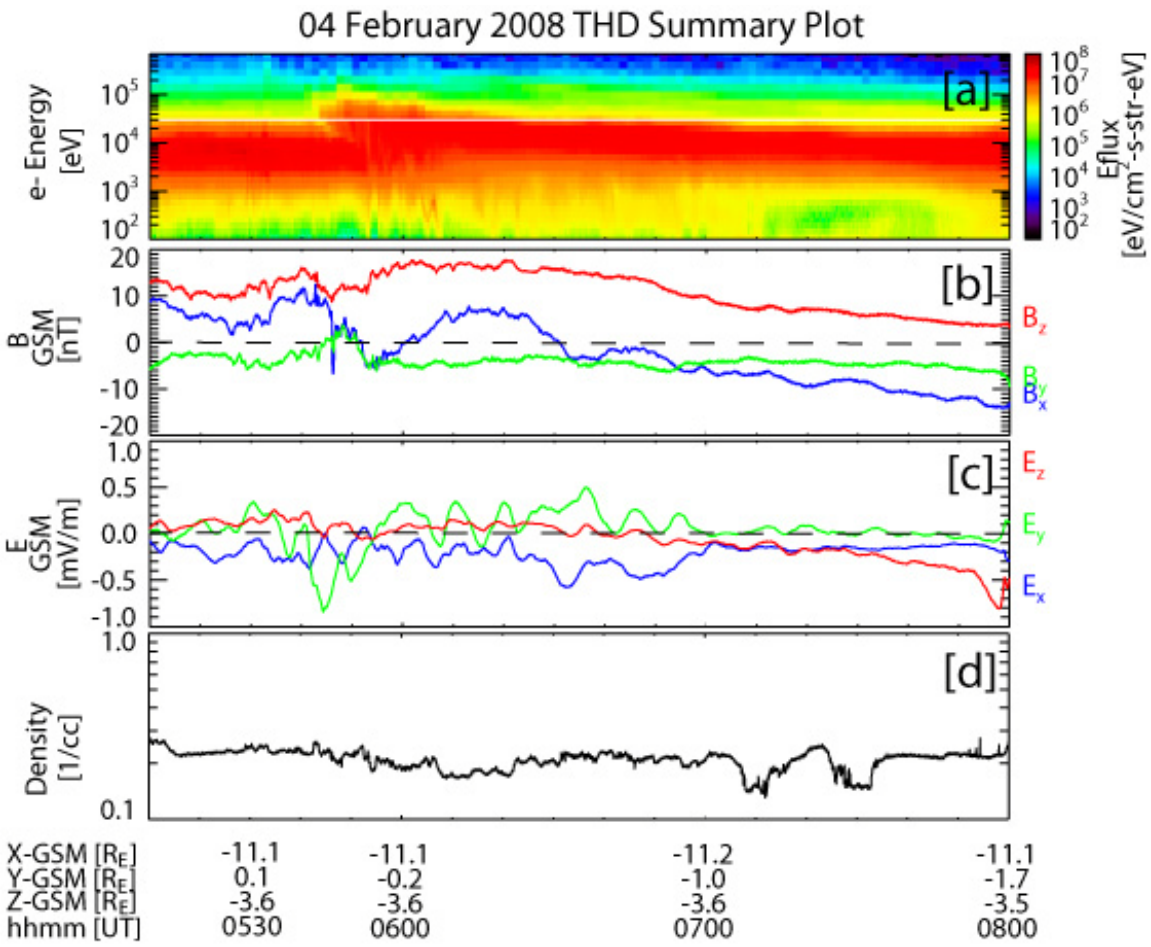

Figure 3.9. THEMIS D data observed on 4 February 2008, similar to Figure 3.5, except Figure 9c: electric field calculated from -**V**x**B** smoothed (via boxcar averaging) over 3 min. THD crosses the neutral sheet (B_x~0 nT) at the time of dispersed injection signature, while at the same time observing a significant $-E_Y$ indicative of tailward flow.

Using the same method as in the previous case but now with four spacecraft, we determined E_{DD} to be 0.24 mV/m. The PSD parameters that were fit to the pre-injection observations are shown in Table 3.3. Because THD and THE were close to each other (separated in X by ~0.5 R_E and in Y by ~1.0 R_E), their observations and PSD parameter values were very similar. Being so close to Earth (X_{GSM}>-5.6, Y_{GSM}<5.6), THB observed high temperatures and no fall-off in the PSD upper energies (i.e., the PSD remained approximately constant for energies >10 keV rather than falling off; see Figure 3.3b).

Table 3.3 Case 2 PSD Fit Parameters				
Parameter	**THA**	**THB**	**THD**	**THE**
N_h [1/cc]	0.008	0.02	0.0018	0.001
T_h [keV]	19.5	700	14	10.5
κ_h	2.8	1.51	4	3.8
N_c [1/cc]	0.0064	0.006	0.021	0.015
T_c [keV]	0.4	4.8	0.68	0.6
κ_c	80	1.51	30	40

In the same format as Figures 3.6 and 3.7 for Case 1, Figures 3.10 and 3.11 show the observed and simulated spectra for the four THEMIS spacecraft that observed the injection. The satellite locations in GSM coordinates are listed (and were previously shown in Figure 3.3). THA observed a dispersed injection starting ~05:42 UT (Figures 3.10a and 3.11a), while THD and THE spectra exhibit dispersion starting just before 05:40 UT (Figures 3.10e and 3.11e, 3,10g and 3.11g, respectively). The gradual eflux increase at energies > 100 keV observed by THA starting around 06:00 UT (and the decrease at those energies at THB starting around 05:55) are both caused by the spacecraft orbital motion—THA to smaller, THB to larger L-shells—and are thus spatial effects and not due to the injections/dips. The low eflux observed in the simulated dip at THA at energies ~15-30 keV (Figures 3.10b and 3.11b) is partly due to the underestimation of the flux values at energies ~30-80 keV in the PSD fitting (see Figure 3.4a). Since this energy range represents the population of particles being swept out to form the dip, their lower PSD is mirrored in the dip.

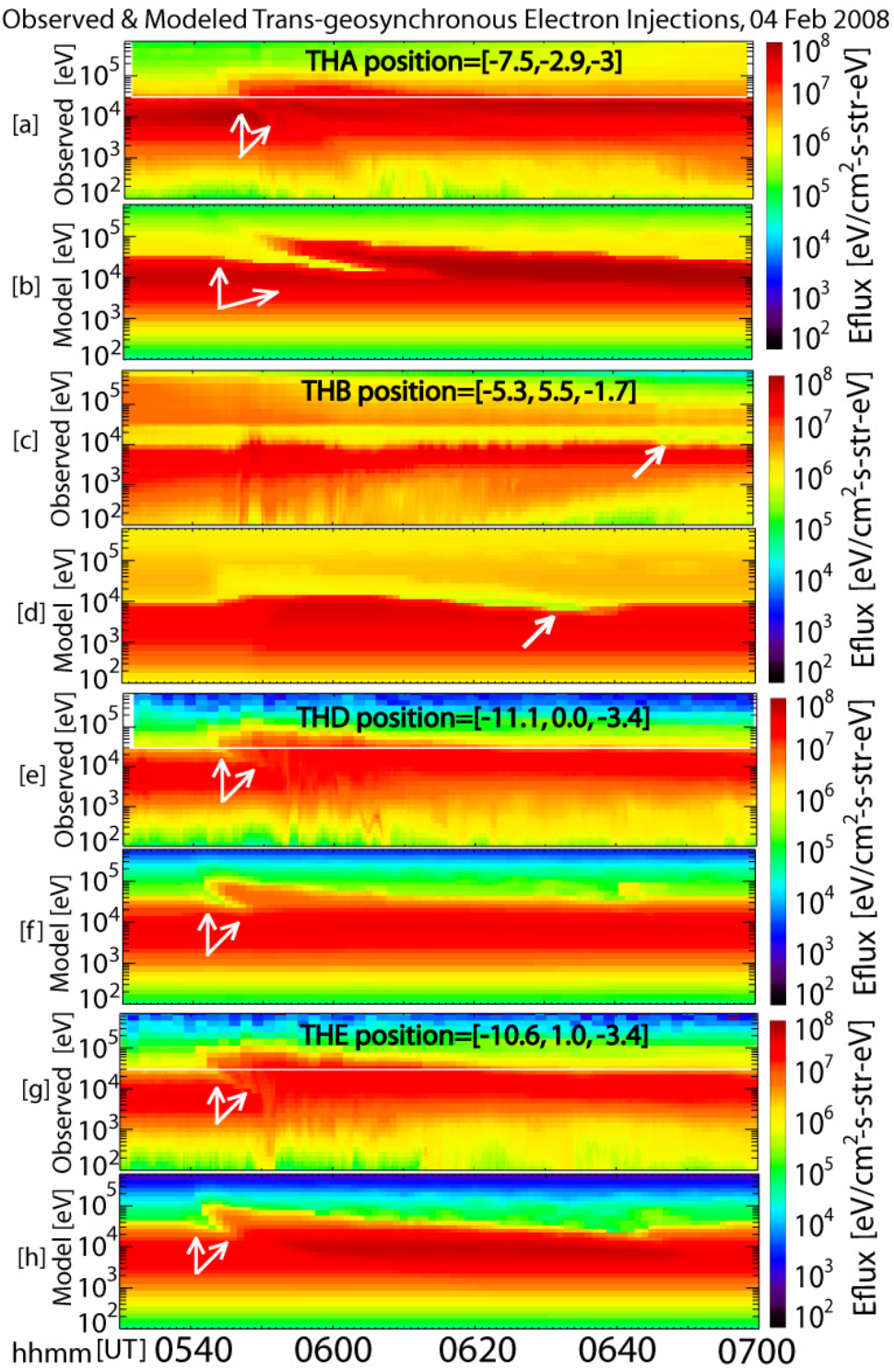

Figure 3.10. Comparison between observed and modeled injections seen in the spectra at four THEMIS spacecraft on 4 February 2008. White arrows point out dips in eflux. Positions listed are those at which the spacecraft observed the injection. E_{DD} = 0.24 mV/m, Ec = 5.5 mV/m, Y_{min} = 3R_E, Y_{max} = 6.4 R_E, L_{vortex} = 8 R_E, X_{min} = -6.0 R_E, t_0 = 05:37, Vx = 4 R_E/min, lifetime at X_{max} = 0 min, ramp down = 50 min.

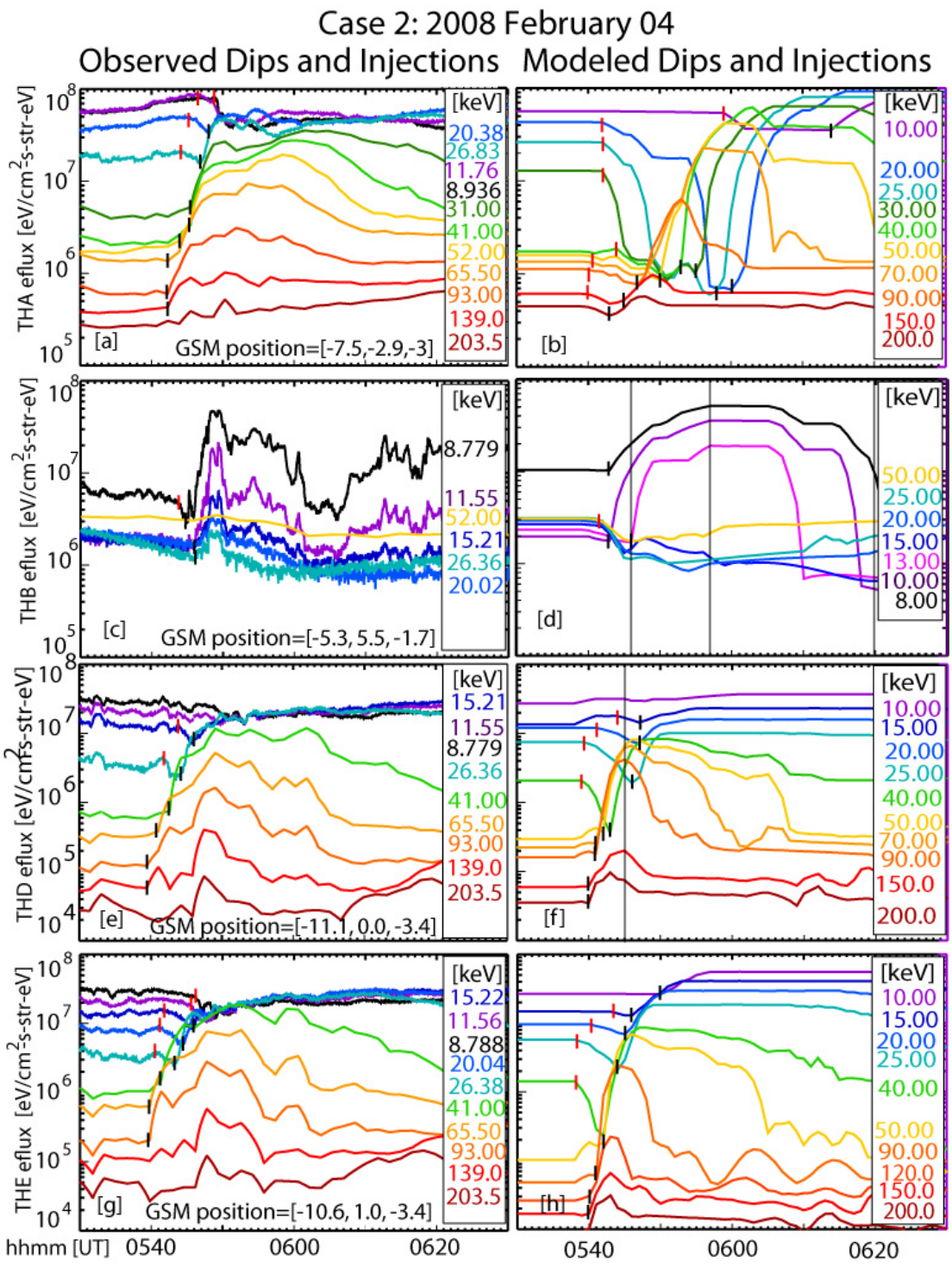

Figure 3.11. Comparison between observed and modeled TGIs using line spectral plots. Red tick marks on individual lines mark where that energy began to dip in eflux. Black tick marks indicate where that energy began to increase in eflux. Azimuthal separation from E_{return} and $E_{channel}$ result in the dispersed dip and injection signatures. Vertical lines and bolded spectral lines in Figures 3.11d and 3.11f mark the times and energies, respectively, that are used for the backtraces in Figures 3.13 and 3.12.

What is especially noteworthy in this event is the clear display of a dispersed eflux depletion (starting at ~30 keV and seen later at ~15 keV) at THD and THE simultaneous to the dispersed injection of particles at higher energies (beginning with ~100 keV). There is also a depletion in eflux following the injection most notable at THB at energies 10-20 keV (Figures 3.9a, 3.11c), though also observable at THD past 07:00 UT (Figure 3.10a) around 20 keV. Though timing and intensity do not always match exactly, all of these depletions were captured by our model.

To replicate these main features, the model $\mathbf{E}_{\mathbf{transient}}$ was stopped at X_{GSM}=-6.0 R_E and has Y_{min}=3 R_E, Y_{max}=6.4 R_E, E_c=5.5 mV/m, L_{vortex}=8 R_E, L_x=1.5 R_E. The flow channel was uncharacteristically far from midnight, centered at Y_{GSM} =4.7 R_E. Similar to Case 1, we treated the rise in eflux as one injection event. Unlike Case 1, however, in which $\mathbf{E}_{\mathbf{transient}}$ suddenly appeared and disappeared instantaneously, here we started $\mathbf{E}_{\mathbf{transient}}$ at X_{GSM} = -20 R_E at t_0 = 05:37 UT and gave the structure a velocity of 4 R_E/min (~425 km/s) in the x-direction. After reaching X_{max}, V=0 and a 50-minute ramp-down time was applied. Though the front moved forward, we kept $\mathbf{E}_{\mathbf{transient}}$'s tail as one of infinite length. An $\mathbf{E}_{\mathbf{transient}}$ travelling with a finite speed was an attempt to account for the fact that THB, the innermost spacecraft, observed the injection later than the other spacecraft. Because it is within the flow while the other spacecraft are east of it, a Case 1-type instantaneous electric field causes THB to observe the injection immediately, prior to the other spacecraft which must wait for particles to drift dawnward to observe them. Constraining the velocity was a trial and error process.

It was fortuitous that THD crossed the central plasma sheet (B_x~0 nT) at the time of the injection when it observed a clear negative component of the Y_{GSM} electric field (green plot in Figure 3.8c at ~05:37-05:56 UT with two more excursions following), consistent with bulk

tailward plasma motion. Because THD is east of the flow channel, we might expect this tailward motion to be caused by the return flow associated with the $\mathbf{E}_{\mathbf{transient}}$ vortex. In fact, at the same time, we observe the dip in eflux at ~15-30 keV which we determined to be caused by return flow. An eflux depletion reaching lower energies than Case 1 is consistent with a stronger return flow, and this is reflected in the need for an L_{vortex} of 8 R_E (allowing a stronger $\mathbf{E}_{\mathbf{return}}$ over a shorter distance than Case 1) for the simulation to capture the dip. While the goal of this study was to simulate the general features of injections and not to match exact field observations (with the simple model we expect to simulate trends, not precise values), it was quite interesting to see that the $\mathbf{E}_{\mathbf{return}}$ used to fit the features (-0.654 mV/m when E_c was at a maximum of 5.5 mV/m) is not far off from the measured value of ~-0.8 mV/m when E_Y goes most negative.

In this case, we show how an orbital configuration including spacecraft located within the flow channel and at varying distances outside the channel can constrain parameters describing the fields associated with the flow, allowing us to explore even more about the physical processes behind particle transport. Inverse velocity dispersion was observed by and simulated for THB which was located at the front of the flow channel. The maximum energy attained by the injected particles at each of the four spacecraft was attained in the simulation. Most noteworthy, the dip in eflux at ~15-30 keV simultaneous to the injection of more energetic particles was replicated, as well as the less extensive dip following the injection. An explanation of the role $\mathbf{E}_{\mathbf{transient}}$ plays in this picture, as well as how our assumptions and parameter choices affect the results, follows in the discussion below.

3.4. General Discussion on the Formation of Injection Features

The simple model utilized here can reproduce the main features of geosynchronous and trans-geosynchronous injections, providing insight into physical processes related to particle injections observed simultaneously at a wide range of distances and local times. Previous models have focused on simulating injections observed at geosynchronous altitudes because of the routine satellite availability there. With the THEMIS dataset now available, we look beyond geosynchronous and show that even simple electric and magnetic field models, such as the one discussed herein, can be used to describe injections anywhere in the tail.

3.4.1 Case 1

In order to understand the processes of particle transport behind the injection signatures, we selected times when interesting features were seen and then backtraced several particle populations observed at energies of interest (Figure 3.12). The tick marks in Figure 3.12 indicate 10-minute intervals throughout the trajectories. The final (observed) particle energy (W_f) as well as the initial particle energy at the source location (W_i) is listed. W_i is therefore the value at L=20 R_E where the trace is stopped, or the value after the backtrace has run for 24 hours (the limits we set to find the eflux). The trajectories, however, have been plotted for less than 24 hours. This was to avoid plotting multiple orbits on top of each other, making it difficult to get a sense of the electron's motion. (Only Figures 3.12c and 3.12d include full orbits in order to show how $\mathbf{E}_{\mathbf{transient}}$ affected the trajectories. The bold tick marks are for the first backtraced orbit; the faint tick marks are for orbits occurring earlier in time.) Arrows labeled "t_0" point to the location in the trajectory when $\mathbf{E}_{\mathbf{transient}}$ turned on, while arrows labeled "t_{end}" point to when $\mathbf{E}_{\mathbf{transient}}$ turned off.

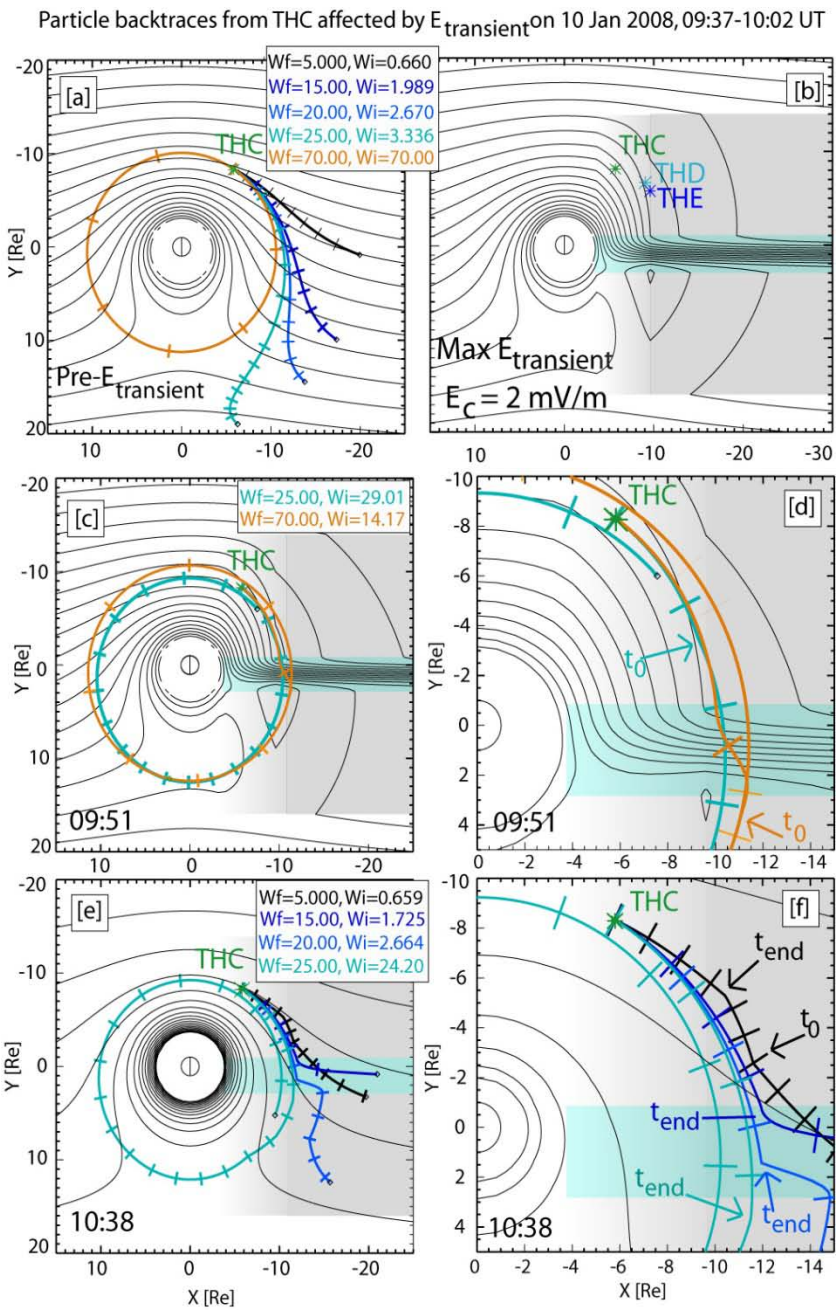

Figure 3.12. Plots of particle backtraces from THC demonstrating particle transport related to **E**$_{\mathbf{transient}}$. Initial (W_i) and final (W_f) particle energies are listed: W_i is at the source (backtraced 24 h or to L = 20 R_E) and W_f is that observed at the spacecraft. Trajectories are not drawn for the full 24 h, but are stopped after the shape of the pre-**E**$_{\mathbf{transient}}$ orbits becomes apparent. The blue and gray shading indicate the regions where $E_{channel}$ and E_{return} are applied in the same manner as Figure 3.4. Contours represent equipotentials (i.e., contours of motion for m = 0 particles) at the given time. (a) Pre- **E**$_{\mathbf{transient}}$, quiescent scenario. (b) Equipotentials when **E**$_{\mathbf{transient}}$ is on with the three THEMIS spacecraft locations indicated. (c, d, e, f) Particle trajectories backtraced from THC at the indicated time of observation (marked by vertical lines in Figure 3.7b). Traces are color-coordinated with the line spectra in Figure 3.7. Left column plots give a broad overview while right column plots zoom in to enhance the features of interest. Tick marks represent 10-min intervals. The faint tick marks in Figures 12c and 12d for the W_f = 70 keV orbit are for previous orbits, as the electron orbited earth twice before **E**$_{\mathbf{transient}}$ arrived. The bold tick marks are for the most recent orbit. The arrows labeled t_0 and t_{end} indicate the locations of

Figure 3.12a depicts the contours of motion for μ=0 particles as well as backtraces for particles observed at THC with energies 5, 15, 20, 25, and 70 keV under nominal dawn-dusk electric field conditions. The 5-25 keV populations at THC are backtraced to 20 R_E where they are stopped, while higher energy populations (i.e., 70 keV) are trapped in closed drift orbits. Figure 3.12b shows the equipotentials under the influence of $\mathbf{E}_{\mathbf{transient}}$ as well as the locations of the three THEMIS spacecraft, clearly to the east of $\mathbf{E}_{\mathbf{channel}}$. Similar to Figure 3.3, we use gray shading to indicate the return flow (where $\mathbf{E}_{\mathbf{return}}$ is applied) and blue shading to indicate the flow channel (where $\mathbf{E}_{\mathbf{transient}}>0$), with the gradient at the nose to represent the decreasing strength of $\mathbf{E}_{\mathbf{channel}}$ and $E_{return}\ \hat{y}$ (recalling that in this transition region of +/-L_x, $E_{return}\ \hat{x}$ appears). We note that as the equations in Appendix 3A show, because $\mathbf{E}_{\mathbf{channel}}$ goes to zero at the edges, the total $\mathbf{E}_{\mathbf{transient}}$ will turn negative where $\mathbf{E}_{\mathbf{channel}} < \mathbf{E}_{\mathbf{vortex}}$. This explains why the flow channel ($\mathbf{E}_{\mathbf{transient}}>0$) is slightly narrower than the width defined by Y_{max} and Y_{min}.

3.4.1.1 Eflux dip prior to and during injection

Prior to the injection in Figures 3.6 and 3.7, we see a slight decrease in eflux at certain energies; for example at THC we see a dip in the ~15-30 keV particles. Our model explains this feature by the return flow. Just as the earthward flow allows particles to break their quasi-steady convection orbits and thus access Alfvén layers closer to Earth, the tailward flow pulls more energetic particles out of their trapped orbits to greater L-shells. In Figures 3.12c and 3.12d we see that the W_f= 25 keV particles are de-energized as they are swept to slightly lower L-shells. Because in Figures 3.12c and 3.12d $\mathbf{E}_{\mathbf{transient}}$ has been on for only 14 minutes, the slower, lower-energy particles that are accelerated in the channel have not yet drifted to the spacecraft. Particles that are closer to the spacecraft when $\mathbf{E}_{\mathbf{transient}}$ turns on can reach it in just 14 minutes; they will

only experience the return flow east of the channel, however. In fact, we can see from Figure 3.7b that a dip exists for several minutes prior to injection for this reason: particles are immediately affected by the return flow THC is embedded in, while those particles injected by the flow burst must first drift to THC's location to be observed. Thus the almost instantaneous dip in the model is due to the wide $\mathbf{E}_{\mathbf{return}}$ which encompasses all of the spacecraft, such that, similar to a dispersionless injection observed when a spacecraft is at the injection site, there is a dispersionless dip when the spacecraft is located within the return flow.

Recall that eflux is a function of PSD times energy squared, and that the PSD remains constant over a particle's trajectory from its source to where it is observed by the spacecraft. Under $\mathbf{E}_{\mathbf{transient}}$'s influence, the location of the source population for each observed energy population changes over time; for instance, the 25 keV population originally initiates at L=20 R_E with an energy of 3.336 keV (Figure 3.12a), but after $\mathbf{E}_{\mathbf{transient}}$ has been on for 14 minutes, the 25 keV population initiates closer to Earth than THC at an energy of 29.01 keV (Figure 3.12c). Because the distribution function decreases with energy, when the source population is changed to a more energetic one over time (such as the case for 25 keV particles observed at THC over time), the PSD decreases. Thus, when particles are no longer convecting earthward in a quiescent state—being energized via betatron acceleration before being observed (lower $W_i \rightarrow$higher PSD) as in Figure 3.12a—but instead are de-energized by moving to higher L-shells and a lower magnetic field at the spacecraft location (higher $W_i \rightarrow$lower PSD) as in Figure 3.12c, the spacecraft observes an eflux depletion. We used the duration of the dip and the energies affected to constrain L_{vortex} to 15 R_E. A smaller L_{vortex}, implying a larger $\mathbf{E}_{\mathbf{return}}$ over a shorter width, results in a deeper dip (lower energies are affected) for a longer period of time (offsetting the arrival time of the injected particles). In this case therefore, being -0.143 mV/m, $\mathbf{E}_{\mathbf{return}}$ is not

very strong compared to the background fields from convection, corotation, and $\nabla\mathbf{B}$ drift, thus particles at most energies are not carried very far tailward.

3.4.1.2 Injection via $\boldsymbol{E_{channel}}$

After the particles which are affected only by the return flow arrive at the spacecraft, the particles injected through the flow channel arrive and we see the dispersed injection. In addition to the W_f=25 keV particle backtraces, Figures 3.12c and 3.12d shows the trajectory of W_f=70 keV particles, one of the earlier injected particle populations to arrive. These trajectories demonstrate a de-energized population arriving simultaneously with an energized population. The W_f= 25keV particles drift slower such that they were only affected by the return flow and did not traverse the channel at all, explaining their loss of energy. The 70 keV particle population, however, drifts faster. These particles were in a trapped orbit at a higher L-shell than THC when $\mathbf{E_{transient}}$ turned on. Located just west of the channel when $\mathbf{E_{transient}}$ turned on, the particles were momentarily knocked tailward by the return flow before entering the channel and being swept towards Earth, gaining energy in the process. When they exit the channel they are only slightly affected by the return flow east of the channel in comparison, and are observed by THC less than 20 minutes later as energized, injected particles. Because of our simplified description of particle distributions across the tail, those particles that have a source other than at the spacecraft L-shell and 20 R_E, such as the 70 keV particles at this time stamp, will have either an over- or under-estimated PSD (as mentioned, the spacecraft location and 20 R_E were the source locations for the PSD fit). The result is the underestimated eflux in the simulation seen at higher energies by THC, since these particles' source is not as well accounted for by the PSD fitting.

As mentioned in section 3.2.2.2, if particles that backtraced to 20 R_E were found to be within the channel, they were permitted to continue backtracing to 22 R_E to allow for a greater eflux increase (due to access to a lower B_z). These particles are meant to model those directly accelerated from the reconnection region where B_z was lower (though not by reconnection itself). They result in the highest eflux values for the less energetic populations in the simulations of Figures 3.6 and 3.7 (typically the initially trapped, more energetic populations drift too fast to initiate in the reconnection region), and are shown by the trace of the W_f=15 keV particles in Figures 3.12e and 3.12f. The W_f=20 keV particles in the same panel were drifting eastward just over 20 minutes in the quiescent field before $\mathbf{E}_{\mathbf{transient}}$ turned on upon which they were caught in the return flow. About 20 min later they encountered $\mathbf{E}_{\mathbf{channel}}$ and were swept earthward for ~5 min until $\mathbf{E}_{\mathbf{transient}}$ turned off (marked by the blue arrow labeled "t_{end}" in Figure 3.12f), and then drifted in the quiescent field again until being observed by THC at 10:38 UT.

In the modeled spectra at THC in Figures 3.6 and 3.7, one can see that eventually less energetic particles follow suit and, upon acceleration and transport from a lower B_z source, are injected and drift to THC's location. The time delay (dispersion) is again due to the fact that less energetic particles drift more slowly. This is further underscored by analyzing W_f=5 keV particles in Figures 3.12e and 3.12f. Following the 10-min tick marks, we see that backtracing from 10:38 UT to when $\mathbf{E}_{\mathbf{transient}}$ turns on (09:37 UT, marked by the black arrow labeled "t_0") puts the particles east of the channel where they cannot be accelerated earthward, but may be affected by $\mathbf{E}_{\mathbf{return}}$. This is why their trace in Figure 3.10g looks largely unaffected; $\mathbf{E}_{\mathbf{transient}}$ was turned off for most of their trajectory and it did not turn on until they had drifted past the channel location. In the meantime, source location particles with energies even lower than W_i=0.659 keV (not shown) *are* accelerated by $\mathbf{E}_{\mathbf{transient}}$ and, after taking an even longer time to drift than the

population traced in Figures 3.12e and 3.12f, are eventually observed by THC as 5 keV particles with elevated eflux.

There is, however, an upper limit in energy under which particles can be backtraced to the reconnection region (within the channel at 20 R_E). This upper limit depends on the channel width and the length of time $\mathbf{E}_{\mathbf{transient}}$ is turned on. Particles that never backtrace to the reconnection region have energies so high that gradient drifts dominate convection across the entire channel width during earthward acceleration. Similar to the 70 keV particles in Figures 3.12c and 3.12d, these more energetic particles were drifting under the nominal field when $\mathbf{E}_{\mathbf{transient}}$ turned on. Their trajectories were slightly affected by the return flow west of the channel until they drifted into the channel, where upon acceleration they continued to drift eastward until they exited the channel and finished drifting to the spacecraft location. Because they drift so fast, they can never be backtraced to the reconnection site since the time it takes to cross the channel is shorter than the time it would take to traverse the magnetotail from the reconnection site to the inner magnetosphere.

3.4.1.3 Summary of Trajectories

In summary, Figures 3.12c-f can be used to demonstrate the main types of trajectories that lead to observed eflux dips or enhancements, sometimes simultaneously. In Figures 3.12e and 3.12f, four trajectories are demonstrated by four different populations observed simultaneously, however the four trajectories can be also be used to explain a time-series of backtraces for a particular energy bin on the spacecraft. Say we are looking at the line spectra for the 25 keV particles observed at THC. First there is a dip, caused by the first type of trajectory (cyan trace in Figures 3.12c and 3.12d), in which particles only experience the return flow east of the flow

channel and are de-energized. After the dip there is a rise in eflux caused by the second type of trajectory (similar to the royal blue trace in Figures 3.12e and 3.12f), in which particles are caught within the return flow but do not cross the entire channel, only gaining a partial amount of the total energy the channel may impart. (Note for the rising eflux, though, that the particles would be caught in the flow when it turned on and thus traverse the eastern half, exiting into the return flow.) The third type of trajectory (navy blue) allows small μ particles the most eflux gain by permitting them to initiate at the reconnection site and to potentially cross the entire channel width. Particles with higher μ that cross the entire channel width will follow trajectories like the yellow trace in Figures 3.12c and 3.12d. Eflux starts to decrease again as particles undergo the third type of trajectory again (royal blue), experiencing the western return flow of the vortex and only crossing a portion of the flow channel width before $\mathbf{E}_{\mathbf{transient}}$ turns off. Finally, those particles that drift so slowly such that they only experience the return flow east of the channel undergo the last type of trajectory (black). These particles may similarly cause a dip in eflux observed by the spacecraft after injection, as pointed to by white arrows in Figure 3.6.

Through backtracing particles, we were able to ascertain information on the process of particle energization and transport that resulted in the injection signatures simulated in section 3.3.1. The trajectories demonstrate how energetic particles with an appreciable $\nabla\mathbf{B}$ drift can be adequately energized while drifting across the flow channel and the equipotentials therein, gaining kinetic energy in the process. They also demonstrate how such particles lose energy by drifting across equipotentials from the opposing electric field in the return flow as they are carried out to lower L-shells having a lower magnetic field. Though the specific parameter values may be tweaked with a more complex model, the processes behind the acceleration described are well-established in this simple picture.

3.4.2 Case 2

For our second case, Figure 3.13 demonstrates select particle trajectories to explain salient features of the injection at THB, in the same format as Figure 3.12 except that tick-marks now represent 20-minute intervals. Spectral features at other spacecraft are similar to those in Case 1 and need not be elaborated upon here, except the notable example of a simultaneous eflux dip and injection observed at THD (Figures 3.10e and 3.10f). Figure 13a shows the backtraces of particles with energies of 8, 10, and 13 keV in the quiescent field prior to $\mathbf{E}_{\mathbf{transient}}$, all trapped within their respective Alfvén layers. Figure 13b depicts the altered μ=0 contours of motion (equipotentials) under the additional influence of $\mathbf{E}_{\mathbf{transient}}$ at its maximum strength as well as the four spacecraft locations in this case.

3.4.2.1 The inverse velocity dispersion

The inverse velocity dispersion observed and modeled at THB can be explained as a temporal effect due to the fact that THB is located within the transition region (X_{GSM} =-6.0 +/- 1.5 R_E) where the strength of $\mathbf{E}_{\mathbf{channel}}$ is decreasing. If THB were located within the channel beyond X_{GSM} =-7.5, it would not observe the inverse velocity dispersion and would instead observe a standard dispersionless injection. However, because E_c is about 27% of its maximum strength at X_{GSM} =-5.3, only the particles having lower μ (and lower initial energies (W_i)) within the vicinity will immediately be affected (Figures 3.13c and 3.13d), W_f=8 keV). This is because the weaker electric field at the nose of the front is not strong enough to break the quasi-steady convection orbits of the higher-μ particles (because their $\nabla\mathbf{B}$ drift term dominates the weaker $\mathbf{E}_{\mathbf{transient}}$), and their drift orbits remain unaffected. Given time, particles that were initially farther downtail but following the same lower-μ trajectories will reach the spacecraft as well (Figures

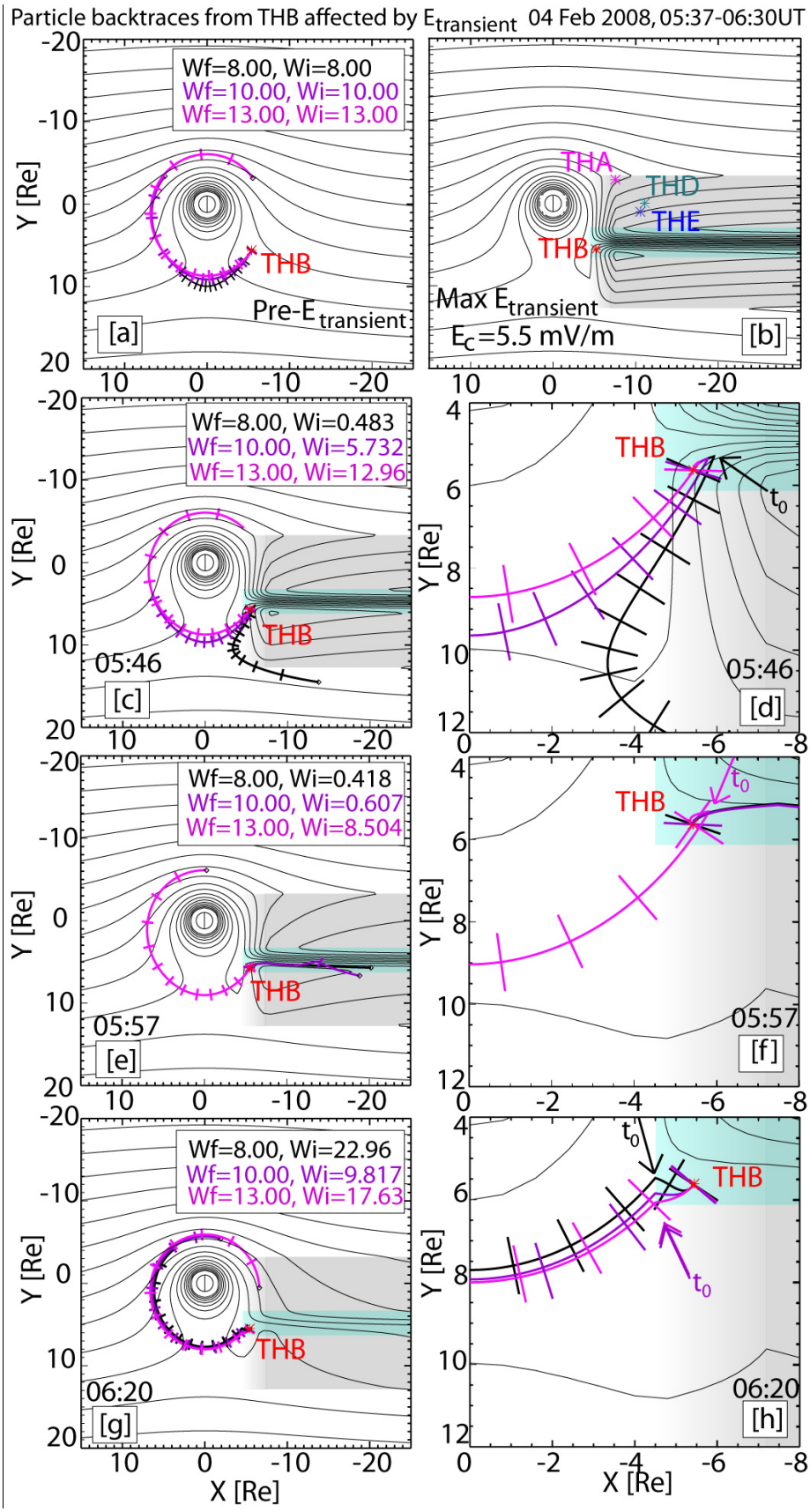

Figure 3.13. Plots of particle backtraces from THB demonstrating particle transport related to $\mathbf{E}_{\mathbf{transient}}$. Tracing, W_i and W_f, contours, and shading follow the same format as Figure 3.12. (a) Pre-$\mathbf{E}_{\mathbf{transient}}$, quiescent scenario. (b) Equipotentials when $E_{transient}$ is at its max strength and has reached X_{max} with the four THEMIS spacecraft locations indicated. (c–h) Particle trajectories backtraced from THB at the indicated time of observation (marked by vertical lines in Figure 3.11d). Traces are color-coordinated with the line spectra in Figure 3.11. Left column plots give a broad overview while right column plots zoom in to enhance the features of interest. Tick marks represent 20-min intervals. Arrows point out the location in the traiectories where the

3.13e and 3.13f), W_f= 10 and 13 keV). Because these started at higher L-shells, greater energization can occur and we observe the eflux increase at higher W_f, resulting in the inverse dispersion. (A stronger E_c applied with the same parameters would allow for higher W_f values than shown.)

In other words, μ=2.36e-5 J/nT particles (having W_f=10 keV at THB) exist all along generalized equipotential contours (which would be drawn as shown but also including the gradient B drift term akin to Figure 3.2). Such particles (called μ_1 from now on) that exist close to THB when the front arrives were pushed in from a trapped orbit, e.g., in Figures 3.13c and 3.13d at 05:46 UT, having W_i=5.732 keV. At 05:57 UT (Figures 3.13e and 3.13f), the μ_1 particles that were picked up around X_{GSM} =-13.5 R_E have had enough time to travel to THB, bringing with them higher eflux as energized particles since they originated beyond the μ_1 Alfvén layer with W_i=0.607 keV. Meanwhile, the W_f= 13 keV particles are much less affected by the injection.

3.4.2.2 Energy limits on observable injection features

Figures 3.13e and 3.13f depict particle backtraces having three different sources observed at 05:57 UT, 20 minutes after $\mathbf{E}_{\mathbf{transient}}$ began at 20 R_E and moved earthward. Similar to Figure 3.12e and 3.12f, Figures 3.13e and 3.13f demonstrates how observed particles under an upper limit in energy (or μ, we could say) can travel from the reconnection region to the spacecraft without $\nabla\mathbf{B}$ drifting too far east to overshoot the spacecraft location. For THB this upper limit is smaller than for the other spacecraft east of the flow channel, since it is located on the western edge of the channel. Thus to be observed by THB, like the W_f=8 keV particles in Figures 3.13e and 3.13f, the particles must drift so slowly that they do not cross much of the channel width as

they are carried inward, or they would otherwise exit the front of the channel to the east of THB or the eastern flank of the channel tailward of THB. The W_f=10 keV particles, for example, are accelerated but drift across the channel too fast to be backtraced to the reconnection region at 20 R_E. Thus, to be observed, such particles first spend time drifting earthward west of the channel and then are picked up by $\mathbf{E_{channel}}$ when the flow front reaches X_{GSM}~-13.5 R_E. On the other hand, W_f=13 keV particles are orbiting just outside the spacecraft L-shell so they are simply nudged inward when the return flow arrives. The result is that particles of these three different energies are all caught in $\mathbf{E_{transient}}$ and reach the spacecraft simultaneously, but less energetic particles have a greater gain in energy flux because they arrive from greater distances (and lower magnetic fields).

We see the largest gain in eflux at energies with source populations that were trapped within their Alfvén layer in the quiescent state, but during injection have source populations located downtail (i.e., W_f=8 keV and 10 keV which are in trapped orbits in Figure 3.13a, but backtrace downtail in Figures 3.13e and 3.13f). This is because these observed energies have the largest change in energization between the quiescent and injection intervals (i.e., the W_f=8 keV initially had W_i=8 keV, but after injection has W_i=0.418 keV. Conversely, less energetic particles that had sources downtail prior to $\mathbf{E_{transient}}$ (e.g., Figure 3.12a, W_f=5 keV) undergo energization of the same magnitude from betatron acceleration when the flow burst quickly carries them in as in the quiescent state. For instance, although no rise in eflux is observed at arbitrary energies below 8 keV at THB in Figures 3.10 and 3.11, particles with these energies are indeed carried earthward by $\mathbf{E_{transient}}$. The eflux remains constant, however, because of negligible energization from $\mathbf{E_{transient}}$ compared to that of particles drifting under nominal fields. Specifically, W_f=0.060 keV particles (not shown) that backtrace to 20 R_E under nominal fields

and W_f=0.060 keV particles that backtrace to 22 R_E under $\mathbf{E}_{\mathbf{transient}}$ each had initial energies of 0.003 keV, thus they experience no change in energization (meaning the same population is observed by the spacecraft at W_f=0.060 keV both before and after injection, so the PSD of the W_f=0.060 keV particles remains constant). This is alternately explained by the fact that these less energetic particles cannot $\nabla\mathbf{B}$ drift fast enough to cross an appreciable distance of the channel width before reaching THB, meaning they cannot gain kinetic energy via crossing the equipotentials within the channel. Of these less energetic particles, some that originate from the reconnection site can undergo increased betatron acceleration since they backtrace to even lower magnetic field values than before (e.g. Figures 3.13e and 3.13f): the 8 keV particles) and have a little more time to drift eastward across the equipotentials before being observed. There appears to be a lower limit in energies, however, in which the change in B_z from 20 R_E to 22 R_E is not great enough to affect the total energization, and these particles drift even slower (i.e., 0.003 keV particles which, whether coming from 20 or 22 R_E, are observed as 0.060 keV particles by THB).

There is also an energy range that exhibits the highest efluxes (dark red in the modeled spectra corresponding to ~10^8 eV/cm^3-s-str-eV, e.g., Figure 3.10h at energies approximately >5 keV and <10 keV), which we found is caused by particles with a large phase space density that undergo large betatron acceleration, traversing an appreciable distance over the channel width (or, potential drop). Higher energy particles originating close to the spacecraft have lower phase space densities (because the distribution function decreases with energy) such that although they cross the entire potential drop, attaining maximum energy gain, they do not achieve such high eflux values (e.g., Figures 3.12c and Figures 3.12d) W_f=70 keV traverses the entire flow channel, but has eflux on the order of 6e5 eV/cm^2-s-str-eV as seen in Figure 3.7b at 09:51 UT).

In studying the trajectories, we found that not all particles within this energy range backtrace to the reconnection region, although all undergo a non-negligible amount of energization compared to before the imposition of $\mathbf{E}_{\mathbf{transient}}$ (unlike the W_f= 0.060 keV particles above). For instance, some may be like the W_f=10 keV particles in Figures 3.13e and 3.13f which were originally within a trapped orbit but, under the influence of $\mathbf{E}_{\mathbf{transient}}$, came from downtail and therefore were vastly energized in comparison. Furthermore, not all particles originating from the reconnection site exhibit such high efluxes, such as the W_f=20 keV particles from Figure 3.12e. This means the PSD found at the source for W_i=1.725 is too low to result in an eflux of ~10^8 eV/cm^2-s-str-eV for 20 keV at THC. Thus we see the importance of the PSD in limiting which energies may have an eflux peaking over 10^8 eV/cm^2-s-str-eV.

It appears, then, that the energy range at which we observe particular injection features is dependent on how much more populations are energized from $\mathbf{E}_{\mathbf{transient}}$ than they were previously (or, by how much W_i changes from quiescent to injection intervals). This in turn is related to how much of the channel width the particles drift across, since a particle crossing the entire channel would convert all of the potential energy from $\mathbf{E}_{\mathbf{channel}}$ into kinetic energy. The eflux increase is also limited by the population's PSD, with lower initial energies having higher PSDs, resulting in higher efluxes at the associated observed, final energies.

3.4.2.3 Eflux dip following the injection

A minimum in eflux on THB exists at energies between 10 and 30 keV after the injection, most noticeable by the green eflux in Figure 3.10c (a white arrow points it out). This is a real spectral feature and not an artifact of instrument response or of ESA – SST instrument inter-calibration. Like the dips prior to dispersed injections on spacecraft east of the channel, this

primarily post-injection dip is also due to the return flow in the vortex: Figures 3.13g and 3.13h at 06:20 UT demonstrate this effect. This is seen not only at THB, but also at the other spacecraft for both events in both the simulation and the data (see especially ~18-30 keV particles from 07:00 UT onward at THD in Figure 3.8a). Figure 3.6 also has white arrows pointing out the post-injection dips seen in Case 1. Specifically, Figures 3.13g and 3.13h show that the slowly orbiting W_f=8, 10, and 13 keV particles were at L-shells closer to Earth than THB. Drifting towards the nose of the flow channel, they were caught up in the westward moving flow in the vortex (E_{return} $\hat{x}$) and were swept outward to a higher L-shell.

A similar effect is seen in Figures 3.12e and 3.12f by the W_f= 25 keV particles. These are swept out to higher L-shells by the return flow at the channel's western flank and then spend the remainder of $\mathbf{E_{transient}}$'s existence losing energy while drifting across the opposing $\mathbf{E_{return}}$ without traversing the channel itself. When $\mathbf{E_{transient}}$ died away and the system returned to its quiescent state, the particles were left at a higher L-shell than they were previously, de-energized from dropping across an eastward-pointing field or equivalently, having moved to a lower magnetic field region. Thus, they were observed at THC having lost energy over time, explaining the observed dip in eflux at those energies.

3.4.2.4 Eflux dip prior to and during injection

Another feature of the THD and THE spectra consistent with the effects of the vortex is seen in Figures 3.10 and 3.11: both spacecraft observed a depletion (dip) in eflux at energies ~15-20 keV at the same time that particle fluxes increased at higher energies around 30-100 keV. This feature is explained by the $\mathbf{E_{return}}$ component of $\mathbf{E_{transient}}$ in a similar fashion as the aforementioned dip at THC in Case 1. Particles with energies of 15-20 keV at THD and THE

that were orbiting closer to Earth with higher energies prior to $\mathbf{E_{transient}}$ find access to higher L-shells because of the return flow, and traveling from a higher to a lower magnetic field. They thus lose energy in the process of drifting across the eastward-directed $\mathbf{E_{return}}$ and generate a dip in eflux observed by the spacecraft. As previously discussed, THA observed a dip as well in even lower energies, more easily seen in Figure 3.11a, which is also captured by the simulation (though we again note that using PSDs fit only to the spacecraft L-shell and 20 R_E are at least partly the cause of the lower eflux dips in the simulation).

Figure 3.14 summarizes the trajectories that particles of various energies take in order to explain this feature as observed at THD at 05:45 UT on 2008-02-04, using 5-min tick marks. (Similar to Figures 3.12 and 3.13, the full 24 hours are not shown for the sake of visual clarity. While W_i is listed at the 24-hour mark, the backtraces only go back one hour.) The lowest energy population (royal blue trajectory, W_f=20 keV) drifts the slowest; therefore to be observed simultaneously with the fast-drifting, more energetic particles, it was located closest to THD when $\mathbf{E_{transient}}$ arrived, putting it within the return flow. Although this population was swept out, its source location is still at 20 R_E; therefore there is a minimal dip in eflux from the quiescent state (see Figures 3.10f and 3.11f). Because it had to drift before being observed, this population contributes to the dispersed nature of the dip. The higher energies that were immediately swept out from their orbits by the return flow contribute to the dispersionless portion of the dip (e.g., 25 and 40 keV at 05:39 in Figure 3.11f), since THD is located within the return flow (similar to our discussion on the dispersionless dip in Case 1 under section 3.5.1.1).

The W_f=25 keV particles (cyan) are similarly slow drifters, and thus, to be observed at the same time, must also be closer to THD when $\mathbf{E_{transient}}$ arrives and are also caught up in the return flow. Unlike the W_f=20 keV particles, prior to $\mathbf{E_{transient}}$'s arrival they were in a trapped

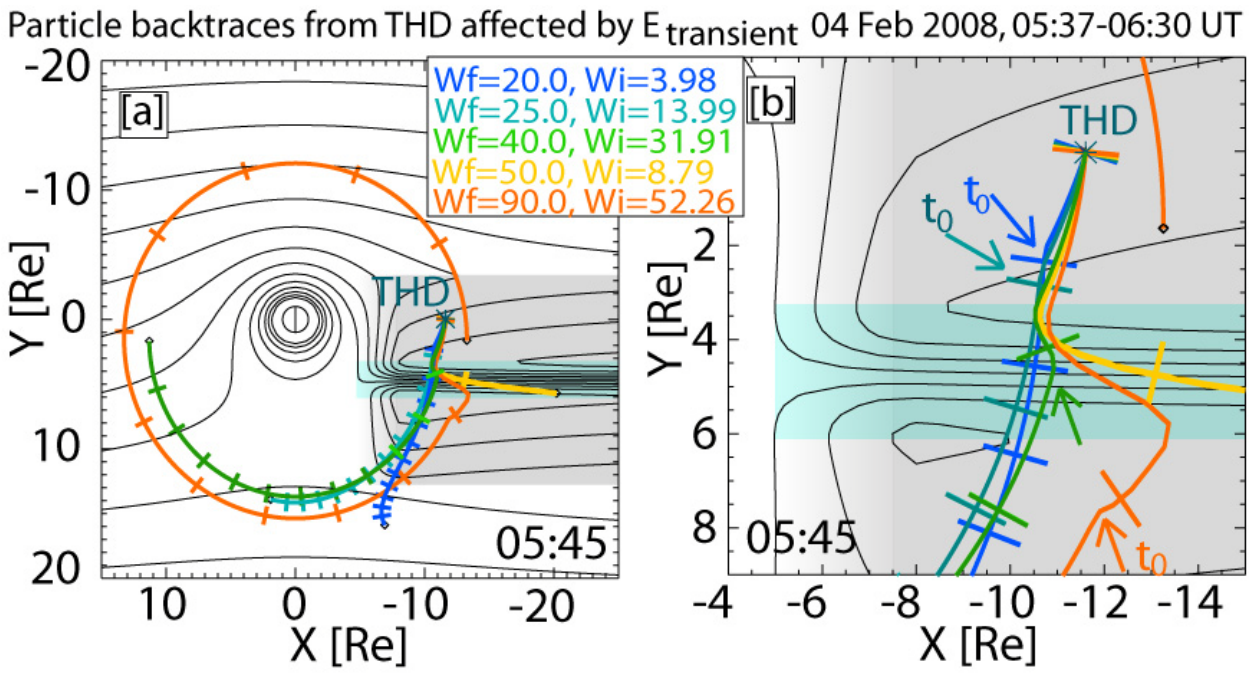

Figure 3.14. (a, b) The same format as Figures 10c and 10d with 5-min tick marks. Traces are color- coordinated with the line spectra in Figure 3.11, and the time of observation is indicated by the vertical line in Figure 3.11f. These are backtraces of particles of different energies during the simultaneous injection at higher energies (i.e., 40, 50 and 90 keV particles) and dip at lower energies (i.e., 20 and 25 keV particles) as observed at THD.

orbit earthward of the spacecraft. Their initial energy (W_i=13.99 keV) is lower than 25 keV because the asymmetrical orbit began 24 hours earlier at a higher L-shell, but there is still eflux depletion because the source population's energy for 25 keV particles found downtail in the quiescent state is W_i=4.992. Since there is overall a decrease in energization from before to after the new populations arrive due to $\mathbf{E}_{\mathbf{transient}}$, depletion in eflux is observed.

Because more energetic particles drift faster, the dip is shorter in duration for the W_f=40 keV spectral line than the W_f=25 keV spectral line since the more energetic injected particles will reach THD first. Because of this, at an earlier timestamp (not shown), the W_f= 40 keV particles (green trace) have a backtrace similar to that of the swept out W_f=25 keV particles. At the time shown, however, we observe W_f=40 keV particles that were in the flow channel's path

when it arrived (as can be seen by the elbow in the green trace, pointed to by the green arrow in Figure 3.14b around X_{GSM} =-11 R_E). This particular particle trajectory demonstrates how after particles only experiencing the return flow arrive, particles that experience both part of the flow channel and the return flow arrive. Having been both accelerated and decelerated, when these particles are observed the corresponding eflux is similar to the quiescent state. Eflux continues to rise over time as particles that drifted longer within the flow channel arrive. In other words, the W_f=40 keV particles later increase in eflux (Figures 3.10e, 3.10f and 3.11e and 3.11f) as their source moves to even lower magnetic field values, as with the W_f=50 keV population (yellow trajectory) in Figure 3.14.

Drifting faster than the W_f=20 and 40 keV populations, the W_f=50 keV particles had enough time to drift across the entire channel (gaining more energy) and to the spacecraft location in order to arrive at the same time as the slower, less energetic particles, which were initially closer to THD. Because of the nature of energy dispersion, given more time, the less energetic particles will traverse the entire channel as well and will be similarly energized, resulting in the dispersed injection signature.

The fastest drifters of the five populations in Figure 3.14, the W_f=90 keV particles (orange trace) drift so quickly that they cross the entire channel faster than the time it would take to carry them via **E**x**B** drift from the reconnection site to the inner magnetosphere. They can therefore never be traced back to the reconnection site. Instead, they are west of the flow channel when it arrives (Figure 3.14b orange arrow: X_{GSM}~-12, Y_{GSM}~7.5) and thus are first carried tailward by the return flow. As they continue drifting eastward they eventually meet the flow channel (~X_{GSM}=-13) and are swept earthward until they drift out of the channel (~X_{GSM}=-11). They then enter the return flow on the eastern flank of the channel, continuing to drift and losing

some of the energy they gained until they are observed by THD. Thus, we see how a fast flow and its accompanying return flow can affect different particle populations such that a spacecraft observes both a dispersed injection and a dispersed eflux dip signature simultaneously.

The W_f= 90 keV trajectory also shows us why higher energy spectral lines see a short duration, strong eflux enhancement, followed by a quick return to quiescent or just above quiescent eflux levels (i.e., Figures 3.7 and 3.11 in both observed and modeled efluxes, particularly for energies above ~50 keV). The short enhancement is caused by particle populations that have drifted across more equipotentials from the channel than the return flow, as with the W_f=90 keV particles in Figure 3.14, allowing for a net energy gain. However, over time, particles that have traversed much or all of the return flow on the western flank of the channel before crossing the flow channel start arriving at the spacecraft. Because the net potential change across $\mathbf{E}_{\mathbf{transient}}$ is zero, the energy gained by crossing the channel is almost negated for particles drifting across most of the structure (having been subjected to most of the return flow in addition to the flow burst). This occurs at higher energies because they are fast drifters and are capable of drifting over the entire transient structure west of the spacecraft before $\mathbf{E}_{\mathbf{transient}}$ dies away. This principle is behind the energy dispersion in eflux fall-off following the injection, as over time less energetic populations arriving at the spacecraft have traversed the entire structure.

We have used particle trajectories from Case 2 to explain why specific injection features are observed by a spacecraft near the earthward extent of the fast flow and its associated transient electric field, as well as to further explore a more distinct example of the eflux dip simultaneous to the dispersed injection of more energetic particles. Most notably, we found the decreasing east-west electric field strength at the nose of the channel in our model (corresponding to the

braking of the flow) can account for the inverse velocity dispersion observed at THB. These trajectories, modified by an incoming transient electric field with a constant velocity, further support our conclusion that energetic particles with appreciable $\nabla\mathbf{B}$ drift are energized by drifting across the enhanced east-west electric field within the narrow flow channel. Less energetic (smaller μ) particles did not observe an appreciable gain in energy since they did not drift across the equipotentials.

3.5. Discussion

3.5.1 Comparison to Previous Studies

One motivation for developing a localized electric field model was to explain the observations of trans-geosynchronous injections. Although TGIs have been observed anywhere from 10-60 R_E, both the flows and the related electric fields are localized there (e.g., *Angelopoulos et al*. [1997]; *Nakamura et al.* [2004]), contrary to prior models used to explain geosynchronous injections (e.g., *Li et al.* [1993; 1998]; *Zaharia et al.* [2004]).

Thus, in contrast to past models, our model describes an electric field associated with a flow channel. The increased bulk flow within the channel and associated dipolarization fronts within them (the "dipolarization front" is a localized signature related to the flow burst; "dipolarization" refers to a global collapse of the field) result in an enhanced electric field within the dipolarizing flow bursts themselves (*Runov et al.*, 2009, 2011; *Zhou et al.*, 2011). The flow channel is therefore localized in Y_{GSM} everywhere downtail, allowing spacecraft at any radial distance to observe dispersed injection signatures. In both our cases, all tail spacecraft (except THB in Case 2, which was near the geosynchronous region and within the flow channel) observed dispersed trans-geosynchronous injections that were correctly simulated by our model.

Our model of a localized electric field channel, even with simple assumptions (i.e., dipole field, uniform source PSD, negligible distortion of magnetic field and exclusion of inductive electric fields) is thus capable of reproducing the main characteristics of trans-geosynchronous observations simultaneously with those of geosynchronous injections. We point out that the electrons in the modeled injections are energized from the electric fields from the flow, and not at the reconnection site itself. Most particles are "picked up" along the way by drifting into the region of enhanced E_Y, while a few encounter the front as it moves earthward and a few originate from the "reconnection region". (The latter are energized more by larger betatron acceleration from starting at a smaller magnetic field.)

Additionally, the model presented herein for the first time incorporates and demonstrates the importance of electric fields due to the return flow. These electric fields allow us to model the depletion (a.k.a. "dip") in energy flux observed prior to and following injections: particles are de-energized as they are carried by the return flow to lower magnetic field strengths and $\nabla\mathbf{B}$ drift across the eastward-directed $\mathbf{E}_{\mathbf{return}}$, providing these spectral features to near-Earth spacecraft. The stronger the return flow (and its corresponding $\mathbf{E}_{\mathbf{return}}$), the wider the energy range of flux depletion. This was demonstrated by the larger range of energies (~15-40 keV) that undergo eflux depletion by THD and THE in Case 2 (Figure 3.10), which has a stronger $\mathbf{E}_{\mathbf{return}}$ than Case 1 (Figure 3.6), in which a smaller range of energies (~20-30 keV) undergo an eflux depletion. In many cases (e.g., see Case 2, THD, THE and—to a lesser extent—THA) as more energetic (>40 keV) particles are "injected", less energetic (~10-40 keV) particles undergo simultaneously an eflux "dip". This was explained as particles affected by the return flow (they either do not encounter the earthward flow channel or they encounter it briefly), yet arrive with the more energetic, injected particles. In other words, often prior or simultaneous to the arrival of injected

particles, ~30-40 keV particles undergo a dip in eflux, followed by less energetic particles dispersed over time. The dispersionless nature of the dips in Case 1 and at energies 25-30 (seen in Figures 3.11f and 3.11h) is due to the spacecraft's location within the return flow, similar to the scenario when a spacecraft observes a dispersionless injection because it is located within the flow channel. The dip dispersion in lower energies comes from those populations which were drifting in from larger distances and then got caught in the return flow, losing energy and arriving at later times.

This dispersed feature validates our hypothesis that the observed depletion is caused by return flow rather than plasma sheet thinning. Plasma sheet thinning during substorm growth phase has been observed at geosynchronous altitudes where spacecraft often observe depletion in energy flux prior to a dispersionless injection. If trans-geosynchronous dips accompanying injections in eflux were due to plasma sheet thinning, however, the depletion would occur at all energies near-simultaneously just prior to the injection, but this has not been observed. We can also rule out the idea that these eflux depletions are of the sort described by *Kistler et al.* [1989; 1999] and *Angelopoulos et al.* [2002] (and references therein) for ions, which were explained by particles on open trajectories (accessible from the tail) that take a long time to arrive at the spacecraft location such that noticeable losses occur, creating a minima in eflux at discrete energies (a few keV). In contrast with the transient depletions we report, these minima were long-lasting (throughout storm-time). The transient depletions have also strong local time dependence (evident by notable differences between the azimuthally separated spacecraft). The storm-time minima described by *Kistler et al.* [1989] were found generally at all MLTs, though the energies affected were different for the dawn-to-noon sector (5-20 keV had a minima) compared with the noon-to-dusk sector (<5 keV). We therefore assert that the eflux dips

reported in this paper that commonly accompany dispersed injections are a result of a different physical process than either plasma sheet thinning or particle losses, and can be used to shed light on the acceleration process itself. Since our model has demonstrated that the electric fields associated with a return flow at the flanks of a fast flow channel can de-energize particles to create the dip, our hypothesis that the electric fields play a large role in particle acceleration is further supported.

3.5.2 Discussion on the Model's Simplifications

3.5.2.1 $\boldsymbol{E}_{transient}$'s Long Duration

We note that the $\mathbf{E}_{\mathbf{transient}}$ duration in both case studies is longer than that of a typical flow burst (1-3 min) and attribute this discrepancy to the appearance of secondary and perhaps even tertiary injections. In Case 1, a secondary injection was observed at THD and THE at ~10:05 UT. This is consistent with the plasma bubble theory mentioned in the introduction, in which multiple plasma bubbles are released via reconnection and travel earthward. Therefore, although a transient electric field lasting 25 minutes is not typically observed, two incoming plasma bursts each carrying an electric field is a viable interpretation for the extended duration. Our steady state picture is thus a simplification describing these two bubbles as one. Similarly, possible secondary and even tertiary injections are observed in Case 2 at both THD and THE simultaneously around 05:47 and 05:58 UT. While we are unable to resolve it, if the observed slight increase in eflux is indeed due to additional injection(s), it is probable that they did not penetrate close enough to Earth for THB to observe them, explaining why the modeled eflux increase extends past the injection duration observed at that spacecraft. Our prolonged pulse duration is thus a simplification consolidating consecutive nearby impulses into one.

It would be very interesting to next seek out and study injection events that are clearly singular. Studying cases in which the enhanced eflux is clearly due to one injection (rather than multiple), one can better constrain the location and spatial extent of $\mathbf{E}_{\mathbf{transient}}$. Through accurate modeling of electric fields of singular fast flow events, we may also be able to better isolate the source location of the injected particles. This would not change the physical picture discussed here, but it would potentially enhance the model's accuracy at predicting particle source locations and impulse properties. Although an isolated case would be best, treating multiple injection events as multiple transient electric fields associated with flow bursts with our model may also address these questions.

3.5.2.2 A Constant Dipole Field

The fact we use a dipole magnetic field instead of a stretched one is not unprecedented [e.g., *Angelopoulos et al.,* 2002; *Ganushkina et al.,* 2005; *Kistler et al.,* 1999; *Li et al.,* 1993; 1998; 2003; *Sarris et al.,* 2002; *Zaharia et al.*, 2000] though we note several of the studies used an asymmetric dipole field. Aside from the fact that we wanted to follow previous studies that used a dipole field approximation, we also used the dipole field because we initially wanted to keep all of our calculations completely analytical. To impose a data-derived, stretched magnetic field model would have required calculating things numerically, and will be considered for the future. For discussions on how using a stretched field compares to a dipole field, we point to studies such as *Zaharia et al.* [2004] and *Ganushkina et al.* [2012]. We may mention here, though, that the slight eflux deficiency in ~30-40 keV populations in our simulation could be due to our dipole field approximation. If we were to impose a more realistic, stretched tail, the source B_z would be lower and the ratio between the final and initial B_z value would be greater. Thus,

the energization would be greater, leading to a higher eflux (e.g., *Zaharia et al.* [2004] found their model to be improved when they stretched the magnetic field). This is questionable, however, since the rest of the populations were well-simulated. Regardless, the dipole approximation accounts for the shape of the injection and its associated dip and can attain the maximum energy of injected particles, thus providing useful information regarding the physical processes that produce the main features of the observed spectra and the main properties of the driver electric field.

Another simplification to the presented model is that we do not include a dipolarization in the magnetic field; it remains a dipole everywhere at all times. One affect this could have is on the particles' trajectories. Previous studies (e.g., *Li et al.,* 1998; *Sarris et al.,* 2002; *Zaharia et al.,* 2000; 2004]) found that particles would initially ∇B drift in the *opposite* direction (westward for ions, eastward for electrons) when they encounter a rising magnetic field at the front because the strong magnetic field of the pulse locally reverses the gradient in B from pointing towards the stronger magnetic field at Earth to the stronger field at the dipolarization front. As the (azimuthally extended in those studies) electromagnetic pulse passes by, the particles again encounter a ∇B in pointing towards Earth and their drift direction returns to normal. In an example from *Zaharia et al*. [2000], the rise in **B** (the effective front width) is 9000 km and the electron only travels ~1 R_E in both the +X and +Y direction on account of the pulse front. Performing a rough estimation using *Runov et al.'s* [2011] results demonstrating a typical front is 500-1000 km thick (so ∇B~20 nT/500 km) and using a typical flow burst speed of 400 km/s, we also found that a 10 keV electron would drift about 1 R_E duskward before the front passed and it returned to its normal drift motion. Since this allows particles to remain in the flow channel slightly longer, it could allow more energetic particles in higher drift orbits to backtrace farther

tailward and thus be energized slightly more, but this would only apply to particles that are directly encountered by the front (like the W_f=40 keV population in Figure 13). This is because the inverse ∇B at the front prevents any particles from drifting azimuthally into it, since dawnward drifting electrons in the background magnetic field would be turned around by the inverse ∇B at the front. Since the front width is quite narrow, this would not affect many particles; however not including this effect could be the cause behind the slight eflux deficiency in the W_f~30-40 keV populations in our simulations. A discussion of the difference in simulation results when a dipolarizing magnetic field is included in the model is included in Chapter 4.

Another effect to consider if a dipolarized flux tube were to be included in the model is the possibility of breaking of the 1st adiabatic invariant when particles drift towards the flank of the flux tube. As electrons drift dawnward toward the flux tube, they will encounter a ∇B in the dawnward direction from the increasing magnetic field strength in the tube. This ∇B will cause their trajectory to turn tailward, and should this turning be sharp (i.e., if there is a sharp bend in the constant magnetic field contours), adiabaticity may be violated if the speed along this bend is fast compared to the ratio of the bend radius of curvature to the gyroperiod.

3.5.2.3 Neglecting ∂B/∂t and the Inductive Electric Field

In keeping a dipole magnetic field at all times everywhere, we make the assumption that the energizing effects of a ∂B/∂t term from the traveling dipolarization front and the resulting induced electric field is much smaller than those from the potential electric fields following the front. We may still estimate what the effects may be by considering recent results describing dipolarization fronts from *Runov et al.* [2011]. The energy gain of a particle interacting with the dipolarizing flux tube can be one of two types, described, e.g., in *Northrop* [1963]:

$$\frac{dW}{dt} = qv_{drift} \cdot E(\boldsymbol{R}, t) + \mu \frac{\partial}{\partial t} B(\boldsymbol{R}, t) \quad (3.13)$$

where q is the particle charge, v_{drift} is the drift velocity, $E(\boldsymbol{R}, t)$ is the total electric field (both potential and inductive field) at the particle's location (**R**) at a given time (t), μ is the particle's first adiabatic invariant, and $\frac{\partial}{\partial t} B(\boldsymbol{R}, t)$ is the rate of change of the magnetic field within the particle's frame of reference. This second term is the heating due to the increase of the field in the frame of the gyrocenter and includes no spatial derivative of the magnetic field to account for gyrocenter motion. Note that for equatorially mirroring particles, no integration along the field line is needed.

The maximum energy gain due to the second term occurs if the particle moves with the tube and is subjected to the full change of the magnetic field in the process. Because *Runov et al.* [2011] found dipolarization fronts to propagate self-similarly (meaning their properties remain unchanging throughout their propagation), with the largest measured in the events presented in detail being ∂B/∂t ~17 nT over 75 seconds that the front took to travel from ~-18 R_E to ~-10 R_E in a ~30 nT field (see their Figure 1), the field changes slowly enough to conserve μ: 30 nT/(17 nT/75 s) ~ 132s >> ~8.9e-4 s electron gyroperiod. Since μ is conserved, the energy gain for a 90° pitch angle electron is equivalent to the energy gain from particle motion into the strong inner magnetospheric field which is already accounted for due to convection, in our calculations. To put it another way, as long as adiabaticity is conserved, for a 90° electron the energy gain is equivalent to its betatron acceleration, $W_f=W_iB_f/B_i$. For any electron that is injected deep enough that the background magnetic field is as strong as the dipolarization front (so $B_f=B_{DF}$), the final energy (W_f) will be the same with or without the front. Or, if the electron drifts out of the pulse and into the background magnetic field, whatever energy was gained from the dipolarization front will be lost, since B_f will be the background magnetic field value. The only

situation in which the electron would be observed with a greater energy gain from the dipolarization front is if it is observed within the narrow area that the dipolarization front exists, while the front is traveling earthward and is larger than the background magnetic field.

Next, we can also discuss the possible effects of an inductive electric field. The portion of the first term in equation 3.11 due to inductive electric fields would be maximized for particles that drift along the periphery of the entire tube, providing an EMF gain of $\pi R^2 * \partial B/\partial t$ ~29 kV (taking R=1 R_E). However, it is unlikely particles will maintain such a path during the motion of the tube across large distances. Rather, particles will drift in and out of the tube gaining a fraction of that energy, in which the maximum energy will be gained by electrons drifting duskward (due to the inverted ∇B mentioned above [*Zaharia et al,* [2000]) along the dawnward inductive field on the front, gaining ~ 4.6 kV / R_E. An inductive field pointing in the opposite direction (duskward) would exist at the trailing edge, de-energizing or energizing particles depending on which direction the ∇B is pointing. Particles drifting through the tube's center (neither the front nor the tail) will gain no energy since they will see an inductive field that changes sign—pointing earthward at the duskward flank of the tube and pointing tailward at the dawnward flank of the tube; additionally, the particles' dawnward or duskward directed drift is perpendicular to the field direction at the center. The net effect on the particles requires further investigation, and depends critically on the specifics of the tube considered as well as the particle trajectories.

3.6. Summary

Using a simple model of transient, localized electric fields associated with flow bursts (typically accompanied by dipolarization fronts) in a dipole magnetic field, we have been able to explain the key properties of inward transport and acceleration of equatorial electrons. Specifically, we have been able to successfully simulate most signatures of trans-geosynchronous electron injections across a wide area in the magnetotail and as close as the geosynchronous region. Therefore our model extends past modeling efforts primarily concerned with the geosynchronous region. The spatially localized nature of the electric field is key to its efficacy in distorting the quiet time Alfvén layers and allowing energized particles access to the strong magnetic field in the inner magnetosphere. The success of this simple model, despite ignoring the increase in B_z that accompanies a dipolarization front and its induced electric field, is a surprise. We postulate that the front's small area may render this term less important than the potential electric field used in our simplified model, and in Chapter 4 we include such an inductive field to fully address this question.. The THEMIS dataset provides a large database of injections from multiple spacecraft separated both azimuthally and radially, presenting an ideal opportunity to study how particles are transported towards the inner magnetosphere. This is important to understanding the seed populations of the outer radiation belt and ring current. Despite our simplified assumptions, many injection features observed by multiple spacecraft can be explained with proper adjustment of our model parameters, enabling us to determine or constrain the properties and importance of the flow burst-related impulsive electric fields. Specifically we have shown that:

1) Energetic particles can ∇B drift fast enough to cross the flow channel's width as they are being transported earthward. Thus the potential drop across the transient fast flow

provides the means to accelerate such particles to large energies, resulting in the observed injections (Figures 3.12, 3.13, and 3.14).

2) The return flow that forms on the eastern and western edges of the flow channel is the cause of the dips in eflux (ranging from ~10-40 keV) before and after the injection. This flow carries particles to higher L-shells, de-energizing them by conservation of the 1st adiabatic invariant (as they simultaneously drift across the return flow's electric field) before they are observed. New populations come in with lower PSDs than those populations observed in the quiescent state, resulting in eflux depletion. Thus, we see how a fast flow and its accompanying return flow can affect different particle populations such that a spacecraft observes both a dispersed injection and a dispersed (or dispersionless) eflux dip simultaneously.
3) The dispersed injection signature as well as the dispersion in the eflux fall-off following injection is due to the well-established concept of differential particle drifts causing energy dispersed injection signatures: electrons of higher energies drift faster and are observed by the spacecraft east of $\mathbf{E}_{\mathbf{channel}}$ first, followed by less energetic electrons (e.g., Figures 3.10e, 3.10f, 3.11e and 3.11f). Similarly, these faster drifting particles will experience more of the return flow west of the flow channel earlier than the slowly drifting particles, meaning much of the energy gained from traversing the flow channel will be negated and the higher energy spectral lines will see a drop-off in eflux earlier.
4) Although localized reconnection may initiate the fast flows, only few injected particles come from the near-Earth reconnection region. Only less energetic particles (below a certain μ) drift slow enough to remain in the flow channel from 22 R_E to smaller L-shells, where the spacecraft can observe them (Figures 3.12e and 3.14). For particles with

energies above this limit to be accelerated by the flow burst their source must lie closer to Earth than the reconnection site, such that the drift time across the channel is comparable to the Earthward transport by the channel electric field (e.g., Figures 3.12c and 3.12d) and 3.14). This energy limit is set by the flow channel width (it takes more time to cross a wider channel) and the peak magnitude of the electric field, E_c (a stronger E_c implies faster earthward transport).

5) The maximum energy of particles affected by injection is also related to both the channel width and the strength of E_c, since a wider and stronger electric field provides a larger potential drop and is thus capable of breaking the drift paths of more energetic particles and carrying them earthward where the magnetic field is larger. We found E_c to be 2 mV/m and 5.5 mV/m in our two cases, consistent with other cases we have examined and in agreement with previous observations.

6) Particles having final energies that are very low do not observe more energization from $\mathbf{E}_{\mathbf{transient}}$ than they did from their drift paths during the quiescent state, since they lack the appreciable ∇B drift necessary to cross the potential drop (e.g., Figures 3.10f and 3.10h), energies less than ~4 keV). These form the lower limit in the energy range affected by the injection.

7) The peak in eflux (dark red in the modeled spectra, eflux ~10^8 eV/cm^2-s-str-eV) was observed at lower energies (i.e., ~5-10 keV). It is caused by particles with large phase space density; such particles undergo large betatron acceleration, traversing an appreciable portion of the channel (potential drop). (Recall that since this is a dispersed injection, it is observed outside of the narrow flow channel. Thus any energy that would have been gained by a 90° pitch angle electron due to $\mu\frac{\partial B}{\partial t}$ of the dipolarization front

would be lost after it drifts out of the dipolarizing flux bundle and into the background magnetic field (assuming adiabaticity.)

The physical picture described herein is capable of explaining the key injection features absent in previous numerical models, namely the dispersion observed in trans-geosynchronous injections and the (often dispersed) energy flux dip observed prior to, during, and following the injection. Although using a more realistic model (i.e., a stretched magnetic field) and a self-consistent electromagnetic pulse description of the flow burst may alter some of the parameters fit to our case studies (such as the exact value of E_c, the channel width, and L_{vortex}), it can only make minor improvements in the model and would not alter the physical picture presented to explain the injection features listed.

Our modeling may also be applied to describe the spatial structure of the electric fields associated with flow bursts that are accelerating and transporting particles, based on observations from distributed spacecraft. To further build upon this capability, ion injection modeling can be helpful as well, though it would involve full particle orbit tracing at locations and times where the 1st invariant is violated. Electron injection observations east of the flow channel and ion injection observations west of the channel can then be used to more accurately constrain the entire electric field system. As current and upcoming missions turn an eye towards the inner magnetosphere, understanding particle acceleration and transport in the magnetotail becomes pivotal as we strive to understand the seed populations in the outer radiation belt and ring current. The localized, transient electric field model used herein can prove useful for a description of both trans-geosynchronous injections and those which penetrate as far as, or even inside, geosynchronous altitudes to possibly replenish the fluxes in the inner magnetosphere.

Appendix 3A

Here we supply the specific functions describing the imposed transient electric field. Recalling equation 3.12 from section 3.2.3, the entire imposed electric field is described by the following:

$$\boldsymbol{E_{transient}} = E_{channel}\hat{\boldsymbol{y}} + E_{return}\hat{\boldsymbol{y}} + E_{return}\hat{\boldsymbol{x}} \tag{3.12}$$

Figure 3.3 demonstrates the pulse electric field imposed upon the dawn-dusk electric field only (neglecting corotation and ∇B drift) to assist the following explanation of the $\mathbf{E}_{\mathbf{transient}}$. Similar to Figure 3.2 it shows the contours of motion, i.e., the equipotential field lines due to the electric fields but for a μ=0 population (no ∇B drift). The electric field related to the earthward motion is within the channel bound by Y_{min} and Y_{max} (the blue box in Figure 3.3):

$$E_{channel}\,\hat{\boldsymbol{y}} = \frac{E_C{}'}{2}\left\{1 + \sin\left[\frac{2\pi\left(Y_{shifted} - Y_{Max\,shifted} - \frac{Y_{width}}{2}\right)}{Y_{width}} + \frac{\pi}{2}\right]\right\} \tag{3A.1}$$

where E_c' is the magnitude of $\mathbf{E}_{\mathbf{channel}}$ at the channel center, and Y_{width} is the width across the channel (Y_{Max}-Y_{Min}). Because $\mathbf{E}_{\mathbf{transient}}$ is the sum of the opposing fields, $\mathbf{E}_{\mathbf{channel}}$ and $\mathbf{E}_{\mathbf{return}}$, E_c' is calculated such that the effective $\mathbf{E}_{\mathbf{transient}}$ magnitude (E_c) equals the value we input for E_c (rather than E_c-E_{return}):

$$E_c{}' = \frac{E_c}{1+\frac{1}{4L_{vortex}}\left(-Y_{width}+\frac{Y_{width}}{2\pi}\left[\sin\left(\frac{2\pi Y_{min}}{Y_{width}}\right)-\sin\left(\frac{2\pi Y_{max}}{Y_{width}}\right)\right]\right)} \tag{3A.2}$$

Y_{max} is the eastward limit of the channel and Y is the Y_{GSM} position where $\mathbf{E}_{\mathbf{channel}}$ is calculated at that moment in the particle trace. Both these values must be shifted to create a reference frame symmetric about the channel center if the channel is located off of midnight (Y=0) by subtracting $(Y_{max} - Y_{width}/2)$ to get $Y_{shifted}$ and $Y_{Max\,shifted}$. (Effectively, to have a symmetric sinusoid about the channel center, the center must be Y'=0, thus the shift in the equation.)

Within +/-L_{vortex} of the channel center (gray box in Figure 3.3), $\mathbf{E_{return}}$ is calculated such that any potential gained in the system from $\mathbf{E_{channel}}$ is exactly canceled by providing a constant $\mathbf{E_{return}}$ in the opposite direction (-E_y):

$$-(E_{return}\hat{\boldsymbol{y}}) = -\frac{d\Phi_{\text{channel}}}{dy} = -\frac{(\Phi_{\text{channel}})_{\text{max}}-0}{2L_{vortex}} \tag{3A.3}$$

$$\text{Where } (\Phi_{\text{channel}})_{\text{max}} = -\int_{\text{Ymax}}^{\text{Ymin}} \text{E}_{\text{channel}} dy$$

$$= -\frac{E_c'}{2}\left\{Y_{min} - Y_{max} + \frac{Y_{width}}{2\pi}\left[\sin\left(\frac{2\pi Y_{min}}{Y_{width}}\right) - \sin\left(\frac{2\pi Y_{max}}{Y_{width}}\right)\right]\right\} \tag{3A.4}$$

Note: $\Phi_{\text{channel}} = (\Phi_{\text{channel}})_{\text{max}}$ at Y_{min} and $\Phi_{\text{channel}} = 0$ at Y_{max}. Also, because of symmetry, we need not shift to a symmetric reference frame as was required to calculate $\mathbf{E_{channel}}$. Thus,

$$E_{return}\hat{\boldsymbol{y}} = \frac{E_c'}{4L_{vortex}}\left\{-Y_{width} + \frac{Y_{width}}{2\pi}\left[\sin\left(\frac{2\pi Y_{min}}{Y_{width}}\right) - \sin\left(\frac{2\pi Y_{max}}{Y_{width}}\right)\right]\right\} \tag{3A.5}$$

This is derived by first calculating the total potential drop across the channel width (Y_{width}). This tells us the equivalent change in potential over the entire $\mathbf{E_{transient}}$ width ($2L_{vortex}$) necessary to cancel that from the channel. Because we set $\mathbf{E_{return}}$ constant, calculating it from $-\frac{d\Phi}{dy}$ is trivial.

$E_{return}\hat{\boldsymbol{x}}$ forms within the transition region (the gradient bound by green vertical lines in Figure 3.3) where the flow is deflected both eastward and westward in the vortex. Meanwhile, representing the braking flow, $E_{channel}\,\hat{\boldsymbol{y}}$ decreases linearly (from E_c' to 0 at the channel center) over 2Lx in X_{GSM} (depicted by the gradient in Figure 3.3):

$$E_{transient}\hat{\boldsymbol{y}} = \frac{E_{channel}\hat{\boldsymbol{y}} + E_{return}\hat{\boldsymbol{y}}}{2}\left(1 - \frac{X}{Lx_{max}} + \frac{X_{max}}{Lx_{max}}\right) \tag{3A.6}$$

and as the potential changes over X,

$$E_{return}\hat{\boldsymbol{x}} = -\frac{d\Phi_{\text{E}_{\text{transient}}}}{dx} = \frac{d}{dx}\frac{\Phi_{\text{E}_{\text{transient}}}}{2}\left(1 - \frac{X - X_{max}}{Lx_{max}}\right) \tag{3A.7}$$

$$= \frac{\Phi_{\text{E}_{\text{transient}}}}{2Lx_{max}} = \frac{\Phi_{\text{E}_{\text{channel}}} + \Phi_{\text{E}_{\text{return}}}}{2Lx_{max}} \tag{3A.8}$$

where X is the X_{GSM} position at which $\mathbf{E}_{\mathbf{transient}}$ is calculated and X_{max} is the location of the earthward front of $\mathbf{E}_{\mathbf{transient}}$. As one can see, the ramp-down in $E_{transient}\hat{\boldsymbol{y}}$ is centralized on X_{max} such that $E_{transient}\hat{\boldsymbol{y}}$ is at full strength at X_{max}-Lx_{max}, and $E_{transient}\hat{\boldsymbol{y}}$ = 0 at X_{max}+Lx_{max}. The same method for closing the potentials has been developed and can easily be used at the tail of $\mathbf{E}_{\mathbf{transient}}$, should a tailward end of $\mathbf{E}_{\mathbf{transient}}$ be required.

Appendix 3B

Here we explain the relationships between the parameters in our $\mathbf{E_{transient}}$ model (both adjustable and constrained/measured) and the injection features. These relationships aid us in choosing parameter sets to best fit simulation to data. For example, the farther east a spacecraft is located from the flow channel (bound by Y_{min} and Y_{max}), the greater the energy dispersion in the electron injection signature. Therefore, the eastward boundary of the channel, defined by the adjustable parameter $Y_{min,}$ will play a large role in the degree of energy dispersion. Meanwhile, a spacecraft located within or westward of the channel helps constrain Y_{max}, the channel's westward boundary. An upper limit for Y_{max} can be set by a spacecraft west of the channel that does not observe an electron injection, though it may observe an ion injection. (Although outside the scope of this paper, the ion injections can easily be included in future studies.) A spacecraft west of the channel may actually observe a slight depletion in electron energy flux as the return flow forms, pulling particles tailward to a lower magnetic field so that they lose energy. This depletion can be fit in the simulation to aid in constraining Y_{max}.

Fitting the eflux observed by a spacecraft within the channel can also aid in constraining Y_{max}, as long as another spacecraft is east of the channel. Recall that for an electron in a westward pointing electric field, the farther eastward it drifts the more kinetic energy it gains as it moves down the electric potential. The opposite is true if the electron moves westward. Determining the maximum energy attainable from the transient field thus requires a spacecraft located west of it. A spacecraft observing a dispersionless injection (i.e., within the channel) would not see the maximum energy attainable from the entire $\mathbf{E_{channel}}$, but would instead observe the maximum energy attainable for particles drifting from Y_{max} to the spacecraft

location (such as THB in Case 2). Therefore, Y_{max} plays a key role in fitting the maximum energy attainable in the injection for both spacecraft (west and within the channel).

E_c, the peak magnitude of the sinusoidal electric field ($\mathbf{E_{channel}}$) bound by Y_{min} and Y_{max}, also plays a role in fitting the maximum energy attainable via the injection. In both cases presented, spacecraft are east of the channel, meaning that they will observe particles that have traversed the entire channel width. As mentioned above, the change in potential across the channel due to $\mathbf{E_{channel}}$ directly decides the maximum energy a particle traversing the channel can attain. Therefore, fitting the maximum energy reached in the injection signature aids in determining the value of E_c.

The vortex half width, L_{vortex}, is another adjustable parameter. In our case studies we show how the return flow can be responsible for the depletion in energy flux at certain energies just prior to and throughout a dispersed injection as well as following an injection. The width L_{vortex} determines the strength of $\mathbf{E_{return}}$, since $\mathbf{E_{return}}$ applied over L_{vortex} cancels out the change in potential across $\mathbf{E_{channel}}$. Thus a larger L_{vortex} results in a weaker $\mathbf{E_{return}}$, since the potential change is spread out over a larger distance. L_{vortex} mostly affects the size of the dip in the spectra prior to injection, so fitting the modeled dip to this observed feature aids in determining L_{vortex}.

The vortex L_{Xmin} and L_{Xmax} are fixed parameters determining the size of the transition region in which earthward flow goes to zero, thus they set how quickly $E_{transient}\,\hat{y}$ ramps down at the front (L_{Xmax}, on the earthward side) and the back (L_{Xmin}, on the tailward side). This value was set to +/-3R_E from X_{max} (a total of 6 R_E for $E_{transient}\,\hat{y}$ to decrease from full strength to zero) for Case 1, and +/-1.5R_E for Case 2. X_{min} and X_{max} therefore define the transition region in

which the transient electric fields in the y-direction decrease in magnitude while an electric field in the x-direction appears as the particles turn [anti]clockwise in the vortex.

The X_{min} parameter, which is the tailward extent of $\mathbf{E}_{\mathbf{transient}}$, is set to "infinity" in both our cases. However, this can be altered should future studies require more sophisticated modeling of a spatially constrained electric field of some length down the tail. The earthward extent, X_{max}, can either be set to geosynchronous altitude based on the fact that injections have been observed there (such as Case 1), or it can be constrained if a spacecraft is fortuitously located earthward of X_{max} (such as Case 2). It has negligible effect on those spacecraft located tailward of the transition region.

The $\mathbf{E}_{\mathbf{transient}}$ start time (t_0) and its velocity in the x-direction ($V_{transient}\,\hat{x}$) can be constrained from the spacecraft data. In the simplest case in which $\mathbf{E}_{\mathbf{transient}}$ is suddenly turned on (i.e. no growth or motion), $V_{transient}\,\hat{x}$ is not a factor and t_0 is simply found based on when the spacecraft observe the injection signature. $V_{transient}\hat{x}$ comes into play when a traveling electric field is desired and can more easily be constrained when the spacecraft are aligned in X_{GSM} down the tail to enable timing. The $\mathbf{E}_{\mathbf{transient}}$ lifetime at X_{max} is measured by how long the spacecraft observed elevated efluxes, and the $\mathbf{E}_{\mathbf{transient}}$ ramp-down is constrained by how long it takes for the spectra to return to the pre-injection level. In this paper the $\mathbf{E}_{\mathbf{transient}}$ lifetime at X_{max} corresponds to the length of time the electric field stays at full strength after reaching X_{max} (i.e., after $V_{transient}\,\hat{x}\rightarrow 0$), and was only included in Case 1. This lifetime, albeit a constrained parameter based on the duration of the elevated fluxes at various spacecraft, is not a main topic of interest since we do not attempt to explain the source of $\mathbf{E}_{\mathbf{transient}}$ other than to say it is enabled by transient reconnection in the midtail. Rather, our interest is in the physics of the particle injection and propagation, including spectral features such as: the dip in eflux near the beginning

of the injection; the max attainable energy; the dispersion in the energy spectrograms; and the depletion in eflux following injections.

CHAPTER 4

Simulation of energetic electron acceleration by the electromagnetic field of a transient, localized dipolarizing flux bundle

4.1 Introduction

In Chapter 3, we presented a simple electric field model and used it to simulate electron injections in order to demonstrate that the narrow, transient electric field observed with fast flows is capable of energizing and transporting electrons. Our localized potential electric field pulse differs from previous analytic models that are azimuthally wide and have both electric and magnetic fields linked via Faraday's Law. The electric fields in these models are entirely inductive; there is no potential component. Although our model could accurately simulate the observations, without a dipolarizing magnetic field component it does not accurately reflect the physics behind an earthward traveling dipolarizing flux bundle. Therefore, as the next step in understanding how particles are transported and energized, we add an earthward traveling electromagnetic field pulse to the model described in Chapter 3 to improve it as well as to determine what role the magnetic field plays as compared to the electric field in the transport and acceleration process.

After reconnection occurs, reconnected field lines are accelerated due to increased curvature force toward Earth. As this flux bundle travels earthward, its magnetic field is also slowly increasing in time, as *Runov et al.* [2011] found a maximum increase in the front magnitude to be ~17 nT as the front moved earthward from ~18 R_E to the ~10 R_E in 75 seconds, or 0.23 nT increase per second. (The point was to demonstrate that the earthward-traveling dipolarization front did not change much throughout its earthward passage.). An inductive

electric field via Faraday's Law is required for a consistent description of the slowly variable magnetic field. Earthward plasma acceleration at and immediately after the dipolarization front occurs from increased curvature force density: because of the increased pressure ahead of the front, there is a decrease in the tailward pressure gradient force ahead of the front while curvature force density increases behind the front due to the increase in the magnetic field magnitude [*Li et al.*, 2011]. While dipolarizing flux bundles (DFBs) are responsible for most flux transport, the magnitude of the flow is significant both before and after each DFB within a bursty bulk flow event [*Liu et al.*, 2014] and has considerable variability. Additionally, as the front moves earthward, plasma is diverted around the plasma bubble, forming vortices [*Keiling et al.*, 2009] and electric fields in the dusk-dawn direction.

Thus, the imbalance between the curvature force and the pressure gradient force results in earthward motion of the plasma, not just behind the front but also in front of it. This motion creates an electric field (**E**=-**V**x**B**). Not all of the flow is related to total flux transport, since some of the flux circulates within the vortices. Ergo, for the purposes of this chapter, we will refer to two components of the total electric field: the "potential electric field", which are the fields related to the vortex and represent no flux transport ($\nabla \times \mathbf{E} = 0$), and the "inductive electric field", which is the field related to flux transport and is related to the changing magnetic field at the equator by Faraday's Law $\left(\nabla \times \mathbf{E} = -\partial \boldsymbol{B}/_{dt}\right)$. In reality these fields cannot be separated observationally, but for modeling purposes the potential electric field allows us to model effects of the flow vortex.

As will be shown later in this chapter, in order to model a dipolarizing magnetic field that matches observations, it is only necessary to use a small inductive electric field (<1.5 mV/m). Thus, our initial, simple vortex flow structure used in Chapter 3 still dominates the particle

acceleration process—though we want to be clear that it is the curvature force of the earthward-traveling DFB that plays the dominant role in accelerating bulk plasma flow, the flow that creates the dawn-dusk electric fields. The vortex (and its potential electric field) is considered driven by one or multiple DFBs, each DFB associated with an inductive electric field pulse. Since the magnetic flux carried by the vortex (read: potential electric field structure) does not make it to the inner magnetosphere, the magnetic field increase associated with the vortex is not significant and therefore a potential flow (which does not change the magnetic field) is sufficient to describe it. This is of course a simplification, since the diverted flux tubes will actually have a slightly decreasing Bz as they are diverted tailward; however, we assume these affects are small since ultimately these flux tubes revert to their original locations.

This is *not* to say that there is no total flux transport. On the contrary, the dipolarizing magnetic field in our model (which has a magnitude matching observations) and its self-consistent electric field are representative of the flux transport, transporting ~0.8 MWb of flux (the typical dipolarizing flux bundle transports between 0.5-1.5 MWb of flux [*Liu et al.*, 2014]). The total electric field in our model is thus a combination of both the inductive and potential electric fields, where the potential electric field magnitude is superimposed on the inductive electric field such that the total electric field approximates the observed $-\mathbf{V}\times\mathbf{B}$, and such that the observed injection is adequately simulated.

Because previous studies have utilized an electromagnetic field pulse before (in which the magnetic and inductive electric fields are self-consistent via Faraday's Law), we adapt their tried-and-true pulse form to fit our purposes. These electromagnetic field pulse models used by *Li et al.* [1998; 2003], *Sarris et al.* [2002], and *Ganushkina et al.* [2013], for example, utilize an electric field of the form:

$$E_\varphi = -\hat{e}_\varphi E_0\left(1 + c_1 cos(\varphi - \varphi_0)\right)^P exp(-\xi^2) \quad (4.1)$$

Where $\xi = [r - r_i + v(r)(t - t_a)]/d$ sets the location of the pulse maximum, $v(r) = a + br$ is the pulse front velocity as a function of radial distance *r*, *d* sets the width of the pulse, $c_1(> 0)$ and *p*(>0) describe the local time dependence of the electric field amplitude (which is largest at φ_0), $t_a = (c_2/v_a)\left(1 - cos(\varphi - \varphi_0)\right)$ is the delay of the pulse from φ_0 to other local times, c_2 sets the magnitude of the delay, v_a is the constant, longitudinal speed of the pulse, and r_i is the pulse initial location which determines its arrival time. This pulse can therefore be described as a radially inward propagating Gaussian electric field pulse (described by $exp(-\xi^2)$) that spreads out azimuthally over time (described by $\left(1 + c_1 cos(\varphi - \varphi_0)\right)^P$), having a magnitude that scales with E_0 and points completely in the φ-direction (see Figure 4.1). The velocity function that decreases with *r* was first implemented by *Sarris et al.* [2002] to account for the braking front.

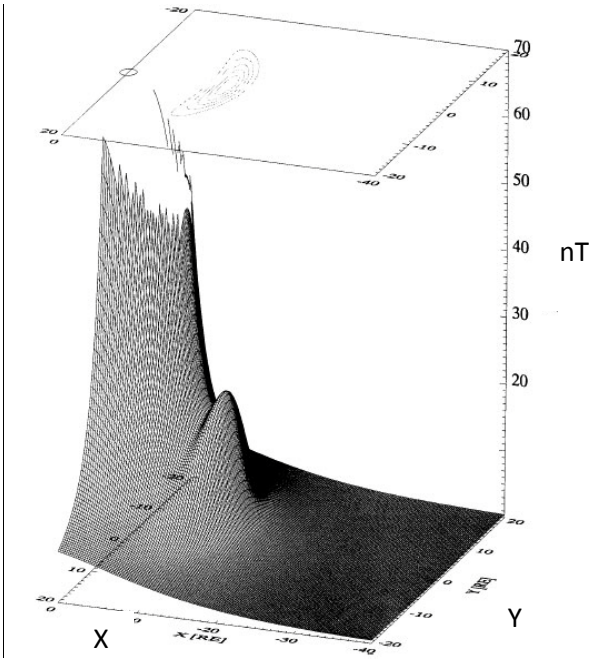

Figure 4.1. The modeled pulse magnetic field of *Sarris et al.* [2002] superimposed on top of the background magnetic field. This is the total magnetic field in the equatorial plane.

Ganushkina et al. [2005; 2013] found that using these equations with the parameters of *Sarris et al.* [2002] directly gives unrealistically high values for the maximum electric and magnetic field magnitudes at midnight (they found that the electric field reaches 60 mV/m and the magnetic field reaches 220 nT at 10 R_E), so they divided E_0 by the normalization coefficient $A_{E_{max}}$ = 1024, thus achieving more realistic values.

Each of these studies relied on the total fields to calculate the drift velocities, described in equations 3.1 and 3.2. None of the studies linked the speed of the front (v(r)) to the drift velocities; v(r) is simply described as a function of radial distance (r). This fact is illustrated in Figure 3.1 (which is Figure 4 from *Zaharia et al.* [2004] particularly their Type I and Type II cases), as well as in Figure 4.2 from *Sarris et al.* [2002], in which the particle trajectory changes as the pulse moves over it faster than the particle's $E \times B$ drift velocity. The azimuthal ∇B drift is initially duskward when the pulse first reaches the electron and the gradient is away from Earth, and then dawnward after the peak of the pulse has passed over the electron and the gradient is once again towards Earth.

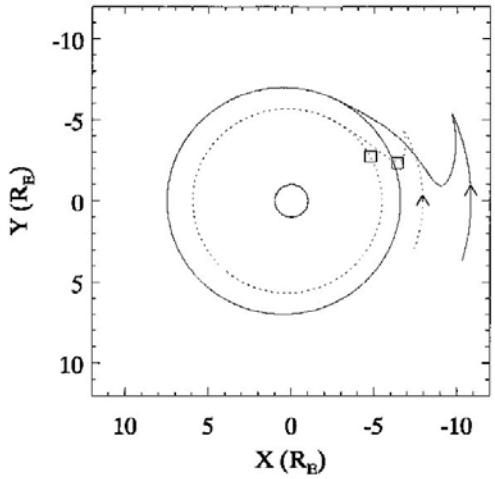

Figure 4.2. Figure 3 from *Sarris et al.* [2002]. Plots the trajectory of two 90° pitch angle electrons that are initially drifting dawnward under the influence of the nominal, background fields, then drift duskward when the pulse first reaches their locations, and finally drift dawnward again as they enter the tail-end of the pulse.

These models have done a reasonable job at simulating injections at geosynchronous orbit, and now that THEMIS provides data farther downtail we have the capability to expand on them by incorporating them into our paradigm of *narrow* earthward-traveling dipolarizing flux bundles with electric fields as the main driver of particle acceleration and transport in the magnetotail. In the following section we will describe how we merge our model of a potential electric field (from Chapter 3) with a narrow electromagnetic field pulse inspired by the pulse described in equation 4.1. Retaining the potential electric field in our model allows us to continue simulating effects of the vortical return flow, which was the first of its kind.

In section 4.3 we will utilize the Case 2 event from Chapter 3 to simulate the injections with our updated model, and will then analyze how the additional magnetic field and inductive electric field alters our results. We revisit Case 2 three times: first, we will utilize the same parameters as in Chapter 3, but now we include the dipolarization and inductive electric field (we call this "simulation 2"). Naturally, these parameters will no longer be the best in order to simulate the injections since we add new components to the previous model, but we do this step in order to see precisely how adding these new fields and removing the infinite length of the channel affects our particle trajectories. Second, we will alter the parameters to match our simulations to the data with the updated model ("simulation 3"). Finally, we rerun simulation 3 with all the same parameters after removing the inductive electric field and magnetic field in order to test whether the changes between simulations 1 and 3 are largely due to the new fields or to the change in the pulse's shape (i.e. spatially constraining the pulse in X_{GSM} instead of having a pulse of infinite length).

The motivation behind this work is to (1) comb out the various roles the electric and magnetic fields play in energizing and transporting electrons by comparing our new simulations

with those of Chapter 3, and (2) to demonstrate with a more realistic model that electrons are indeed accelerated and transported towards the inner magnetosphere via these transient, narrow structures.

4.2 The Transient Electromagnetic Field Model

As in Chapter 3, we rely upon an adapted numerical model [*Angelopoulos et al*., 2002] of particle guiding-center (G.C.) motion in prescribed electric fields in the magnetosphere in which particle motion is determined by integrating the relativistic equations of motion of the guiding-center in a dipole field and an instantaneous arbitrary global convection pattern. We again only investigate equatorially mirroring particles here, and direct the reader to section 3.2 for appropriate equations and descriptions of particle motion and phase space density calculations.

To describe the inductive electric field, we have modified equation 4.1 to a simpler form which travels in the x-direction (instead of along *r*) and has only a y-component (instead of φ-component) to match our potential electric field model described in Chapter 3:

$$\mathrm{E_{inductive}} = \mathrm{E_{ind}}\exp\{-[(\mathrm{Y}-\mathrm{Y_0})^2/\mathrm{W}^2]\}\sum_{i=1}^{8}\mathrm{Emax_i}\exp\{-[(\mathrm{X}-\mathrm{X0_i}-\mathrm{V_x t})/\mathrm{d_i}]^2\} \qquad (4.2)$$

Our pulse does not expand azimuthally, but instead is described by a Gaussian function across a width (W) in $\mathrm{Y_{GSM}}$ via the term $\exp\{-[(\mathrm{Y}-\mathrm{Y_0})^2/\mathrm{W}^2]\}$ where $\mathrm{Y_0}$ is the pulse center. Similar to equation 4.1, we utilize a Gaussian form that describes both the length of the electric field (albeit along $\mathrm{X_{GSM}}$ instead of *r*) as well as the speed of the earthward-traveling front: $\exp\{-[(\mathrm{X}-\mathrm{X0_i}-\mathrm{V_x t})/\mathrm{d_i}]^2\}$. We have modified this term, however, by summing eight Gaussian functions that together create a more realistic electromagnetic field pulse that matches observations of a very steep dipolarization front followed by a gradual fall-off behind the front.

Previous studies utilizing equation 1 had pulses with a gradually increasing front, allowing for particles to ∇B drift towards the dusk as we saw in Figure 4.2. Each of the eight Gaussians were weighted by $Emax_i$ (which has no unit) and had different initial peak locations ($X0_i$) and widths (determined by d_i). The various coefficients are as follows: $Emax_1$=0.1, $Emax_2$=0.4, $Emax_3$=0.35, $Emax_4$=0.3, $Emax_5$=0.3, $Emax_6$=0.15, $Emax_7$=0.05, $Emax_8$=0.05, $X0_1$=-22.0 R_E, $X0_2$=-22.1 R_E, $X0_3$=-22.5 R_E, $X0_4$=-23.0 R_E, $X0_5$=-24.0 R_E, $X0_6$=-26.0, $X0_7$=-29.0, $X0_8$=-32.0 R_E (converted to kilometers in the calculation), d_1=0.157$\sqrt{2}$ R_E, d_2=0.314$\sqrt{2}$ R_E, d_3=0.5$\sqrt{2}$ R_E, d_4=0.75$\sqrt{2}$, d_5=$\sqrt{2}$ R_E, d_6=1.75$\sqrt{2}$, d_7=2$\sqrt{2}$, d_8=2.5$\sqrt{2}$ R_E (converted to kilometers in the calculation). E_{ind} is a term in mV/m that determines the magnitude of the electric field. The term *t* is in seconds after the pulse is turned on. The terms X and Y are input in kilometers. Figure 4.3 demonstrates the magnitude of the inductive electric field along X_{GSM}.

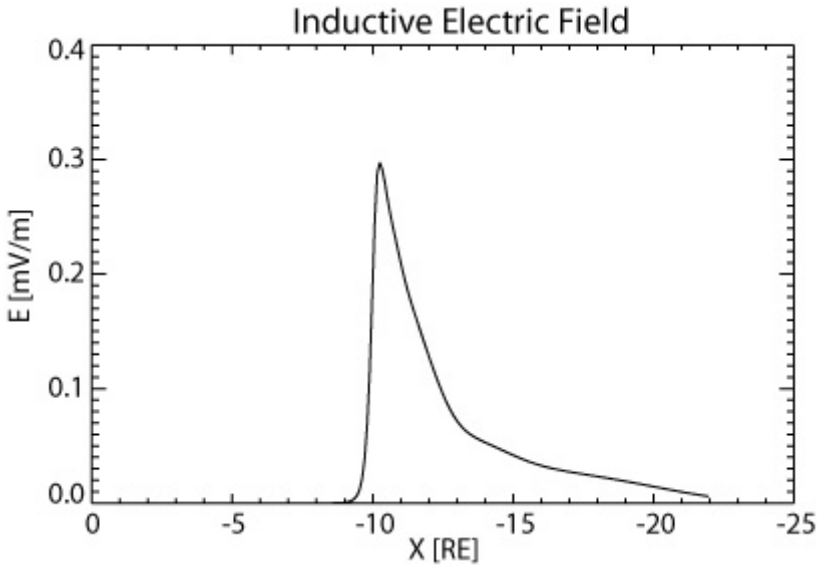

Figure 4.3. Our inductive electric field is described by the summation of eight Gaussian functions. Its shape was modeled after observations which often see a sharp peak in the electric field right after the front followed by a gradual fall-off. (Note that we cannot differentiate if an electric field is “inductive” or “potential” in the observations. So we made an assumption that our inductive electric field would follow this shape, which also allows us to model the magnetic field through Faraday’s Law to match magnetic field observations.)

In prior models [e.g., *Sarris et al.*, 2002; *Li et al.*, 2003; *Ganushkina et al.*, 2013], the pulse's earthward velocity was described as a linear drop-off along r to mimic the pulse's deceleration in the near-Earth region: $v(r) = a + br$. This may have worked in the regime of interest (approximately 10 R_E to geosynchronous altitude), but for our purposes we needed to develop a velocity profile that would be appropriate from -22 R_E to within geosynchronous orbit. Previous studies [*Ohtani et al.*, 2004; *Liu et al.*, 2014] have demonstrated that inward propagating bursty bulk flows have a fairly constant velocity until they reach the inner magnetosphere where they suddenly brake. To model this, we use a velocity profile illustrated in Figure 4.4 and defined as:

$$Vx = \frac{Vc}{-(x_{RE}{}^2)} + Vp \tag{4.3}$$

where V_C and V_P set the magnitude of the velocity in km/s as well as where the fast braking occurs, and Vx=0 where $x \leq \sqrt{\frac{Vc}{Vp}}$ (in other words, no negative velocities after Vx goes to zero).

As with the previously developed model described in the introduction, our model is not fully self-consistent because we do not link the front velocity within the given magnetic field to the electric field magnitude. In other words, the front velocity is not $\mathbf{E} \times \mathbf{B}/\mathrm{B}^2$; however, in simulation 3, we do use the relationship as a guideline in setting our potential electric field magnitude and velocity parameters. (We also note that electromagnetic signals may propagate in fast mode ahead of the flow.) Instead, the potential electric field (E_{pot}) falls off at the same rate as the velocity:

$$E_{pot} = E_{pot_0} \frac{Vx(x_{max}(t))}{Vx(X0_1)} \tag{4.4}$$

where E_{pot} in equation 4.4 is the same as E_C presented in Chapter 3. This is a simplification, but in the future it would be easy to alter E_{pot} to reflect the fact that it would maintain its strength

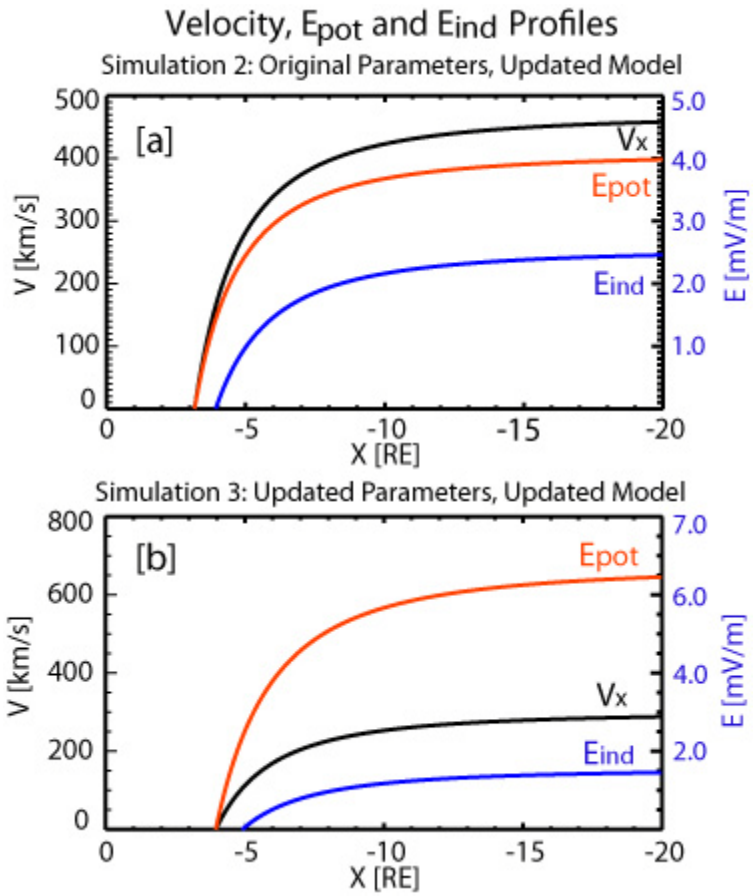

Figure 4.4. Velocity profile (black), E_{pot} profile (orange), and E_{ind} profile (blue) plotted versus X_{GSM}. (a) This velocity profile was chosen to match the constant velocity used in Chapter 3 (simulation 1) of 425 km/s. The E_{ind} profile was chosen to fit the magnetic field observations from $\int \nabla \times E \, dt$. The E_{pot} profile was chosen so that summing $E_{potential}$ with $E_{inductive}$ would match the total electric field used in simulation 1 (5.5 mV/m) as closely as possible. (b) This profile was used in our case study to fit our simulations from the updated model to the data (simulation 3). The profiles may be altered for other cases to reflect faster flow bursts, or flow bursts that brake at larger distances along X.

since, although the velocity decreases, the magnetic field increases as the pulse moves closer to Earth. We have changed the name to reflect that E_{pot} determines the magnitude of the potential electric field, not the entire electric field within the flow channel (which was the case previously). The inductive electric field (E_{ind}) falls off at a slightly faster rate:

$$E_{ind} = E_{ind_0} \frac{\frac{Vc}{-(0.65x_{max}{}^2)} + Vp}{\frac{Vc}{-(X0_1{}^2)} + Vp} \tag{4.5}$$

where X_{max} is the location of the first Gaussian's peak electric field, making E_{ind} a function of time (not location) as the pulse travels earthward (Figure 4.4). As we will describe later, this X_{max} is the same X_{max} that we use to describe the potential electric field's earthward extent along X. The reasons we set E_{ind} to fall off faster than the velocity are (1) so that we can create a "remnant" Bz signature that physically corresponds to more dipolarized field lines following the front (i.e., flux pileup) and (2) to prevent the dipolarizing magnetic field from increasing to unrealistic values. As the pulse slows down, it takes longer to pass over an observation point, spending more time at that location. Because the magnetic field is calculated as an integration of the curl of the inductive electric field over time, the magnetic field will increase dramatically as the pulse decelerates and spends more time at a given location. Setting the inductive electric field to decrease at a faster rate than the rate of velocity decrease mitigates the problem and results in a realistic signature without imposing a large normalization factor as in *Ganushkina et al.* [2005; 2013]. The magnetic field is calculated from the inductive electric field using Faraday's Law:

$$\delta Bz(x,y,t) = -\int_0^t \nabla \times E_{inductive}(x,y,t)\, dt \qquad (4.6)$$

where

$$\nabla \times E_{inductive}(x,y,t) = 2E_{ind}\exp\{-[(Y-Y_0)^2/W^2]\} \times$$

$$\sum_{i=1}^{8} Emax_i \exp\{-[(X - X0_i - V_x t)/d_i]^2\}\,[(X - X0_i - V_x t)/d_i]\left[\left(1 - 2V_c t/X^3\right)/d_i\right] \qquad (4.7)$$

The mathematical reason we obtain a remnant Bz behind the pulse when we impose a decreasing $E_{inductive}$ is explained when we consider equation 4.7. If the pulse were traveling at a constant speed with a constant electric field magnitude, the curl of $E_{inductive}$ would be equal and opposite on either side of the pulse peak. In other words, the integrated effect is a magnetic field that rises with the rising $E_{inductive}$ and goes back to zero as $E_{inductive}$ returns to zero. If $E_{inductive}$ is

decreasing, however, then as the pulse passes over an observation point, the magnitude of the curl of $E_{inductive}$ will be less in the pulse's tail than it was at the front. Thus, instead of completely canceling out the magnetic field associated with the front of the pulse, a remnant magnetic field is left behind. In application, this represents the dipolarized flux tube after the dipolarization front has passed and contributes to flux pileup.

At this point, our pulse is essentially a modified version of the pulses used in previous studies, being composed of eight Gaussian functions instead of one, having a velocity profile that falls off with $1/x^2$ instead of with –x, and having a width that remains constant and is described by a Gaussian across Y_{GSM} instead of an azimuthally expanding width described by a cosine function. To incorporate the potential electric field (and thus, the return flow), our new equation for $E_{transient}$ becomes the sum of the two electric fields:

$$E_{transient} = E_{inductive} + E_{potential} \tag{4.8}$$

where $E_{potential}$ is described by the equation for $E_{transient}$ in Chapter 3 (3.12, 3A.1-3A.8), and $E_{transient}$ in equation 4.8 is now redefined as the sum of the two electric field terms (Figures 4.5a-c and 4.6a-c).

Linking the two terms in time and space required connecting X_{max} and X_{min} (which define the earthward and tailward extent of $E_{potential}$) with $E_{inductive}$ as it travels earthward. We did this by putting X_{max} where the first Gaussian pulse peaks (initially at $X0_1$) and X_{min} where the last Gauusian pulse peaks (initially at $X0_6$). The Lx_{max} and Lx_{min} terms, which determine how quickly $E_{potential}$ falls off at the front (X_{max}) and at the tail of the pulse (X_{min}), respectively, were originally kept constant as described in Chapter 3. Because the length of the pulse along X_{GSM} shortens as the pulse moves earthward as a result of the x-dependent velocity profile, it is not

appropriate to set Lx_{max} and Lx_{min} as constants. Therefore, we allow the two terms to shrink as the pulse shrinks by defining them as follows:

$$Lx_{max} = Lx_{min} = (X_{max} - X_{min})/10 \quad (4.9)$$

Thus, as the distance between X_{max} and X_{min} decreases, so do the values Lx_{max} and Lx_{min}.

The updated model therefore has a new parameter set which merges the parameters from Table 3.1 with the new parameters introduced in this section. These parameters are described in Table 4.1.

Table 4.1. Model Parameters

Parameter	Type	Description
E_{ind0}	Adjustable	Sets magnitude of inductive electric field
E_{pot0}	Adjustable	Sets magnitude of potential electric field
Y_{min}	Adjustable	Minimum extent in Y of Etransient
Y_{max}	Adjustable	Maximum extent in Y of Etransient
L_{vortex}	Adjustable	Distance from Etransient center to apply opposing **E**
t_0	Measured/Constrained	Etransient start time
V_C	Constrained	Sets velocity magnitude and brake location
V_P	Constrained	Sets velocity magnitude and brake location
E_{DD}	Measured/Modeled	Magnitude of dawn-dusk electric field
X_{min}	Fixed	Tailward extent of Etransient
X_{max}	Fixed	Earthward extent of Etransient
Lx_{min}	Fixed	Distance it takes for vortex to turn on tailward side
Lx_{max}	Fixed	Distance it takes for vortex to turn on earthward side

Figures 4.5 and 4.6 illustrate the electromagnetic field pulse by plotting the Y-component of the fields in the equatorial plane. The slightly negative region in 4.5a—4.5c and 4.6a—4.6c represents the portion of $E_{transient}$-$\hat{y}$ that points in the dusk-to-dawn direction as defined by L_{vortex}, the region affiliated with the return (tailward) flow at the flanks of the incoming dipolarizing flux bundle. The positive region in 4.5a—4.5c and 4.6a—4.6c corresponds to the dawn-to-dusk electric field, which is a sum of both potential and inductive electric fields. The parameters used in Figure 4.5 are the original parameters used to simulate the injections in Chapter 3, but with the

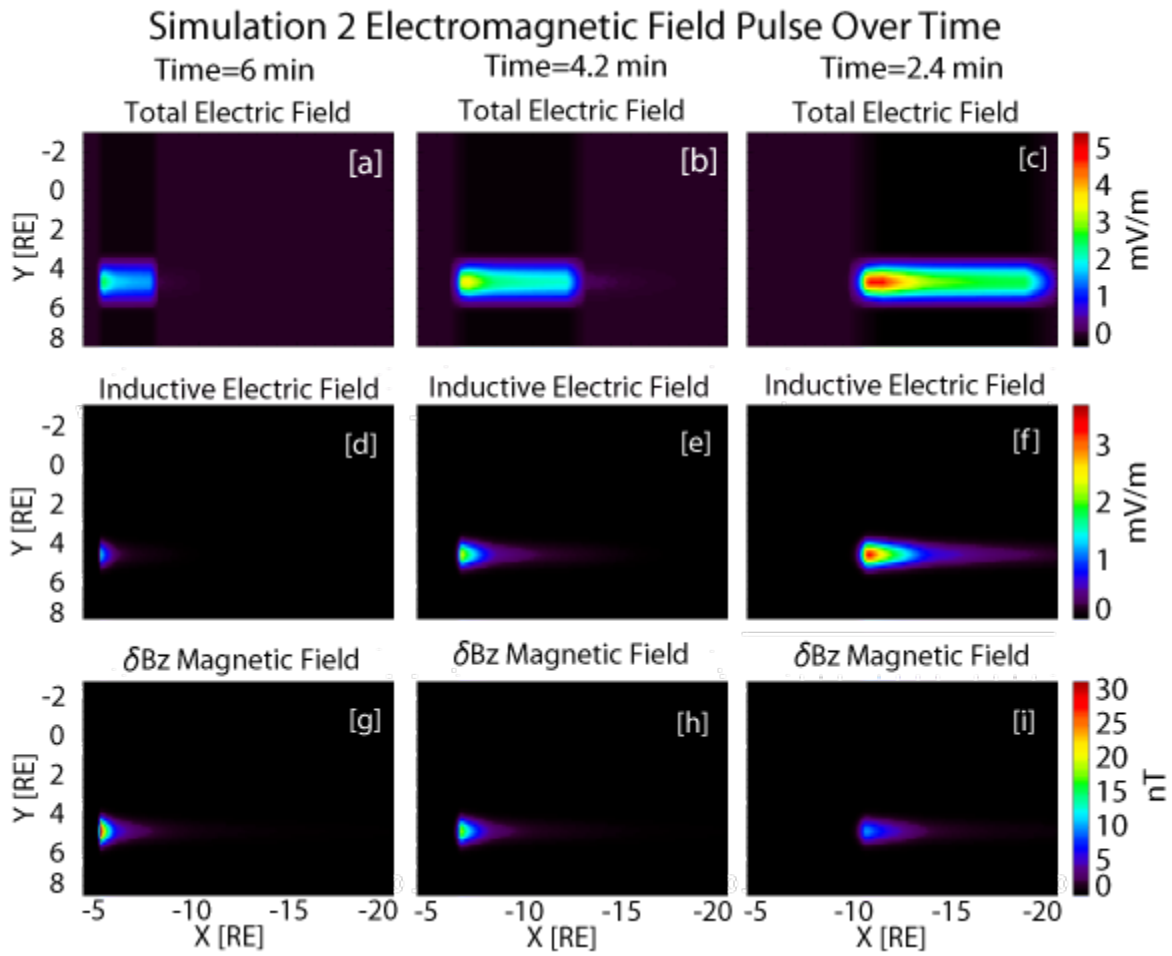

Figure 4.5. Simulation 2 pulse: created with the same parameters used in simulation 1 (from Chapter 3), but with the updated model that includes a dipolarizing magnetic field and inductive electric field. Read from right to left to view pulse's earthward motion. Three snapshots in time of the (a-c) total electric field, (d-f) inductive electric field, and (g-i) the change in magnetic field from the dipolarizing flux bundle plotted in X_{GSM} and Y_{GSM} at the equator. The snapshots in time are at 2.4 min, 4.2 min, and 6 min after the pulse turns on, ascending in time from right to left to aid the eye as the pulse travels earthward (from right to left). The color bar for the electric fields only plots the Y-component, thus the X-component at the front and tail from the return flow is not shown. The magnetic field reaches peak values in (g) where the pulse velocity has decreased substantially. Physically this represents the dipolarized magnetic field increasing over time. Since we calculate B from E in the model, a slower moving pulse means the electric field takes a longer time to pass over a specific location in space, resulting in a larger magnetic field since we integrate the curl of E over time. The different rows have different color scales to have the best resolution for determining values.

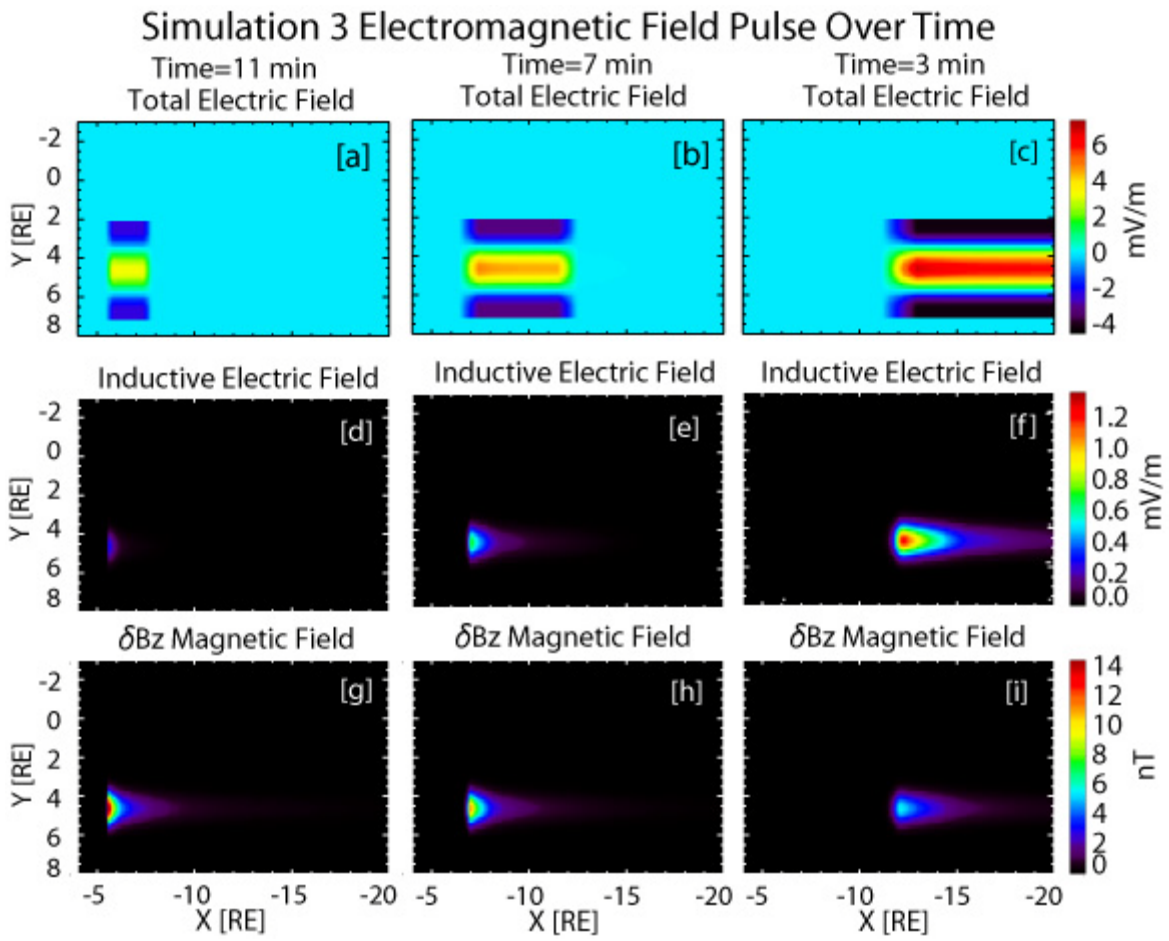

Figure 4.6. Simulation 3 pulse: created using parameters that gave us the best data-model comparison when we simulated the injections with the updated model. Read from right to left to view pulse's earthward motion Three snapshots in time of the (a-c) total electric field, (d-f) inductive electric field, and (g-i) the change in magnetic field from the dipolarizing flux bundle plotted in X_{GSM} and Y_{GSM} at the equator. The snapshots in time are at 3 min, 7 min, and 11 min after the pulse turns on, ascending in time from right to left to aid the eye as the pulse travels earthward (from right to left). The color bar for the electric fields only plots the Y-component, thus the X-component at the front and tail from the return flow is not shown. The magnetic field reaches peak values in (g) where the pulse velocity has decreased substantially. Physically this represents the dipolarized magnetic field increasing over time. Since we calculate B from E in the model, a slower moving pulse means the electric field takes a longer time to pass over a specific location in space, resulting in a larger magnetic field since we integrate the curl of E over time. The different rows have different color scales to have the best resolution for determining values.

updated model (simulation 2). The parameters used in Figure 4.6 were used to accurately simulate the injections with the updated model (simulation 3). Should another case be modeled that requires a larger magnetic field, we can easily alter the parameters to allow for that. We do note, however, that the values for the δBz in our case study reflect the values found statistically in *Liu et al.* [2013; 2014] as well as our statistics from Figures 2.3, 2.4, and 2.7 on the Bz/Bz_0 relationship.

4.3 Case Study: Simulating 04 Feb 2008 Injection

As we saw in Chapter 3, a simple model of localized, impulsive electric fields could accurately simulate injection observations. This fact suggests that the electric fields play a large role in the electron transport and acceleration process, but including the dipolarizing magnetic field that is also observed along with fast flows is necessary to complete the picture and to ascertain what role they may play in energizing electrons. In order to best understand what difference the magnetic field makes, we revisit the 04 February 2008 case study and simulate it with the updated model described in section 4.2. We utilize the same phase space density parameters as in Chapter 3.

We first ran the simulation with the updated model using the parameters applied in Chapter 3 that resulted in a good data-model comparison. These parameters can be found in Table 4.2 (simulation 2). The velocity profile (Figure 4.4a) was chosen to best match the constant, 425 km/s velocity that we gave $E_{transient}$ in simulation 1. The Y_{max}, Y_{min}, and L_{vor} parameters (which describe the location and width of $E_{transient}$ as well as the width of the return flow at its flanks) were kept the same. The point of this excersise is to see how the simulations are altered when the only change is the inclusion of the dipolarizing magnetic field. The total

electric field remains approximately the same. This is achieved by first choosing an inductive electric field profile (Figure 4.4a) that gives a magnetic field that matches observations, and then including a potential electric field such that their addition comes to the total electric field used in simulation 1 (5.5 mV/m). Since our electric field is decreasing in magnitude as the pulse moves earthward, the 5.5 mV/m was an estimate between the THD, THE, and THA locations in X_{GSM}. (Meaning, the total electric field was a bit higher than 5.5 mV/m at -11 R_E in X_{GSM} (THD) and a bit lower at -7.6 R_E in X_{GSM} (THA).)

To estimate an appropriate magnetic field, we used the observations by THB (Figure 4.7) as well as the median δBz values observed in the statistical studies of dipolarization fronts by *Liu et al.* [2013; 2014] (Figure 4.8). To separate the δBz observed at THB from the background magnetic field, we subtracted the Tysganenko 1996 (T96) model of the Earth's magnetic field [*Tsyganenko,*1995] from the observations (Figure 4.7c). This showed a δBz of about 7 nT. A superposed epoch analysis by *Liu et al.* [2014] of leading dipolarizing flux bundles shows the median δBz to be about 6-7 nT as well. This does not suggest that the peak δBz of the pulse is ~ 6-7 nT, since the spacecraft would have to be located at the center of the front to observe the peak; thus, the peak of the pulse may be higher than what is observed. Indeed, studies have reported dipolarization fronts on the order of 15-30 nT, e.g. *Runov et al.* [2011]. We use this fact as well in our pulse design by attempting to keep the peak around that level (Figures 4.5 and 4.6 panels g-i).

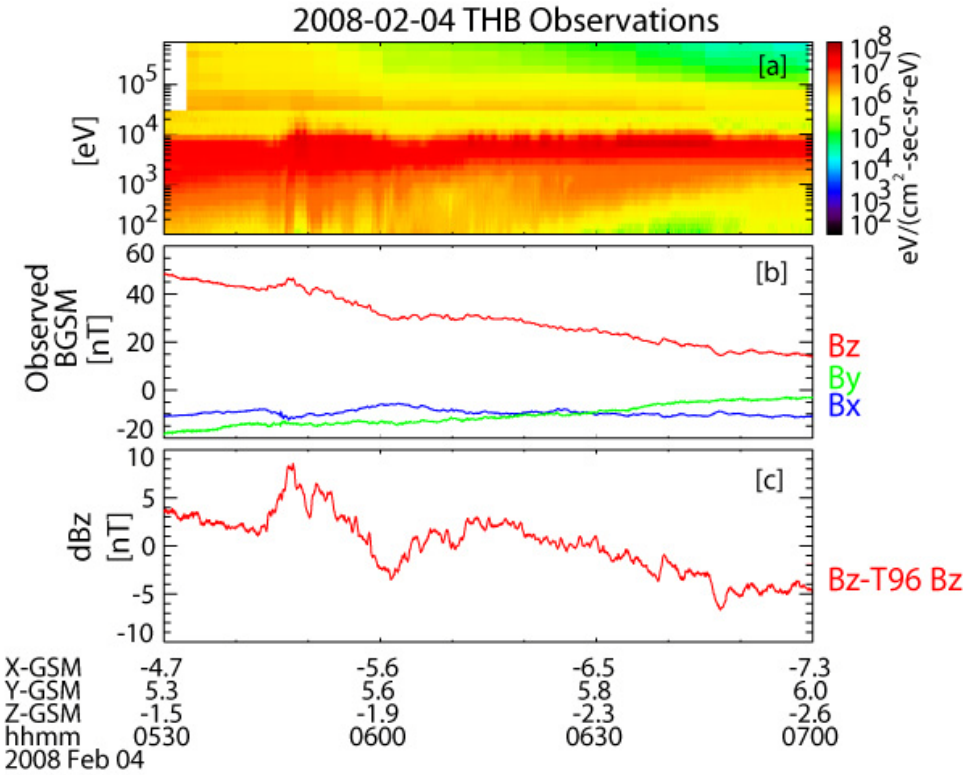

Figure 4.7. Observations made at THB. (a) Energy flux. (b) Magnetic field in GSM-coordinates. (c) The change in Bz calculated by subtracting the background field (T96) from the observations. The maximum increase in Bz reaches about 7 nT.

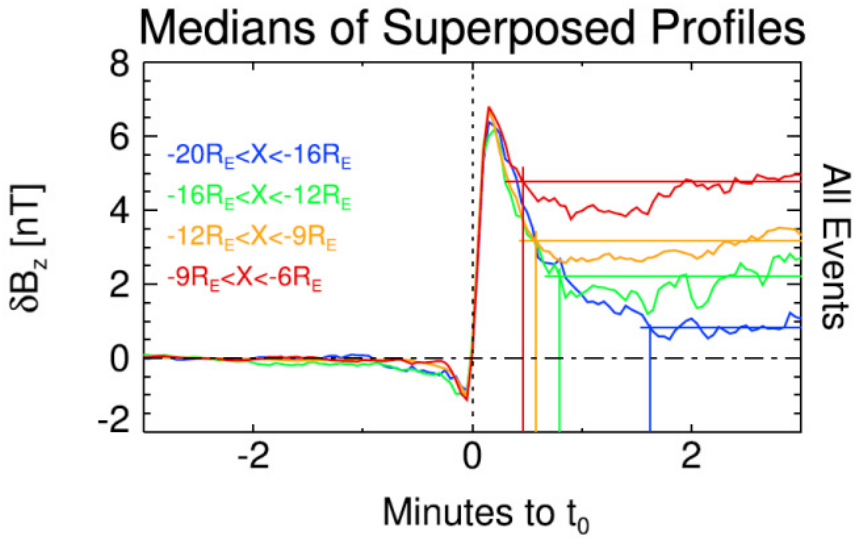

Figure 4.8. Detrended Bz, adapted from Figure 4 of *Liu et al.* [2014]. Demonstrates the median change in Bz observed at the dipolarization front. Different colored lines represent different distances from Earth, explained in the color-coded key. The closer to Earth that the dipolarization is observed, the larger the remnant Bz (flux pileup) is following the front.

Figure 4.9 shows the δBz that THB observed in simulation 2. The simulated δBz is on the order of what was observed, and the parameters used resulted in a pulse peak δBz that reflects past observartions. There are a few reasons why the simulated δBz peak is a couple nT less than what was observed at THB. The δBz peak could be increased by either (1) increasing the inductive electric field magnitude, (2) decreasing the velocity of the pulse (so that the electric field spends more time at a particular location, increasing the magnetic field), or (3) by shifting the pulse location so that THB is located more centrally within the pulse channel. In order to match the parameters used in simulation 1, the pulse velocity was set. Similarly, the location of the pulse channel is set to match the width and location of the pulse from simulation 1. Thus, the only parameter we can alter in order to change the peak δBz is the inductive electric field magnitude. Recall, however, that we wanted to maintain a total electric field that matched the parameters from simulation 1 (5.5 mV/m), meaning that the amount of electric field put into the inductive electric field component had to be taken out of the potential electric field component. To get a δBz of ~7 nT required that the entire electric field be composed of the inductive electric field (otherwise, the total electric field would exceed ~5.5 mV/m). This results in a very large peak δBz at the center of the pulse (>40 nT). Additionally, in order to keep a return flow in the simulation, we had to keep part of the potential electric field component. Therefore, we compromised by using a slightly smaller δBz.

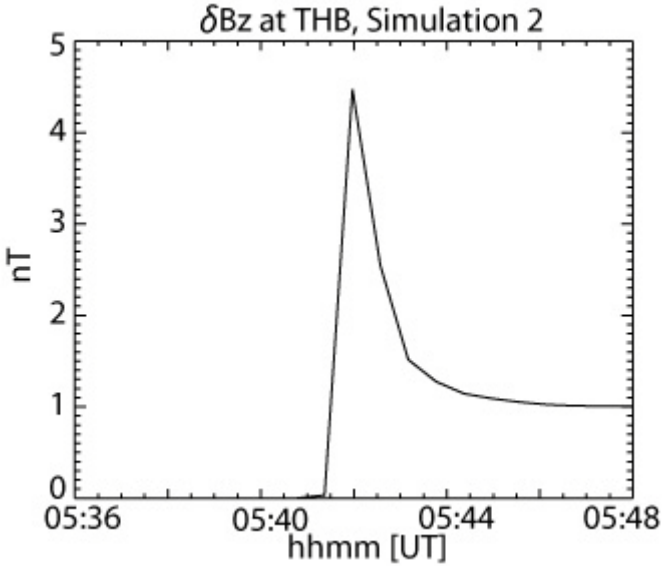

Figure 4.9. The δBz that THB observed in simulation 2.

We found that the parameters from simulation 1 no longer gave us a good data-model comparison when they were used in our updated model. Therefore, our second step was to supply new parameters to in order to find the best data-model comparison with the new model (see Table 4.2). We refer to these simulations as "simulation 3". We find that these simulations capture the best data-model comparison of all. As with simulation 1, we tried multiple parameter sets until a good fit between the obesrved and simulated energy flux was found. Since the fitting process focused on the energy flux, we did not set out to perfectly fit the observed δBz to the simulated δBz, but we did use the observations (Figure 4.8) and previous statistical studies (Figure 4.7) as guidelines. The δBz observed by THB in simulation 3 is plotted in Figure 4.10.

Table 4.2. Adjustable and Constrained Parameters for Simulations 2 and 3

Parameter	E_{ind0} [mV/m]	E_{pot0} [mV/m]	Y_{min} [R_E]	Y_{max} [R_E]	L_{vortex} [R_E]	t_0 [UT]	V_C [R_E^2]	V_P [km/s]	E_{DD} [mV/m]
Sim. 2	4.0	2.5	3.0	6.4	8.0	5:36	4700	470	2.4
Sim. 3	1.5	6.5	2.6	6.7	2.5	5:33	4700	300	2.4

Note that this figure is the modeled δBz observed by a specific spacecraft in a specific case. THB was located close to Earth where the DFB is braking, thus the increase in δBz is at a slower rate than what is typically observed farther downtail (e.g. by *Runov et al.* [2011]). Because the DFB is traveling much more slowly, it takes a longer time for the peak of the magnetic field in the pulse to pass over the spacecraft's location. We see this effect in the data in Figure 4.7, which is what Figure 4.10 is simulating: the magnetic field takes at least 2-3 minutes to rise. Also note that THB in this case was located at the duskward edge of the pulse, therefore it did not observe the peak increase in δBz that occurred dawnward of THB's location (see Figure 4.6, where the peak is ~15 nT).

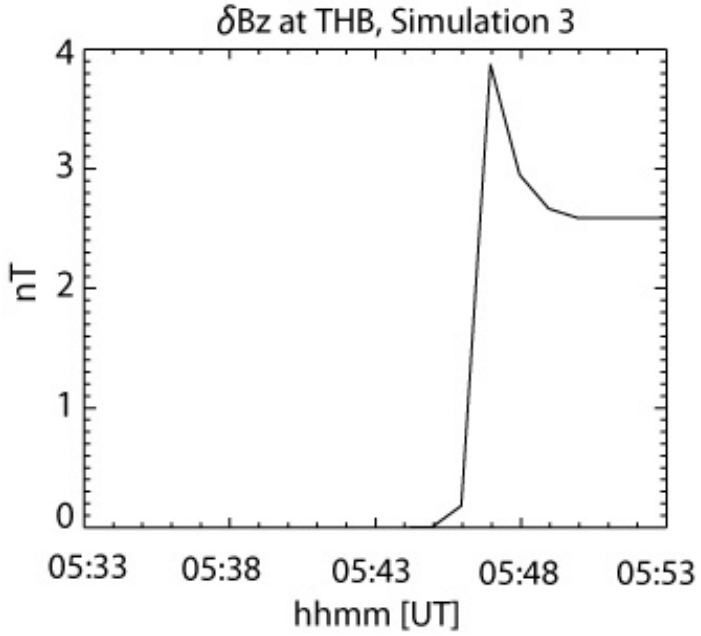

Figure 4.10. The δBz that THB observed in simulation 3. The constant δBz after the pulse of about 2.6 nT is representative of the flux pileup observed at THB, which was at the duskward edge of the pulse. The slow ramp up of δBz is consistent with observations (see Figure 4.7) and is due to the fact that THB is located near Earth where the DFB is slowing down. Its slower speed means the rate at which the front passes over the spacecraft will be much lower than the rate at which it passes over spacecraft farther down the tail (such as in *Runov et al.* [2011]), where the DFB speed is faster.

To visualize how the different models compare in simulating the observations, we include Figures 4.11-4.14. Each figure depicts the energy flux spectrograms for one of the four spacecraft that observed the event on 04 February 2008. Each figure displays the observations followed by the results from the three simulations. We include a line spectrogram of the data to compare with the line spectrogram of simulation 3 as we did for simulation 1 in Chapter 3. We must recall that the elevated energy flux in this case study lasts for a very long time. Looking at the data, we can decifer that the event may be composed of three or more individual injections. This is not uncommon, as was discussed in our statistical study in Chapter 2. As we mentioned in Chapter 3, we ramped $E_{transient}$ down over a period of 50 min to account for the multiple injections. Because our updated model is spatially confined along X, unlike the model in simulation 1 which extends infinitely downtail, we do not have the option to ramp it down slowly over time. Thus, instead of focusing on matching the duration of the multiple injection event, we focus on matching the initial injection signatures: its dispersion (or lack of dispersion), the timing between the four spacecraft that observed the injection, the energy channels that observe the injection signature, and the properties of the dispersed dip in energy flux that was observed at lower energy channels. In a future study, we may include multiple pulses to mimic the multiple injections, but at this time we choose to keep the study simple and simulate just the initial injection.

THB observed an inversely dispersed injection, a dipolarizing flux bundle, and associated electric field, meaning that it was within the flow channel. In Figure 4.11, we see that simulation 2 does not catch the injection, but only observes a slight depletion in eflux around 9-10 keV. Simulation 3, however, captures the entire injection very well, including such features as the dip at 8-9 keV just before the injection, the inverse dispersion, and the injection's duration. Utilizing

particle backtraced trajectories, we will explain the cause of the features in the following section. THE is the next spacecraft dawnward of THB and observes a dispersed injection. In Figure 4.12, we see that while simulation 2 does capture an injection, it does not simulate the observed dispersed depletion in eflux simultaneous to the injection. Simulation 3, however, does a fine job simulating the dispersed depletion even more accurately than simulation 1. THD is located 1 R_E dawnward of THE and also observes a dispersed injection with a simultaneous dispersed depletion, though the depletion at THD cuts off at higher energy channels than the depletion at THE (Figure 4.13). This depletion was captured in simulation 1, but the energy flux decreased to levels lower than observed by about an order of magnitude. Simulation 2 did not catch the depletion at all. Simulation 3, however, accurately portrays the energy channels that observe the depletion as well as the energy flux observed. THA, farthest to the dawn, also observed a dispersed injection and dispersed depletion at lower energies (Figure 4.14). In simulation 1, the very wide, long-lasting return flow resulted in a very deep depletion. Simulations 2 and 3 did not have this issue. We will discuss the reasons in the following section. The injection modeled in simulation 2 came much later in time, but in simulation 3 it was more punctual.

Thus far, we have described our updated model of the impulsive, localized electric and magnetic field pulse, demonstrated the new simulation results, and provided the parameters we used for the new simulations. In the following section, we will utilize particle backtracing to explain how the prominent injection features are formed.

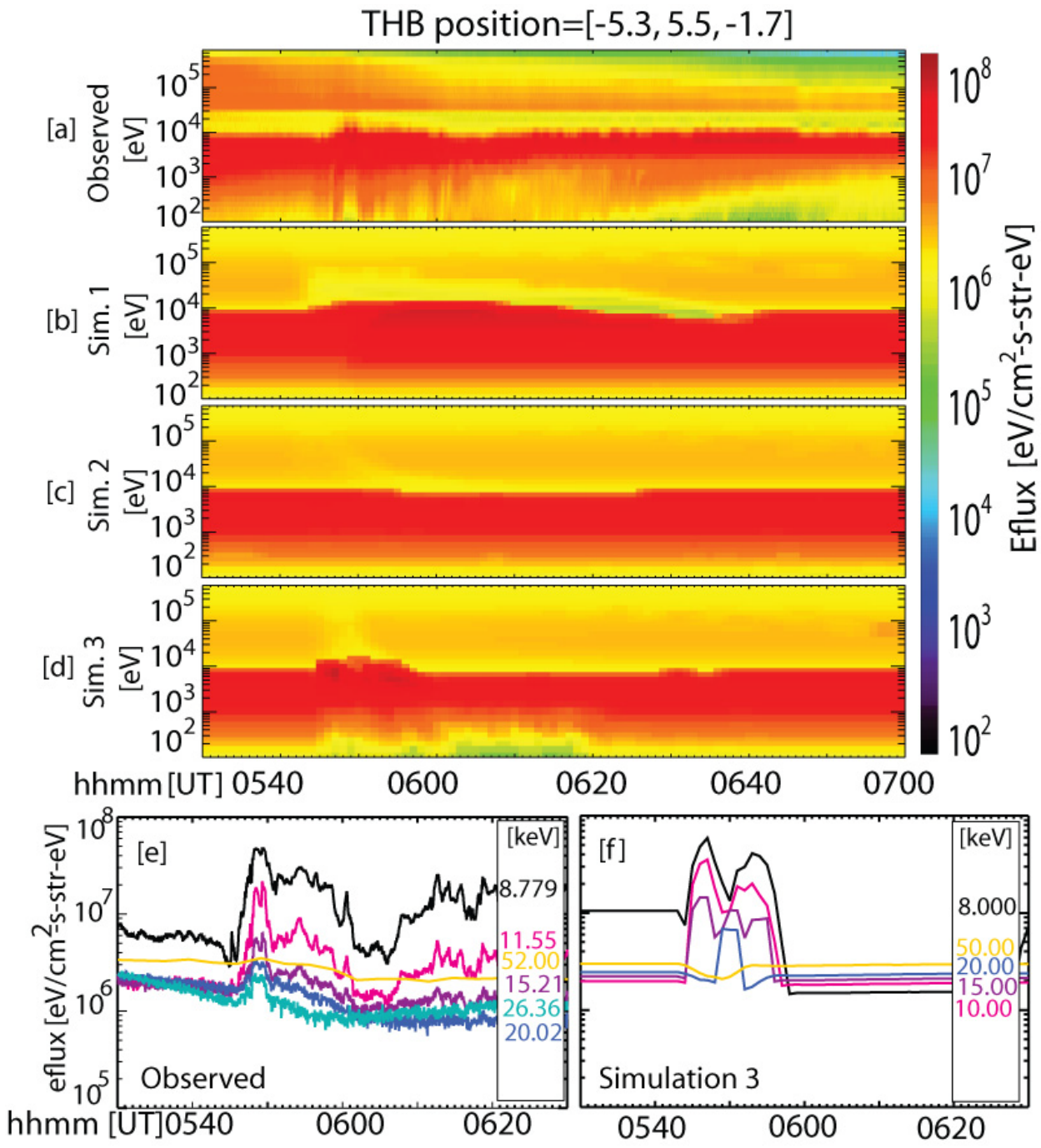

Figure 4.11. (a) THB observed a dispersionless (or more specifically, an inversely dispersed) injection around 05:45 UT. (b) The simulation 1 injection resulted from a localized, earthward traveling impulsive electric field. (c) Simulation 2 utilized the same parameters as simulation 1, but with an updated model that includes an earthward traveling electromagnetic field pulse along with the original potential electric fields. (d) Simulation 3 finds the best data-model comparison using the updated model and adjusted parameters.

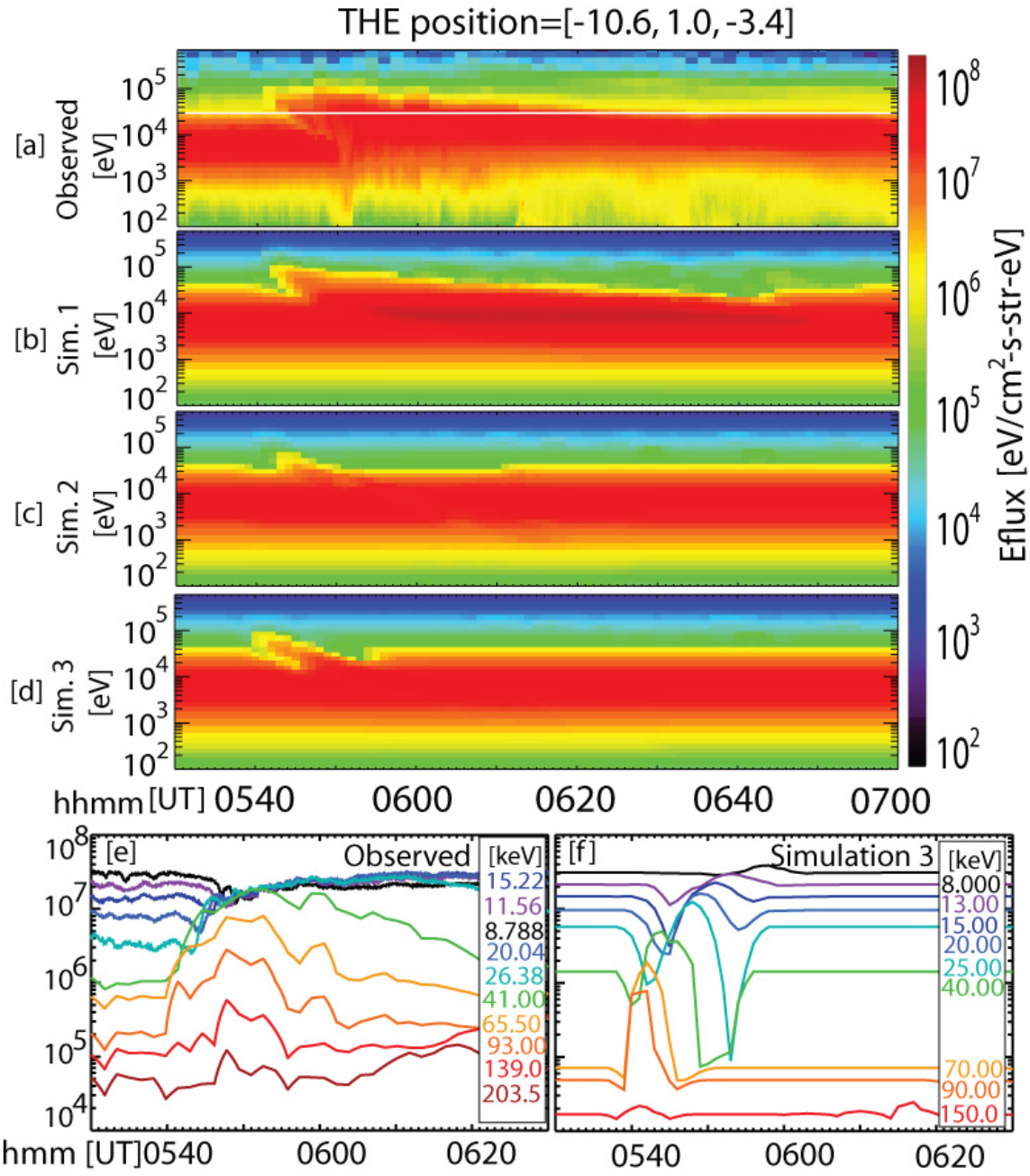

Figure 4.12. (a) THE observed a dispersed injection around 05:40 UT at energies from about 20-65 keV. It simultaneously observes a dispersed depletion in energy flux from about 10-26 keV. THE observed a second injection around 05:46 UT and a third around 05:57 UT. (b) The simulation 1 injection resulted from a localized, earthward traveling impulsive electric field which took 50 min to ramp down. This allowed the model to simulate the duration of the elevated energy flux which resulted from the three or more injections observed in the data. (c) Simulation 2 utilized the same parameters as simulation 1, but with an updated model that includes an earthward traveling electromagnetic field pulse along with the original potential electric fields. The pulse design does not include a slow ramp down. (d) Simulation 3 finds the best data-model comparison using the updated model and adjusted parameters. The pulse design does not include a slow ramp down, so simulation 3 only models the first injection observed.

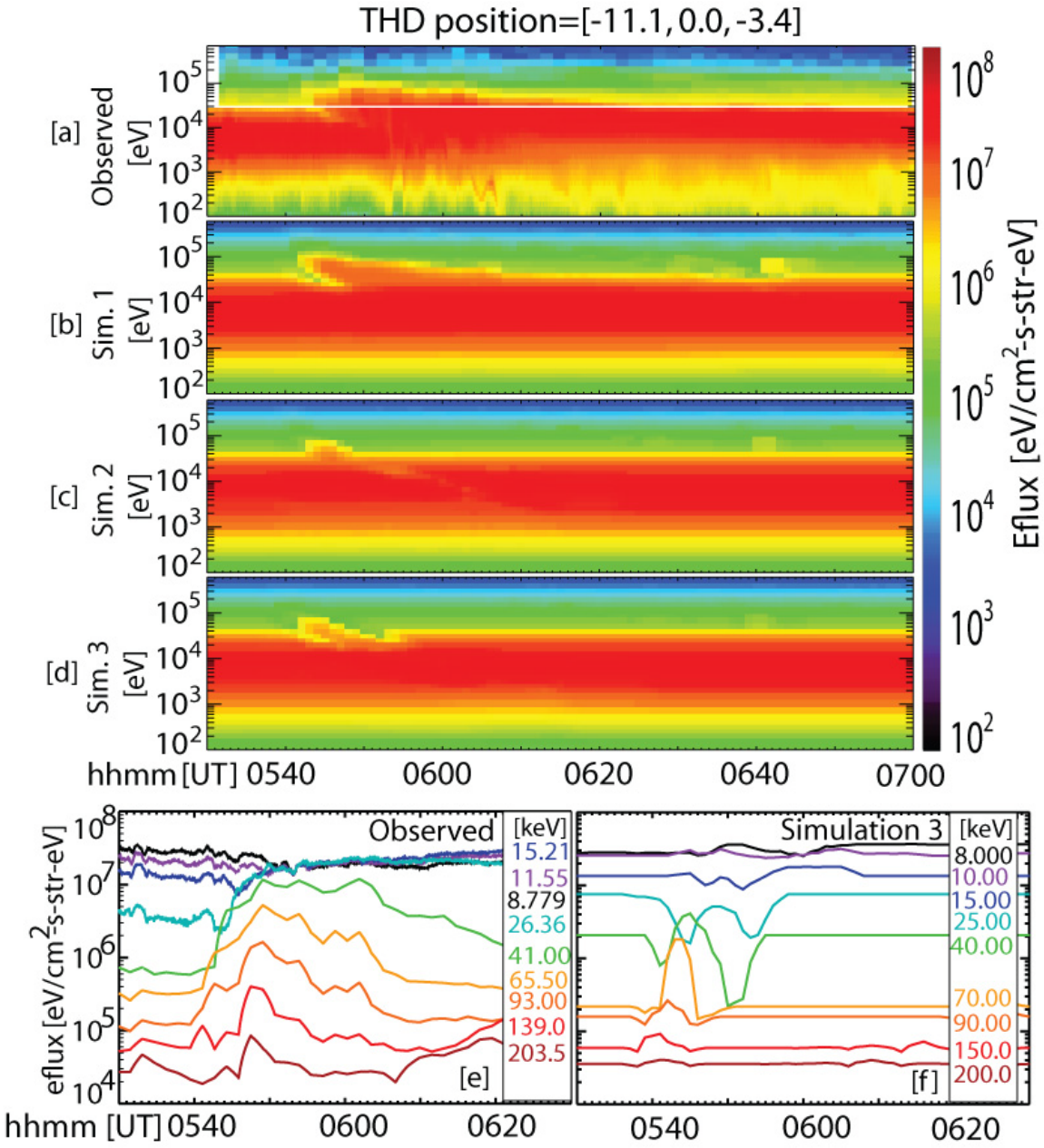

Figure 4.13. (a) THD observed a dispersed injection around 05:40 UT at energies from about 20-140 keV. It simultaneously observes a dispersed depletion in energy flux from about 15-30 keV. THD observed a second injection around 05:46 UT and a third around 05:58 UT. (b) The simulation 1 injection resulted from a localized, earthward traveling impulsive electric field which took 50 min to ramp down. This allowed the model to simulate the duration of the elevated energy flux which resulted from the three or more injections observed in the data. (c) Simulation 2 utilized the same parameters as simulation 1, but with an updated model that includes an earthward traveling electromagnetic field pulse along with the original potential electric fields. The pulse design does not include a slow ramp down. (d) Simulation 3 finds the best data-model comparison using the updated model and adjusted parameters. The pulse design does not include a slow ramp down, so simulation 3 only models the first injection observed.

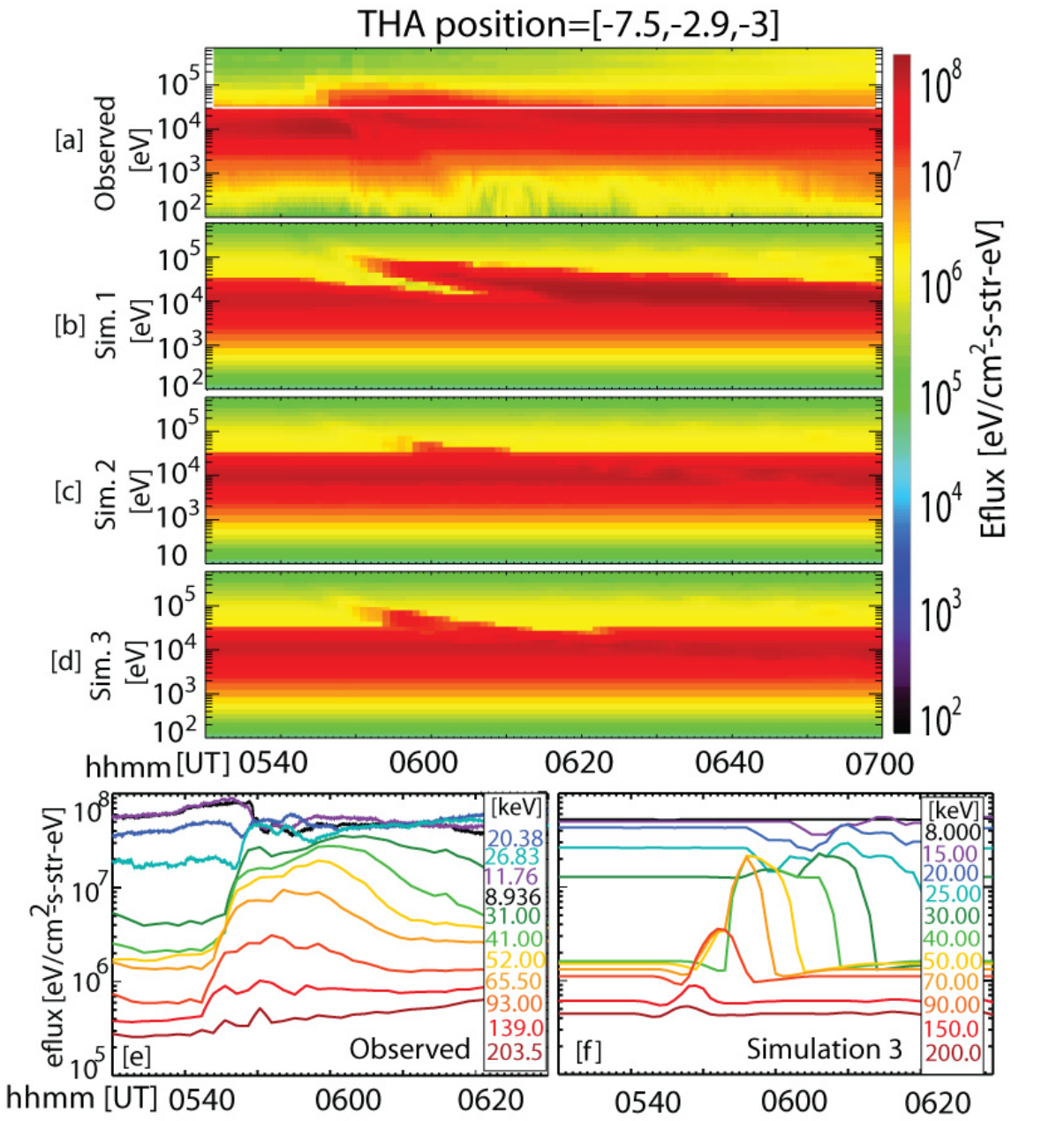

Figure 4.14. (a) THA observed a dispersed injection around 05:43 UT starting at 140 keV and going down to about 20 keV, the lower energies more visibly increasing in eflux around 05:45 UT. It simultaneously observes a dispersed depletion in energy flux from about 26 keV down to at least 5 keV. THD observed a second injection around 05:49 UT starting around 200 keV (b) The simulation 1 injection resulted from a localized, earthward traveling impulsive electric field which took 50 min to ramp down. This allowed the model to simulate the duration of the elevated energy flux which resulted from the multiple injections observed in the data. (c) Simulation 2 utilized the same parameters as simulation 1, but with an updated model that includes an earthward traveling electromagnetic field pulse along with the original potential electric fields. The pulse design does not include a slow ramp down. (d) Simulation 3 finds the best data-model comparison using the updated model and adjusted parameters. The pulse design does not include a slow ramp down, so simulation 3 only models the first injection observed.

4.4 Discussion

Now that we have demonstrated that our updated model is capable of simulating the observed injections, we can backtrace particles from the spacecraft location in order to determine their source location and how they gained (or lost) energy. As in Chapter 3, we use the guiding center equations of motion to trace 90° pitch angle electron trajectories under the magnetic and electric fields involved, including the pulse fields, the background dipole magnetic field, the background convection electric field (E_{DD}=0.24 mV/m from our Case 2 study), and the corotation electric field. We utilized this tool to discover, and now demonstrate, that although particle drifts are indeed affected by the new ∇B introduced by the pulse, the changes in the spectra between simulations are largely due to the pulse's new shape. The fact that the flow channel no longer continues infinitely tailward for about 50 min (simulation 1) has marked effects on our simulation results. As a reminder from Chapter 3 [*Northrop*, 1963],

$$\frac{dW}{dt} = q v_{drift} \cdot E(\boldsymbol{R}, t) + \mu \frac{\partial}{\partial t} B(\boldsymbol{R}, t) \tag{3.13}$$

where W= energy, q=electron charge, E=electric field, μ=1st adiabatic invarient ($W_{\perp}/B$), and B=magnetic field. Since we are only considering 90° pitch angle particles, dW/dt will be equivalent to μdB/dt, where dB/dt is the total change in the magnetic field throughout the trajectory due both to the temporally increasing dipolarization within the DFB pulse (term 2) and the changing magnetic field in the electron's frame of reference as the electron drifts into stronger (or weaker) magnetic fields (for 90° pitch angle electrons this energy gain is equivalent to that of the first term, which is the energy gain as the particle drifts across a potential drop).

*4.4.1 The Importance of -**V**×**B** and the Pulse Length*

The first marked difference between simulations is the injection modeled at THB by simulations 1 and 3, but missed by simulation 2. We drew particle trajectories in Chapter 3 (which used an infinitely long electric field pulse) that showed particles with very low μ can travel earthward along the duskward edge of the flow channel without appreciable dawnward drift, resulting in their observation at THB (which was located at the duskward edge of the channel). However, when we use the updated model presented in this chapter, using simulation 1 parameters (we call this simulation 2), the only particles that make it to THB's location are those swept out from lower L-shells (Figure 4.15).

This results not in an injection, but a depletion in energy flux. We can see in Figure 4.15 that the particles observed at energies 8 and 10 keV were originally on trapped orbits. After the pulse reaches THB's location (Figures 4.15(c-f)), we can see that these particle populations were first swept duskward by the vortex ($E_{potential}\,\hat{x}$), then as they drift closer to the pulse again the ∇B from the remnant dipolarization (flux pileup) bends their trajectories more tailward before they are observed by THB.

So although simulation 1 also had a depletion prior to the injection, there is a difference between the two models that results in simulation 2 never seeing the eflux increase after the decrease. This difference is the length of the pulse downtail. Traveling at ~425 km/s, the pulse front is traveling much faster than the **E**×**B** drift of particles in a ~5.5 mV/m electric field and the given magnetic field. Doing a quick calculation at R=15 R_E in a dipole field with a δBz of 6 nT and an electric field of 5.5 mV/m, the particle velocity would only be ~225 km/s. Thus, the importance of keeping an electric field in line with -**V**×**B** for the more realistic model is demonstrated. The reason this discrepancy did not appear in simulation 1 is because of $\mathbf{E}_{\mathbf{transient}}$'s

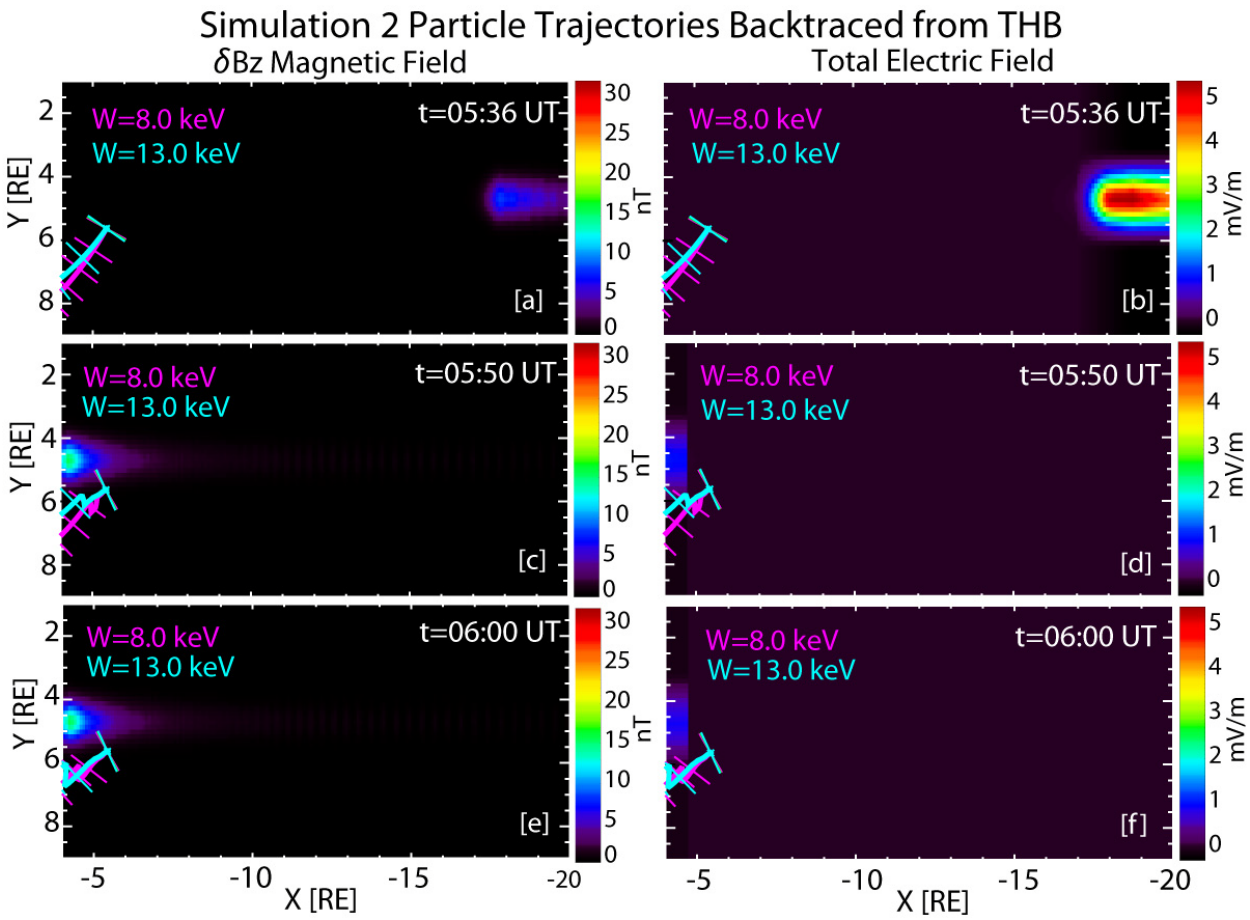

Figure 4.15. Particle trajectories backtraced in time from THB's location. The left column plots the trajectories on top of the pulse's magnetic field (δBz) while the right column plots the trajectories on top of the pulse's total electric field. The stated time is the time at which particles are observed and backtraced from. The pulse is also plotted at this time. The stated energies are the particle energies when they are observed by THB. In (a) and (b) the particle traces are unaffected by the pulse. In (c-f) the particles are swept out to higher L-shells, losing energy in the process. Tick marks are every 5 min.

infinite length along X_{GSM} and its long duration. Although the front traveled at almost twice the speed of the particles, the particles could still make it to THB at a later time. In simulation 2, the pulse is spatially constrained, so although it can still carry particles a good distance towards Earth, it will eventually leave the particles behind. We see this in Figures 4.16g and 4.16h, where each particle population is eventually left behind and begins to ∇B and curvature drift outside of the pulse's influence.

This sheds light on the other simulation 2 spectra. The commonality between the simulations for each spacecraft in simulation 2 is a small (or negligible) depletion in eflux and a weak injection signature (or in the case of THB, no injection signature). One reason for the missing depletion is that we turned down the potential electric field in order to add an inductive electric field such that their total (dawn-dusk component) was still ~5.5 mV/m. This also turns down the dusk-dawn component (E_{return}) of the potential electric field, which is behind the depletion in eflux (because it carries particles out to higher L-shells and lower magnetic fields). Another factor in the missing depletion is the short pulse duration. When the pulse existed for 50 min as it did in simulation 1, there was time for the slow-drifting, less energetic particles to drift across the entire E_{return} region dawnward of the flow, allowing for the greatest energy loss. In simulation 2, these slow-drifters hardly begin to drift across E_{return} before it has passed them by. In summary, when E_{return} is weaker and shorter in duration, as it is in simulation 2, it cannot affect the particle trajectories as much, meaning less depletion.

As for the weaker injection, we see from Figure 4.16 that particles cannot keep up with the fast, short pulse. Only a select few populations can originate downtail and be carried in past 10 R_E (pink trajectory in Figure 4.16), traveling as far as they do because they happened to be caught up in the center of the pulse where the electric field is strongest, so particle velocity is fastest. Those particles which enter the pulse on its flanks (the cyan and green trajectories in Figure 4.16) are in a weaker electric field, so they are left behind even earlier and do not make it in. The result is a weaker injection.

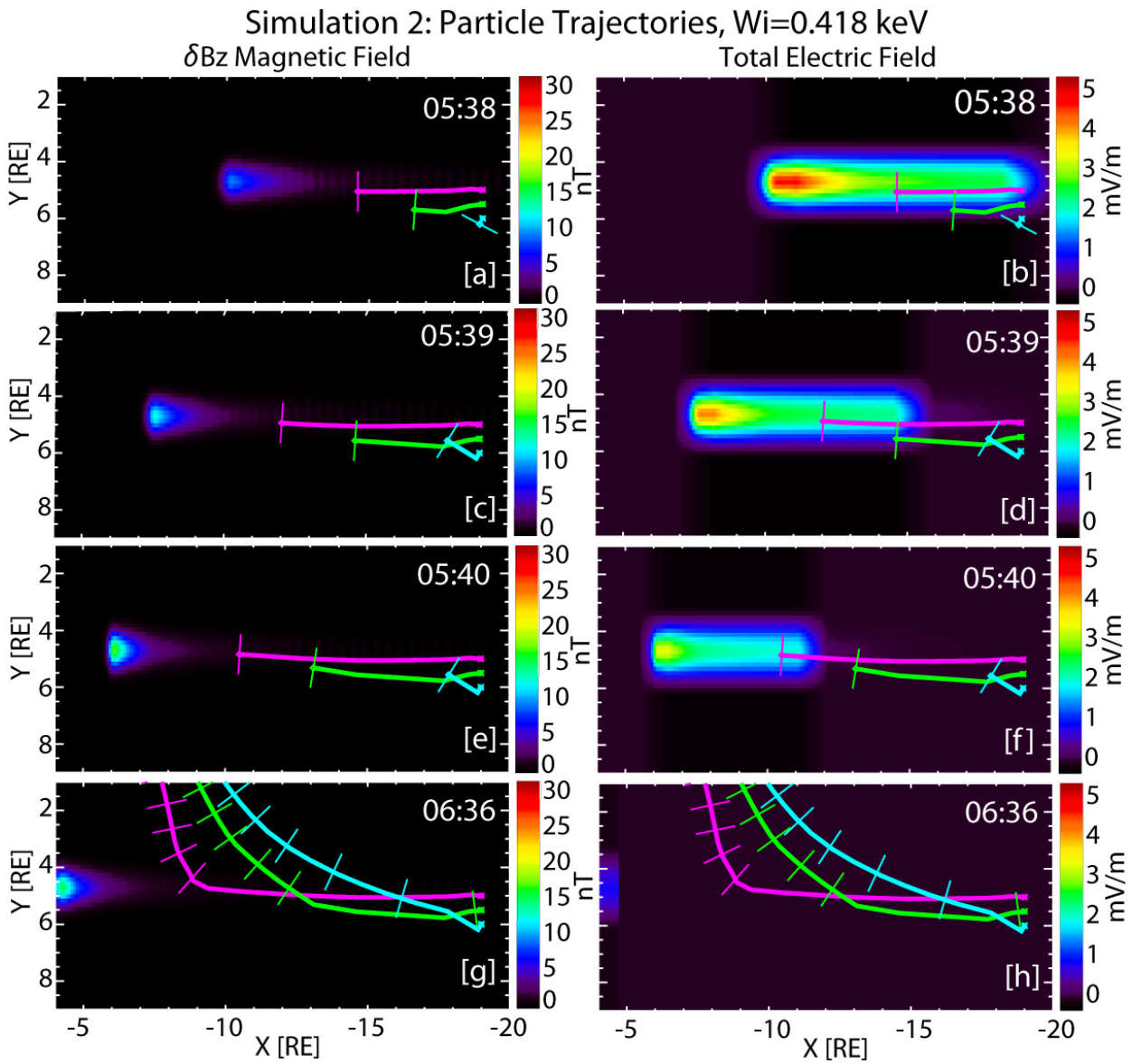

Figure 4.16. Particle trajectories traced forward in time. The initial energy for each population is 0.418 keV. The left column plots the trajectories on top of the pulse's magnetic field (δBz) while the right column plots the trajectories on top of the pulse's total electric field. The trajectories start when the pulse begins at 05:36 UT. In each panel, the particles are traced forward in time until the time stated in the panel. The pulse is also plotted at this time. The tick marks in (g) and (h) are every 5 min. Following the pulse and trajectories over time, we see that the particles could not keep up with the pulse speed.

Therefore, in order to simulate the injections with our updated model, we adjusted the parameters so that the electric field magnitude reflects the pulse velocity better, achieving a more physically appropriate representation of the earthward traveling DFB as well as better simulation

results. In addition to this, we adjusted the rest of the parameters (Table 4.2) to render the best data-model comparison we could find. Since that was achieved and presented in section 4.2, we now continue our analysis of the simulations using particle backtraces.

4.4.2 The Effect of a Shorter Pulse on the Depletion

As we discussed in section 4.4.1, simulation 2 shed light on the fact that a shorter pulse in time and space will result in less of an eflux depletion at energies lower than the injection. We will now explore that in simulation 3, using particle trajectories to demonstrate. In simulation 1, THA observed the longest, deepest depletion out of the four spacecraft (Figures 3.10, 4.17). Simulation 2 lacked a depletion, and simulation 3 has a very weak one. We can see from the particle trajectories in Figure 4.17 how the higher energies (30-50 keV) were carried in from downtail to higher L-shells, gaining energy via betatron acceleration and then drifting to THA, the spacecraft farthest from the pulse. The highest energy (150 keV) even had time to traverse over the entire pulse and be observed at 05:56 UT alongside the lower energies being injected. We can actually see with the 150 keV population how the particles are affected by the increased gradient in magnetic field from the pulse. These particles first traveled downtail and then turned earthward as they encircled the peak in δBz.

The lowest energies (10-20 keV and lower), however, drift too slowly to ever have encountered any of the pulse. These particles were not accelerated by the channel nor decelerated by the return flow. The pulse was simply too transient (moves by quickly) and too spatially limited for these slow drifters to have ever been near it. This is in contrast with simulation 1, which lasted for 50 min and allowed these slow drifters time to travel through the pulse and then

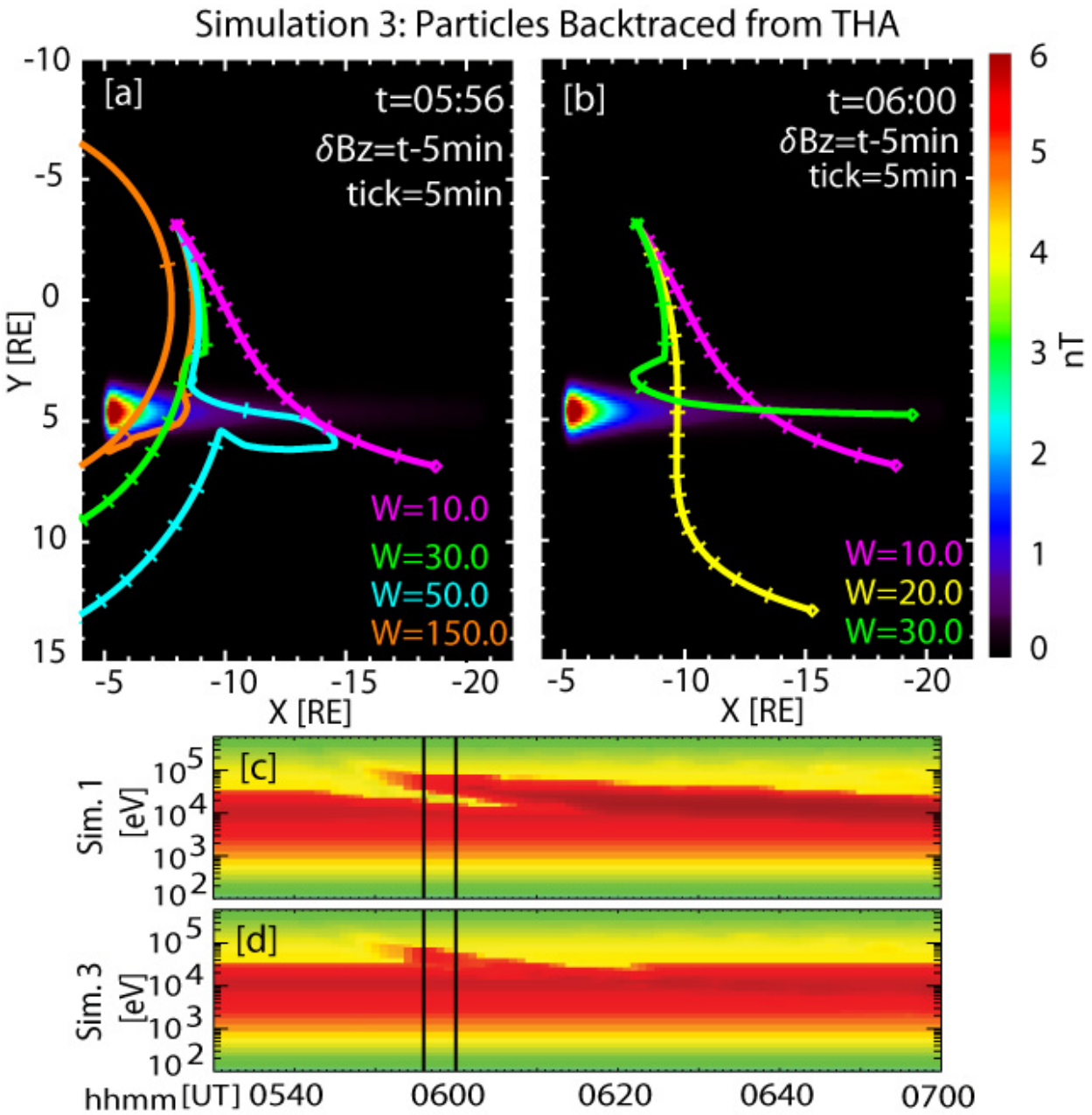

Figure 4.17. Particle trajectories backtraced in time from THA's location. (a) Plots the trajectories on top of the pulse's magnetic field (δBz) at 05:56 UT. (b) Plots the trajectories on top of the pulse's magnetic field (δBz) at 06:00. The stated time is the time at which particles are observed and backtraced from. The pulse is plotted 5 min earlier to better show what was affecting the particles. The stated energies are the particle energies when they are observed by THA. (c) Two vertical lines mark the times at which the backtraces were taken in (a) and (b). Tick marks are every 5 min. Although the 20 keV population saw a depletion in simulation 1, it does not in simulation 3 because it never encountered the pulse.

drift to THA's location. Therefore, our updated model, being more temporally and spatially constrained, results in more realistic levels of eflux depletion observed at injection.

Our updated model similarly produces better results for THE and THD as well. Comparing the three simulations (THE, THD, and THA), we see that another factor that decides which energy ranges will observe an eflux depletion is the spacecraft's location from the pulse. This effect was previously discussed when we mentioned that THA lacks a depletion because the lower energy particles do not drift fast enough to be affected by the pulse and to be observed by THA at the same time THA observes injection at higher energies. The spread between the populations has increased too much. It is further demonstrated by noting that THE, which is the closest to the pulse, observes a depletion to lower energy channels than THD. THD in turn is closer to the pulse than THA, thus it observes a depletion to lower energy channels than THA. Because THE is much closer to the pulse, those slow-drifters that lost energy (since they were only affected by the return flow) have time to make it to THE at the same time as the higher energies in the injection.

Figure 4.18 demonstrates this fact. In 4.18a and 4.18b, we see that the highest energies (40 and 70 keV) are being carried earthward by the pulse from the reconnection site. The less energetic particles (15 and 30 keV) drift more slowly, so to be observed simultaneously with the 40 keV and 70 keV populations, they must originate closer to THE. This means that they never encounter the dawn-dusk electric field in the pulse's center, but only the dusk-dawn electric field at the flanks. Thus, they are swept out and lose energy (akin to Figure 3.14 which explained this effect at THD in simulation 1). Note that because these less energetic populations had to originate close to THE, they would only encounter the return flow if THE was also close to the pulse. This is why THE observes a depletion while THA does not.

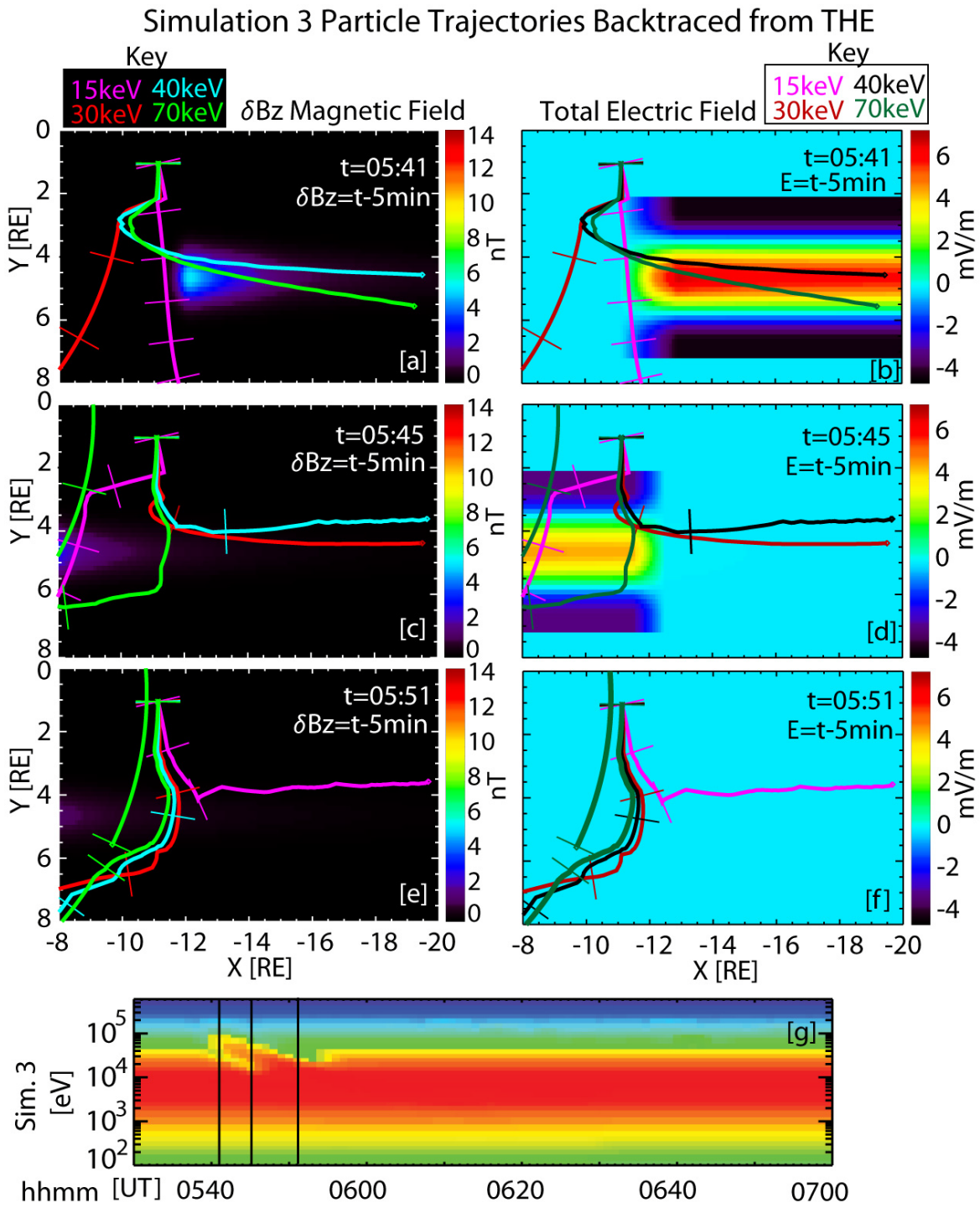

Figure 4.18. Particle trajectories backtraced in time from THE's location. The left column plots the trajectories on top of the pulse's magnetic field (δBz) while the right column plots the trajectories on top of the pulse's total electric field. The stated time is the time at which particles are observed and backtraced from. The pulse is plotted 5 min earlier to better show how it affects the trajectories. The stated energies are the particle energies when they are observed by THE. (g) Three vertical lines mark the times at which the backtraces were taken in panels a-f. Tick marks are every 5 min.

The magnitude of the dusk-dawn electric field will also result in a depletion at lower energies. In simulation 3, L_{vortex} is narrower (2.5 R_E) than in simulation 2 (8 R_E). Per our definition, E_{return} is stronger in simulation 3, affecting the Alfvén layers of a greater range in μ and resulting in more energy loss. This can be understood as faster tailward flows which can carry particles farther downtail to weaker magnetic fields, causing them to lose energy.

4.4.3 The Effect of the δBz on Particle Trajectories

Moving forward in time to 05:45 UT, we see in Figures 4.18c and 4.18d that the 30 and 40 keV populations originate far downtail. The 15 keV population, however, encountered more of the return flow and thus has a deeper depletion in eflux. The 70 keV population, on the other hand, drifting much faster, had time to arrive from the dusk side of the pulse at the same time as the less energetic particles that either came from downtail (30, 40 keV) or were swept out in the return flow (15 keV). We can see from Figure 4.18d that the 70 keV particles were swept out from the return flow on the duskward flank of the pulse, and after reaching the pulse's tail end encountered the remnant dipolarized Bz which accounts for flux pileup. When this happened, the particles ∇B drifted around the peak in δBz. This effect is even more pronounced in Figures 4.18e and 4.18f. At this snapshot in time, we see that the trajectories of the more energetic populations are largely affected by the additional gradient in the magnetic field from the remnant δBz (the flux pileup) after the electric field has already passed by. We see the effect in the 30-70 keV traces as the particles drift dawnward until they sense the additional ∇B, then turn tailward around X=-9.5 R_E until the flux pileup is not so great and the remnant δBz is less strong (X=-11.5 R_E). At this point, the particles sense a stronger gradient towards earth and again travel more in the dawnward direction until the gradient shifts towards the dusk and their trajectories

turn earthward (~X=-9.5 R_E). The result is that the particles partly encircle the peak in δBz until they drift far enough away that they do not sense it anymore. At this point (X~11 R_E, Y~3 R_E), they begin to ∇B and curvature drift under the effects of the dipole magnetic field alone. We can see from Figures 4.18e and 4.18f that the result of a remnant Bz (flux pileup) in the pre-midnight sector on electron trajectories is that electrons drift out to higher L-shells than where they were previously drifting, which results in eflux depletion following the injection. If the pulse were exactly at midnight, then the ∇B drift around the pulse would be symmetric, and the particles would find themselves back on the same drift orbits. Even so, this asymmetrical effect is quite small.

From Figure 4.18c, we can see from the 40 keV electron trajectory that if the electrons are slightly dawnward of the pulse front, the gradient in B (pointing in the Y direction) would cause the electrons to move earthward, contributing to the overall earthward transport. In fact, when the electrons are slightly ahead of the peak in the front, the gradient in B not only points in the Y direction but also has a component in the –X direction relative to the electrons' location. This means in addition to earthward motion, the electrons will undergo some duskward motion due to the pulse, which will aid in keeping them within the pulse for a longer time without ∇B drifting out (from the background magnetic field).

Although the noticeable effect of the δBz is minor, this is not to say that flux transport does not occur. When we calculate the amount of flux transported by the pulse,

$$\Phi_B = \iint_S \mathbf{B} \cdot d\mathbf{S} \tag{4.10}$$

we found $\Phi_B = 0.8$ MWb. *Liu et al.* [2014] found the typical dipolarizing flux bundle transports 0.5-1.5 MWb, meaning our simulated flux transport falls within the expected range.

4.4.4 A Dispersed Injection Summarized

To make our points from the previous sections clearer, we have created Figure 4.19 that shows particle trajectories ending at THE at 05:45 UT over time (based on Figures 4.18c and 4.18d) . Each panel is a snapshot in time that shows where the particles are at that time and the path that they have yet to follow in order to be observed at 05:45 UT by THE. One could think of each trajectory as an extended tape measure that is being rolled back to the final point (THE), such that the closer in time we approach 05:45, the less of the plotted trajectory is left to travel. We plot these trajectories on top of the δBz pulse (left column) and on top of the total electric field (right column) which are plotted at the stated time in eacn panel, in order to make clear why the particles are moving the way they are. The backtraces from 05:45 UT at THE demonstrate each type of trajectory: (1) The least energetic population (15 keV) drifts the slowest, and in order to be observed simultaneously as the more energetic populations at 05:45 UT must originate closer to THE. This means it never encounters the earthward flow, but is instead caught up in the tailward flow dawnward of the earthward flow channel and is carried out to higher L-shells. Since it loses energy in the process, it contributes to the depletion observed before and during the injection at higher energies. (2) The middle range energies (30 and 40 keV) are injected at 05:45 UT, having originated far downtail and gaining the maximum amount of energy. (3) The most energetic population (70 keV) drifts so fast that it actually contributes to the depletion following the injection, since it is carried out to higher L-shells and lower magnetic fields by the return flow on the duskward edge of the flow channel before it drifts around the δBz portion of the pulse.

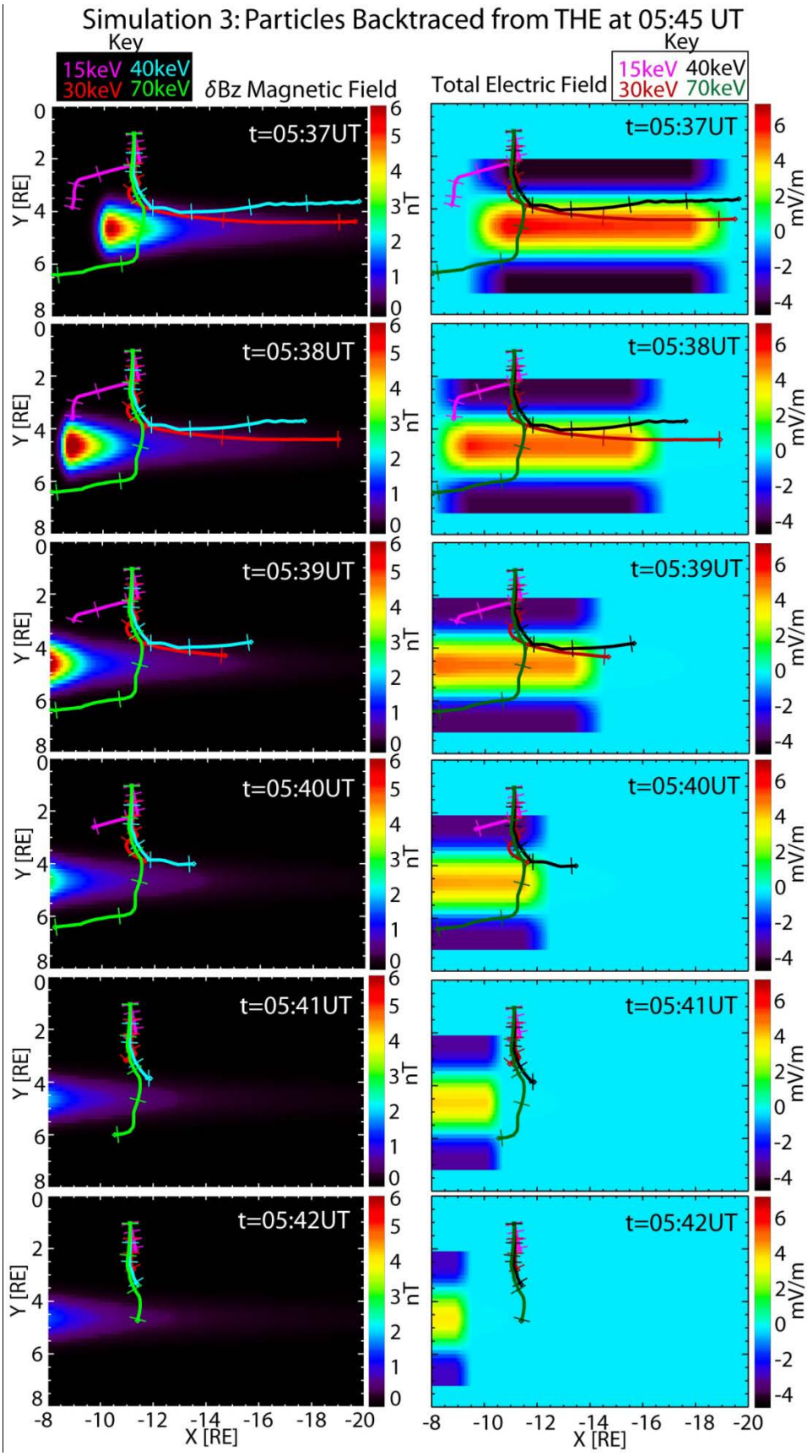

Figure 4.19. Particle trajectories backtraced in time from THE's location. The left column plots the trajectories on top of the pulse's magnetic field (δBz) while the right column plots the trajectories on top of the pulse's total electric field. The stated time is the time at which particles are observed and backtraced from. The pulse is also plotted at this time. The stated energies are the particle energies when they are observed by THE. Tick marks are every 1 min. Reading from top to bottom, the panels can be viewed as snapshots in time each minute as the pulse moves earthward and the particles drift towards THE.

4.4.5 The Injection at the Acceleration Site

Having analyzed the dispersed injections, we next look at the particle trajectories backtraced from THB for simulation 3 (Figure 4.20) in order to understand how the particles observed within the flow channel are energized and where they came from. We have plotted backtraces from three points in time, one when there was a slight dip in eflux just before the injection, one at the beginning of the injection, and another later in the injection. Similar to other cases of eflux depletion, Figures 4.18a and 4.18b depict particle populations which were drawn out from lower L-shells, losing energy by moving into a lower magnetic field (betatron "deceleration"). Although THB is within the flow channel, it observes these particles first because of the diverted flow (the vortex) at the head of the front and the strong tailward gradient in the magnetic field from the pulse.

At 05:46 UT, we see that the particles were swept up from their drift orbits by the pulse and injected. Because the pulse quickly slows down, the particles can actually pass over the front and are sharply swept duskward by both the vortex (representing the diverting flow) and ∇B drift, since the strong gradient in B from the pulse points tailward when the particles are located earthward of the front. After this sharp duskward turn, they are observed by THB as injected particles. Later in the injection, we see that the more energetic population (15 keV) is no longer injected, but is swept out from a combination of the tailward portion of the vortex (return flow) and the intensified ∇B drift from the sharp gradient in B at the front. The lower energies (8 keV), however, are carried in all the way from the "near-earth reconnection site" downtail, demonstrating that the azimuthally localized pulse that is also radially constrained is also capable of transporting particles across large distances (despite being finite in length)

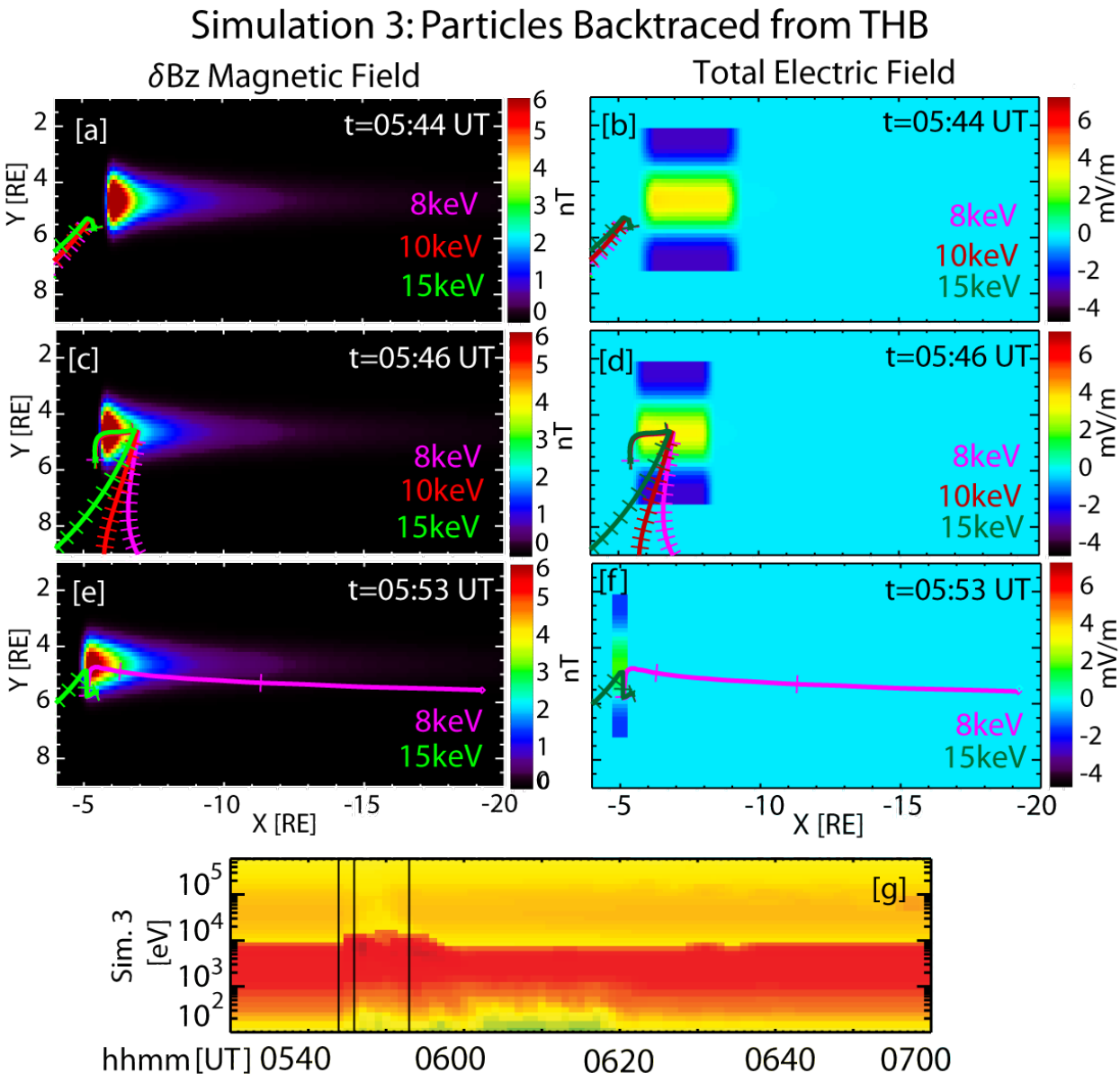

Figure 4.20. Particle trajectories backtraced in time from THB's location. The left column plots the trajectories on top of the pulse's magnetic field (δBz) while the right column plots the trajectories on top of the pulse's total electric field. The stated time is the time at which particles are observed and backtraced from. The pulse is also plotted at this time. The stated energies are the particle energies when they are observed by THB. (g) Three vertical lines mark the times at which the backtraces were taken in panels a-f. In (a) and (b) the particles are swept out to higher L-shells, losing energy in the process. In (c) and (d) the particles are swept up by the pulse as they were ∇B and curvature drifting and are injected. In (e) and (f) the 8 keV population came all the way from downtail, while the 15 keV population was swept duskward by the tail end of the vortex. Tick marks are every 5 min.

4.5 Conclusions

In this chapter, we have described our updated model for a localized, transient electromagnetic field pulse and have demonstrated its efficacy in simulating electron injections. The modeled dipolarizing flux bundle relies upon parameters that match realistic δBz observations, electric fields and flows. The depletions in energy flux observed at lower energies simultaneous to the injection at higher energies was better simulated than in our intial, simplified model of an infinitely long, earthward-traveling electric field vortical structure.

The particle trajectories provided insight to the cause behind the simulation changes and improvements. While the particle traces showed that indeed particle trajectories are altered by the δBz included in the updated model, we found that the these alterations affect the spectra minimally. For the most part, particles that were impacted by the δBz would drift around the peak, circling back to approximately the same location in X and continuing on approximately the same drift orbit. Because the pulse was located in the pre-midnight sector, there was a small asymmetry which meant particles would lose a little energy in this process.

Although the δBz appears to have little effect on the spectra, we found that the updated pulse shape has more dramatic effects. Because the updated pulse is shorter in length and duration, spacecraft that are farther away from the pulse (THA) do not observe appreciable eflux depletion at the time of injection. The injection duration is, naturally, much shorter. However, the observations of elevated eflux that last ~30 min can be explained by the fact that typically multiple injections are occurring simultaneously at different locations in the tail. The integrated effect is a lengthy duration of eflux enhancement that could be modeled in the future with multiple pulses.

To demonstrate that the δBz plays a minor role the simulated spectra and that the injections are largely a result of the electric fields at play, we reran simulation 3 but removed the inductive electric field, which removed the δBz from the pulse (simulation 4). Figure 4.21 compares simulation 3 with simulation 4 for all four spacecraft. The two simulations are nearly identical. Simulation 4 actually shows slightly more enhanced eflux most notably at THE and THA in the latter portion of the injection. This is because simulation 4 lacks the additional δBz which (in the pre-midnight sector) causes particles to drift slightly tailward of their normal drift shells, losing energy along the way.

As we hypothesized in Chapter 3, we can again postulate that had one of the spacecraft been located at the center of the pulse, where δBz is greatest, a larger increase in eflux would have been observed due to betatron acceleration. This is intuitive (assuming adiabaticity), because electrons that drift outside of the pulse would lose any energy gained from δBz after they enter the lower background magnetic field. This means any dispersed injection must be a signature of the energy gained when the electrons drifted across the potential drop formed from the total electric field. This of course places extreme limits on the spacecraft location for it to observe the maximum energy gain possible by a pulse. We therefore conclude that the case of a spacecraft being at the pulse center would not be common amongst injection observations, but rather an exceptional, rare occurrence. In fact, from Chapter 2 we saw that 352 of the 1624 dispersionless electron injections were coincident with ion dispersionless injections, implying that only 22% of the dispersionless injections were located at the pulse center. This spatial limitation on electron energization via the dipolarized magnetic field can be further verified with future studies that look for such a configuration. To be clear, the fact that δBz plays little role in the energizing process does not mean there is no flux transport. We calculated 0.8 MWeb of flux

transported by the dipolarizing flux bundle modeled in simulation 3, which falls within the 0.5-1.5 MWb range determined by *Liu et al.* [2014] to be the typical flux transported by a DFB.

Now that we have successfully simulated electron injections with a more realistic model of the earthward traveling dipolarizing flux bundle, we can say with even more confidence that the localized, transient DFBs are capable of carrying particles from the near-Earth reconnection site to the inner magnetosphere where they are observed as injections. This model can explain the trans-geosynchronous injections we observe downtail, unlike previous models of an azimuthally wide injection front that moves earthward from ~9-11 R_E. The dipolarization is required to drive the flows as the field lines race earthward, so in that sense the dipolarization plays a pivotal role. However, it is not the δBz that directly energizes the particles. Instead, it is the narrow flow channel that carries the particles into higher magnetic fields closer to Earth (betatron acceleration). In other words, electrons are energized as they ∇B and curvature drift across the flow channel, gaining energy as they cross the potential drop created by the dawn-dusk electric field within the earthward flow. The results in this chapter therefore do not negate what was analyzed and discovered in Chapter 3 with our simple model. Instead, our updated model supports our previous conclusions while painting a clearer picture of the phenomenology behind injections.

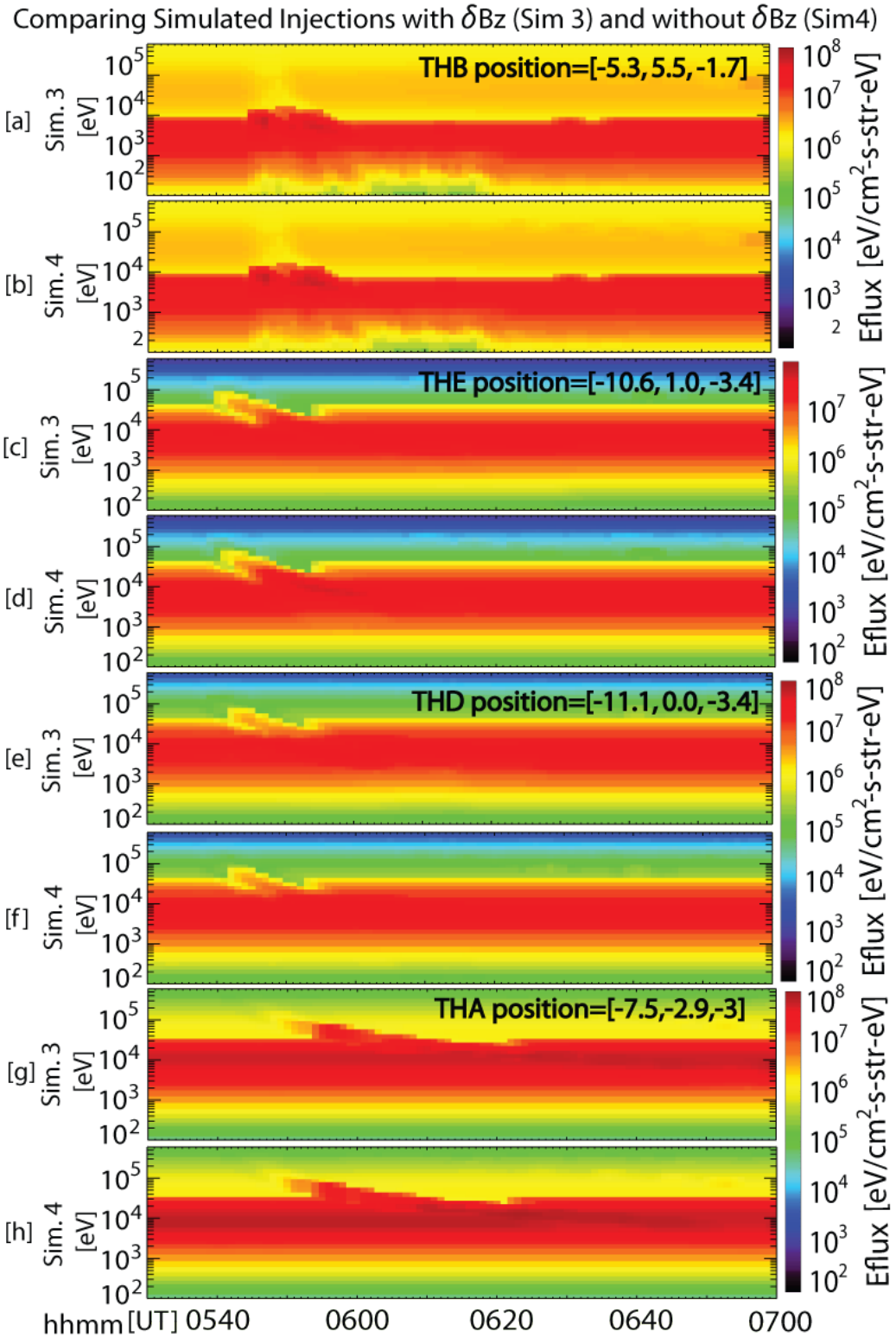

Figure 4.21. Comparison between simulation 3, which has a δBz and inductive electric field component, and simulation 4, which neglects these terms. The simulations are almost identical, except that simulation 4 has slightly enhanced eflux most obvious in THE and THA.

CHAPTER 5

Conclusions and Future Work

5.1 Conclusions

Injections play a pivotal role in populating the inner magnetosphere with particles, thus understanding how they occur is essential to linking the outer magnetosphere to the inner magnetosphere and to understanding radiation belt dynamics. Previously, this understanding was based predominantly on geosynchronous satellite data because of the plethora of satellites located there and the dearth of satellites located downtail. Statistical studies, case studies, and models were utilized to develop the idea of an azimuthally wide "injection boundary" that separates hot particles from cold particles moving earthward from ~9-11 R_E towards geosynchronous orbit. This model of particle energization, however, cannot explain the observations of trans-geosynchronous injections farther downtail that has been observed in the past and more recently (and frequently) by THEMIS. This thesis provided an alternative model to the injection process, suggesting that instead, particles are transported and energized by localized, transient dipolarizing flux bundles and their related fields and flows that follow magnetotail reconnection.

5.1.2 Injection Correlation with BBF Phenomenology

In Chapter 2, I utilized a statistical study of 1624 dispersionless, 1201 dispersed, and 345 inversely dispersed electron injections and 1277 dispersionless, 690 dispersed, and 75 inversely dispersed ion injections to determine that injections are correlated with other bursty bulk flow features, suggesting that injections are indeed due to these transient, localized structures. Using a

superposed epoch analysis, I showed a good correlation between injections and fast flows, dipolarizations, enhanced electric fields, and increases in geomagnetic activity (|AL| index). Not only are injections correlated with |AL| enhancements, but BBFs and DFBs have also been correlated with |AL| increases. I plotted injection occurrence rates in the magnetotail, finding that they are predominantly located in the pre-midnight sector, akin to BBFs, DFBs, and observations of near-Earth reconnection.

When I plotted the occurrence rates of "coincident injections" (when a spacecraft observes both electron and ion injections at the same time) against the occurrence rates of electron-only and ion-only injection observations, I found that coincident injections were observed with highest probability at a location right between the peak probabilities in electron-only and ion-only injections. I also found many more electron-only and ion-only injections than coincident injections. These findings suggest that coincident injections are observed when the spacecraft is fortuitously in the center of the narrow flow channel. If it is off to the side of the channel, even just outside of it, it may observe a dispersionless electron-only or ion-only injection. It would not observe the other species because of particle drift motion: the electrons drift towards the dawn, and the ions towards the dusk. The only reason we would observe so few coincident injections is if the acceleration site is very narrow, making the likelihood of the spacecraft being in the right location at the right time much more slim than if the acceleration site was azimuthally wide.

All of these findings point to injections being the result of particle transport and acceleration within the transient, localized flows that come with dipolarizing flux bundles.

5.1.3. Injection Contribution to Plasma Sheet Heating

In Chapter 2, I also utilized the injection database to study the change in both spectral hardening and energy flux before and after injection as well as at different levels of geomagnetic activity. Similar to a previous study by *Christon et al*. [1988], I found that there was little spectral hardening after a single injection. However, I found there was increased spectral hardening with increased geomagnetic activity. I also found that the energy flux both before and after injection was higher during enhanced activity. Previous studies [*Liu et al.*, 2012; *Rostoker et al.*, 1991] have shown that dipolarizing flux bundles are accompanied by current "wedgelets", a small version of the substorm current wedge. They contribute to the large scale substorm current wedge while enhancing our measure of geomagnetic activity, the |AL| index. In the context of our observations, we conclude that the plasma sheet heating as is an integral effect of multiple injections, each occurring with each incoming DFB. Thus, the more reconnection occurs during a substorm, the more DFBs are created, the larger the substorm current wedge and |AL| index grow and, more pertinent to our observations, the more injections occur, so ultimately the greater heating of the plasma sheet.

5.1.4 A DFB-Electric Field Model that Simulates Injections

Chapter 2 provided observational evidence that BBFs/DFBs harbor the localized, transient acceleration sites that generate injections. Chapters 3 and 4 demonstrate that the electric fields within localized, transient BBFs/DFBs are capable of creating sudden increases in electron fluxes (injections) and of transporting particles into the inner magnetosphere. In Chapter 3, I first designed a simple electric field pulse to model the electric fields typically observed concurrently with earthward flows. What made this model particularly effective was its vortical nature.

Because I wished to model the flow vortices observed in the magnetotail [i.e. *Keiling et al.* 2009], I designed the electric field pulse to have opposing, dusk-dawn fields flanking the dawn-dusk electric field at the center. These opposing fields are related to the tailward flows that are observed as plasma ahead of the DFB/bubble is diverted around the earthward traveling DFB. These fields are responsible for the dispersed depletion in energy flux that is observed simultaneously at lower energies with the dispersed injection signature.

Next, I updated the model to capture the electromagnetic field associated with earthward traveling DFBs more realistically. I kept the electrostatic field vortex model developed in Chapter 3, but added to it an electromagnetic field pulse obtained by modifying the analytical equations for the *Li et al*. [1998; 2003] pulse model. The latter provides the magnetic field self-consistently with the inductive electric field via Faraday's Law. While merging the two pulses and creating a more realistic description of the fields, I also had to remove the simplification of an infinite pulse length and fixed pulse duration (it was 50 min in the simple model of Chapter 3). The revised, realistic pulse travels earthward as a coherent structure that has a front and a tail. I found that the updated model provided a better data-model comparison. However, the major improvement in the spectra, compared to earlier results, was not due to the addition of the electromagnetic field pulse. Instead, the principal improvements were caused by the change in the pulse's size and duration. The eflux depletion data-model comparison was improved because, while the long-lasting, infinitely long return flow of the earlier, simpler model operated long enough to sweep out low-energy, slow-drifting particles and create unrealistically deep minima, the short-term, smaller return flow was not present long enough for the slow particles to drift and lose energy, thereby removing the unphysical deep minima.

To verify that the realistic addition of the electromagnetic component of the pulse played a small role in particle energization compared to the electric fields, I reran the simulation with all of the same parameters except I removed the inductive electric field and its corresponding δBz from the pulse. The resulting simulation was almost identical to the simulation that utilized the full electromagnetic model including the inductive electric field and associated δBz. The modeling revealed that: (1) a localized, transient electromagnetic field pulse consistent with typical earthward-traveling DFBs is capable of transporting electrons from the near-Earth reconnection site to the inner magnetosphere, picking up more particles along the way and accelerating them to higher energies, and (2) the dipolarization is not itself the key energizer; instead it is the electric fields involved in the surrounding (potential) flow. This is not to say that the dipolarization front is not crucial; in fact, the dipolarization following magnetotail reconnection is what drives the neighboring flows and electric fields. As individual particles ∇B and curvature drift across the potential drop of the electric field associated with the bulk plasma motion, they either gain energy if they drift across the duskward field of the fast flow channel, or lose energy if they drift across the dawnward field of the return flow.

5.2 Future Work

This thesis sets the stage for many future studies. The injection database could be probed further. Events that correspond to the same injection observed at multiple satellites across the magnetotail could be identified and considered for further multi-point studies. Do we observe the same features of an expanding front towards the dawn and dusk that *Thomsen et al.* [2001], found at geosynchronous orbit? Or are the *Thomsen et al.* [2001] findings the result of flow diversion at geosynchronous and therefore not observable farther downtail?

These multi-case studies could also be modeled with our updated, more realistic yet still simple model of the localized, transient electromagnetic field pulse. Modeling these events would help us to constrain typical flow channel widths, typical return flow strengths and extent, typical electric field magnitudes, etc. Furthermore, events could be modeled with multiple pulses (rather than just one), which would more realistically follow observations of multiple injection events, DFBs and BBFs occurring throughout the tail. This endeavor would also prove whether or not multiple pulses are indeed capable of simulating the long duration of eflux enhancement that we observed in the cases presented herein.

Taking the modeling even further, we can utilize the model's capability to trace off-equatorial pitch-angle particles to study the effects of the incoming pulse on various pitch angles. A study by *Runov et al*. [2013] showed that in several cases, if the spacecraft was located near the neutral sheet when it observed a dipolarization front, then it observed a pancake distribution (enhancement of equatorial pitch angle particles) behind the front. Meanwhile, if the spacecraft was located away from the neutral sheet, it observed a cigar-shaped distribution behind the front. Modeling particles of different pitch angles could explain how these particular distributions are generated behind the dipolarization front and provide a deeper understanding of the acceleration mechanism during particle injections.

5.3 Final Summary

Contrary to previous prevailing opinion, particle injections in the magnetotail are the result of transient, localized, earthward-traveling flow bursts, driven by dipolarizing flux bundles which create strong, dawn-dusk electric fields. These electric fields are capable of locally opening up the Alfvén layer, transporting particles that were previously drifting outside the

Alfvén layer into the radiation belts. The more energetic particles originate closer to the observed injection, while lower energies may originate further down the tail, as far out as the near-Earth reconnection site. Depletions in energy flux occur when inner magnetospheric particles move to higher L-shells, either due to the vortical return flow or due to the enhanced gradient in the magnetic field from the pulse which switches the particles' ∇B drift direction. These conclusions allow us to understand and to explain particle injections observed anywhere throughout the magnetotail. They also provide a link between the radiation belts and their seed population, particles from the outer magnetosphere.

APPENDIX 1

JOHN WILEY AND SONS LICENSE
TERMS AND CONDITIONS

May 16, 2014

This is a License Agreement between Christine Gabrielse ("You") and John Wiley and Sons ("John Wiley and Sons") provided by Copyright Clearance Center ("CCC"). The license consists of your order details, the terms and conditions provided by John Wiley and Sons, and the payment terms and conditions.

All payments must be made in full to CCC. For payment instructions, please see information listed at the bottom of this form.

License Number	3382710352301
License date	May 05, 2014
Licensed content publisher	John Wiley and Sons
Licensed content publication	Journal of Geophysical Research: Space Physics
Licensed content title	Characterization of geostationary particle signatures based on the 'Injection Boundary' Model
Licensed copyright line	Copyright © 1983 by the American Geophysical Union.
Licensed content author	B. H. Mauk,C.-I. Meng
Licensed content date	Sep 20, 2012
Start page	3055
End page	3071
Type of use	Dissertation/Thesis
Requestor type	University/Academic
Format	Print and electronic
Portion	Figure/table
Number of figures/tables	1
Original Wiley figure/table number(s)	Figure 1
Will you be translating?	No
Title of your thesis / dissertation	Magnetospheric Particle Injections and their Relation to Impulsive, Localized Electric Fields
Expected completion date	Jun 2014

Expected size (number of pages)	208
Total	0.00 USD

TERMS AND CONDITIONS

This copyrighted material is owned by or exclusively licensed to John Wiley & Sons, Inc. or one of its group companies (each a"Wiley Company") or handled on behalf of a society with which a Wiley Company has exclusive publishing rights in relation to a particular work (collectively "WILEY"). By clicking “accept” in connection with completing this licensing transaction, you agree that the following terms and conditions apply to this transaction (along with the billing and payment terms and conditions established by the Copyright Clearance Center Inc., ("CCC's Billing and Payment terms and conditions"), at the time that you opened your Rightslink account (these are available at any time at http://myaccount.copyright.com).

Terms and Conditions

- The materials you have requested permission to reproduce or reuse (the "Wiley Materials") are protected by copyright.

- You are hereby granted a personal, non-exclusive, non-sub licensable (on a stand-alone basis), non-transferable, worldwide, limited license to reproduce the Wiley Materials for the purpose specified in the licensing process. This license is for a one-time use only and limited to any maximum distribution number specified in the license. The first instance of republication or reuse granted by this licence must be completed within two years of the date of the grant of this licence (although copies prepared before the end date may be distributed thereafter). The Wiley Materials shall not be used in any other manner or for any other purpose, beyond what is granted in the license. Permission is granted subject to an appropriate acknowledgement given to the author, title of the material/book/journal and the publisher. You shall also duplicate the copyright notice that appears in the Wiley publication in your use of the Wiley Material. Permission is also granted on the understanding that nowhere in the text is a previously published source acknowledged for all or part of this Wiley Material. Any third party content is expressly excluded from this permission.

- With respect to the Wiley Materials, all rights are reserved. Except as expressly granted by the terms of the license, no part of the Wiley Materials may be copied, modified, adapted (except for minor reformatting required by the new Publication), translated, reproduced, transferred or distributed, in any form or by any means, and no derivative works may be made based on the Wiley Materials without the prior permission of the respective copyright owner. You may not alter, remove or suppress in any manner any copyright, trademark or other notices displayed by the Wiley Materials. You may not license, rent, sell, loan, lease, pledge, offer as security, transfer or assign the Wiley Materials on a stand-

alone basis, or any of the rights granted to you hereunder to any other person.

- The Wiley Materials and all of the intellectual property rights therein shall at all times remain the exclusive property of John Wiley & Sons Inc, the Wiley Companies, or their respective licensors, and your interest therein is only that of having possession of and the right to reproduce the Wiley Materials pursuant to Section 2 herein during the continuance of this Agreement. You agree that you own no right, title or interest in or to the Wiley Materials or any of the intellectual property rights therein. You shall have no rights hereunder other than the license as provided for above in Section 2. No right, license or interest to any trademark, trade name, service mark or other branding ("Marks") of WILEY or its licensors is granted hereunder, and you agree that you shall not assert any such right, license or interest with respect thereto.

- NEITHER WILEY NOR ITS LICENSORS MAKES ANY WARRANTY OR REPRESENTATION OF ANY KIND TO YOU OR ANY THIRD PARTY, EXPRESS, IMPLIED OR STATUTORY, WITH RESPECT TO THE MATERIALS OR THE ACCURACY OF ANY INFORMATION CONTAINED IN THE MATERIALS, INCLUDING, WITHOUT LIMITATION, ANY IMPLIED WARRANTY OF MERCHANTABILITY, ACCURACY, SATISFACTORY QUALITY, FITNESS FOR A PARTICULAR PURPOSE, USABILITY, INTEGRATION OR NON-INFRINGEMENT AND ALL SUCH WARRANTIES ARE HEREBY EXCLUDED BY WILEY AND ITS LICENSORS AND WAIVED BY YOU

- WILEY shall have the right to terminate this Agreement immediately upon breach of this Agreement by you.
- You shall indemnify, defend and hold harmless WILEY, its Licensors and their respective directors, officers, agents and employees, from and against any actual or threatened claims, demands, causes of action or proceedings arising from any breach of this Agreement by you.

- IN NO EVENT SHALL WILEY OR ITS LICENSORS BE LIABLE TO YOU OR ANY OTHER PARTY OR ANY OTHER PERSON OR ENTITY FOR ANY SPECIAL, CONSEQUENTIAL, INCIDENTAL, INDIRECT, EXEMPLARY OR PUNITIVE DAMAGES, HOWEVER CAUSED, ARISING OUT OF OR IN CONNECTION WITH THE DOWNLOADING, PROVISIONING, VIEWING OR USE OF THE MATERIALS REGARDLESS OF THE FORM OF ACTION, WHETHER FOR BREACH OF CONTRACT, BREACH OF WARRANTY, TORT, NEGLIGENCE, INFRINGEMENT OR OTHERWISE (INCLUDING, WITHOUT LIMITATION, DAMAGES BASED ON LOSS OF PROFITS, DATA, FILES, USE, BUSINESS OPPORTUNITY OR CLAIMS OF THIRD PARTIES), AND WHETHER OR NOT THE PARTY HAS BEEN ADVISED OF THE POSSIBILITY OF SUCH DAMAGES. THIS LIMITATION SHALL APPLY NOTWITHSTANDING ANY FAILURE OF ESSENTIAL PURPOSE OF ANY LIMITED REMEDY PROVIDED HEREIN.

- Should any provision of this Agreement be held by a court of competent jurisdiction to be illegal, invalid, or unenforceable, that provision shall be deemed amended to achieve as nearly as possible the same economic effect as the original provision, and the legality, validity and enforceability of the remaining provisions of this Agreement shall not be affected or impaired thereby.

- The failure of either party to enforce any term or condition of this Agreement shall not constitute a waiver of either party's right to enforce each and every term and condition of

this Agreement. No breach under this agreement shall be deemed waived or excused by either party unless such waiver or consent is in writing signed by the party granting such waiver or consent. The waiver by or consent of a party to a breach of any provision of this Agreement shall not operate or be construed as a waiver of or consent to any other or subsequent breach by such other party.

- This Agreement may not be assigned (including by operation of law or otherwise) by you without WILEY's prior written consent.

- Any fee required for this permission shall be non-refundable after thirty (30) days from receipt by the CCC.

- These terms and conditions together with CCC's Billing and Payment terms and conditions (which are incorporated herein) form the entire agreement between you and WILEY concerning this licensing transaction and (in the absence of fraud) supersedes all prior agreements and representations of the parties, oral or written. This Agreement may not be amended except in writing signed by both parties. This Agreement shall be binding upon and inure to the benefit of the parties' successors, legal representatives, and authorized assigns.

- In the event of any conflict between your obligations established by these terms and conditions and those established by CCC's Billing and Payment terms and conditions, these terms and conditions shall prevail.

- WILEY expressly reserves all rights not specifically granted in the combination of (i) the license details provided by you and accepted in the course of this licensing transaction, (ii) these terms and conditions and (iii) CCC's Billing and Payment terms and conditions.

- This Agreement will be void if the Type of Use, Format, Circulation, or Requestor Type was misrepresented during the licensing process.

- This Agreement shall be governed by and construed in accordance with the laws of the State of New York, USA, without regards to such state's conflict of law rules. Any legal action, suit or proceeding arising out of or relating to these Terms and Conditions or the breach thereof shall be instituted in a court of competent jurisdiction in New York County in the State of New York in the United States of America and each party hereby consents and submits to the personal jurisdiction of such court, waives any objection to venue in such court and consents to service of process by registered or certified mail, return receipt requested, at the last known address of such party.

WILEY OPEN ACCESS TERMS AND CONDITIONS

Wiley Publishes Open Access Articles in fully Open Access Journals and in Subscription journals offering Online Open. Although most of the fully Open Access journals publish open access articles under the terms of the Creative Commons Attribution (CC BY) License only, the subscription journals and a few of the Open Access Journals offer a choice of Creative Commons Licenses:: Creative Commons Attribution (CC-BY) license Creative Commons Attribution Non-Commercial (CC-BY-NC) license and Creative Commons

Attribution Non-Commercial-NoDerivs (CC-BY-NC-ND) License. The license type is clearly identified on the article.

Copyright in any research article in a journal published as Open Access under a Creative Commons License is retained by the author(s). Authors grant Wiley a license to publish the article and identify itself as the original publisher. Authors also grant any third party the right to use the article freely as long as its integrity is maintained and its original authors, citation details and publisher are identified as follows: [Title of Article/Author/Journal Title and Volume/Issue. Copyright (c) [year] [copyright owner as specified in the Journal]. Links to the final article on Wiley's website are encouraged where applicable.

The Creative Commons Attribution License

The Creative Commons Attribution License (CC-BY) allows users to copy, distribute and transmit an article, adapt the article and make commercial use of the article. The CC-BY license permits commercial and non-commercial re-use of an open access article, as long as the author is properly attributed.

The Creative Commons Attribution License does not affect the moral rights of authors, including without limitation the right not to have their work subjected to derogatory treatment. It also does not affect any other rights held by authors or third parties in the article, including without limitation the rights of privacy and publicity. Use of the article must not assert or imply, whether implicitly or explicitly, any connection with, endorsement or sponsorship of such use by the author, publisher or any other party associated with the article.

For any reuse or distribution, users must include the copyright notice and make clear to others that the article is made available under a Creative Commons Attribution license, linking to the relevant Creative Commons web page.

To the fullest extent permitted by applicable law, the article is made available as is and without representation or warranties of any kind whether express, implied, statutory or otherwise and including, without limitation, warranties of title, merchantability, fitness for a particular purpose, non-infringement, absence of defects, accuracy, or the presence or absence of errors.

Creative Commons Attribution Non-Commercial License

The Creative Commons Attribution Non-Commercial (CC-BY-NC) License permits use, distribution and reproduction in any medium, provided the original work is properly cited and is not used for commercial purposes.(see below)

Creative Commons Attribution-Non-Commercial-NoDerivs License

The Creative Commons Attribution Non-Commercial-NoDerivs License (CC-BY-NC-ND) permits use, distribution and reproduction in any medium, provided the original work is

properly cited, is not used for commercial purposes and no modifications or adaptations are made. (see below)

Use by non-commercial users

For non-commercial and non-promotional purposes, individual users may access, download, copy, display and redistribute to colleagues Wiley Open Access articles, as well as adapt, translate, text- and data-mine the content subject to the following conditions:

- The authors' moral rights are not compromised. These rights include the right of "paternity" (also known as "attribution" - the right for the author to be identified as such) and "integrity" (the right for the author not to have the work altered in such a way that the author's reputation or integrity may be impugned).

- Where content in the article is identified as belonging to a third party, it is the obligation of the user to ensure that any reuse complies with the copyright policies of the owner of that content.

- If article content is copied, downloaded or otherwise reused for non-commercial research and education purposes, a link to the appropriate bibliographic citation (authors, journal, article title, volume, issue, page numbers, DOI and the link to the definitive published version on **Wiley Online Library**) should be maintained. Copyright notices and disclaimers must not be deleted.

- Any translations, for which a prior translation agreement with Wiley has not been agreed, must prominently display the statement: "This is an unofficial translation of an article that appeared in a Wiley publication. The publisher has not endorsed this translation."

Use by commercial "for-profit" organisations

Use of Wiley Open Access articles for commercial, promotional, or marketing purposes requires further explicit permission from Wiley and will be subject to a fee. Commercial purposes include:

- Copying or downloading of articles, or linking to such articles for further redistribution, sale or licensing;

- Copying, downloading or posting by a site or service that incorporates advertising with such content;

- The inclusion or incorporation of article content in other works or services (other than normal quotations with an appropriate citation) that is then available for sale or licensing, for a fee (for example, a compilation produced for marketing purposes, inclusion in a sales pack)

- Use of article content (other than normal quotations with appropriate citation) by for-profit organisations for promotional purposes

- Linking to article content in e-mails redistributed for promotional, marketing or educational purposes;
- Use for the purposes of monetary reward by means of sale, resale, licence, loan, transfer or other form of commercial exploitation such as marketing products
- Print reprints of Wiley Open Access articles can be purchased from: corporatesales@wiley.com

Further details can be found on Wiley Online Library
http://olabout.wiley.com/WileyCDA/Section/id-410895.html

Other Terms and Conditions:

v1.9

If you would like to pay for this license now, please remit this license along with your payment made payable to "COPYRIGHT CLEARANCE CENTER" otherwise you will be invoiced within 48 hours of the license date. Payment should be in the form of a check or money order referencing your account number and this invoice number 501295250.
Once you receive your invoice for this order, you may pay your invoice by credit card. Please follow instructions provided at that time.

Make Payment To:
Copyright Clearance Center
Dept 001
P.O. Box 843006
Boston, MA 02284-3006

For suggestions or comments regarding this order, contact RightsLink Customer Support: customercare@copyright.com or +1-877-622-5543 (toll free in the US) or +1-978-646-2777.

Gratis licenses (referencing $0 in the Total field) are free. Please retain this printable license for your reference. No payment is required.

APPENDIX 2

JOHN WILEY AND SONS LICENSE
TERMS AND CONDITIONS

May 16, 2014

This is a License Agreement between Christine Gabrielse ("You") and John Wiley and Sons ("John Wiley and Sons") provided by Copyright Clearance Center ("CCC"). The license consists of your order details, the terms and conditions provided by John Wiley and Sons, and the payment terms and conditions.

All payments must be made in full to CCC. For payment instructions, please see information listed at the bottom of this form.

License Number	3382710635596
License date	May 05, 2014
Licensed content publisher	John Wiley and Sons
Licensed content publication	Journal of Geophysical Research: Space Physics
Licensed content title	Characteristic plasma properties during dispersionless substorm injections at geosynchronous orbit
Licensed copyright line	Copyright 1997 by the American Geophysical Union.
Licensed content author	J. Birn,M. F. Thomsen,J. E. Borovsky,G. D. Reeves,D. J. McComas,R. D. Belian
Licensed content date	Sep 20, 2012
Start page	2309
End page	2324
Type of use	Dissertation/Thesis
Requestor type	University/Academic
Format	Print and electronic
Portion	Figure/table
Number of figures/tables	1
Original Wiley figure/table number(s)	Plate 2
Will you be translating?	No
Title of your thesis / dissertation	Magnetospheric Particle Injections and their Relation to Impulsive, Localized Electric Fields
Expected completion date	Jun 2014
Expected size (number of pages)	208
Total	0.00 USD

TERMS AND CONDITIONS

This copyrighted material is owned by or exclusively licensed to John Wiley & Sons, Inc. or one of its group companies (each a"Wiley Company") or handled on behalf of a society with which a Wiley Company has exclusive publishing rights in relation to a particular work (collectively "WILEY"). By clicking “accept” in connection with completing this licensing transaction, you agree that the following terms and conditions apply to this transaction (along with the billing and payment terms and conditions established by the Copyright Clearance Center Inc., ("CCC's Billing and Payment terms and conditions"), at the time that you opened your Rightslink account (these are available at any time at http://myaccount.copyright.com).

Terms and Conditions

- The materials you have requested permission to reproduce or reuse (the "Wiley Materials") are protected by copyright.

- You are hereby granted a personal, non-exclusive, non-sub licensable (on a stand-alone basis), non-transferable, worldwide, limited license to reproduce the Wiley Materials for the purpose specified in the licensing process. This license is for a one-time use only and limited to any maximum distribution number specified in the license. The first instance of republication or reuse granted by this licence must be completed within two years of the date of the grant of this licence (although copies prepared before the end date may be distributed thereafter). The Wiley Materials shall not be used in any other manner or for any other purpose, beyond what is granted in the license. Permission is granted subject to an appropriate acknowledgement given to the author, title of the material/book/journal and the publisher. You shall also duplicate the copyright notice that appears in the Wiley publication in your use of the Wiley Material. Permission is also granted on the understanding that nowhere in the text is a previously published source acknowledged for all or part of this Wiley Material. Any third party content is expressly excluded from this permission.

- With respect to the Wiley Materials, all rights are reserved. Except as expressly granted by the terms of the license, no part of the Wiley Materials may be copied, modified, adapted (except for minor reformatting required by the new Publication), translated, reproduced, transferred or distributed, in any form or by any means, and no derivative works may be made based on the Wiley Materials without the prior permission of the respective copyright owner. You may not alter, remove or suppress in any manner any copyright, trademark or other notices displayed by the Wiley Materials. You may not license, rent, sell, loan, lease, pledge, offer as security, transfer or assign the Wiley Materials on a stand-alone basis, or any of the rights granted to you hereunder to any other person.

- The Wiley Materials and all of the intellectual property rights therein shall at all times remain the exclusive property of John Wiley & Sons Inc, the Wiley

Companies, or their respective licensors, and your interest therein is only that of having possession of and the right to reproduce the Wiley Materials pursuant to Section 2 herein during the continuance of this Agreement. You agree that you own no right, title or interest in or to the Wiley Materials or any of the intellectual property rights therein. You shall have no rights hereunder other than the license as provided for above in Section 2. No right, license or interest to any trademark, trade name, service mark or other branding ("Marks") of WILEY or its licensors is granted hereunder, and you agree that you shall not assert any such right, license or interest with respect thereto.

- NEITHER WILEY NOR ITS LICENSORS MAKES ANY WARRANTY OR REPRESENTATION OF ANY KIND TO YOU OR ANY THIRD PARTY, EXPRESS, IMPLIED OR STATUTORY, WITH RESPECT TO THE MATERIALS OR THE ACCURACY OF ANY INFORMATION CONTAINED IN THE MATERIALS, INCLUDING, WITHOUT LIMITATION, ANY IMPLIED WARRANTY OF MERCHANTABILITY, ACCURACY, SATISFACTORY QUALITY, FITNESS FOR A PARTICULAR PURPOSE, USABILITY, INTEGRATION OR NON-INFRINGEMENT AND ALL SUCH WARRANTIES ARE HEREBY EXCLUDED BY WILEY AND ITS LICENSORS AND WAIVED BY YOU

- WILEY shall have the right to terminate this Agreement immediately upon breach of this Agreement by you.
- You shall indemnify, defend and hold harmless WILEY, its Licensors and their respective directors, officers, agents and employees, from and against any actual or threatened claims, demands, causes of action or proceedings arising from any breach of this Agreement by you.

- IN NO EVENT SHALL WILEY OR ITS LICENSORS BE LIABLE TO YOU OR ANY OTHER PARTY OR ANY OTHER PERSON OR ENTITY FOR ANY SPECIAL, CONSEQUENTIAL, INCIDENTAL, INDIRECT, EXEMPLARY OR PUNITIVE DAMAGES, HOWEVER CAUSED, ARISING OUT OF OR IN CONNECTION WITH THE DOWNLOADING, PROVISIONING, VIEWING OR USE OF THE MATERIALS REGARDLESS OF THE FORM OF ACTION, WHETHER FOR BREACH OF CONTRACT, BREACH OF WARRANTY, TORT, NEGLIGENCE, INFRINGEMENT OR OTHERWISE (INCLUDING, WITHOUT LIMITATION, DAMAGES BASED ON LOSS OF PROFITS, DATA, FILES, USE, BUSINESS OPPORTUNITY OR CLAIMS OF THIRD PARTIES), AND WHETHER OR NOT THE PARTY HAS BEEN ADVISED OF THE POSSIBILITY OF SUCH DAMAGES. THIS LIMITATION SHALL APPLY NOTWITHSTANDING ANY FAILURE OF ESSENTIAL PURPOSE OF ANY LIMITED REMEDY PROVIDED HEREIN.

- Should any provision of this Agreement be held by a court of competent jurisdiction to be illegal, invalid, or unenforceable, that provision shall be deemed amended to achieve as nearly as possible the same economic effect as the original provision, and the legality, validity and enforceability of the remaining provisions of this

Agreement shall not be affected or impaired thereby.

- The failure of either party to enforce any term or condition of this Agreement shall not constitute a waiver of either party's right to enforce each and every term and condition of this Agreement. No breach under this agreement shall be deemed waived or excused by either party unless such waiver or consent is in writing signed by the party granting such waiver or consent. The waiver by or consent of a party to a breach of any provision of this Agreement shall not operate or be construed as a waiver of or consent to any other or subsequent breach by such other party.

- This Agreement may not be assigned (including by operation of law or otherwise) by you without WILEY's prior written consent.

- Any fee required for this permission shall be non-refundable after thirty (30) days from receipt by the CCC.

- These terms and conditions together with CCC's Billing and Payment terms and conditions (which are incorporated herein) form the entire agreement between you and WILEY concerning this licensing transaction and (in the absence of fraud) supersedes all prior agreements and representations of the parties, oral or written. This Agreement may not be amended except in writing signed by both parties. This Agreement shall be binding upon and inure to the benefit of the parties' successors, legal representatives, and authorized assigns.

- In the event of any conflict between your obligations established by these terms and conditions and those established by CCC's Billing and Payment terms and conditions, these terms and conditions shall prevail.

- WILEY expressly reserves all rights not specifically granted in the combination of (i) the license details provided by you and accepted in the course of this licensing transaction, (ii) these terms and conditions and (iii) CCC's Billing and Payment terms and conditions.

- This Agreement will be void if the Type of Use, Format, Circulation, or Requestor Type was misrepresented during the licensing process.

- This Agreement shall be governed by and construed in accordance with the laws of the State of New York, USA, without regards to such state's conflict of law rules. Any legal action, suit or proceeding arising out of or relating to these Terms and Conditions or the breach thereof shall be instituted in a court of competent jurisdiction in New York County in the State of New York in the United States of America and each party hereby consents and submits to the personal jurisdiction of such court, waives any objection to venue in such court and consents to service of process by registered or certified mail, return receipt requested, at the last known address of such party.

WILEY OPEN ACCESS TERMS AND CONDITIONS

Wiley Publishes Open Access Articles in fully Open Access Journals and in Subscription journals offering Online Open. Although most of the fully Open Access journals publish open access articles under the terms of the Creative Commons Attribution (CC BY) License only, the subscription journals and a few of the Open Access Journals offer a choice of Creative Commons Licenses:: Creative Commons Attribution (CC-BY) license Creative Commons Attribution Non-Commercial (CC-BY-NC) license and Creative Commons Attribution Non-Commercial-NoDerivs (CC-BY-NC-ND) License. The license type is clearly identified on the article.

Copyright in any research article in a journal published as Open Access under a Creative Commons License is retained by the author(s). Authors grant Wiley a license to publish the article and identify itself as the original publisher. Authors also grant any third party the right to use the article freely as long as its integrity is maintained and its original authors, citation details and publisher are identified as follows: [Title of Article/Author/Journal Title and Volume/Issue. Copyright (c) [year] [copyright owner as specified in the Journal]. Links to the final article on Wiley's website are encouraged where applicable.

The Creative Commons Attribution License

The Creative Commons Attribution License (CC-BY) allows users to copy, distribute and transmit an article, adapt the article and make commercial use of the article. The CC-BY license permits commercial and non-commercial re-use of an open access article, as long as the author is properly attributed.

The Creative Commons Attribution License does not affect the moral rights of authors, including without limitation the right not to have their work subjected to derogatory treatment. It also does not affect any other rights held by authors or third parties in the article, including without limitation the rights of privacy and publicity. Use of the article must not assert or imply, whether implicitly or explicitly, any connection with, endorsement or sponsorship of such use by the author, publisher or any other party associated with the article.

For any reuse or distribution, users must include the copyright notice and make clear to others that the article is made available under a Creative Commons Attribution license, linking to the relevant Creative Commons web page.

To the fullest extent permitted by applicable law, the article is made available as is and without representation or warranties of any kind whether express, implied, statutory or otherwise and including, without limitation, warranties of title, merchantability, fitness for a particular purpose, non-infringement, absence of defects, accuracy, or the presence or absence of errors.

Creative Commons Attribution Non-Commercial License

The Creative Commons Attribution Non-Commercial (CC-BY-NC) License permits use, distribution and reproduction in any medium, provided the original work is properly cited and is not used for commercial purposes.(see below)

Creative Commons Attribution-Non-Commercial-NoDerivs License

The Creative Commons Attribution Non-Commercial-NoDerivs License (CC-BY-NC-ND) permits use, distribution and reproduction in any medium, provided the original work is properly cited, is not used for commercial purposes and no modifications or adaptations are made. (see below)

Use by non-commercial users

For non-commercial and non-promotional purposes, individual users may access, download, copy, display and redistribute to colleagues Wiley Open Access articles, as well as adapt, translate, text- and data-mine the content subject to the following conditions:

- The authors' moral rights are not compromised. These rights include the right of "paternity" (also known as "attribution" - the right for the author to be identified as such) and "integrity" (the right for the author not to have the work altered in such a way that the author's reputation or integrity may be impugned).
- Where content in the article is identified as belonging to a third party, it is the obligation of the user to ensure that any reuse complies with the copyright policies of the owner of that content.
- If article content is copied, downloaded or otherwise reused for non-commercial research and education purposes, a link to the appropriate bibliographic citation (authors, journal, article title, volume, issue, page numbers, DOI and the link to the definitive published version on **Wiley Online Library**) should be maintained. Copyright notices and disclaimers must not be deleted.
- Any translations, for which a prior translation agreement with Wiley has not been agreed, must prominently display the statement: "This is an unofficial translation of an article that appeared in a Wiley publication. The publisher has not endorsed this translation."

Use by commercial "for-profit" organisations

Use of Wiley Open Access articles for commercial, promotional, or marketing purposes requires further explicit permission from Wiley and will be subject to a fee. Commercial purposes include:

- Copying or downloading of articles, or linking to such articles for further redistribution, sale or licensing;
- Copying, downloading or posting by a site or service that incorporates advertising

with such content;

- The inclusion or incorporation of article content in other works or services (other than normal quotations with an appropriate citation) that is then available for sale or licensing, for a fee (for example, a compilation produced for marketing purposes, inclusion in a sales pack)

- Use of article content (other than normal quotations with appropriate citation) by for-profit organisations for promotional purposes

- Linking to article content in e-mails redistributed for promotional, marketing or educational purposes;

- Use for the purposes of monetary reward by means of sale, resale, licence, loan, transfer or other form of commercial exploitation such as marketing products

- Print reprints of Wiley Open Access articles can be purchased from: corporatesales@wiley.com

Further details can be found on Wiley Online Library
http://olabout.wiley.com/WileyCDA/Section/id-410895.html

Other Terms and Conditions:

v1.9

If you would like to pay for this license now, please remit this license along with your payment made payable to "COPYRIGHT CLEARANCE CENTER" otherwise you will be invoiced within 48 hours of the license date. Payment should be in the form of a check or money order referencing your account number and this invoice number 501295254.
Once you receive your invoice for this order, you may pay your invoice by credit card. Please follow instructions provided at that time.

Make Payment To:
Copyright Clearance Center
Dept 001
P.O. Box 843006
Boston, MA 02284-3006

For suggestions or comments regarding this order, contact RightsLink Customer Support: customercare@copyright.com or +1-877-622-5543 (toll free in the US) or +1-978-646-2777.

Gratis licenses (referencing $0 in the Total field) are free. Please retain this printable license for your reference. No payment is required.

APPENDIX 3

JOHN WILEY AND SONS LICENSE
TERMS AND CONDITIONS

May 16, 2014

This is a License Agreement between Christine Gabrielse ("You") and John Wiley and Sons ("John Wiley and Sons") provided by Copyright Clearance Center ("CCC"). The license consists of your order details, the terms and conditions provided by John Wiley and Sons, and the payment terms and conditions.

All payments must be made in full to CCC. For payment instructions, please see information listed at the bottom of this form.

License Number	3382720046800
License date	May 05, 2014
Licensed content publisher	John Wiley and Sons
Licensed content publication	Journal of Geophysical Research: Space Physics
Licensed content title	Transport of the plasma sheet electrons to the geostationary distances
Licensed copyright line	©2012. American Geophysical Union. All Rights Reserved.
Licensed content author	N. Y. Ganushkina,O. A. Amariutei,Y. Y. Shprits,M. W. Liemohn
Licensed content date	Jan 31, 2013
Start page	82
End page	98
Type of use	Dissertation/Thesis
Requestor type	University/Academic
Format	Print and electronic
Portion	Figure/table
Number of figures/tables	1
Original Wiley figure/table number(s)	Figure 4
Will you be translating?	No
Title of your thesis / dissertation	Magnetospheric Particle Injections and their Relation to Impulsive, Localized Electric Fields
Expected completion date	Jun 2014
Expected size (number of pages)	208
Total	0.00 USD

TERMS AND CONDITIONS

This copyrighted material is owned by or exclusively licensed to John Wiley & Sons, Inc. or one of its group companies (each a"Wiley Company") or handled on behalf of a society with which a Wiley Company has exclusive publishing rights in relation to a particular work (collectively "WILEY"). By clicking “accept” in connection with completing this licensing transaction, you agree that the following terms and conditions apply to this transaction (along with the billing and payment terms and conditions established by the Copyright Clearance Center Inc., ("CCC's Billing and Payment terms and conditions"), at the time that you opened your Rightslink account (these are available at any time at http://myaccount.copyright.com).

Terms and Conditions

- The materials you have requested permission to reproduce or reuse (the "Wiley Materials") are protected by copyright.

- You are hereby granted a personal, non-exclusive, non-sub licensable (on a stand-alone basis), non-transferable, worldwide, limited license to reproduce the Wiley Materials for the purpose specified in the licensing process. This license is for a one-time use only and limited to any maximum distribution number specified in the license. The first instance of republication or reuse granted by this licence must be completed within two years of the date of the grant of this licence (although copies prepared before the end date may be distributed thereafter). The Wiley Materials shall not be used in any other manner or for any other purpose, beyond what is granted in the license. Permission is granted subject to an appropriate acknowledgement given to the author, title of the material/book/journal and the publisher. You shall also duplicate the copyright notice that appears in the Wiley publication in your use of the Wiley Material. Permission is also granted on the understanding that nowhere in the text is a previously published source acknowledged for all or part of this Wiley Material. Any third party content is expressly excluded from this permission.

- With respect to the Wiley Materials, all rights are reserved. Except as expressly granted by the terms of the license, no part of the Wiley Materials may be copied, modified, adapted (except for minor reformatting required by the new Publication), translated, reproduced, transferred or distributed, in any form or by any means, and no derivative works may be made based on the Wiley Materials without the prior permission of the respective copyright owner. You may not alter, remove or suppress in any manner any copyright, trademark or other notices displayed by the Wiley Materials. You may not license, rent, sell, loan, lease, pledge, offer as security, transfer or assign the Wiley Materials on a stand-alone basis, or any of the rights granted to you hereunder to any other person.

- The Wiley Materials and all of the intellectual property rights therein shall at all times remain the exclusive property of John Wiley & Sons Inc, the Wiley

Companies, or their respective licensors, and your interest therein is only that of having possession of and the right to reproduce the Wiley Materials pursuant to Section 2 herein during the continuance of this Agreement. You agree that you own no right, title or interest in or to the Wiley Materials or any of the intellectual property rights therein. You shall have no rights hereunder other than the license as provided for above in Section 2. No right, license or interest to any trademark, trade name, service mark or other branding ("Marks") of WILEY or its licensors is granted hereunder, and you agree that you shall not assert any such right, license or interest with respect thereto.

- NEITHER WILEY NOR ITS LICENSORS MAKES ANY WARRANTY OR REPRESENTATION OF ANY KIND TO YOU OR ANY THIRD PARTY, EXPRESS, IMPLIED OR STATUTORY, WITH RESPECT TO THE MATERIALS OR THE ACCURACY OF ANY INFORMATION CONTAINED IN THE MATERIALS, INCLUDING, WITHOUT LIMITATION, ANY IMPLIED WARRANTY OF MERCHANTABILITY, ACCURACY, SATISFACTORY QUALITY, FITNESS FOR A PARTICULAR PURPOSE, USABILITY, INTEGRATION OR NON-INFRINGEMENT AND ALL SUCH WARRANTIES ARE HEREBY EXCLUDED BY WILEY AND ITS LICENSORS AND WAIVED BY YOU

- WILEY shall have the right to terminate this Agreement immediately upon breach of this Agreement by you.
- You shall indemnify, defend and hold harmless WILEY, its Licensors and their respective directors, officers, agents and employees, from and against any actual or threatened claims, demands, causes of action or proceedings arising from any breach of this Agreement by you.

- IN NO EVENT SHALL WILEY OR ITS LICENSORS BE LIABLE TO YOU OR ANY OTHER PARTY OR ANY OTHER PERSON OR ENTITY FOR ANY SPECIAL, CONSEQUENTIAL, INCIDENTAL, INDIRECT, EXEMPLARY OR PUNITIVE DAMAGES, HOWEVER CAUSED, ARISING OUT OF OR IN CONNECTION WITH THE DOWNLOADING, PROVISIONING, VIEWING OR USE OF THE MATERIALS REGARDLESS OF THE FORM OF ACTION, WHETHER FOR BREACH OF CONTRACT, BREACH OF WARRANTY, TORT, NEGLIGENCE, INFRINGEMENT OR OTHERWISE (INCLUDING, WITHOUT LIMITATION, DAMAGES BASED ON LOSS OF PROFITS, DATA, FILES, USE, BUSINESS OPPORTUNITY OR CLAIMS OF THIRD PARTIES), AND WHETHER OR NOT THE PARTY HAS BEEN ADVISED OF THE POSSIBILITY OF SUCH DAMAGES. THIS LIMITATION SHALL APPLY NOTWITHSTANDING ANY FAILURE OF ESSENTIAL PURPOSE OF ANY LIMITED REMEDY PROVIDED HEREIN.

- Should any provision of this Agreement be held by a court of competent jurisdiction to be illegal, invalid, or unenforceable, that provision shall be deemed amended to achieve as nearly as possible the same economic effect as the original provision, and the legality, validity and enforceability of the remaining provisions of this

Agreement shall not be affected or impaired thereby.

- The failure of either party to enforce any term or condition of this Agreement shall not constitute a waiver of either party's right to enforce each and every term and condition of this Agreement. No breach under this agreement shall be deemed waived or excused by either party unless such waiver or consent is in writing signed by the party granting such waiver or consent. The waiver by or consent of a party to a breach of any provision of this Agreement shall not operate or be construed as a waiver of or consent to any other or subsequent breach by such other party.

- This Agreement may not be assigned (including by operation of law or otherwise) by you without WILEY's prior written consent.

- Any fee required for this permission shall be non-refundable after thirty (30) days from receipt by the CCC.

- These terms and conditions together with CCC's Billing and Payment terms and conditions (which are incorporated herein) form the entire agreement between you and WILEY concerning this licensing transaction and (in the absence of fraud) supersedes all prior agreements and representations of the parties, oral or written. This Agreement may not be amended except in writing signed by both parties. This Agreement shall be binding upon and inure to the benefit of the parties' successors, legal representatives, and authorized assigns.

- In the event of any conflict between your obligations established by these terms and conditions and those established by CCC's Billing and Payment terms and conditions, these terms and conditions shall prevail.

- WILEY expressly reserves all rights not specifically granted in the combination of (i) the license details provided by you and accepted in the course of this licensing transaction, (ii) these terms and conditions and (iii) CCC's Billing and Payment terms and conditions.

- This Agreement will be void if the Type of Use, Format, Circulation, or Requestor Type was misrepresented during the licensing process.

- This Agreement shall be governed by and construed in accordance with the laws of the State of New York, USA, without regards to such state's conflict of law rules. Any legal action, suit or proceeding arising out of or relating to these Terms and Conditions or the breach thereof shall be instituted in a court of competent jurisdiction in New York County in the State of New York in the United States of America and each party hereby consents and submits to the personal jurisdiction of such court, waives any objection to venue in such court and consents to service of process by registered or certified mail, return receipt requested, at the last known address of such party.

WILEY OPEN ACCESS TERMS AND CONDITIONS

Wiley Publishes Open Access Articles in fully Open Access Journals and in Subscription journals offering Online Open. Although most of the fully Open Access journals publish open access articles under the terms of the Creative Commons Attribution (CC BY) License only, the subscription journals and a few of the Open Access Journals offer a choice of Creative Commons Licenses:: Creative Commons Attribution (CC-BY) license Creative Commons Attribution Non-Commercial (CC-BY-NC) license and Creative Commons Attribution Non-Commercial-NoDerivs (CC-BY-NC-ND) License. The license type is clearly identified on the article.

Copyright in any research article in a journal published as Open Access under a Creative Commons License is retained by the author(s). Authors grant Wiley a license to publish the article and identify itself as the original publisher. Authors also grant any third party the right to use the article freely as long as its integrity is maintained and its original authors, citation details and publisher are identified as follows: [Title of Article/Author/Journal Title and Volume/Issue. Copyright (c) [year] [copyright owner as specified in the Journal]. Links to the final article on Wiley's website are encouraged where applicable.

The Creative Commons Attribution License

The Creative Commons Attribution License (CC-BY) allows users to copy, distribute and transmit an article, adapt the article and make commercial use of the article. The CC-BY license permits commercial and non-commercial re-use of an open access article, as long as the author is properly attributed.

The Creative Commons Attribution License does not affect the moral rights of authors, including without limitation the right not to have their work subjected to derogatory treatment. It also does not affect any other rights held by authors or third parties in the article, including without limitation the rights of privacy and publicity. Use of the article must not assert or imply, whether implicitly or explicitly, any connection with, endorsement or sponsorship of such use by the author, publisher or any other party associated with the article.

For any reuse or distribution, users must include the copyright notice and make clear to others that the article is made available under a Creative Commons Attribution license, linking to the relevant Creative Commons web page.

To the fullest extent permitted by applicable law, the article is made available as is and without representation or warranties of any kind whether express, implied, statutory or otherwise and including, without limitation, warranties of title, merchantability, fitness for a particular purpose, non-infringement, absence of defects, accuracy, or the presence or absence of errors.

Creative Commons Attribution Non-Commercial License

The Creative Commons Attribution Non-Commercial (CC-BY-NC) License permits use, distribution and reproduction in any medium, provided the original work is properly cited and is not used for commercial purposes.(see below)

Creative Commons Attribution-Non-Commercial-NoDerivs License

The Creative Commons Attribution Non-Commercial-NoDerivs License (CC-BY-NC-ND) permits use, distribution and reproduction in any medium, provided the original work is properly cited, is not used for commercial purposes and no modifications or adaptations are made. (see below)

Use by non-commercial users

For non-commercial and non-promotional purposes, individual users may access, download, copy, display and redistribute to colleagues Wiley Open Access articles, as well as adapt, translate, text- and data-mine the content subject to the following conditions:

- The authors' moral rights are not compromised. These rights include the right of "paternity" (also known as "attribution" - the right for the author to be identified as such) and "integrity" (the right for the author not to have the work altered in such a way that the author's reputation or integrity may be impugned).
- Where content in the article is identified as belonging to a third party, it is the obligation of the user to ensure that any reuse complies with the copyright policies of the owner of that content.
- If article content is copied, downloaded or otherwise reused for non-commercial research and education purposes, a link to the appropriate bibliographic citation (authors, journal, article title, volume, issue, page numbers, DOI and the link to the definitive published version on **Wiley Online Library**) should be maintained. Copyright notices and disclaimers must not be deleted.
- Any translations, for which a prior translation agreement with Wiley has not been agreed, must prominently display the statement: "This is an unofficial translation of an article that appeared in a Wiley publication. The publisher has not endorsed this translation."

Use by commercial "for-profit" organisations

Use of Wiley Open Access articles for commercial, promotional, or marketing purposes requires further explicit permission from Wiley and will be subject to a fee. Commercial purposes include:

- Copying or downloading of articles, or linking to such articles for further redistribution, sale or licensing;
- Copying, downloading or posting by a site or service that incorporates advertising

with such content;

- The inclusion or incorporation of article content in other works or services (other than normal quotations with an appropriate citation) that is then available for sale or licensing, for a fee (for example, a compilation produced for marketing purposes, inclusion in a sales pack)

- Use of article content (other than normal quotations with appropriate citation) by for-profit organisations for promotional purposes

- Linking to article content in e-mails redistributed for promotional, marketing or educational purposes;

- Use for the purposes of monetary reward by means of sale, resale, licence, loan, transfer or other form of commercial exploitation such as marketing products

- Print reprints of Wiley Open Access articles can be purchased from: corporatesales@wiley.com

Further details can be found on Wiley Online Library
http://olabout.wiley.com/WileyCDA/Section/id-410895.html

Other Terms and Conditions:

v1.9

If you would like to pay for this license now, please remit this license along with your payment made payable to "COPYRIGHT CLEARANCE CENTER" otherwise you will be invoiced within 48 hours of the license date. Payment should be in the form of a check or money order referencing your account number and this invoice number 501295262.
Once you receive your invoice for this order, you may pay your invoice by credit card. Please follow instructions provided at that time.

Make Payment To:
Copyright Clearance Center
Dept 001
P.O. Box 843006
Boston, MA 02284-3006

For suggestions or comments regarding this order, contact RightsLink Customer Support: customercare@copyright.com or +1-877-622-5543 (toll free in the US) or +1-978-646-2777.

Gratis licenses (referencing $0 in the Total field) are free. Please retain this printable license for your reference. No payment is required.

APPENDIX 4

JOHN WILEY AND SONS LICENSE
TERMS AND CONDITIONS

May 16, 2014

This is a License Agreement between Christine Gabrielse ("You") and John Wiley and Sons ("John Wiley and Sons") provided by Copyright Clearance Center ("CCC"). The license consists of your order details, the terms and conditions provided by John Wiley and Sons, and the payment terms and conditions.

All payments must be made in full to CCC. For payment instructions, please see information listed at the bottom of this form.

License Number	3382720190308
License date	May 05, 2014
Licensed content publisher	John Wiley and Sons
Licensed content publication	Journal of Geophysical Research: Space Physics
Licensed content title	A THEMIS multicase study of dipolarization fronts in the magnetotail plasma sheet
Licensed copyright line	Copyright 2011 by the American Geophysical Union.
Licensed content author	A. Runov,V. Angelopoulos,X.-Z. Zhou,X.-J. Zhang,S. Li,F. Plaschke,J. Bonnell
Licensed content date	May 24, 2011
Start page	n/a
End page	n/a
Type of use	Dissertation/Thesis
Requestor type	University/Academic
Format	Print and electronic
Portion	Figure/table
Number of figures/tables	1
Original Wiley figure/table number(s)	Figure 5
Will you be translating?	No
Title of your thesis / dissertation	Magnetospheric Particle Injections and their Relation to Impulsive, Localized Electric Fields
Expected completion date	Jun 2014
Expected size (number of pages)	208
Total	0.00 USD

TERMS AND CONDITIONS

This copyrighted material is owned by or exclusively licensed to John Wiley & Sons, Inc. or one of its group companies (each a"Wiley Company") or handled on behalf of a society with which a Wiley Company has exclusive publishing rights in relation to a particular work (collectively "WILEY"). By clicking “accept” in connection with completing this licensing transaction, you agree that the following terms and conditions apply to this transaction (along with the billing and payment terms and conditions established by the Copyright Clearance Center Inc., ("CCC's Billing and Payment terms and conditions"), at the time that you opened your Rightslink account (these are available at any time at http://myaccount.copyright.com).

Terms and Conditions

- The materials you have requested permission to reproduce or reuse (the "Wiley Materials") are protected by copyright.

- You are hereby granted a personal, non-exclusive, non-sub licensable (on a stand-alone basis), non-transferable, worldwide, limited license to reproduce the Wiley Materials for the purpose specified in the licensing process. This license is for a one-time use only and limited to any maximum distribution number specified in the license. The first instance of republication or reuse granted by this licence must be completed within two years of the date of the grant of this licence (although copies prepared before the end date may be distributed thereafter). The Wiley Materials shall not be used in any other manner or for any other purpose, beyond what is granted in the license. Permission is granted subject to an appropriate acknowledgement given to the author, title of the material/book/journal and the publisher. You shall also duplicate the copyright notice that appears in the Wiley publication in your use of the Wiley Material. Permission is also granted on the understanding that nowhere in the text is a previously published source acknowledged for all or part of this Wiley Material. Any third party content is expressly excluded from this permission.

- With respect to the Wiley Materials, all rights are reserved. Except as expressly granted by the terms of the license, no part of the Wiley Materials may be copied, modified, adapted (except for minor reformatting required by the new Publication), translated, reproduced, transferred or distributed, in any form or by any means, and no derivative works may be made based on the Wiley Materials without the prior permission of the respective copyright owner. You may not alter, remove or suppress in any manner any copyright, trademark or other notices displayed by the Wiley Materials. You may not license, rent, sell, loan, lease, pledge, offer as security, transfer or assign the Wiley Materials on a stand-alone basis, or any of the rights granted to you hereunder to any other person.

- The Wiley Materials and all of the intellectual property rights therein shall at all times remain the exclusive property of John Wiley & Sons Inc, the Wiley Companies, or their respective licensors, and your interest therein is only that of

having possession of and the right to reproduce the Wiley Materials pursuant to Section 2 herein during the continuance of this Agreement. You agree that you own no right, title or interest in or to the Wiley Materials or any of the intellectual property rights therein. You shall have no rights hereunder other than the license as provided for above in Section 2. No right, license or interest to any trademark, trade name, service mark or other branding ("Marks") of WILEY or its licensors is granted hereunder, and you agree that you shall not assert any such right, license or interest with respect thereto.

- NEITHER WILEY NOR ITS LICENSORS MAKES ANY WARRANTY OR REPRESENTATION OF ANY KIND TO YOU OR ANY THIRD PARTY, EXPRESS, IMPLIED OR STATUTORY, WITH RESPECT TO THE MATERIALS OR THE ACCURACY OF ANY INFORMATION CONTAINED IN THE MATERIALS, INCLUDING, WITHOUT LIMITATION, ANY IMPLIED WARRANTY OF MERCHANTABILITY, ACCURACY, SATISFACTORY QUALITY, FITNESS FOR A PARTICULAR PURPOSE, USABILITY, INTEGRATION OR NON-INFRINGEMENT AND ALL SUCH WARRANTIES ARE HEREBY EXCLUDED BY WILEY AND ITS LICENSORS AND WAIVED BY YOU

- WILEY shall have the right to terminate this Agreement immediately upon breach of this Agreement by you.
- You shall indemnify, defend and hold harmless WILEY, its Licensors and their respective directors, officers, agents and employees, from and against any actual or threatened claims, demands, causes of action or proceedings arising from any breach of this Agreement by you.

- IN NO EVENT SHALL WILEY OR ITS LICENSORS BE LIABLE TO YOU OR ANY OTHER PARTY OR ANY OTHER PERSON OR ENTITY FOR ANY SPECIAL, CONSEQUENTIAL, INCIDENTAL, INDIRECT, EXEMPLARY OR PUNITIVE DAMAGES, HOWEVER CAUSED, ARISING OUT OF OR IN CONNECTION WITH THE DOWNLOADING, PROVISIONING, VIEWING OR USE OF THE MATERIALS REGARDLESS OF THE FORM OF ACTION, WHETHER FOR BREACH OF CONTRACT, BREACH OF WARRANTY, TORT, NEGLIGENCE, INFRINGEMENT OR OTHERWISE (INCLUDING, WITHOUT LIMITATION, DAMAGES BASED ON LOSS OF PROFITS, DATA, FILES, USE, BUSINESS OPPORTUNITY OR CLAIMS OF THIRD PARTIES), AND WHETHER OR NOT THE PARTY HAS BEEN ADVISED OF THE POSSIBILITY OF SUCH DAMAGES. THIS LIMITATION SHALL APPLY NOTWITHSTANDING ANY FAILURE OF ESSENTIAL PURPOSE OF ANY LIMITED REMEDY PROVIDED HEREIN.

- Should any provision of this Agreement be held by a court of competent jurisdiction to be illegal, invalid, or unenforceable, that provision shall be deemed amended to achieve as nearly as possible the same economic effect as the original provision, and the legality, validity and enforceability of the remaining provisions of this

Agreement shall not be affected or impaired thereby.

- The failure of either party to enforce any term or condition of this Agreement shall not constitute a waiver of either party's right to enforce each and every term and condition of this Agreement. No breach under this agreement shall be deemed waived or excused by either party unless such waiver or consent is in writing signed by the party granting such waiver or consent. The waiver by or consent of a party to a breach of any provision of this Agreement shall not operate or be construed as a waiver of or consent to any other or subsequent breach by such other party.

- This Agreement may not be assigned (including by operation of law or otherwise) by you without WILEY's prior written consent.

- Any fee required for this permission shall be non-refundable after thirty (30) days from receipt by the CCC.

- These terms and conditions together with CCC's Billing and Payment terms and conditions (which are incorporated herein) form the entire agreement between you and WILEY concerning this licensing transaction and (in the absence of fraud) supersedes all prior agreements and representations of the parties, oral or written. This Agreement may not be amended except in writing signed by both parties. This Agreement shall be binding upon and inure to the benefit of the parties' successors, legal representatives, and authorized assigns.

- In the event of any conflict between your obligations established by these terms and conditions and those established by CCC's Billing and Payment terms and conditions, these terms and conditions shall prevail.

- WILEY expressly reserves all rights not specifically granted in the combination of (i) the license details provided by you and accepted in the course of this licensing transaction, (ii) these terms and conditions and (iii) CCC's Billing and Payment terms and conditions.

- This Agreement will be void if the Type of Use, Format, Circulation, or Requestor Type was misrepresented during the licensing process.

- This Agreement shall be governed by and construed in accordance with the laws of the State of New York, USA, without regards to such state's conflict of law rules. Any legal action, suit or proceeding arising out of or relating to these Terms and Conditions or the breach thereof shall be instituted in a court of competent jurisdiction in New York County in the State of New York in the United States of America and each party hereby consents and submits to the personal jurisdiction of such court, waives any objection to venue in such court and consents to service of process by registered or certified mail, return receipt requested, at the last known address of such party.

WILEY OPEN ACCESS TERMS AND CONDITIONS

Wiley Publishes Open Access Articles in fully Open Access Journals and in Subscription journals offering Online Open. Although most of the fully Open Access journals publish open access articles under the terms of the Creative Commons Attribution (CC BY) License only, the subscription journals and a few of the Open Access Journals offer a choice of Creative Commons Licenses:: Creative Commons Attribution (CC-BY) license Creative Commons Attribution Non-Commercial (CC-BY-NC) license and Creative Commons Attribution Non-Commercial-NoDerivs (CC-BY-NC-ND) License. The license type is clearly identified on the article.

Copyright in any research article in a journal published as Open Access under a Creative Commons License is retained by the author(s). Authors grant Wiley a license to publish the article and identify itself as the original publisher. Authors also grant any third party the right to use the article freely as long as its integrity is maintained and its original authors, citation details and publisher are identified as follows: [Title of Article/Author/Journal Title and Volume/Issue. Copyright (c) [year] [copyright owner as specified in the Journal]. Links to the final article on Wiley's website are encouraged where applicable.

The Creative Commons Attribution License

The Creative Commons Attribution License (CC-BY) allows users to copy, distribute and transmit an article, adapt the article and make commercial use of the article. The CC-BY license permits commercial and non-commercial re-use of an open access article, as long as the author is properly attributed.

The Creative Commons Attribution License does not affect the moral rights of authors, including without limitation the right not to have their work subjected to derogatory treatment. It also does not affect any other rights held by authors or third parties in the article, including without limitation the rights of privacy and publicity. Use of the article must not assert or imply, whether implicitly or explicitly, any connection with, endorsement or sponsorship of such use by the author, publisher or any other party associated with the article.

For any reuse or distribution, users must include the copyright notice and make clear to others that the article is made available under a Creative Commons Attribution license, linking to the relevant Creative Commons web page.

To the fullest extent permitted by applicable law, the article is made available as is and without representation or warranties of any kind whether express, implied, statutory or otherwise and including, without limitation, warranties of title, merchantability, fitness for a particular purpose, non-infringement, absence of defects, accuracy, or the presence or absence of errors.

Creative Commons Attribution Non-Commercial License

The Creative Commons Attribution Non-Commercial (CC-BY-NC) License permits use, distribution and reproduction in any medium, provided the original work is properly cited and is not used for commercial purposes.(see below)

Creative Commons Attribution-Non-Commercial-NoDerivs License

The Creative Commons Attribution Non-Commercial-NoDerivs License (CC-BY-NC-ND) permits use, distribution and reproduction in any medium, provided the original work is properly cited, is not used for commercial purposes and no modifications or adaptations are made. (see below)

Use by non-commercial users

For non-commercial and non-promotional purposes, individual users may access, download, copy, display and redistribute to colleagues Wiley Open Access articles, as well as adapt, translate, text- and data-mine the content subject to the following conditions:

- The authors' moral rights are not compromised. These rights include the right of "paternity" (also known as "attribution" - the right for the author to be identified as such) and "integrity" (the right for the author not to have the work altered in such a way that the author's reputation or integrity may be impugned).
- Where content in the article is identified as belonging to a third party, it is the obligation of the user to ensure that any reuse complies with the copyright policies of the owner of that content.
- If article content is copied, downloaded or otherwise reused for non-commercial research and education purposes, a link to the appropriate bibliographic citation (authors, journal, article title, volume, issue, page numbers, DOI and the link to the definitive published version on **Wiley Online Library**) should be maintained. Copyright notices and disclaimers must not be deleted.
- Any translations, for which a prior translation agreement with Wiley has not been agreed, must prominently display the statement: "This is an unofficial translation of an article that appeared in a Wiley publication. The publisher has not endorsed this translation."

Use by commercial "for-profit" organisations

Use of Wiley Open Access articles for commercial, promotional, or marketing purposes requires further explicit permission from Wiley and will be subject to a fee. Commercial purposes include:

- Copying or downloading of articles, or linking to such articles for further redistribution, sale or licensing;
- Copying, downloading or posting by a site or service that incorporates advertising

with such content;

- The inclusion or incorporation of article content in other works or services (other than normal quotations with an appropriate citation) that is then available for sale or licensing, for a fee (for example, a compilation produced for marketing purposes, inclusion in a sales pack)

- Use of article content (other than normal quotations with appropriate citation) by for-profit organisations for promotional purposes

- Linking to article content in e-mails redistributed for promotional, marketing or educational purposes;

- Use for the purposes of monetary reward by means of sale, resale, licence, loan, transfer or other form of commercial exploitation such as marketing products

- Print reprints of Wiley Open Access articles can be purchased from: corporatesales@wiley.com

Further details can be found on Wiley Online Library
http://olabout.wiley.com/WileyCDA/Section/id-410895.html

Other Terms and Conditions:

v1.9

If you would like to pay for this license now, please remit this license along with your payment made payable to "COPYRIGHT CLEARANCE CENTER" otherwise you will be invoiced within 48 hours of the license date. Payment should be in the form of a check or money order referencing your account number and this invoice number 501295265.
Once you receive your invoice for this order, you may pay your invoice by credit card. Please follow instructions provided at that time.

Make Payment To:
Copyright Clearance Center
Dept 001
P.O. Box 843006
Boston, MA 02284-3006

For suggestions or comments regarding this order, contact RightsLink Customer Support: customercare@copyright.com or +1-877-622-5543 (toll free in the US) or +1-978-646-2777.

Gratis licenses (referencing $0 in the Total field) are free. Please retain this printable license for your reference. No payment is required.

APPENDIX 5

JOHN WILEY AND SONS LICENSE
TERMS AND CONDITIONS

May 16, 2014

This is a License Agreement between Christine Gabrielse ("You") and John Wiley and Sons ("John Wiley and Sons") provided by Copyright Clearance Center ("CCC"). The license consists of your order details, the terms and conditions provided by John Wiley and Sons, and the payment terms and conditions.

All payments must be made in full to CCC. For payment instructions, please see information listed at the bottom of this form.

License Number	3382720561258
License date	May 05, 2014
Licensed content publisher	John Wiley and Sons
Licensed content publication	Journal of Geophysical Research: Space Physics
Licensed content title	Substorm injection modeling with nondipolar, time-dependent background field
Licensed copyright line	Copyright 2004 by the American Geophysical Union.
Licensed content author	Sorin Zaharia,J. Birn,R. H. W. Friedel,G. D. Reeves,M. F. Thomsen,C. Z. Cheng
Licensed content date	Oct 23, 2004
Start page	n/a
End page	n/a
Type of use	Dissertation/Thesis
Requestor type	University/Academic
Format	Print and electronic
Portion	Figure/table
Number of figures/tables	1
Original Wiley figure/table number(s)	Figure 4
Will you be translating?	No
Title of your thesis / dissertation	Magnetospheric Particle Injections and their Relation to Impulsive, Localized Electric Fields
Expected completion date	Jun 2014
Expected size (number of pages)	208
Total	0.00 USD

TERMS AND CONDITIONS

This copyrighted material is owned by or exclusively licensed to John Wiley & Sons, Inc. or one of its group companies (each a"Wiley Company") or handled on behalf of a society with which a Wiley Company has exclusive publishing rights in relation to a particular work (collectively "WILEY"). By clicking “accept” in connection with completing this licensing transaction, you agree that the following terms and conditions apply to this transaction (along with the billing and payment terms and conditions established by the Copyright Clearance Center Inc., ("CCC's Billing and Payment terms and conditions"), at the time that you opened your Rightslink account (these are available at any time at http://myaccount.copyright.com).

Terms and Conditions

- The materials you have requested permission to reproduce or reuse (the "Wiley Materials") are protected by copyright.

- You are hereby granted a personal, non-exclusive, non-sub licensable (on a stand-alone basis), non-transferable, worldwide, limited license to reproduce the Wiley Materials for the purpose specified in the licensing process. This license is for a one-time use only and limited to any maximum distribution number specified in the license. The first instance of republication or reuse granted by this licence must be completed within two years of the date of the grant of this licence (although copies prepared before the end date may be distributed thereafter). The Wiley Materials shall not be used in any other manner or for any other purpose, beyond what is granted in the license. Permission is granted subject to an appropriate acknowledgement given to the author, title of the material/book/journal and the publisher. You shall also duplicate the copyright notice that appears in the Wiley publication in your use of the Wiley Material. Permission is also granted on the understanding that nowhere in the text is a previously published source acknowledged for all or part of this Wiley Material. Any third party content is expressly excluded from this permission.

- With respect to the Wiley Materials, all rights are reserved. Except as expressly granted by the terms of the license, no part of the Wiley Materials may be copied, modified, adapted (except for minor reformatting required by the new Publication), translated, reproduced, transferred or distributed, in any form or by any means, and no derivative works may be made based on the Wiley Materials without the prior permission of the respective copyright owner. You may not alter, remove or suppress in any manner any copyright, trademark or other notices displayed by the Wiley Materials. You may not license, rent, sell, loan, lease, pledge, offer as security, transfer or assign the Wiley Materials on a stand-alone basis, or any of the rights granted to you hereunder to any other person.

- The Wiley Materials and all of the intellectual property rights therein shall at all times remain the exclusive property of John Wiley & Sons Inc, the Wiley

Companies, or their respective licensors, and your interest therein is only that of having possession of and the right to reproduce the Wiley Materials pursuant to Section 2 herein during the continuance of this Agreement. You agree that you own no right, title or interest in or to the Wiley Materials or any of the intellectual property rights therein. You shall have no rights hereunder other than the license as provided for above in Section 2. No right, license or interest to any trademark, trade name, service mark or other branding ("Marks") of WILEY or its licensors is granted hereunder, and you agree that you shall not assert any such right, license or interest with respect thereto.

- NEITHER WILEY NOR ITS LICENSORS MAKES ANY WARRANTY OR REPRESENTATION OF ANY KIND TO YOU OR ANY THIRD PARTY, EXPRESS, IMPLIED OR STATUTORY, WITH RESPECT TO THE MATERIALS OR THE ACCURACY OF ANY INFORMATION CONTAINED IN THE MATERIALS, INCLUDING, WITHOUT LIMITATION, ANY IMPLIED WARRANTY OF MERCHANTABILITY, ACCURACY, SATISFACTORY QUALITY, FITNESS FOR A PARTICULAR PURPOSE, USABILITY, INTEGRATION OR NON-INFRINGEMENT AND ALL SUCH WARRANTIES ARE HEREBY EXCLUDED BY WILEY AND ITS LICENSORS AND WAIVED BY YOU

- WILEY shall have the right to terminate this Agreement immediately upon breach of this Agreement by you.
- You shall indemnify, defend and hold harmless WILEY, its Licensors and their respective directors, officers, agents and employees, from and against any actual or threatened claims, demands, causes of action or proceedings arising from any breach of this Agreement by you.

- IN NO EVENT SHALL WILEY OR ITS LICENSORS BE LIABLE TO YOU OR ANY OTHER PARTY OR ANY OTHER PERSON OR ENTITY FOR ANY SPECIAL, CONSEQUENTIAL, INCIDENTAL, INDIRECT, EXEMPLARY OR PUNITIVE DAMAGES, HOWEVER CAUSED, ARISING OUT OF OR IN CONNECTION WITH THE DOWNLOADING, PROVISIONING, VIEWING OR USE OF THE MATERIALS REGARDLESS OF THE FORM OF ACTION, WHETHER FOR BREACH OF CONTRACT, BREACH OF WARRANTY, TORT, NEGLIGENCE, INFRINGEMENT OR OTHERWISE (INCLUDING, WITHOUT LIMITATION, DAMAGES BASED ON LOSS OF PROFITS, DATA, FILES, USE, BUSINESS OPPORTUNITY OR CLAIMS OF THIRD PARTIES), AND WHETHER OR NOT THE PARTY HAS BEEN ADVISED OF THE POSSIBILITY OF SUCH DAMAGES. THIS LIMITATION SHALL APPLY NOTWITHSTANDING ANY FAILURE OF ESSENTIAL PURPOSE OF ANY LIMITED REMEDY PROVIDED HEREIN.

- Should any provision of this Agreement be held by a court of competent jurisdiction to be illegal, invalid, or unenforceable, that provision shall be deemed amended to achieve as nearly as possible the same economic effect as the original provision, and the legality, validity and enforceability of the remaining provisions of this

Agreement shall not be affected or impaired thereby.

- The failure of either party to enforce any term or condition of this Agreement shall not constitute a waiver of either party's right to enforce each and every term and condition of this Agreement. No breach under this agreement shall be deemed waived or excused by either party unless such waiver or consent is in writing signed by the party granting such waiver or consent. The waiver by or consent of a party to a breach of any provision of this Agreement shall not operate or be construed as a waiver of or consent to any other or subsequent breach by such other party.

- This Agreement may not be assigned (including by operation of law or otherwise) by you without WILEY's prior written consent.

- Any fee required for this permission shall be non-refundable after thirty (30) days from receipt by the CCC.

- These terms and conditions together with CCC's Billing and Payment terms and conditions (which are incorporated herein) form the entire agreement between you and WILEY concerning this licensing transaction and (in the absence of fraud) supersedes all prior agreements and representations of the parties, oral or written. This Agreement may not be amended except in writing signed by both parties. This Agreement shall be binding upon and inure to the benefit of the parties' successors, legal representatives, and authorized assigns.

- In the event of any conflict between your obligations established by these terms and conditions and those established by CCC's Billing and Payment terms and conditions, these terms and conditions shall prevail.

- WILEY expressly reserves all rights not specifically granted in the combination of (i) the license details provided by you and accepted in the course of this licensing transaction, (ii) these terms and conditions and (iii) CCC's Billing and Payment terms and conditions.

- This Agreement will be void if the Type of Use, Format, Circulation, or Requestor Type was misrepresented during the licensing process.

- This Agreement shall be governed by and construed in accordance with the laws of the State of New York, USA, without regards to such state's conflict of law rules. Any legal action, suit or proceeding arising out of or relating to these Terms and Conditions or the breach thereof shall be instituted in a court of competent jurisdiction in New York County in the State of New York in the United States of America and each party hereby consents and submits to the personal jurisdiction of such court, waives any objection to venue in such court and consents to service of process by registered or certified mail, return receipt requested, at the last known address of such party.

The Creative Commons Attribution Non-Commercial (CC-BY-NC) License permits use, distribution and reproduction in any medium, provided the original work is properly cited and is not used for commercial purposes.(see below)

Creative Commons Attribution-Non-Commercial-NoDerivs License

The Creative Commons Attribution Non-Commercial-NoDerivs License (CC-BY-NC-ND) permits use, distribution and reproduction in any medium, provided the original work is properly cited, is not used for commercial purposes and no modifications or adaptations are made. (see below)

Use by non-commercial users

For non-commercial and non-promotional purposes, individual users may access, download, copy, display and redistribute to colleagues Wiley Open Access articles, as well as adapt, translate, text- and data-mine the content subject to the following conditions:

- The authors' moral rights are not compromised. These rights include the right of "paternity" (also known as "attribution" - the right for the author to be identified as such) and "integrity" (the right for the author not to have the work altered in such a way that the author's reputation or integrity may be impugned).
- Where content in the article is identified as belonging to a third party, it is the obligation of the user to ensure that any reuse complies with the copyright policies of the owner of that content.
- If article content is copied, downloaded or otherwise reused for non-commercial research and education purposes, a link to the appropriate bibliographic citation (authors, journal, article title, volume, issue, page numbers, DOI and the link to the definitive published version on **Wiley Online Library**) should be maintained. Copyright notices and disclaimers must not be deleted.
- Any translations, for which a prior translation agreement with Wiley has not been agreed, must prominently display the statement: "This is an unofficial translation of an article that appeared in a Wiley publication. The publisher has not endorsed this translation."

Use by commercial "for-profit" organisations

Use of Wiley Open Access articles for commercial, promotional, or marketing purposes requires further explicit permission from Wiley and will be subject to a fee. Commercial purposes include:

- Copying or downloading of articles, or linking to such articles for further redistribution, sale or licensing;
- Copying, downloading or posting by a site or service that incorporates advertising

with such content;

- The inclusion or incorporation of article content in other works or services (other than normal quotations with an appropriate citation) that is then available for sale or licensing, for a fee (for example, a compilation produced for marketing purposes, inclusion in a sales pack)

- Use of article content (other than normal quotations with appropriate citation) by for-profit organisations for promotional purposes

- Linking to article content in e-mails redistributed for promotional, marketing or educational purposes;

- Use for the purposes of monetary reward by means of sale, resale, licence, loan, transfer or other form of commercial exploitation such as marketing products

- Print reprints of Wiley Open Access articles can be purchased from: corporatesales@wiley.com

Further details can be found on Wiley Online Library
http://olabout.wiley.com/WileyCDA/Section/id-410895.html

Other Terms and Conditions:

v1.9

If you would like to pay for this license now, please remit this license along with your payment made payable to "COPYRIGHT CLEARANCE CENTER" otherwise you will be invoiced within 48 hours of the license date. Payment should be in the form of a check or money order referencing your account number and this invoice number 501295269.
Once you receive your invoice for this order, you may pay your invoice by credit card. Please follow instructions provided at that time.

Make Payment To:
Copyright Clearance Center
Dept 001
P.O. Box 843006
Boston, MA 02284-3006

For suggestions or comments regarding this order, contact RightsLink Customer Support: customercare@copyright.com or +1-877-622-5543 (toll free in the US) or +1-978-646-2777.

Gratis licenses (referencing $0 in the Total field) are free. Please retain this printable license for your reference. No payment is required.

APPENDIX 6

JOHN WILEY AND SONS LICENSE
TERMS AND CONDITIONS

May 16, 2014

This is a License Agreement between Christine Gabrielse ("You") and John Wiley and Sons ("John Wiley and Sons") provided by Copyright Clearance Center ("CCC"). The license consists of your order details, the terms and conditions provided by John Wiley and Sons, and the payment terms and conditions.

All payments must be made in full to CCC. For payment instructions, please see information listed at the bottom of this form.

License Number	3382720774458
License date	May 05, 2014
Licensed content publisher	John Wiley and Sons
Licensed content publication	Journal of Geophysical Research: Space Physics
Licensed content title	Modeling energetic particle injections in dynamic pulse fields with varying propagation speeds
Licensed copyright line	Copyright 2002 by the American Geophysical Union.
Licensed content author	Theodore E. Sarris,Xinlin Li,N. Tsaggas,N. Paschalidis
Licensed content date	Mar 5, 2002
Start page	SMP 1-1
End page	SMP 1-10
Type of use	Dissertation/Thesis
Requestor type	University/Academic
Format	Print and electronic
Portion	Figure/table
Number of figures/tables	1
Original Wiley figure/table number(s)	Figure 3
Will you be translating?	No
Title of your thesis / dissertation	Magnetospheric Particle Injections and their Relation to Impulsive, Localized Electric Fields
Expected completion date	Jun 2014
Expected size (number of pages)	208
Total	0.00 USD

TERMS AND CONDITIONS

This copyrighted material is owned by or exclusively licensed to John Wiley & Sons, Inc. or one of its group companies (each a"Wiley Company") or handled on behalf of a society with which a Wiley Company has exclusive publishing rights in relation to a particular work (collectively "WILEY"). By clicking “accept” in connection with completing this licensing transaction, you agree that the following terms and conditions apply to this transaction (along with the billing and payment terms and conditions established by the Copyright Clearance Center Inc., ("CCC's Billing and Payment terms and conditions"), at the time that you opened your Rightslink account (these are available at any time at http://myaccount.copyright.com).

Terms and Conditions

- The materials you have requested permission to reproduce or reuse (the "Wiley Materials") are protected by copyright.

- You are hereby granted a personal, non-exclusive, non-sub licensable (on a stand-alone basis), non-transferable, worldwide, limited license to reproduce the Wiley Materials for the purpose specified in the licensing process. This license is for a one-time use only and limited to any maximum distribution number specified in the license. The first instance of republication or reuse granted by this licence must be completed within two years of the date of the grant of this licence (although copies prepared before the end date may be distributed thereafter). The Wiley Materials shall not be used in any other manner or for any other purpose, beyond what is granted in the license. Permission is granted subject to an appropriate acknowledgement given to the author, title of the material/book/journal and the publisher. You shall also duplicate the copyright notice that appears in the Wiley publication in your use of the Wiley Material. Permission is also granted on the understanding that nowhere in the text is a previously published source acknowledged for all or part of this Wiley Material. Any third party content is expressly excluded from this permission.

- With respect to the Wiley Materials, all rights are reserved. Except as expressly granted by the terms of the license, no part of the Wiley Materials may be copied, modified, adapted (except for minor reformatting required by the new Publication), translated, reproduced, transferred or distributed, in any form or by any means, and no derivative works may be made based on the Wiley Materials without the prior permission of the respective copyright owner. You may not alter, remove or suppress in any manner any copyright, trademark or other notices displayed by the Wiley Materials. You may not license, rent, sell, loan, lease, pledge, offer as security, transfer or assign the Wiley Materials on a stand-alone basis, or any of the rights granted to you hereunder to any other person.

- The Wiley Materials and all of the intellectual property rights therein shall at all times remain the exclusive property of John Wiley & Sons Inc, the Wiley

Companies, or their respective licensors, and your interest therein is only that of having possession of and the right to reproduce the Wiley Materials pursuant to Section 2 herein during the continuance of this Agreement. You agree that you own no right, title or interest in or to the Wiley Materials or any of the intellectual property rights therein. You shall have no rights hereunder other than the license as provided for above in Section 2. No right, license or interest to any trademark, trade name, service mark or other branding ("Marks") of WILEY or its licensors is granted hereunder, and you agree that you shall not assert any such right, license or interest with respect thereto.

- NEITHER WILEY NOR ITS LICENSORS MAKES ANY WARRANTY OR REPRESENTATION OF ANY KIND TO YOU OR ANY THIRD PARTY, EXPRESS, IMPLIED OR STATUTORY, WITH RESPECT TO THE MATERIALS OR THE ACCURACY OF ANY INFORMATION CONTAINED IN THE MATERIALS, INCLUDING, WITHOUT LIMITATION, ANY IMPLIED WARRANTY OF MERCHANTABILITY, ACCURACY, SATISFACTORY QUALITY, FITNESS FOR A PARTICULAR PURPOSE, USABILITY, INTEGRATION OR NON-INFRINGEMENT AND ALL SUCH WARRANTIES ARE HEREBY EXCLUDED BY WILEY AND ITS LICENSORS AND WAIVED BY YOU

- WILEY shall have the right to terminate this Agreement immediately upon breach of this Agreement by you.
- You shall indemnify, defend and hold harmless WILEY, its Licensors and their respective directors, officers, agents and employees, from and against any actual or threatened claims, demands, causes of action or proceedings arising from any breach of this Agreement by you.

- IN NO EVENT SHALL WILEY OR ITS LICENSORS BE LIABLE TO YOU OR ANY OTHER PARTY OR ANY OTHER PERSON OR ENTITY FOR ANY SPECIAL, CONSEQUENTIAL, INCIDENTAL, INDIRECT, EXEMPLARY OR PUNITIVE DAMAGES, HOWEVER CAUSED, ARISING OUT OF OR IN CONNECTION WITH THE DOWNLOADING, PROVISIONING, VIEWING OR USE OF THE MATERIALS REGARDLESS OF THE FORM OF ACTION, WHETHER FOR BREACH OF CONTRACT, BREACH OF WARRANTY, TORT, NEGLIGENCE, INFRINGEMENT OR OTHERWISE (INCLUDING, WITHOUT LIMITATION, DAMAGES BASED ON LOSS OF PROFITS, DATA, FILES, USE, BUSINESS OPPORTUNITY OR CLAIMS OF THIRD PARTIES), AND WHETHER OR NOT THE PARTY HAS BEEN ADVISED OF THE POSSIBILITY OF SUCH DAMAGES. THIS LIMITATION SHALL APPLY NOTWITHSTANDING ANY FAILURE OF ESSENTIAL PURPOSE OF ANY LIMITED REMEDY PROVIDED HEREIN.

- Should any provision of this Agreement be held by a court of competent jurisdiction to be illegal, invalid, or unenforceable, that provision shall be deemed amended to achieve as nearly as possible the same economic effect as the original provision, and the legality, validity and enforceability of the remaining provisions of this

Agreement shall not be affected or impaired thereby.

- The failure of either party to enforce any term or condition of this Agreement shall not constitute a waiver of either party's right to enforce each and every term and condition of this Agreement. No breach under this agreement shall be deemed waived or excused by either party unless such waiver or consent is in writing signed by the party granting such waiver or consent. The waiver by or consent of a party to a breach of any provision of this Agreement shall not operate or be construed as a waiver of or consent to any other or subsequent breach by such other party.

- This Agreement may not be assigned (including by operation of law or otherwise) by you without WILEY's prior written consent.

- Any fee required for this permission shall be non-refundable after thirty (30) days from receipt by the CCC.

- These terms and conditions together with CCC's Billing and Payment terms and conditions (which are incorporated herein) form the entire agreement between you and WILEY concerning this licensing transaction and (in the absence of fraud) supersedes all prior agreements and representations of the parties, oral or written. This Agreement may not be amended except in writing signed by both parties. This Agreement shall be binding upon and inure to the benefit of the parties' successors, legal representatives, and authorized assigns.

- In the event of any conflict between your obligations established by these terms and conditions and those established by CCC's Billing and Payment terms and conditions, these terms and conditions shall prevail.

- WILEY expressly reserves all rights not specifically granted in the combination of (i) the license details provided by you and accepted in the course of this licensing transaction, (ii) these terms and conditions and (iii) CCC's Billing and Payment terms and conditions.

- This Agreement will be void if the Type of Use, Format, Circulation, or Requestor Type was misrepresented during the licensing process.

- This Agreement shall be governed by and construed in accordance with the laws of the State of New York, USA, without regards to such state's conflict of law rules. Any legal action, suit or proceeding arising out of or relating to these Terms and Conditions or the breach thereof shall be instituted in a court of competent jurisdiction in New York County in the State of New York in the United States of America and each party hereby consents and submits to the personal jurisdiction of such court, waives any objection to venue in such court and consents to service of process by registered or certified mail, return receipt requested, at the last known address of such party.

WILEY OPEN ACCESS TERMS AND CONDITIONS

Wiley Publishes Open Access Articles in fully Open Access Journals and in Subscription journals offering Online Open. Although most of the fully Open Access journals publish open access articles under the terms of the Creative Commons Attribution (CC BY) License only, the subscription journals and a few of the Open Access Journals offer a choice of Creative Commons Licenses:: Creative Commons Attribution (CC-BY) license Creative Commons Attribution Non-Commercial (CC-BY-NC) license and Creative Commons Attribution Non-Commercial-NoDerivs (CC-BY-NC-ND) License. The license type is clearly identified on the article.

Copyright in any research article in a journal published as Open Access under a Creative Commons License is retained by the author(s). Authors grant Wiley a license to publish the article and identify itself as the original publisher. Authors also grant any third party the right to use the article freely as long as its integrity is maintained and its original authors, citation details and publisher are identified as follows: [Title of Article/Author/Journal Title and Volume/Issue. Copyright (c) [year] [copyright owner as specified in the Journal]. Links to the final article on Wiley's website are encouraged where applicable.

The Creative Commons Attribution License

The Creative Commons Attribution License (CC-BY) allows users to copy, distribute and transmit an article, adapt the article and make commercial use of the article. The CC-BY license permits commercial and non-commercial re-use of an open access article, as long as the author is properly attributed.

The Creative Commons Attribution License does not affect the moral rights of authors, including without limitation the right not to have their work subjected to derogatory treatment. It also does not affect any other rights held by authors or third parties in the article, including without limitation the rights of privacy and publicity. Use of the article must not assert or imply, whether implicitly or explicitly, any connection with, endorsement or sponsorship of such use by the author, publisher or any other party associated with the article.

For any reuse or distribution, users must include the copyright notice and make clear to others that the article is made available under a Creative Commons Attribution license, linking to the relevant Creative Commons web page.

To the fullest extent permitted by applicable law, the article is made available as is and without representation or warranties of any kind whether express, implied, statutory or otherwise and including, without limitation, warranties of title, merchantability, fitness for a particular purpose, non-infringement, absence of defects, accuracy, or the presence or absence of errors.

Creative Commons Attribution Non-Commercial License

The Creative Commons Attribution Non-Commercial (CC-BY-NC) License permits use, distribution and reproduction in any medium, provided the original work is properly cited and is not used for commercial purposes.(see below)

Creative Commons Attribution-Non-Commercial-NoDerivs License

The Creative Commons Attribution Non-Commercial-NoDerivs License (CC-BY-NC-ND) permits use, distribution and reproduction in any medium, provided the original work is properly cited, is not used for commercial purposes and no modifications or adaptations are made. (see below)

Use by non-commercial users

For non-commercial and non-promotional purposes, individual users may access, download, copy, display and redistribute to colleagues Wiley Open Access articles, as well as adapt, translate, text- and data-mine the content subject to the following conditions:

- The authors' moral rights are not compromised. These rights include the right of "paternity" (also known as "attribution" - the right for the author to be identified as such) and "integrity" (the right for the author not to have the work altered in such a way that the author's reputation or integrity may be impugned).
- Where content in the article is identified as belonging to a third party, it is the obligation of the user to ensure that any reuse complies with the copyright policies of the owner of that content.
- If article content is copied, downloaded or otherwise reused for non-commercial research and education purposes, a link to the appropriate bibliographic citation (authors, journal, article title, volume, issue, page numbers, DOI and the link to the definitive published version on **Wiley Online Library**) should be maintained. Copyright notices and disclaimers must not be deleted.
- Any translations, for which a prior translation agreement with Wiley has not been agreed, must prominently display the statement: "This is an unofficial translation of an article that appeared in a Wiley publication. The publisher has not endorsed this translation."

Use by commercial "for-profit" organisations

Use of Wiley Open Access articles for commercial, promotional, or marketing purposes requires further explicit permission from Wiley and will be subject to a fee. Commercial purposes include:

- Copying or downloading of articles, or linking to such articles for further redistribution, sale or licensing;
- Copying, downloading or posting by a site or service that incorporates advertising

with such content;

- The inclusion or incorporation of article content in other works or services (other than normal quotations with an appropriate citation) that is then available for sale or licensing, for a fee (for example, a compilation produced for marketing purposes, inclusion in a sales pack)

- Use of article content (other than normal quotations with appropriate citation) by for-profit organisations for promotional purposes

- Linking to article content in e-mails redistributed for promotional, marketing or educational purposes;

- Use for the purposes of monetary reward by means of sale, resale, licence, loan, transfer or other form of commercial exploitation such as marketing products

- Print reprints of Wiley Open Access articles can be purchased from: corporatesales@wiley.com

Further details can be found on Wiley Online Library
http://olabout.wiley.com/WileyCDA/Section/id-410895.html

Other Terms and Conditions:

v1.9

If you would like to pay for this license now, please remit this license along with your payment made payable to "COPYRIGHT CLEARANCE CENTER" otherwise you will be invoiced within 48 hours of the license date. Payment should be in the form of a check or money order referencing your account number and this invoice number 501295272.
Once you receive your invoice for this order, you may pay your invoice by credit card. Please follow instructions provided at that time.

Make Payment To:
Copyright Clearance Center
Dept 001
P.O. Box 843006
Boston, MA 02284-3006

For suggestions or comments regarding this order, contact RightsLink Customer Support: customercare@copyright.com or +1-877-622-5543 (toll free in the US) or +1-978-646-2777.

Gratis licenses (referencing $0 in the Total field) are free. Please retain this printable license for your reference. No payment is required.

APPENDIX 7

JOHN WILEY AND SONS LICENSE
TERMS AND CONDITIONS

May 16, 2014

This is a License Agreement between Christine Gabrielse ("You") and John Wiley and Sons ("John Wiley and Sons") provided by Copyright Clearance Center ("CCC"). The license consists of your order details, the terms and conditions provided by John Wiley and Sons, and the payment terms and conditions.

All payments must be made in full to CCC. For payment instructions, please see information listed at the bottom of this form.

License Number	3382720696274
License date	May 05, 2014
Licensed content publisher	John Wiley and Sons
Licensed content publication	Journal of Geophysical Research: Space Physics
Licensed content title	Modeling energetic particle injections in dynamic pulse fields with varying propagation speeds
Licensed copyright line	Copyright 2002 by the American Geophysical Union.
Licensed content author	Theodore E. Sarris,Xinlin Li,N. Tsaggas,N. Paschalidis
Licensed content date	Mar 5, 2002
Start page	SMP 1-1
End page	SMP 1-10
Type of use	Dissertation/Thesis
Requestor type	University/Academic
Format	Print and electronic
Portion	Figure/table
Number of figures/tables	1
Original Wiley figure/table number(s)	Figure 4
Will you be translating?	No
Title of your thesis / dissertation	Magnetospheric Particle Injections and their Relation to Impulsive, Localized Electric Fields
Expected completion date	Jun 2014
Expected size (number of pages)	208
Total	0.00 USD

TERMS AND CONDITIONS

This copyrighted material is owned by or exclusively licensed to John Wiley & Sons, Inc. or one of its group companies (each a"Wiley Company") or handled on behalf of a society with which a Wiley Company has exclusive publishing rights in relation to a particular work (collectively "WILEY"). By clicking “accept” in connection with completing this licensing transaction, you agree that the following terms and conditions apply to this transaction (along with the billing and payment terms and conditions established by the Copyright Clearance Center Inc., ("CCC's Billing and Payment terms and conditions"), at the time that you opened your Rightslink account (these are available at any time at http://myaccount.copyright.com).

Terms and Conditions

- The materials you have requested permission to reproduce or reuse (the "Wiley Materials") are protected by copyright.

- You are hereby granted a personal, non-exclusive, non-sub licensable (on a stand-alone basis), non-transferable, worldwide, limited license to reproduce the Wiley Materials for the purpose specified in the licensing process. This license is for a one-time use only and limited to any maximum distribution number specified in the license. The first instance of republication or reuse granted by this licence must be completed within two years of the date of the grant of this licence (although copies prepared before the end date may be distributed thereafter). The Wiley Materials shall not be used in any other manner or for any other purpose, beyond what is granted in the license. Permission is granted subject to an appropriate acknowledgement given to the author, title of the material/book/journal and the publisher. You shall also duplicate the copyright notice that appears in the Wiley publication in your use of the Wiley Material. Permission is also granted on the understanding that nowhere in the text is a previously published source acknowledged for all or part of this Wiley Material. Any third party content is expressly excluded from this permission.

- With respect to the Wiley Materials, all rights are reserved. Except as expressly granted by the terms of the license, no part of the Wiley Materials may be copied, modified, adapted (except for minor reformatting required by the new Publication), translated, reproduced, transferred or distributed, in any form or by any means, and no derivative works may be made based on the Wiley Materials without the prior permission of the respective copyright owner. You may not alter, remove or suppress in any manner any copyright, trademark or other notices displayed by the Wiley Materials. You may not license, rent, sell, loan, lease, pledge, offer as security, transfer or assign the Wiley Materials on a stand-alone basis, or any of the rights granted to you hereunder to any other person.

- The Wiley Materials and all of the intellectual property rights therein shall at all times remain the exclusive property of John Wiley & Sons Inc, the Wiley

Companies, or their respective licensors, and your interest therein is only that of having possession of and the right to reproduce the Wiley Materials pursuant to Section 2 herein during the continuance of this Agreement. You agree that you own no right, title or interest in or to the Wiley Materials or any of the intellectual property rights therein. You shall have no rights hereunder other than the license as provided for above in Section 2. No right, license or interest to any trademark, trade name, service mark or other branding ("Marks") of WILEY or its licensors is granted hereunder, and you agree that you shall not assert any such right, license or interest with respect thereto.

- NEITHER WILEY NOR ITS LICENSORS MAKES ANY WARRANTY OR REPRESENTATION OF ANY KIND TO YOU OR ANY THIRD PARTY, EXPRESS, IMPLIED OR STATUTORY, WITH RESPECT TO THE MATERIALS OR THE ACCURACY OF ANY INFORMATION CONTAINED IN THE MATERIALS, INCLUDING, WITHOUT LIMITATION, ANY IMPLIED WARRANTY OF MERCHANTABILITY, ACCURACY, SATISFACTORY QUALITY, FITNESS FOR A PARTICULAR PURPOSE, USABILITY, INTEGRATION OR NON-INFRINGEMENT AND ALL SUCH WARRANTIES ARE HEREBY EXCLUDED BY WILEY AND ITS LICENSORS AND WAIVED BY YOU

- WILEY shall have the right to terminate this Agreement immediately upon breach of this Agreement by you.
- You shall indemnify, defend and hold harmless WILEY, its Licensors and their respective directors, officers, agents and employees, from and against any actual or threatened claims, demands, causes of action or proceedings arising from any breach of this Agreement by you.

- IN NO EVENT SHALL WILEY OR ITS LICENSORS BE LIABLE TO YOU OR ANY OTHER PARTY OR ANY OTHER PERSON OR ENTITY FOR ANY SPECIAL, CONSEQUENTIAL, INCIDENTAL, INDIRECT, EXEMPLARY OR PUNITIVE DAMAGES, HOWEVER CAUSED, ARISING OUT OF OR IN CONNECTION WITH THE DOWNLOADING, PROVISIONING, VIEWING OR USE OF THE MATERIALS REGARDLESS OF THE FORM OF ACTION, WHETHER FOR BREACH OF CONTRACT, BREACH OF WARRANTY, TORT, NEGLIGENCE, INFRINGEMENT OR OTHERWISE (INCLUDING, WITHOUT LIMITATION, DAMAGES BASED ON LOSS OF PROFITS, DATA, FILES, USE, BUSINESS OPPORTUNITY OR CLAIMS OF THIRD PARTIES), AND WHETHER OR NOT THE PARTY HAS BEEN ADVISED OF THE POSSIBILITY OF SUCH DAMAGES. THIS LIMITATION SHALL APPLY NOTWITHSTANDING ANY FAILURE OF ESSENTIAL PURPOSE OF ANY LIMITED REMEDY PROVIDED HEREIN.

- Should any provision of this Agreement be held by a court of competent jurisdiction to be illegal, invalid, or unenforceable, that provision shall be deemed amended to achieve as nearly as possible the same economic effect as the original provision, and the legality, validity and enforceability of the remaining provisions of this

Agreement shall not be affected or impaired thereby.

- The failure of either party to enforce any term or condition of this Agreement shall not constitute a waiver of either party's right to enforce each and every term and condition of this Agreement. No breach under this agreement shall be deemed waived or excused by either party unless such waiver or consent is in writing signed by the party granting such waiver or consent. The waiver by or consent of a party to a breach of any provision of this Agreement shall not operate or be construed as a waiver of or consent to any other or subsequent breach by such other party.

- This Agreement may not be assigned (including by operation of law or otherwise) by you without WILEY's prior written consent.

- Any fee required for this permission shall be non-refundable after thirty (30) days from receipt by the CCC.

- These terms and conditions together with CCC's Billing and Payment terms and conditions (which are incorporated herein) form the entire agreement between you and WILEY concerning this licensing transaction and (in the absence of fraud) supersedes all prior agreements and representations of the parties, oral or written. This Agreement may not be amended except in writing signed by both parties. This Agreement shall be binding upon and inure to the benefit of the parties' successors, legal representatives, and authorized assigns.

- In the event of any conflict between your obligations established by these terms and conditions and those established by CCC's Billing and Payment terms and conditions, these terms and conditions shall prevail.

- WILEY expressly reserves all rights not specifically granted in the combination of (i) the license details provided by you and accepted in the course of this licensing transaction, (ii) these terms and conditions and (iii) CCC's Billing and Payment terms and conditions.

- This Agreement will be void if the Type of Use, Format, Circulation, or Requestor Type was misrepresented during the licensing process.

- This Agreement shall be governed by and construed in accordance with the laws of the State of New York, USA, without regards to such state's conflict of law rules. Any legal action, suit or proceeding arising out of or relating to these Terms and Conditions or the breach thereof shall be instituted in a court of competent jurisdiction in New York County in the State of New York in the United States of America and each party hereby consents and submits to the personal jurisdiction of such court, waives any objection to venue in such court and consents to service of process by registered or certified mail, return receipt requested, at the last known address of such party.

WILEY OPEN ACCESS TERMS AND CONDITIONS

Wiley Publishes Open Access Articles in fully Open Access Journals and in Subscription journals offering Online Open. Although most of the fully Open Access journals publish open access articles under the terms of the Creative Commons Attribution (CC BY) License only, the subscription journals and a few of the Open Access Journals offer a choice of Creative Commons Licenses:: Creative Commons Attribution (CC-BY) license Creative Commons Attribution Non-Commercial (CC-BY-NC) license and Creative Commons Attribution Non-Commercial-NoDerivs (CC-BY-NC-ND) License. The license type is clearly identified on the article.

Copyright in any research article in a journal published as Open Access under a Creative Commons License is retained by the author(s). Authors grant Wiley a license to publish the article and identify itself as the original publisher. Authors also grant any third party the right to use the article freely as long as its integrity is maintained and its original authors, citation details and publisher are identified as follows: [Title of Article/Author/Journal Title and Volume/Issue. Copyright (c) [year] [copyright owner as specified in the Journal]. Links to the final article on Wiley's website are encouraged where applicable.

The Creative Commons Attribution License

The Creative Commons Attribution License (CC-BY) allows users to copy, distribute and transmit an article, adapt the article and make commercial use of the article. The CC-BY license permits commercial and non-commercial re-use of an open access article, as long as the author is properly attributed.

The Creative Commons Attribution License does not affect the moral rights of authors, including without limitation the right not to have their work subjected to derogatory treatment. It also does not affect any other rights held by authors or third parties in the article, including without limitation the rights of privacy and publicity. Use of the article must not assert or imply, whether implicitly or explicitly, any connection with, endorsement or sponsorship of such use by the author, publisher or any other party associated with the article.

For any reuse or distribution, users must include the copyright notice and make clear to others that the article is made available under a Creative Commons Attribution license, linking to the relevant Creative Commons web page.

To the fullest extent permitted by applicable law, the article is made available as is and without representation or warranties of any kind whether express, implied, statutory or otherwise and including, without limitation, warranties of title, merchantability, fitness for a particular purpose, non-infringement, absence of defects, accuracy, or the presence or absence of errors.

Creative Commons Attribution Non-Commercial License

The Creative Commons Attribution Non-Commercial (CC-BY-NC) License permits use, distribution and reproduction in any medium, provided the original work is properly cited and is not used for commercial purposes.(see below)

Creative Commons Attribution-Non-Commercial-NoDerivs License

The Creative Commons Attribution Non-Commercial-NoDerivs License (CC-BY-NC-ND) permits use, distribution and reproduction in any medium, provided the original work is properly cited, is not used for commercial purposes and no modifications or adaptations are made. (see below)

Use by non-commercial users

For non-commercial and non-promotional purposes, individual users may access, download, copy, display and redistribute to colleagues Wiley Open Access articles, as well as adapt, translate, text- and data-mine the content subject to the following conditions:

- The authors' moral rights are not compromised. These rights include the right of "paternity" (also known as "attribution" - the right for the author to be identified as such) and "integrity" (the right for the author not to have the work altered in such a way that the author's reputation or integrity may be impugned).
- Where content in the article is identified as belonging to a third party, it is the obligation of the user to ensure that any reuse complies with the copyright policies of the owner of that content.
- If article content is copied, downloaded or otherwise reused for non-commercial research and education purposes, a link to the appropriate bibliographic citation (authors, journal, article title, volume, issue, page numbers, DOI and the link to the definitive published version on **Wiley Online Library**) should be maintained. Copyright notices and disclaimers must not be deleted.
- Any translations, for which a prior translation agreement with Wiley has not been agreed, must prominently display the statement: "This is an unofficial translation of an article that appeared in a Wiley publication. The publisher has not endorsed this translation."

Use by commercial "for-profit" organisations

Use of Wiley Open Access articles for commercial, promotional, or marketing purposes requires further explicit permission from Wiley and will be subject to a fee. Commercial purposes include:

- Copying or downloading of articles, or linking to such articles for further redistribution, sale or licensing;
- Copying, downloading or posting by a site or service that incorporates advertising

with such content;

- The inclusion or incorporation of article content in other works or services (other than normal quotations with an appropriate citation) that is then available for sale or licensing, for a fee (for example, a compilation produced for marketing purposes, inclusion in a sales pack)

- Use of article content (other than normal quotations with appropriate citation) by for-profit organisations for promotional purposes

- Linking to article content in e-mails redistributed for promotional, marketing or educational purposes;

- Use for the purposes of monetary reward by means of sale, resale, licence, loan, transfer or other form of commercial exploitation such as marketing products

- Print reprints of Wiley Open Access articles can be purchased from: corporatesales@wiley.com

Further details can be found on Wiley Online Library
http://olabout.wiley.com/WileyCDA/Section/id-410895.html

Other Terms and Conditions:

v1.9

If you would like to pay for this license now, please remit this license along with your payment made payable to "COPYRIGHT CLEARANCE CENTER" otherwise you will be invoiced within 48 hours of the license date. Payment should be in the form of a check or money order referencing your account number and this invoice number 501295271.
Once you receive your invoice for this order, you may pay your invoice by credit card. Please follow instructions provided at that time.

Make Payment To:
Copyright Clearance Center
Dept 001
P.O. Box 843006
Boston, MA 02284-3006

For suggestions or comments regarding this order, contact RightsLink Customer Support: customercare@copyright.com or +1-877-622-5543 (toll free in the US) or +1-978-646-2777.

Gratis licenses (referencing $0 in the Total field) are free. Please retain this printable license for your reference. No payment is required.

APPENDIX 8

JOHN WILEY AND SONS LICENSE
TERMS AND CONDITIONS

May 16, 2014

This is a License Agreement between Christine Gabrielse ("You") and John Wiley and Sons ("John Wiley and Sons") provided by Copyright Clearance Center ("CCC"). The license consists of your order details, the terms and conditions provided by John Wiley and Sons, and the payment terms and conditions.

All payments must be made in full to CCC. For payment instructions, please see information listed at the bottom of this form.

License Number	3382721013165
License date	May 05, 2014
Licensed content publisher	John Wiley and Sons
Licensed content publication	Journal of Geophysical Research: Space Physics
Licensed content title	Statistical characteristics of particle injections throughout the equatorial magnetotail
Licensed copyright line	©2014. American Geophysical Union. All Rights Reserved.
Licensed content author	C. Gabrielse,V. Angelopoulos,A. Runov,D. L. Turner
Licensed content date	Apr 2, 2014
Start page	n/a
End page	n/a
Type of use	Dissertation/Thesis
Requestor type	Author of this Wiley article
Format	Print and electronic
Portion	Full article
Will you be translating?	No
Title of your thesis / dissertation	Magnetospheric Particle Injections and their Relation to Impulsive, Localized Electric Fields
Expected completion date	Jun 2014
Expected size (number of pages)	208
Total	0.00 USD

TERMS AND CONDITIONS

This copyrighted material is owned by or exclusively licensed to John Wiley & Sons, Inc. or one of its group companies (each a "Wiley Company") or handled on behalf of a society with which a Wiley Company has exclusive publishing rights in relation to a particular work (collectively "WILEY"). By clicking “accept” in connection with completing this licensing transaction, you agree that the following terms and conditions apply to this transaction (along with the billing and payment terms and conditions established by the Copyright Clearance Center Inc., ("CCC's Billing and Payment terms and conditions"), at the time that you opened your Rightslink account (these are available at any time at http://myaccount.copyright.com).

Terms and Conditions

- The materials you have requested permission to reproduce or reuse (the "Wiley Materials") are protected by copyright.

- You are hereby granted a personal, non-exclusive, non-sub licensable (on a stand-alone basis), non-transferable, worldwide, limited license to reproduce the Wiley Materials for the purpose specified in the licensing process. This license is for a one-time use only and limited to any maximum distribution number specified in the license. The first instance of republication or reuse granted by this licence must be completed within two years of the date of the grant of this licence (although copies prepared before the end date may be distributed thereafter). The Wiley Materials shall not be used in any other manner or for any other purpose, beyond what is granted in the license. Permission is granted subject to an appropriate acknowledgement given to the author, title of the material/book/journal and the publisher. You shall also duplicate the copyright notice that appears in the Wiley publication in your use of the Wiley Material. Permission is also granted on the understanding that nowhere in the text is a previously published source acknowledged for all or part of this Wiley Material. Any third party content is expressly excluded from this permission.

- With respect to the Wiley Materials, all rights are reserved. Except as expressly granted by the terms of the license, no part of the Wiley Materials may be copied, modified, adapted (except for minor reformatting required by the new Publication), translated, reproduced, transferred or distributed, in any form or by any means, and no derivative works may be made based on the Wiley Materials without the prior permission of the respective copyright owner. You may not alter, remove or suppress in any manner any copyright, trademark or other notices displayed by the Wiley Materials. You may not license, rent, sell, loan, lease, pledge, offer as security, transfer or assign the Wiley Materials on a stand-alone basis, or any of the rights granted to you hereunder to any other person.

- The Wiley Materials and all of the intellectual property rights therein shall at all times remain the exclusive property of John Wiley & Sons Inc, the Wiley Companies, or their respective licensors, and your interest therein is only that of

having possession of and the right to reproduce the Wiley Materials pursuant to Section 2 herein during the continuance of this Agreement. You agree that you own no right, title or interest in or to the Wiley Materials or any of the intellectual property rights therein. You shall have no rights hereunder other than the license as provided for above in Section 2. No right, license or interest to any trademark, trade name, service mark or other branding ("Marks") of WILEY or its licensors is granted hereunder, and you agree that you shall not assert any such right, license or interest with respect thereto.

- NEITHER WILEY NOR ITS LICENSORS MAKES ANY WARRANTY OR REPRESENTATION OF ANY KIND TO YOU OR ANY THIRD PARTY, EXPRESS, IMPLIED OR STATUTORY, WITH RESPECT TO THE MATERIALS OR THE ACCURACY OF ANY INFORMATION CONTAINED IN THE MATERIALS, INCLUDING, WITHOUT LIMITATION, ANY IMPLIED WARRANTY OF MERCHANTABILITY, ACCURACY, SATISFACTORY QUALITY, FITNESS FOR A PARTICULAR PURPOSE, USABILITY, INTEGRATION OR NON-INFRINGEMENT AND ALL SUCH WARRANTIES ARE HEREBY EXCLUDED BY WILEY AND ITS LICENSORS AND WAIVED BY YOU

- WILEY shall have the right to terminate this Agreement immediately upon breach of this Agreement by you.
- You shall indemnify, defend and hold harmless WILEY, its Licensors and their respective directors, officers, agents and employees, from and against any actual or threatened claims, demands, causes of action or proceedings arising from any breach of this Agreement by you.

- IN NO EVENT SHALL WILEY OR ITS LICENSORS BE LIABLE TO YOU OR ANY OTHER PARTY OR ANY OTHER PERSON OR ENTITY FOR ANY SPECIAL, CONSEQUENTIAL, INCIDENTAL, INDIRECT, EXEMPLARY OR PUNITIVE DAMAGES, HOWEVER CAUSED, ARISING OUT OF OR IN CONNECTION WITH THE DOWNLOADING, PROVISIONING, VIEWING OR USE OF THE MATERIALS REGARDLESS OF THE FORM OF ACTION, WHETHER FOR BREACH OF CONTRACT, BREACH OF WARRANTY, TORT, NEGLIGENCE, INFRINGEMENT OR OTHERWISE (INCLUDING, WITHOUT LIMITATION, DAMAGES BASED ON LOSS OF PROFITS, DATA, FILES, USE, BUSINESS OPPORTUNITY OR CLAIMS OF THIRD PARTIES), AND WHETHER OR NOT THE PARTY HAS BEEN ADVISED OF THE POSSIBILITY OF SUCH DAMAGES. THIS LIMITATION SHALL APPLY NOTWITHSTANDING ANY FAILURE OF ESSENTIAL PURPOSE OF ANY LIMITED REMEDY PROVIDED HEREIN.

- Should any provision of this Agreement be held by a court of competent jurisdiction to be illegal, invalid, or unenforceable, that provision shall be deemed amended to achieve as nearly as possible the same economic effect as the original provision, and the legality, validity and enforceability of the remaining provisions of this

Agreement shall not be affected or impaired thereby.

- The failure of either party to enforce any term or condition of this Agreement shall not constitute a waiver of either party's right to enforce each and every term and condition of this Agreement. No breach under this agreement shall be deemed waived or excused by either party unless such waiver or consent is in writing signed by the party granting such waiver or consent. The waiver by or consent of a party to a breach of any provision of this Agreement shall not operate or be construed as a waiver of or consent to any other or subsequent breach by such other party.

- This Agreement may not be assigned (including by operation of law or otherwise) by you without WILEY's prior written consent.

- Any fee required for this permission shall be non-refundable after thirty (30) days from receipt by the CCC.

- These terms and conditions together with CCC's Billing and Payment terms and conditions (which are incorporated herein) form the entire agreement between you and WILEY concerning this licensing transaction and (in the absence of fraud) supersedes all prior agreements and representations of the parties, oral or written. This Agreement may not be amended except in writing signed by both parties. This Agreement shall be binding upon and inure to the benefit of the parties' successors, legal representatives, and authorized assigns.

- In the event of any conflict between your obligations established by these terms and conditions and those established by CCC's Billing and Payment terms and conditions, these terms and conditions shall prevail.

- WILEY expressly reserves all rights not specifically granted in the combination of (i) the license details provided by you and accepted in the course of this licensing transaction, (ii) these terms and conditions and (iii) CCC's Billing and Payment terms and conditions.

- This Agreement will be void if the Type of Use, Format, Circulation, or Requestor Type was misrepresented during the licensing process.

- This Agreement shall be governed by and construed in accordance with the laws of the State of New York, USA, without regards to such state's conflict of law rules. Any legal action, suit or proceeding arising out of or relating to these Terms and Conditions or the breach thereof shall be instituted in a court of competent jurisdiction in New York County in the State of New York in the United States of America and each party hereby consents and submits to the personal jurisdiction of such court, waives any objection to venue in such court and consents to service of process by registered or certified mail, return receipt requested, at the last known address of such party.

WILEY OPEN ACCESS TERMS AND CONDITIONS

Wiley Publishes Open Access Articles in fully Open Access Journals and in Subscription journals offering Online Open. Although most of the fully Open Access journals publish open access articles under the terms of the Creative Commons Attribution (CC BY) License only, the subscription journals and a few of the Open Access Journals offer a choice of Creative Commons Licenses:: Creative Commons Attribution (CC-BY) license Creative Commons Attribution Non-Commercial (CC-BY-NC) license and Creative Commons Attribution Non-Commercial-NoDerivs (CC-BY-NC-ND) License. The license type is clearly identified on the article.

Copyright in any research article in a journal published as Open Access under a Creative Commons License is retained by the author(s). Authors grant Wiley a license to publish the article and identify itself as the original publisher. Authors also grant any third party the right to use the article freely as long as its integrity is maintained and its original authors, citation details and publisher are identified as follows: [Title of Article/Author/Journal Title and Volume/Issue. Copyright (c) [year] [copyright owner as specified in the Journal]. Links to the final article on Wiley's website are encouraged where applicable.

The Creative Commons Attribution License

The Creative Commons Attribution License (CC-BY) allows users to copy, distribute and transmit an article, adapt the article and make commercial use of the article. The CC-BY license permits commercial and non-commercial re-use of an open access article, as long as the author is properly attributed.

The Creative Commons Attribution License does not affect the moral rights of authors, including without limitation the right not to have their work subjected to derogatory treatment. It also does not affect any other rights held by authors or third parties in the article, including without limitation the rights of privacy and publicity. Use of the article must not assert or imply, whether implicitly or explicitly, any connection with, endorsement or sponsorship of such use by the author, publisher or any other party associated with the article.

For any reuse or distribution, users must include the copyright notice and make clear to others that the article is made available under a Creative Commons Attribution license, linking to the relevant Creative Commons web page.

To the fullest extent permitted by applicable law, the article is made available as is and without representation or warranties of any kind whether express, implied, statutory or otherwise and including, without limitation, warranties of title, merchantability, fitness for a particular purpose, non-infringement, absence of defects, accuracy, or the presence or absence of errors.

Creative Commons Attribution Non-Commercial License

The Creative Commons Attribution Non-Commercial (CC-BY-NC) License permits use, distribution and reproduction in any medium, provided the original work is properly cited and is not used for commercial purposes.(see below)

Creative Commons Attribution-Non-Commercial-NoDerivs License

The Creative Commons Attribution Non-Commercial-NoDerivs License (CC-BY-NC-ND) permits use, distribution and reproduction in any medium, provided the original work is properly cited, is not used for commercial purposes and no modifications or adaptations are made. (see below)

Use by non-commercial users

For non-commercial and non-promotional purposes, individual users may access, download, copy, display and redistribute to colleagues Wiley Open Access articles, as well as adapt, translate, text- and data-mine the content subject to the following conditions:

- The authors' moral rights are not compromised. These rights include the right of "paternity" (also known as "attribution" - the right for the author to be identified as such) and "integrity" (the right for the author not to have the work altered in such a way that the author's reputation or integrity may be impugned).
- Where content in the article is identified as belonging to a third party, it is the obligation of the user to ensure that any reuse complies with the copyright policies of the owner of that content.
- If article content is copied, downloaded or otherwise reused for non-commercial research and education purposes, a link to the appropriate bibliographic citation (authors, journal, article title, volume, issue, page numbers, DOI and the link to the definitive published version on **Wiley Online Library**) should be maintained. Copyright notices and disclaimers must not be deleted.
- Any translations, for which a prior translation agreement with Wiley has not been agreed, must prominently display the statement: "This is an unofficial translation of an article that appeared in a Wiley publication. The publisher has not endorsed this translation."

Use by commercial "for-profit" organisations

Use of Wiley Open Access articles for commercial, promotional, or marketing purposes requires further explicit permission from Wiley and will be subject to a fee. Commercial purposes include:

- Copying or downloading of articles, or linking to such articles for further redistribution, sale or licensing;
- Copying, downloading or posting by a site or service that incorporates advertising

with such content;

- The inclusion or incorporation of article content in other works or services (other than normal quotations with an appropriate citation) that is then available for sale or licensing, for a fee (for example, a compilation produced for marketing purposes, inclusion in a sales pack)

- Use of article content (other than normal quotations with appropriate citation) by for-profit organisations for promotional purposes

- Linking to article content in e-mails redistributed for promotional, marketing or educational purposes;

- Use for the purposes of monetary reward by means of sale, resale, licence, loan, transfer or other form of commercial exploitation such as marketing products

- Print reprints of Wiley Open Access articles can be purchased from: corporatesales@wiley.com

Further details can be found on Wiley Online Library
http://olabout.wiley.com/WileyCDA/Section/id-410895.html

Other Terms and Conditions:

v1.9

If you would like to pay for this license now, please remit this license along with your payment made payable to "COPYRIGHT CLEARANCE CENTER" otherwise you will be invoiced within 48 hours of the license date. Payment should be in the form of a check or money order referencing your account number and this invoice number 501295279.
Once you receive your invoice for this order, you may pay your invoice by credit card. Please follow instructions provided at that time.

Make Payment To:
Copyright Clearance Center
Dept 001
P.O. Box 843006
Boston, MA 02284-3006

For suggestions or comments regarding this order, contact RightsLink Customer Support: customercare@copyright.com or +1-877-622-5543 (toll free in the US) or +1-978-646-2777.

Gratis licenses (referencing $0 in the Total field) are free. Please retain this printable license for your reference. No payment is required.

APPENDIX 9

JOHN WILEY AND SONS LICENSE
TERMS AND CONDITIONS

May 16, 2014

This is a License Agreement between Christine Gabrielse ("You") and John Wiley and Sons ("John Wiley and Sons") provided by Copyright Clearance Center ("CCC"). The license consists of your order details, the terms and conditions provided by John Wiley and Sons, and the payment terms and conditions.

All payments must be made in full to CCC. For payment instructions, please see information listed at the bottom of this form.

License Number	3382720963682
License date	May 05, 2014
Licensed content publisher	John Wiley and Sons
Licensed content publication	Journal of Geophysical Research: Space Physics
Licensed content title	The effects of transient, localized electric fields on equatorial electron acceleration and transport toward the inner magnetosphere
Licensed copyright line	©2012. American Geophysical Union. All Rights Reserved.
Licensed content author	C. Gabrielse,V. Angelopoulos,A. Runov,D. L. Turner
Licensed content date	Oct 10, 2012
Start page	n/a
End page	n/a
Type of use	Dissertation/Thesis
Requestor type	Author of this Wiley article
Format	Print and electronic
Portion	Full article
Will you be translating?	No
Title of your thesis / dissertation	Magnetospheric Particle Injections and their Relation to Impulsive, Localized Electric Fields
Expected completion date	Jun 2014
Expected size (number of pages)	208
Total	0.00 USD

TERMS AND CONDITIONS

This copyrighted material is owned by or exclusively licensed to John Wiley & Sons, Inc. or one of its group companies (each a"Wiley Company") or handled on behalf of a society with which a Wiley Company has exclusive publishing rights in relation to a particular work (collectively "WILEY"). By clicking “accept” in connection with completing this licensing transaction, you agree that the following terms and conditions apply to this transaction (along with the billing and payment terms and conditions established by the Copyright Clearance Center Inc., ("CCC's Billing and Payment terms and conditions"), at the time that you opened your Rightslink account (these are available at any time at http://myaccount.copyright.com).

Terms and Conditions

- The materials you have requested permission to reproduce or reuse (the "Wiley Materials") are protected by copyright.

- You are hereby granted a personal, non-exclusive, non-sub licensable (on a stand-alone basis), non-transferable, worldwide, limited license to reproduce the Wiley Materials for the purpose specified in the licensing process. This license is for a one-time use only and limited to any maximum distribution number specified in the license. The first instance of republication or reuse granted by this licence must be completed within two years of the date of the grant of this licence (although copies prepared before the end date may be distributed thereafter). The Wiley Materials shall not be used in any other manner or for any other purpose, beyond what is granted in the license. Permission is granted subject to an appropriate acknowledgement given to the author, title of the material/book/journal and the publisher. You shall also duplicate the copyright notice that appears in the Wiley publication in your use of the Wiley Material. Permission is also granted on the understanding that nowhere in the text is a previously published source acknowledged for all or part of this Wiley Material. Any third party content is expressly excluded from this permission.

- With respect to the Wiley Materials, all rights are reserved. Except as expressly granted by the terms of the license, no part of the Wiley Materials may be copied, modified, adapted (except for minor reformatting required by the new Publication), translated, reproduced, transferred or distributed, in any form or by any means, and no derivative works may be made based on the Wiley Materials without the prior permission of the respective copyright owner. You may not alter, remove or suppress in any manner any copyright, trademark or other notices displayed by the Wiley Materials. You may not license, rent, sell, loan, lease, pledge, offer as security, transfer or assign the Wiley Materials on a stand-alone basis, or any of the rights granted to you hereunder to any other person.

- The Wiley Materials and all of the intellectual property rights therein shall at all times remain the exclusive property of John Wiley & Sons Inc, the Wiley Companies, or their respective licensors, and your interest therein is only that of

having possession of and the right to reproduce the Wiley Materials pursuant to Section 2 herein during the continuance of this Agreement. You agree that you own no right, title or interest in or to the Wiley Materials or any of the intellectual property rights therein. You shall have no rights hereunder other than the license as provided for above in Section 2. No right, license or interest to any trademark, trade name, service mark or other branding ("Marks") of WILEY or its licensors is granted hereunder, and you agree that you shall not assert any such right, license or interest with respect thereto.

- NEITHER WILEY NOR ITS LICENSORS MAKES ANY WARRANTY OR REPRESENTATION OF ANY KIND TO YOU OR ANY THIRD PARTY, EXPRESS, IMPLIED OR STATUTORY, WITH RESPECT TO THE MATERIALS OR THE ACCURACY OF ANY INFORMATION CONTAINED IN THE MATERIALS, INCLUDING, WITHOUT LIMITATION, ANY IMPLIED WARRANTY OF MERCHANTABILITY, ACCURACY, SATISFACTORY QUALITY, FITNESS FOR A PARTICULAR PURPOSE, USABILITY, INTEGRATION OR NON-INFRINGEMENT AND ALL SUCH WARRANTIES ARE HEREBY EXCLUDED BY WILEY AND ITS LICENSORS AND WAIVED BY YOU

- WILEY shall have the right to terminate this Agreement immediately upon breach of this Agreement by you.
- You shall indemnify, defend and hold harmless WILEY, its Licensors and their respective directors, officers, agents and employees, from and against any actual or threatened claims, demands, causes of action or proceedings arising from any breach of this Agreement by you.

- IN NO EVENT SHALL WILEY OR ITS LICENSORS BE LIABLE TO YOU OR ANY OTHER PARTY OR ANY OTHER PERSON OR ENTITY FOR ANY SPECIAL, CONSEQUENTIAL, INCIDENTAL, INDIRECT, EXEMPLARY OR PUNITIVE DAMAGES, HOWEVER CAUSED, ARISING OUT OF OR IN CONNECTION WITH THE DOWNLOADING, PROVISIONING, VIEWING OR USE OF THE MATERIALS REGARDLESS OF THE FORM OF ACTION, WHETHER FOR BREACH OF CONTRACT, BREACH OF WARRANTY, TORT, NEGLIGENCE, INFRINGEMENT OR OTHERWISE (INCLUDING, WITHOUT LIMITATION, DAMAGES BASED ON LOSS OF PROFITS, DATA, FILES, USE, BUSINESS OPPORTUNITY OR CLAIMS OF THIRD PARTIES), AND WHETHER OR NOT THE PARTY HAS BEEN ADVISED OF THE POSSIBILITY OF SUCH DAMAGES. THIS LIMITATION SHALL APPLY NOTWITHSTANDING ANY FAILURE OF ESSENTIAL PURPOSE OF ANY LIMITED REMEDY PROVIDED HEREIN.

- Should any provision of this Agreement be held by a court of competent jurisdiction to be illegal, invalid, or unenforceable, that provision shall be deemed amended to achieve as nearly as possible the same economic effect as the original provision, and the legality, validity and enforceability of the remaining provisions of this

Agreement shall not be affected or impaired thereby.

- The failure of either party to enforce any term or condition of this Agreement shall not constitute a waiver of either party's right to enforce each and every term and condition of this Agreement. No breach under this agreement shall be deemed waived or excused by either party unless such waiver or consent is in writing signed by the party granting such waiver or consent. The waiver by or consent of a party to a breach of any provision of this Agreement shall not operate or be construed as a waiver of or consent to any other or subsequent breach by such other party.

- This Agreement may not be assigned (including by operation of law or otherwise) by you without WILEY's prior written consent.

- Any fee required for this permission shall be non-refundable after thirty (30) days from receipt by the CCC.

- These terms and conditions together with CCC's Billing and Payment terms and conditions (which are incorporated herein) form the entire agreement between you and WILEY concerning this licensing transaction and (in the absence of fraud) supersedes all prior agreements and representations of the parties, oral or written. This Agreement may not be amended except in writing signed by both parties. This Agreement shall be binding upon and inure to the benefit of the parties' successors, legal representatives, and authorized assigns.

- In the event of any conflict between your obligations established by these terms and conditions and those established by CCC's Billing and Payment terms and conditions, these terms and conditions shall prevail.

- WILEY expressly reserves all rights not specifically granted in the combination of (i) the license details provided by you and accepted in the course of this licensing transaction, (ii) these terms and conditions and (iii) CCC's Billing and Payment terms and conditions.

- This Agreement will be void if the Type of Use, Format, Circulation, or Requestor Type was misrepresented during the licensing process.

- This Agreement shall be governed by and construed in accordance with the laws of the State of New York, USA, without regards to such state's conflict of law rules. Any legal action, suit or proceeding arising out of or relating to these Terms and Conditions or the breach thereof shall be instituted in a court of competent jurisdiction in New York County in the State of New York in the United States of America and each party hereby consents and submits to the personal jurisdiction of such court, waives any objection to venue in such court and consents to service of process by registered or certified mail, return receipt requested, at the last known address of such party.

WILEY OPEN ACCESS TERMS AND CONDITIONS

Wiley Publishes Open Access Articles in fully Open Access Journals and in Subscription journals offering Online Open. Although most of the fully Open Access journals publish open access articles under the terms of the Creative Commons Attribution (CC BY) License only, the subscription journals and a few of the Open Access Journals offer a choice of Creative Commons Licenses:: Creative Commons Attribution (CC-BY) license Creative Commons Attribution Non-Commercial (CC-BY-NC) license and Creative Commons Attribution Non-Commercial-NoDerivs (CC-BY-NC-ND) License. The license type is clearly identified on the article.

Copyright in any research article in a journal published as Open Access under a Creative Commons License is retained by the author(s). Authors grant Wiley a license to publish the article and identify itself as the original publisher. Authors also grant any third party the right to use the article freely as long as its integrity is maintained and its original authors, citation details and publisher are identified as follows: [Title of Article/Author/Journal Title and Volume/Issue. Copyright (c) [year] [copyright owner as specified in the Journal]. Links to the final article on Wiley's website are encouraged where applicable.

The Creative Commons Attribution License

The Creative Commons Attribution License (CC-BY) allows users to copy, distribute and transmit an article, adapt the article and make commercial use of the article. The CC-BY license permits commercial and non-commercial re-use of an open access article, as long as the author is properly attributed.

The Creative Commons Attribution License does not affect the moral rights of authors, including without limitation the right not to have their work subjected to derogatory treatment. It also does not affect any other rights held by authors or third parties in the article, including without limitation the rights of privacy and publicity. Use of the article must not assert or imply, whether implicitly or explicitly, any connection with, endorsement or sponsorship of such use by the author, publisher or any other party associated with the article.

For any reuse or distribution, users must include the copyright notice and make clear to others that the article is made available under a Creative Commons Attribution license, linking to the relevant Creative Commons web page.

To the fullest extent permitted by applicable law, the article is made available as is and without representation or warranties of any kind whether express, implied, statutory or otherwise and including, without limitation, warranties of title, merchantability, fitness for a particular purpose, non-infringement, absence of defects, accuracy, or the presence or absence of errors.

Creative Commons Attribution Non-Commercial License

The Creative Commons Attribution Non-Commercial (CC-BY-NC) License permits use, distribution and reproduction in any medium, provided the original work is properly cited and is not used for commercial purposes.(see below)

Creative Commons Attribution-Non-Commercial-NoDerivs License

The Creative Commons Attribution Non-Commercial-NoDerivs License (CC-BY-NC-ND) permits use, distribution and reproduction in any medium, provided the original work is properly cited, is not used for commercial purposes and no modifications or adaptations are made. (see below)

Use by non-commercial users

For non-commercial and non-promotional purposes, individual users may access, download, copy, display and redistribute to colleagues Wiley Open Access articles, as well as adapt, translate, text- and data-mine the content subject to the following conditions:

- The authors' moral rights are not compromised. These rights include the right of "paternity" (also known as "attribution" - the right for the author to be identified as such) and "integrity" (the right for the author not to have the work altered in such a way that the author's reputation or integrity may be impugned).
- Where content in the article is identified as belonging to a third party, it is the obligation of the user to ensure that any reuse complies with the copyright policies of the owner of that content.
- If article content is copied, downloaded or otherwise reused for non-commercial research and education purposes, a link to the appropriate bibliographic citation (authors, journal, article title, volume, issue, page numbers, DOI and the link to the definitive published version on **Wiley Online Library**) should be maintained. Copyright notices and disclaimers must not be deleted.
- Any translations, for which a prior translation agreement with Wiley has not been agreed, must prominently display the statement: "This is an unofficial translation of an article that appeared in a Wiley publication. The publisher has not endorsed this translation."

Use by commercial "for-profit" organisations

Use of Wiley Open Access articles for commercial, promotional, or marketing purposes requires further explicit permission from Wiley and will be subject to a fee. Commercial purposes include:

- Copying or downloading of articles, or linking to such articles for further redistribution, sale or licensing;
- Copying, downloading or posting by a site or service that incorporates advertising

with such content;

- The inclusion or incorporation of article content in other works or services (other than normal quotations with an appropriate citation) that is then available for sale or licensing, for a fee (for example, a compilation produced for marketing purposes, inclusion in a sales pack)

- Use of article content (other than normal quotations with appropriate citation) by for-profit organisations for promotional purposes

- Linking to article content in e-mails redistributed for promotional, marketing or educational purposes;

- Use for the purposes of monetary reward by means of sale, resale, licence, loan, transfer or other form of commercial exploitation such as marketing products

- Print reprints of Wiley Open Access articles can be purchased from: corporatesales@wiley.com

Further details can be found on Wiley Online Library
http://olabout.wiley.com/WileyCDA/Section/id-410895.html

Other Terms and Conditions:

v1.9

If you would like to pay for this license now, please remit this license along with your payment made payable to "COPYRIGHT CLEARANCE CENTER" otherwise you will be invoiced within 48 hours of the license date. Payment should be in the form of a check or money order referencing your account number and this invoice number 501295278.
Once you receive your invoice for this order, you may pay your invoice by credit card. Please follow instructions provided at that time.

Make Payment To:
Copyright Clearance Center
Dept 001
P.O. Box 843006
Boston, MA 02284-3006

For suggestions or comments regarding this order, contact RightsLink Customer Support: customercare@copyright.com or +1-877-622-5543 (toll free in the US) or +1-978-646-2777.

Gratis licenses (referencing $0 in the Total field) are free. Please retain this printable license for your reference. No payment is required.

BIBLIOGRAPHY

Akasofu, S.-I. (1964), The development of the auroral substorm, *Planet. Space Sci.*, 12, 2826 273-282, doi:10.1016/0032-0633(64)90151-5.

Angelopoulos, V., W. Baumjohann, C. F. Kennel, F. V. Coroniti, M. G. Kivelson, R. Pellat, R. J.Walker, H. Lühr, and G. Paschmann (1992), Bursty Bulk Flows in the Inner Central Plasma Sheet, *J. Geophys. Res.*, 97(A4), 4027–4039, doi:10.1029/91JA02701.

Angelopoulos, V., C. F. Kennel, F. V. Coroniti, R. Pellat, H. E. Spence, M. G. Kivelson, R. J. Walker, W. Baumjohann, W. C. Feldman, J. T. Gosling, C. T. Russell, Characteristics of ion flow in the quiet state of the inner plasma sheet. *Geophys. Res. Lett*. 20, 1711–1714 (1993).

Angelopoulos, V., C. F. Kennel, F.V. Coroniti, R. Pellat, M. G. Kivelson, R. J. Walker, C. T. Russell, W. Baumjohann, W. C. Feldman, J. T. Gosling (1994a), Statistical characteristics of bursty bulk flow events, *J. Geophys. Res*., 99, A11, doi:10.1029/94JA01263.

Angelopoulos, V., T.D. Phan, D.E. Larson, F.S. Mozer, R.P. Lin, K. Tsuruda, H. Hayakawa, T. Mukai, S. Kokubun, T. Yamamoto, D.J. Williams, R.W. McEntire, R.P. Lepping, G.K. Parks, M. Brittnacher, G. Germany, J. Spann, H.J. Singer, and K. Yumoto (1994b) "Magnetotail flow bursts: association to global magnetospheric circulation, relationship to ionospheric activity and direct evidence for localization", *Geophys. Res. Lett*., v. 24, p.2271-74.

Angelopoulos, V., et al. (1997), Magnetotail flow bursts: Association to global magnetospheric circulation, relationship to ionospheric activity and direct evidence for localization, *Geophys. Res. Lett*., 24(18), 2271–2274, doi:10.1029/97GL02355.

Angelopoulos, V., M. Temerin, I. Roth, F. S. Mozer, D. Weimer, and M. R. Hairston, (2002), Testing global storm-time electric field models using particle spectra on multiple spacecraft, *J. Geophys. Res*., 107(A8), 1194, doi:10.1029/2001JA900174.

Angelopoulos, V., et al., *Space Sci Rev* (2008) 141: 453–476, doi 10.1007/s11214-008-9378-4

Anderson, K.A. (1965), Energetic Electron Fluxes in Tail of Geomagnetic Field, *Journal of Geophysical Research*, 70(19), 4741-&, doi:10.1029/JZ070i019p04741.

Armstrong, T. P., and S. M. Krimigis (1968), Observations of Protons in the Magnetosphere and 1275 Magnetotail with Explorer 33, *J. Geophys. Res*., 73(1), 143–152, doi:10.1029/JA073i001p00143.

Auster, H. U., et al. (2008), The THEMIS Fluxgate Magnetometer, *Space Sci. Rev*., 141, 235-264, doi:10.1007/s11214-008-9365-9.

Baker, D. N., Pulkkinen, T. I., Angelopoulos, V., Baumjohann, W., and McPherron, R. L.: The neutral line model of substorms: Past results and present view, *J. Geophys. Res*., 101, 12975–13010, doi:10.1029/95JA03753, 1996.

Birn, J., M. F. Thomsen, J. E. Borovsky, G. D. Reeves, D. J. McComas, and R. Belian (1997a), Characteristic plasma properties during dispersionless substorm injections at geosynchronous orbit, *J. Geophys. Res.*, 102(A2), 2309.

Birn, J., M. F. Thomsen, J. E. Borovsky, G. D. Reeves, D. J. McComas, R. D. Belian, and M. Hesse (1997b), Substorm ion injections: Geosynchronous observations and test particle orbits in three-dimensional dynamic MHD fields, *J. Geophys. Res*., 102(A2), 2325–2341, doi:10.1029/96JA03032.

Birn, J., M. F. Thomsen, J. E. Borovsky, G. D. Reeves, D. J. McComas, R. D. Belian, and M. Hesse (1998), Substorm electron injections: Geosynchronous observations and test particle simulations, *J. Geophys. Res.*, 103(A5), 9235.

Birn, J. M., J. Raeder, Y. L. Wang, R. A. Wolf, and M. Hesse (2004), On the propagation of bubbles in the magnetotail, *Ann. Geophys*., 22, 1773–1786, doi:10.5194/angeo-22-1773-2004.

Birn, J., R. Nakamura, E. V. Panov, and M. Hesse (2011), Bursty bulk flows and dipolarization in MHD simulations of magnetotail reconnection, *J. Geophys. Res*., 116, A01210, doi:10.1029/2010JA016083.

Chen, Y., Reeves, G. D. & Friedel, R. H. W. *Nature Phys*. 3, 614-617 (2007)

Christon, S. P., D. G. Mitchell, D. J. Williams, L. A. Frank, C. Y. Huang, and T. E. Eastman (1988), Energy spectra of plasma sheet ions and electrons from ~50 eV/e to ~1 MeV during plasma temperature transitions, *J. Geophys. Res*., 93(A4), 2562–2572, doi:10.1029/JA093iA04p02562.

Christon, S. P., D. J. Williams, D. G. Mitchell, L. A. Frank, and C. Y. Huang (1989), Spectral characteristics of plasma sheet ion and electron populations during undisturbed geomagnetic conditions, *J. Geophys. Res*., 94(A10), 13,409–13,424, doi:10.1029/JA094iA10p13409.

Delcourt, D. C. (2002), Particle acceleration by inductive electric fields in the inner magnetosphere, *J. Atmos. Sol. Terr. Phys*., 64(5–6), 551–559, doi:10.1016/S1364-826(02)00012-3.

Dubyagin, S., V. Sergeev, S. Apatenkov, V. Angelopoulos, A. Runov, R. Nakamura, W. Baumjohann, J. McFadden, and D. Larson (2011), Can flow bursts penetrate into the inner magnetosphere, *Geophys. Res. Lett*., 38, L08102, doi:10.1029/2011GL047016.

Eastwood, J. P., T. D. Phan, M. Øieroset, and M. A. Shay (2010), Average properties of the magnetic reconnection ion diffusion region in the Earth's magnetotail: The 2001–2005 Cluster observations and comparison with simulations, *J. Geophys. Res*., 115, A08215, doi:10.1029/2009JA014962.

Gabrielse, C., V. Angelopoulos, A. Runov, and D. L. Turner (2012), The effects of transient, localized electric fields on equatorial electron acceleration and transport toward the inner magnetosphere, *J. Geophys. Res*., 117, A10213, doi:10.1029/2012JA017873.

Gabrielse, C., V. Angelopoulos, A. Runov, and D. L. Turner (2014), Statistical characteristics of particle injections throughout the equatorial magnetotail, *J. Geophys. Res. Space Physics*, 119, 2512–2535, doi:10.1002/2013JA019638.

Galeev, A. A. (1979) Reconnection in the magnetotail, *Space Sci. Rev.* **23**, 411.

Gallardo-Lacourt, B., Y. Nishimura, L. R. Lyons, S. Zou, V. Angelopoulos, E. Donovan, K. A. McWilliams, J. M. Ruohoniemi, and N. Nishitani (2014), Coordinated SuperDARN THEMIS ASI observations of mesoscale flow bursts associated with auroral streamers, *J. Geophys. Res. Space Physics*, 119, 142–150, doi:10.1002/2013JA019245.

Ganushkina, N. Y., T. I. Pulkkinen, and T. Fritz (2005), Role of substorm associated impulsive electric fields in the ring current development during storms, *Ann. Geophys*., 23(2), 579–591, doi:10.5194/angeo-23-579-2005.

Ganushkina, N. Y., S. Dubyagin, M. Kubyshkina, M. Liemohn, and A. Runov (2012), Inner magnetosphere currents during the CIR/HSS storm on July 21–23, 2009, *J. Geophys. Res*., 117, A00L04, doi:10.1029/2011JA017393.

Ganushkina N. Yu., O. Amariutei, Y. Y. Shprits, and M. Liemohn (2013), Transport of the plasma sheet electrons to the geostationary distances, *J. Geophys. Res*., 118, doi:10.1029/2012JA017923.

Gloeckler, G., and D. C. Hamilton (1987), AMPTE ion composition results, *Phys. Scr*, T18, 73–84, doi:10.1088/0031-8949/1987/T18/009.

Imber, S. M., J. A. Slavin, H. U. Auster, and V. Angelopoulos (2011), A THEMIS survey of flux ropes and traveling compression regions: Location of the near-Earth reconnection site during solar minimum, *J. Geophys. Res*., 116, A02201, doi:10.1029/2010JA016026.

Kappenman, J. G., L. J. Zanetti, and W. A. Radasky, Geomagnetic storm forecasts and the power industry, *Eos Trans. AGU*, 78, 37–45, 1997.

Keika et al. (2009), Observations of plasma vorticies in the vicinity of flow-braking: A case study, *Ann. Geophys*., 27, 3009-3017.

Keiling et al. (2009), Substorm current wedge driven by plasma flow vorticies: THEMIS observations, *J. Geophys. Res*., 114, A00C22, doi:10.1029/2009JA014114.

Kistler, L. M., F. M. Ipavich, D. C. Hamilton, G. Gloeckler, B. Wilken, G. Kremser, and W. Stüdemann (1989), Energy spectra of the major ion species in the ring current during geomagnetic storms, *J. Geophys. Res*., 94(A4), 3579–3599, doi:10.1029/JA094iA04p03579.

Kistler, L. M., et al. (1999), Testing electric field models using ring current ion energy spectra from the Equator-S ion composition (ESIC) instrument, *Ann. Geophys*., 17, 1611, doi:10.1007/s00585-999-1611-2.

Kivelson, M., C. T. Russell, *Introduction to Space Physics*. New York: Cambridge University Press, 1995. Print.

Kletzing, C. A., J. D. Scudder, E. E. Dors, and C. Curto (2003), Auroral source region: Plasma properties of the high-latitude plasma sheet, *J. Geophys. Res*., 108(A10), 1360, doi:10.1029/2002JA009678.

Konradi, A. (1966), Electron and Proton Fluxes in the Tail of the Magnetosphere, *J. Geophys. Res.*, 71(9), 2317–2325, doi:10.1029/JZ071i009p02317.

Konradi, A., C. L. Semar, and T. A. Fritz, Substorm-injected protons and electrons and the injection boundary model, *J. Geophys. Res*., 80, 543, 1975.

Lanzerotti, L. J., C. S. Roberts, and W. L. Brown (1967), Temporal Variations in the Electron Flux at Synchronous Altitudes, *J. Geophys. Res.*, 72(23), 5893–5902, 1350 doi:10.1029/JZ072i023p05893.

Lennartsson, W., and E. G. Shelley (1986), Survey of 0.1- to 16-keV/e plasma sheet ion composition, *J. Geophys. Res*., 91(A3), 3061–3076, doi:10.1029/JA091iA03p03061.

Li, S.-S., V. Angelopoulos, A. Runov, X.-Z. Zhou, J. McFadden, D. Larson, J. Bonnell, and U. Auster (2011), On the force balance around dipolarization fronts within bursty bulk flows, *J. Geophys. Res*., 116, A00I35, doi:10.1029/2010JA015884.

Li, X., I. Roth, M. Temerin, J. Wygant, M. K. Hudson, and J. B. Blake (1993), Simulation of the prompt energization and transport of radiation particles during the March 23, 1991 SSC, *Geophys. Res. Lett*., 20(22), 2423–2426, doi:10.1029/93GL02701.

Li, X., D. N. Baker, M. Temerin, G. Reeves, and R. Belian (1998), Simulation of dispersionless injections and drift echoes of energetic electrons associated with substorms, *Geophys. Res. Lett*., 25(20), 3763–3766, doi:10.1029/1998GL900001.

Li, X., T. E. Sarris, D. N. Baker, W. K. Peterson, and H. J. Singer (2003), Simulation of energetic particle injections associated with a substorm on August 27, 2001, *Geophys. Res. Lett*., 30(1), 1004, doi:10.1029/2002GL015967.

Liu, J., V. Angelopoulos, A. Runov, and X.-Z. Zhou (2013), On the current sheets surrounding dipolarizing flux bundles in the magnetotail: The case for wedgelets, *J. Geophys. Res. Space Physics*, 118, 2000–2020, doi: 10.1002/jgra.50092.

Liu, J., V. Angelopoulos, X.-Z. Zhou, and A. Runov (2014), Magnetic flux transport by dipolarizing flux bundles, *J. Geophys. Res. Space Physics*, 119, 909–926, doi:10.1002/2013JA019395.

Lopez, R. E., and T. vonRosenvinge (1993), A statistical relationship between the geosynchronous magnetic field and substorm electrojet magnitude, *J. Geophys. Res*., 98(A3), 3851–3857, doi:10.1029/92JA01660.

Lyons, L. R., Y. Nishimura, X. Xing, A. Runov, V. Angelopoulos, E. Donovan, and T. Kikuchi (2012), Coupling of dipolarization front flow bursts to substorm expansion phase phenomena within the magnetosphere and ionosphere, *J. Geophys. Res*., 117, A02212, doi:10.1029/2011JA017265.

Lyons, L. R., Y. Nishimura, E. Donovan, and V. Angelopoulos (2013), Distinction between auroral substorm onset and traditional ground magnetic onset signatures, *J. Geophys. Res. Space Physics*, 118, 4080–4092, doi:10.1002/jgra.50384

Mauk, B. H., and C. E. McIlwain, Correlation of Kp with the substorm injected plasma boundary, *J. Geophys. Res.,* 79, 3193, 1974.

Mauk, B., and C.-I. Meng, Characterization of geostationary particle signatures based on the 1368 ‘‘injection boundary’’ mode, *J. Geophys. Res*., 88, 3055, 1983.

McIlwain, C. (1974), Substorm injection boundaries, in Magnetospheric Physics, edited by B. M. McCormac, p. 143, D. Reidel, Hingham, Mass.

McFadden, J. P., C. W. Carlson, D. Larson, M. Ludlam, R. Abiad, B. Elliott, P. Turin, M. Marckwordt, and V. Angelopoulos (2008), The THEMIS ESA Plasma Instrument and In-fight Calibration, *Space Sci. Rev*., 141, 277-302, doi:10.1007/s11214-008-9440-2.

McPherron, R. L., Russell, C. T., and Aubry, M. P.: Satellite studies of magnetospheric substorms on August 15, 1968: 9. Phenomenological model for substorms, *J. Geophys. Res*., 78, 3133–3149, 1973.

McPherron, R. L., T.-S. Hsu, J. Kissinger, X. Chu, and V. Angelopoulos (2011), Characteristics of plasma flows at the inner edge of the plasma sheet, *J. Geophys. Res*., 116, A00I33, doi:10.1029/2010JA015923.

Moore, T. E., et al. (1981), Propagating substorm injection fronts, *J. Geophys. Res*., 86(A8), 6713–6726, doi:10.1029/JA086iA08p06713.

Nagai, T., I. Shinohara, S. Zenitani, R. Nakamura, T. K. M. Nakamura, M. Fujimoto, Y. Saito, and T. Mukai (2013), Three-dimensional structure of magnetic reconnection in the magnetotail from Geotail observations, *J. Geophys. Res. Space Physics*, 118, 1667–1678, doi:10.1002/jgra.50247.

Nakamura, R., et al. (2004), Spatial scale of high-speed flows in the plasma sheet observed by Cluster, *Geophys. Res. Lett.*, 31, L09804, doi:10.1029/2004GL019558.

Northrop, T. G. (1963), The Adiabatic Motion of Charged Particles, Intersci. Publ., New York.

Ohtani, S., and S. Kokubun (1991), Magnetic properties of the high-latitude tail boundary: Draping of magnetosheath field lines and tail-aligned current, *J. Geophys. Res.*, 96(A6), 9521–9530, doi:10.1029/91JA00570.

Ohtani, S., M. A. Shay, and T. Mukai (2004), Temporal structure of the fast convective flow in the plasma sheet: Comparison between observations and two-fluid simulations, *J. Geophys. Res.*, 109, A03210, doi:10.1029/2003JA010002.

Ohtani, S., Y. Miyashita, H. Singer, and T. Mukai (2009), Tailward flows with positive BZ in the near-Earth plasma sheet, *J. Geophys. Res.*, 114, A06218, doi:10.1029/2009JA014159.

Panov, E. V., et al. (2010), Multiple overshoot and rebound of a bursty bulk flow, *Geophys. Res. Lett.*, 37, L08103, doi:10.1029/2009GL041971.

Peterson, W. K., R. D. Sharp, E. G. Shelley, R. G. Johnson, and H. Balsiger (1981), Energetic ion composition of the plasma sheet, *J. Geophys. Res.*, 86(A2), 761–767, doi:10.1029/JA086iA02p00761.

Pontius, D. H., Jr., and R. A. Wolf (1990), Transient flux tubes in the terrestrial magnetosphere, *Geophys. Res. Lett.*, 17(1), 49–52, doi:10.1029/GL017i001p00049.

Raj, A., T. Phan, R. P. Lin, and V. Angelopoulos, Wind survey of high-speed bulk flows and field-aligned beams in the near-Earth plasma sheet, *J. Geophys. Res.*, 107(A12), 1419, doi:10.1029/2001JA007547, 2002.

Rostoker, G. (1991), Some observational constraints for substorm models, Magnetospheric Substorms, *Geophys. Monogr. Ser.*, AGU, 64, 61-72, doi:10.1029/GM064p0061.

Runov, A., et al. (2005), Reconstruction of the magnetotail current sheet structure using multi-point Cluster measurements, *Planet. Space Sci.*, 53, 237–243.

Runov, A., et al. (2009), THEMIS observations of an earthward- propagating dipolarization 1393 front, *Geophys. Res. Lett.*, 36, L14106, doi:10.1029/2009GL038980.

Runov, A., et al. (2011) A THEMIS multicase study of dipolarization fronts in the magnetotail plasma sheet, *J. Geophys. Res.*, 116, A05216, doi:10.1029/2010JA016316.

Runov, A., V. Angelopoulos, C. Gabrielse, X.-Z. Zhou, D. Turner, F. Plaschke, Electron fluxes and pitch-angle distributions at dipolarization fronts: THEMIS multi-point observations, *J. Geophys. Res.*, doi: 10.1002/jgra.50121, 2013

Sarafopoulos, D.V. and E. T. Sarris, Inverse Velocity Dispersion of Energetic Particle Bursts in the Plasma Sheet, *Planet. Space Sci.*,Vol. 36, No. 11, 1988, pp. 1181-1199, doi: 10.1016/0032-0633(88)90072-4.

Sarris, E.T., S. M. Krimigis, and T. P.Armstrong (1976), Observations of magnetospheric bursts of high-energy protons and electrons at 35 with Imp 7, *J. Geophys. Res.*, 81(13), 2341–2355, doi:10.1029/JA081i013p02341.

Sarris, E. T. and Axford, W. I. (1979) Energetic protons near the plasma sheet boundary. *Nature* 277, 460.

Sarris, T. E., X. Li, N. Tsaggas, and N. Paschalidis (2002), Modeling energetic particle injections in dynamic pulse fields with varying propagation speeds, *J. Geophys. Res.*, 107(A3), 1033, doi:10.1029/2001JA900166.

Schödel, R., R. Nakamura, W. Baumjohann, and T. Mukai (2001), Rapid flux transport and plasma sheet reconfiguration, *J. Geophys. Res.*, 106(A5), 8381–8390, doi:10.1029/2000JA900159.

Semenov, V. S., T. Penz, V. V. Ivanova, V. A. Sergeev, H. K. Biernat, R. Nakamura, M. F. Heyn, I. V. Kubyshkin, and I. B. Ivanov (2005), Reconstruction of the reconnection rate from Cluster measurements: First results, *J. Geophys. Res.*, 110, A11217, doi:10.1029/2005JA011181.

Sergeev, V. A., L. I. Vagina, R. D. Elphinstone, J. S. Murphree, D. J. Hearn, L. L. Cogger, and M. L. Johnson (1996a), Comparison of UV optical signatures with the substorm current wedge as predicted by an inversion algorithm, *J. Geophys. Res.*, 101(A2), 2615 – 2627, doi:10.1029/
95JA00537.

Sergeev, V. A., V. Angelopoulos, J. T. Gosling, C. A. Cattell, and C. T. Russell (1996b), Detection of localized, plasma-depleted flux tubes or bubbles in the midtail plasma sheet, *J. Geophys. Res.*, 101(A5), 10,817–10,826, doi:10.1029/96JA00460.

Sergeev, V. A., Yahnin, D. A., Liou, K., Thomsen, M. F., and Reeves, G. D.: Narrow Plasma Streams as a candidate to populate the inner magnetosphere, *Geophys. Monogr. Ser.*, p. 155, 2005

Sergeev, V. A., I. A. Chernyaev, S. V. Dubyagin, Y. Miyashita, V. Angelopoulos, P. D. Boakes, R. Nakamura, and M. G. Henderson (2012), Energetic particle injections to geostationary orbit: Relationship to flow bursts and magnetospheric state, *J. Geophys. Res.*, 117, A10207, doi:10.1029/2012JA017773

Shi, Y., E. Zesta, L. R. Lyons, J. Yang, A. Boudouridis, Y. S. Ge, J. M. Ruohoniemi, and S. Mende (2012), Two-dimensional ionospheric flow pattern associated with auroral streamers, *J. Geophys. Res.*, 117, A02208, doi:10.1029/2011JA017110.

Sibeck, D. G., and V. Angelopoulos (2008), THEMIS Science Objectives and Mission Phases, *Space Sci. Rev*., 141, 35-59, doi:10.1007/s11214-008-9393-5.

Taylor, J. R., An Introduction to Error Analysis: The Study of Uncertainties in Physical Measurements, 2nd Ed. Sausalito: University Science Books, 1997. Print.

Thomsen, M. F., J. Birn, J. E. Borovsky, K. Morzinski, D. J. McComas, and G. D. Reeves (2001), Two-satellite observations of substorm injections at geosynchronous orbit, *J. Geophys. Res*., 106(A5), 8405–8416, doi:10.1029/2000JA000080.

Tsyganenko, N. A., and D. P. Stern (1996), Modeling the global magnetic field of the large-scale Birkeland current systems, *J. Geophys. Res*., 101(A12), 27,187–27,198, doi:10.1029/96JA02735.

Turner, D. L., X. Li, G. D. Reeves, and H. J. Singer (2010), On phase space density radial gradients of Earth's outer-belt electrons prior to sudden solar wind pressure enhancements: Results from distinctive events and a superposed epoch analysis, *J. Geophys. Res*., 115, A01205, doi:10.1029/2009JA014423.

Vasyliunas, V. M. (1968), A survey of low-energy electrons in the evening sector of the magnetosphere with OGO 1 and OGO 3, *J. Geophys. Res*., 73(9), 2839–2884, doi:10.1029/JA073i009p02839.

Walker, R. J., and M. G. Kivelson (1975), Energization of electrons at synchronous orbit by substorm-associated cross-magnetosphere electric fields, *J. Geophys. Res*., 80(16), 2074–2082, doi:10.1029/JA080i016p02074.

Wang, C.-P., L. R. Lyons, T. Nagai, J. M. Weygand, and R. W. McEntire (2007), Sources, transport, and distributions of plasma sheet ions and electrons and dependences on interplanetary parameters under northward interplanetary magnetic field, *J. Geophys. Res*., 112, A10224, doi:10.1029/2007JA012522.

Wing, S., and P. T. Newell (1998), Central plasma sheet ion properties as inferred from ionospheric observations, *J. Geophys. Res*., 103(A4), 6785–6800, doi:10.1029/97JA02994.

Wolf, R. A., Y. Wan, X. Xing, J.-C. Zhang, and S. Sazykin (2009), Entropy and plasma sheet transport, *J. Geophys. Res*., 114, A00D05, doi:10.1029/2009JA014044.

Yang, J., F. R. Toffoletto, R. A. Wolf, S. Sazykin, R. W. Spiro, P. C. Brandt, M. G. Henderson, and H. U. Frey (2008), Rice Convection Model simulation of the 18 April 2002 sawtooth event and evidence for interchange instability, *J. Geophys. Res*., 113, A11214, doi:10.1029/2008JA013635.

Yang, J., F. R. Toffoletto, R. A. Wolf, and S. Sazykin (2011), RCM-E simulation of ion acceleration during an idealized plasma sheet bubble injection, *J. Geophys. Res*., 116, A05207, doi:10.1029/2010JA016346.

Zaharia, S., C. Z. Cheng, Jay R. Johnson (2000), Particle transport and energization in association with substorms, *J. Geophys. Res*., 105, A8, doi:10.1029/1999JA000407.

Zhou, X.-Z., V. Angelopoulos, V. A. Sergeev, and A. Runov (2011), On the nature of precursor flows upstream of advancing dipolarization fronts, *J. Geophys. Res*., 116, A03222, doi:10.1029/2010JA016165.

Zelenyi, L. M., Lipatov, A. S., Lominadze, D. G. and Takatkishvili, A. A. (1984), The dynamics of the energetic proton bursts in the course of the magnetic field topology reconstruction in the Earth's magnetotail, *Planet. Space Sci.*, **32**, 313.